THE UNIVERSITY OF CHICAGO

INTEGRATING SURFACE ACOUSTIC WAVES AND MICROFLUIDIC FLOWS TO
CONTROL NANOPARTICLES AND LIQUID CRYSTALS

A DISSERTATION SUBMITTED TO
THE FACULTY OF THE PRITZKER SCHOOL OF MOLECULAR ENGINEERING
IN CANDIDACY FOR THE DEGREE OF
DOCTOR OF PHILOSOPHY

BY
GUSTAVO ANDRÉS VÁSQUEZ MONTOYA

CHICAGO, ILLINOIS
AUGUST 2023

CONTENTS

LIST OF FIGURES

LIST OF TABLES

AKNOWLEDGEMENTS

I will start by thanking my friends and loved ones, for giving me the strength to persevere in the completion of this work. I dedicate this book to my family, for the sacrifice and love of my parents, and the warm support of my brothers and sister. I dedicate this book to my friend Allan D. Rodriguez-Aristizabal, for his unconditional support in the darkest moments. A special dedication to Rachel Holcomb, for her inspiring kindness and love.

I am grateful to my advisors, Juan de Pablo and Melody Swartz, to whom I have deep respect and admiration. Their patience, counsel, and trust where instrumental throughout my doctoral journey. This project was only possible due to the amazing research community of the Pritzker School of Molecular Engineering and the University of Chicago, as such a complex interdisciplinary endeavor was bolstered by the incredible collaborative environment among outstanding scientists and engineers. I want to thank the members of both labs, for embracing and helping me with advice, mentoring and friendship. Special acknowledgments to Dr. Jose Adrian Martinez-Gonzalez, Dr. Antonio Tavera-Vazquez, and Tadej Emersic, for their guidance, mentorship, and profound contributions to this work.

I am deeply grateful to Professor Juan Pablo Hernandez-Ortiz, for his invaluable support. His expertise and guidance over the years has deeply influenced my professional development, and I thank him for the encouragement to pursue my doctoral studies.

I have had the privilege of working with exceptional colleagues from a broad variety of fields, including in no particular order: Dr. Lea Maillat, Dr. Priscilla Briquez, Dr. Sylvie Hauert, Dr. Renata Mezyk-Kopec, Dr. Shann Yu, Dr. Andrew Tremain, Lorenzo Netti, Dr. Audrey Bienfait, Dr. Melody Lim, Dr. Hoang Van Phan, Dr. Jonathan Matthews, Prof. Savas Tay, Prof. Mustafa Guller, Prof. Monirosadat (Sanaz) Sadati, Prof. Orlando Guzman,

ABSTRACT

Microfluidic technologies have enabled precise manipulation of small volumes of fluids reducing sample consumption, enhancing reaction control, increasing throughput, and facilitating automation. Important challenges to be addressed include precise particle manipulation, separation of complex samples, and integration of functionalities. Achieving high-resolution manipulation, particularly for small-scale particles, demands advanced techniques and precise flow control challenging when dealing with multiple particle types or heterogeneous populations. Thus, efficient separation, sorting, and characterization of such samples is critical. In parallel, microfluidic solutions can integrate optical components with fluidic systems, enabling on-chip optical analysis, sensing and manipulation that leverage the interaction of light with fluids. Optofluidics technologies faces challenges in the alignment of optical components, integration of light sources and detectors, and the optimization of fluidic and optical interfaces. Here, liquid crystals offer benefits, enhancing their functionality and performance being highly tunable and reconfigurable structured materials. The integration of acoustic waves into microfluidic devices have been applied to address challenges in mixing, atomizing, droplet manipulation, and particle manipulation for Lab-on-a-chip applications with an emphasis on actuation of micro-objects, such as droplets, bacteria, red blood cells, cancer cells, exosomes, and extracellular vesicles. This technology offers a label-free, contactless filtration approach. However, the acoustofluidic filtration of nanoparticles has proven to be challenging and no reliable approach has put forth to separate nanoparticles from microparticles and smaller molecules in solution.

This dissertation explores the implementation of acoustic waves in microfluidic devices to engineer solutions in two emerging field in microfluidics: I) acoustofluidic nanoparticle purification; and II) optofluidic applications with liquid crystals.

From the interaction of waves with fluids emerge two distinct mechanisms that are commonly at odds: the acoustic radiation force and the acoustic streaming. In this work, a microfluidic platform that combines both mechanism driving the separation of 150-300 nm particles from micron-size particles and small molecules in solution is presented. This strategy shows differential separation of particles yielding 83% particle recovery and 75% reduction in concentration of solutes. The acoustic focusing and separation in microfluidic channels separates both polystyrene particles and extracellular vesicles from cell culture. Supporting numerical simulations identify asymmetries in the force fields acting on the particles arising from changes in wave amplitude as the mechanism driving particle displacement. Taken together, the findings presented here show a novel method of acoustofluidic purification towards continuous, high-throughput, and highly automatable point-of-care purification systems.

In addition, this work characterizes the effects of microfluidic flows and acoustic fields on the molecular orientation and optical response of nematic liquid crystals. After introducing acoustic waves in confinement, previously unknown structures are identified which are rationalized in terms of a state diagram as a function of the strengths of the flow and the acoustic field. The new structures are interpreted by relying on calculations with a free energy functional expressed in terms of the tensorial order parameter, using continuum theory simulations in the Landau-de Gennes framework. Taken together, the findings presented here offer promise for the development of new systems based on combinations of sound, flow, and confinement.

CHAPTER 1

INTRODUCTION AND BACKGROUND

In this chapter, we provide a detailed description of the background needed to better understand the scope and impact of the research work presented in the following chapters. The description will focus on three main areas that coalesce to give rise to our unique field of study: I) Nanoparticle technology; II) The study and application of liquid crystals: and III) The use of acoustic waves in microchannels.

1.1 Nanoparticles: Properties, Synthesis and applications

Generally, the term nanoparticle is used to group all material aggregates and structures that have a size < 1 μm. Thus, nanoparticles are made of different types of molecules or materials and have different shapes, size distributions, and molecular structures; they can be spherical, cylindrical, tubular, conical, hollow core, spiral, flat or irregular, ranging from 1 nm to 500 nm in size. Similarly, the particle surface can be a uniform, irregular or with a rich and varied molecular composition. Some nanoparticles are crystalline or amorphous with single or multi crystal solids either loose or agglomerated [1, 2]. A plethora of products and services make use of nanoparticles to confer additional properties or to circumvent traditional limitations of bulk materials. Researchers have explored for decades how to produce nanometer-size materials and structures that exhibit unique and innovative properties. The interest in nanoparticles lies on the unique physical, chemical, and biological properties not commonly found in their bulk counterparts or to their respective particles at higher scales. For most nanoparticles,

the desirable properties arise due to an increase of surface area, reactivity, chemical stability, enhanced mechanical strength or improved transport, as well as structural characteristics such as nanoparticle size, composition, and morphology[1, 3, 4]. Inorganic nanoparticles have been used extensively as catalytic[5], therapeutic[6], and plasmonic materials[7]. Valuable chemical industry products are a result of designing and tuning properties within a material through the incorporation of nanoparticles: I) Additives for color, thermal and light stability or improved strength significantly improve the value of polymer blends; II) Hardness can be added to a product using small, hard particles. III) UV-radiation absorption, magnetization, color, or reflectivity can be added to an otherwise sensitive material base in the form of nanoparticles.[8] Alternatively, Nanotechnologists have developed tools of potential interest for chemical, cell, and disease biology research. Biocompatible carriers have been developed to solubilize and stabilize compounds and to target locations in live cells and animals while attenuating toxicities[4]. In addition, Nano-imaging agents capable of high-resolution snapshots of biological processes in real time at single-molecule resolution, in live cells, and in vivo have been developed. Nano-sensors can detect wide ranges of bio-analytes within live cells and in vivo, allowing researchers to better interrogate chemical or biological perturbations[4]. Therapeutic delivery and stable signal transduction from biocompatible nano-reporters, along with high-resolution imaging modalities, can be used to gain insights into important biological processes. Soluble nanoparticles may serve as templates for nanopores that are otherwise difficult to manufacture, especially at large scale[4]. Particularly sustainable particles are based on limestone, and permit nanopore introduction at low environmental burden[8]. Current interest in ensembles of inorganic nanoparticles is motivated by our ability to exploit their collective properties and the possibility of using these properties in functional devices. Ensembles of nanoparticles can be used to improve the mechanical properties of composite materials, and they can also allow multiple tasks to be performed simultaneously or in sequence. Ensembles of nanoparticles can also display new electronic, magnetic, and optical properties because of interactions between the excitons, magnetic moments, or surface plasmons of individual nanoparticles. It should be possible to exploit these

properties in devices, and the directionality and long-range order found in ensembles, if the spacing and alignment of individual nanoparticles can be controlled[9].

1.1.1 Categories of nanoparticles

Nanoparticles include a broad spectrum of particles with different compositions, shapes, functions, and properties. Thus, most methods to categorize nanoparticles are bound to have many special cases and exceptions. Nevertheless, some relevant groups of nanoparticles are worth highlighting for their significance in industrial or medical applications. Traditionally, nanoparticles have been categorized by the chemical industry as a function of material classes: metals[10], oxides[11] and polymers[12] particles. More recently however, nanoparticles have been classified into three distinct groups: I) Inorganic; II) Organic; and III) carbon-based nanoparticles[1].
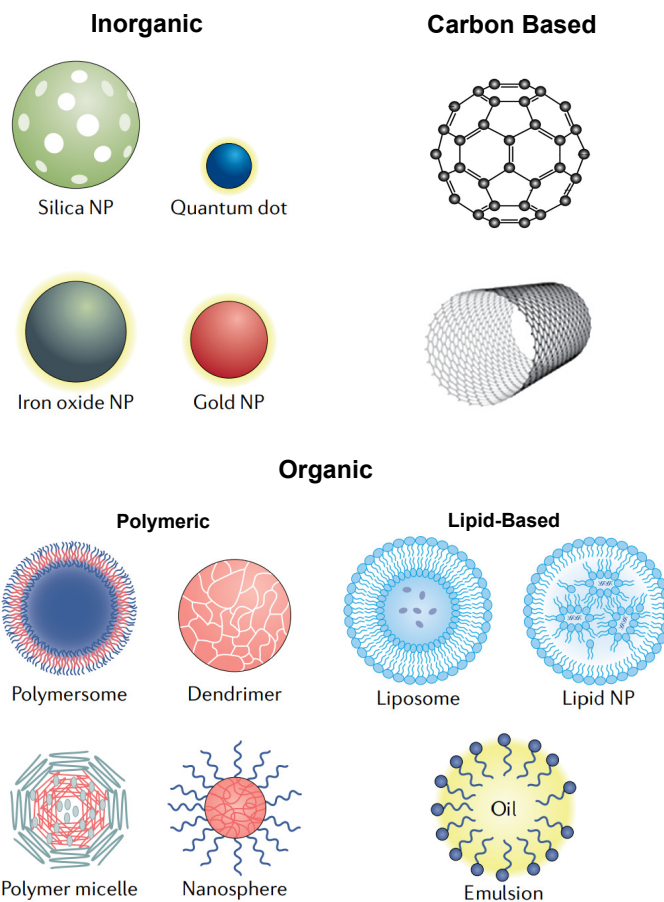
FIGURE 1.1: **Classes of Nanoparticles.** Schematic representation of different types of nanoparticles. Each class has unique properties confering specific advantages for different applications. Adapted from [13].

Inorganic nanoparticles:

Inorganic nanoparticles are particles that are not made up of carbon. Instead, they are composed of metal and metal oxides. Metal based nanoparticles are synthesized from metals to nanometric sizes either by destructive or constructive methods, being able to synthesize nanometer-sized particles with almost all the metals[1, 14]. Commonly used metals for nanoparticle synthesis include aluminum, cadmium, cobalt, copper, gold, iron, lead, silver, and zinc[15]. These nanoparticles have sizes as low as 10 to 100nm, high surface area to volume ratio, high pore size, high surface charge and surface charge density, crystalline and amorphous structures, spherical and cylindrical shapes and color, reactivity, and sensitivity to environmental factors. Moisture, heat and sunlight can alter metallic nanoparticles properties and chemical composition[15, 16]. Thus, Metal oxide-based nanoparticles are synthesized to modify the properties of their respective metal-based nanoparticles. Nanoparticles of iron that oxidize to iron oxide (Fe_2O_3) can increase their reactivity. Similarly, other Metal oxide nanoparticles are synthesized due to their increased reactivity and efficiency including particles made of Aluminum oxide (Al_2O_3); Cerium oxide (CeO_2); Iron oxide (Fe_2O_3); Magnetite (Fe_3O_4); Silicon dioxide (SiO_2); Titanium oxide (TiO_2); or Zinc oxide (ZnO)[15, 1, 17].

Organic nanoparticles:

These nanoparticles are formed by the aggregation or self-assembly of multiple types of biomolecules including lipids, polysaccharides, nucleic acids, small peptides, and proteins. Organic nanoparticles are biodegradable and non-toxic while exhibiting greater flexibility and compressibility to their inorganic counterparts[15]. However, Organic nanoparticles have significantly lower half-life and shelf-life as well as photosensitivity and heat denaturation. Some particles can show a hollow core, different hydrophobic and hydrophilic behaviors and tunable permeability[15, 16]. These unique characteristics makes them an ideal choice for drug delivery. Their drug carrying capacity, stability as delivery systems, the size, composition, surface morphology, determines their field of applications and their efficiency. In addition, organic nanoparticles can be

safely injected in live organisms for targeted drug delivery. Commonly knows examples of organic nanoparticles include Dendrimers, micelles, liposomes, exosomes, and other extracellular vesicles[1].

Carbon-based nanoparticles:

Nanoparticles made completely out of carbon are knows as carbon based. They can be classified into fullerenes, carbon nano tubes (CNT), carbon nanofibers and carbon black[15, 1]. Fullerenes are spherical carbon molecules made up of carbon atoms held together by sp2 hybridization. About 28 to 1500 carbon atoms forms the spherical structure with diameters up to 8.2 nm for a single layer and 4 to 36 nm for multi-layered fullerenes. In contrast, graphene is a hexagonal network of carbon in a honeycomb lattice made up by atoms in a two-dimensional planar surface with a graphene sheet thickness around 1 nm. Carbon Nano Tubes (CNT) are graphene nano-foils where the honeycomb lattice wound into hollow cylinders to form nanotubes of diameters as low as 0.7 nm and as large as 100 nm for multi-layered CNT. The length of CNT varies between a few micrometers to several millimeters with hollow or closed ends. Similarly, Carbon Nanofibers are graphene nano-foils wound into a cone or cup shape instead of a regular cylindrical tube. Lastly, the term carbon black is used to denote an amorphous material made up of carbon derived from the incomplete combustion of coal or petroleum products. Generally spherical in shape with diameters from 20 to 70 nm., the interaction between the carbon black particles is sufficiently strong to promote the formation of 500 nm agglomerates[15, 1].

1.1.2 Properties of Nanoparticles

The properties of nanoparticles can be divided into physical and chemical in nature. The physical properties of nanoparticles include I) optical properties such as the reflected color, its light penetration, absorption and reflection capabilities, UV absorption and reflection in solution, or the coupling of solitons and excitons; II) mechanical properties such as elastic, ductile, tensile strengths, flexibility, compressibility, and their rheology; III) Thermal properties including conductivity and heat capacity as well as

thermal stability. IV) hydrophilicity and hydrophobicity; V) diffusion, suspension, and settling characteristics; VI) Magnetic and electrical properties such as conductivity, semi conductivity and resistivity. The chemical properties of nanoparticles include I) the reactivity with the target and the catalytic efficiency; II) the stability and sensitivity to factors such as moisture, atmosphere, heat, and light; III) The antibacterial, anti-fungal, disinfection, and toxicity properties of the nanoparticles for biomedical and environmental applications; IV) the corrosive, anti-corrosive, oxidation, reduction, and flammability characteristics of the nanoparticles. V) The surface composition and reactivity as well as the surface adsorption and potential functionalization.[15, 1] Ensembles of nanoparticles show properties that may be quite different from those of discrete nanoparticles and corresponding bulk materials[9]. This are evident when analyzing biological nanoparticles with unique enzymatic and transportation capabilities such as exosomes. With the advancement in techniques for the synthesis of complex Inorganic nanoparticles, new collective properties originating from the coupling of the surface plasmons, excitons or magnetic moments of individual nanoparticles, or from a coherent state of the collections of nanoparticles can be observed. For example, coherent vibration of nanocrystals has been found for self-assembled face-centered cubic supra-crystals of silver nanoparticles[18, 9, 19].

1.1.3 Synthesis of nanoparticles

Despite tremendous advances in the synthesis of inorganic particles using conventional approaches5, it has been challenging to precisely control a particle's structure without tedious synthetic tuning. In addition, only recently are we able to create libraries of well-defined and systematically varied particle structures that are compatible with high-throughput screening using Nanoreactors. Most synthesis methods cannot reliably create this library, resulting in a lack of availability for the chemical and diagnostics industries[3]. Nanoparticles rarely form spontaneously, and their large surface area usually demands for sophisticated manufacturing routes. In general, two synthesis pathways can be distinguished: I) The Bottom-up or constructive method involve the build-up of material from atom to clusters to nanoparticles. bottom-up meth-

ods for nanoparticle production include colloidal synthesis, chemical vapor deposition (CVD), spinning, pyrolysis, biosynthesis and molecular self-assembly [1]; II) The top-down method or destructive method, where bulk material is reduced or fractionated to nanometer-size particles. Mechanical milling, nanolithography, laser ablation, sputtering and thermal decomposition are some of the most widely used top-down synthesis methods[1].

Bottom-up synthesis methods:

Colloidal synthesis:

As the preferred bottom-up method due to its simplicity, colloidal synthesis is a wet-chemical process that uses a chemical solution acting as a precursor for an integrated system of discrete particles. Here, Raw material may be transformed into a distinct molecular intermediate through a chemical dissolution process. That intermediate is then reacted in a kinetically controlled way, or using interface stabilizing reagents yielding the desire nanoparticle [20]. The precursor is dispersed in a solvent either by shaking, stirring or sonication resulting in a system containing a liquid and a solid phase. A phase separation is carried out to recover the nanoparticles by various methods such as sedimentation, filtration and centrifugation and the moisture is further removed by drying[21]. Metal oxides and chlorides are the typically used as precursors[22]. The best-known examples of this methods are I) the preparation of quantum dots using a capping agent; and II) the preparation of silver nanoparticles from silver nitrate[8].

Chemical Vapor Deposition (CVD):

CVD deposits a thin film of gaseous reactants onto a substrate. The deposition is carried out in a reaction chamber at ambient temperature by combining gas molecules. A chemical reaction occurs when a heated substrate comes into contact with the combined gas[23]. This reaction produces a thin film of product on the substrate surface that is recovered and used. Substrate temperature is the influencing factor in CVD. This method yields highly pure, uniform, hard and strong nanoparticles, but requires special equipment that can produce highly toxic gaseous by-products[24].

Spinning disc reactor (SDR):

The synthesis of nanoparticles by spinning is carried out by a spinning disc reactor (SDR). Here, a rotating disc is placed inside a chamber controlling parameters such as temperature and pressure. The reactor is generally filled with an inert gas to avoid unwanted chemical reactions[17]. The disc is rotated at different speed where the precursor and water are pumped in. The spinning causes the atoms or molecules to fuse together forming nanoparticles that are then precipitated, collected, and dried[25]. The various operating parameters such as the liquid flow rate, disc rotation speed, liquid/precursor ratio, location of feed, disc surface, etc. determines the characteristics nanoparticles synthesized from SDR[1, 17].

Pyrolysis:

Pyrolysis is the most used process in industries for large scale production of nanoparticles. It involves burning a precursor with flame followed by collection and separation of the produced particles. Carbon black is a key example of nanoparticle products derived from pyrolysis. In this synthesis method, the precursor is either a liquid or a vapor fed into the furnace at high pressure through a small hole where it burns[26]. The combustion or by-product gases are then classified to recover the nanoparticles. Despite the environmental challenges associated with this method, pyrolysis provides a simple, efficient, cost effective, and continuous process with high yield[26].

Biosynthesis:

This method uses bacteria, plants, fungi, or animal cells along with the precursors to leverage their metabolism and extraordinary catalytic abilities to produce or modify nanoparticles. Thus, the biosynthesized nanoparticles have unique and enhanced properties. Through this method, engineers and scientist can manufacture highly complex nanoparticles with a broad variety of unique properties and functions that can be used in biomedical applications[27]. Biosynthesis is a green and environmentally friendly approach for the synthesis of nanoparticles that are nontoxic and biodegradable[28].

Nanoreactors:

Nanoreactors are small reaction vessels with maximum dimensions in the nanometer range. They allow chemical reactions to occur within them while isolated from the surrounding environment and they can be used either to achieve large-scale chemical transformations or to template the synthesis of complex nanoparticles[29]. Nanoreactors have emerged as exceptional alternatives to traditional methods of synthesizing nanoparticles[30], because their confined volumes provide an isolated space for particle nucleation and growth, where the morphology and chemical contents of the reactor and its subsequent processing dictate the final particle structure[3]. Solution-based nanoreactors, for our purposes, include any colloidal container that can be manipulated in solution. These nanoreactors have a 3D structure that encapsulates the metal precursor either through physical entrapment or binding to internal moieties. Solution-based nanoreactors allow the mass transfer of reducing agents into the reactor and do not allow the transfer of precursor salts or zero-valent atoms out. In general, fast-reduction schemes are preferred, such that, upon incorporation of the reducing agent, nucleation rapidly commences, and super-critical nuclei are recruited into larger particles, which do not escape the reactor due to diffusion constraints[29, 31]. solution-based nanoreactor syntheses are attractive because of their greater throughput, scalability, and ability to generate uniform structures in terms of size and shape. Examples of solution-based nanoreactors include Dendrimers, microemulsions, proteins, liposomes and vesicles, hollow shells, polymer assemblies and droplet-based microfluidics[3]. Substrate-confined nanoreactors are reactors in which at least one of the reactor boundaries is terminated by a solid substrate, creating a diffusion constraint at that interface. The goal of many substrate-confined nanoparticle syntheses is to achieve control over the position and arrangement of nanoparticles. In this realm, substrate-confined nanoreactor methods perform remarkably well. Many alternative nanolithography techniques, including those that employed nanoreactors, were invented as next-generation alternatives to conventional top-down lithographic techniques, such as photolithography and e-beam lithography. Conventional lithography strategies have since vastly outperformed expec-

tations in terms of transistor density limits[32] and new applications of these technologies have emerged, for example, in single-particle experiments, where a single particle's structure–property– performance relationships can be mapped uniquely[33]. For these reasons, nanoreactors that provide both structure and position control on a surface have great potential to address a significant synthetic challenge discussed previously: the preparation of position-encoded libraries for high-throughput screening. Examples of substrate-confined nanoreactors include porous solid templates, scanning probe templated synthesis, block copolymer micelle nanolithography[33].

Nanoparticle self-assembly:

Self-assembly provides a simple and low-cost method for producing ensembles of nanoparticles in a controllable manner[9]. This Assembly is governed by the balance of attractive forces such as covalent or hydrogen bonding, electrostatic attraction, depletion forces or dipole–dipole interactions; and repulsive forces such as steric forces and electrostatic repulsion. Self-organization of nanoparticles generates a variety of structures, including chains[34, 35], sheets[36], vesicles[35, 37], three-dimensional (3D) crystals[38] or more complex 3D architectures[39]. In addition, a broad range of objects such as functionalized surfaces[40, 41], carbon nanotubes[42], block-copolymers[43], viruses[44] or DNA molecules[45] can be used as templates for nanoparticle organization[46]. Strong interactions between a template and precursors lead to the arrangement of nanoparticles in structures that are predefined by the template shape and functionalization. Assisted self-assembly on the other hand employs electric or magnetic fields, shear or light offering a combination of speed and precision, as well as the ability to manipulate nanoparticle assemblies[9].

Top-down synthesis methods:

Mechanical milling:

Among the various top-down methods, mechanical milling is the most extensively used to produce various nanoparticles. Here, suitable powder charge is placed in a high energy mill, along with a suitable milling medium. The objective of milling is to reduce the

particle size and blending of particles in new phases. The different type of ball milling can be used for synthesis of nanomaterials in which balls impact upon the powder charge[47]. Plastic deformation is an influencing factor in mechanical milling leading to particle warping, fracture, and decrease in particle size. Conversely cold-welding may leads to increase in particle sizes[1]. Despite these issues promoting polydispersity during nanoparticle production using mechanical milling, this method remains a simple, low cost and in high yield strategy used in multiple industrial applications[48].

Nanolithography:

Nanolithography allows the fabrication of nanometric scale structures using light exposure into a photosensitive material that selectively removes a portion of material to create the desired shape and structure. There are various nano-lithographic processes including optical, electron-beam, multiphoton, nanoimprint and scanning probe lithography[49]. This method allows spatial control on the position of the nanoparticles and can be used to create complex arrays and distributions of particles with desired shape and size. Importantly, this method the requirement expensive equipment and specialized highly trained personnel[50].

Laser ablation.

Laser Ablation Synthesis is a common method for nanoparticle production where the irradiation of a metal submerged in a liquid solution by a laser beam condenses a plasma plume that produces nanoparticles[51]. It is a reliable top-down method that provides an alternative solution to conventional chemical reduction of metals to synthesis metal-based nanoparticles. This method provides a stable synthesis of nanoparticles in organic solvents and water that does not require any stabilizing agent or chemicals. Thus, it is considered as a green alternative for top-down synthesis[15].

Sputtering:

Sputtering is the deposition of nanoparticles on a surface by ejecting particles from it by colliding with ions[52]. Sputtering is usually a deposition of thin layer of nanopar-

11

ticles followed by annealing. The thickness of the layer, temperature and duration of annealing, substrate type, etc. determines the shape and size of the nanoparticles[53].

Thermal decomposition:

Thermal decomposition is an endothermic chemical decomposition produced by heat that breaks the chemical bonds in the compound[14]. The specific temperature at which an element chemically decomposes is the decomposition temperature. The nanoparticles are produced by decomposing the metal at specific temperatures undergoing a chemical reaction producing secondary products[16, 1].

1.1.4 Overview of nanoparticle applications

With the multitude of unique properties that can be achieved by using or adding nanoparticles into materials or processes, it not surprising that a broad array of applications has been developed over the years. Although this list is not comprehensive, it does highlight the multitude of exciting developments originated or under development that use nanoparticle technologies.

Additives:

Perhaps the oldest and most stablished use of nanoparticles, specially in the chemical industry, involves the addition of nanoparticles to a formulation, mixture, or material to provide or enhance its properties. Examples of nanoparticle additives include I) addition of TiO2 particles or o submicron size TiO2 aerosols as the key ingredient to white paint due to TiO2 high whitening properties[8]; II) SiO2 aerosols as Industrial base chemical; III) Polymer fillers used to alter the permeability of polymer films by dispersing platelet fillers in a polymer matrix[8]. The particles reduce permeability of the film by orders of magnitude compared to the polymer alone[54]. Applied flakes include nanoclays, graphite, mica or vermiculite; IV) Inorganic UV absorbing pigments based on titania and zinc oxide were introduced at large scale into polymers, consumer goods and surface treatments; V) Amorphous silica used as rheology additive in powders, anti-caking agent in food products, as additive in animal feed, or as support for
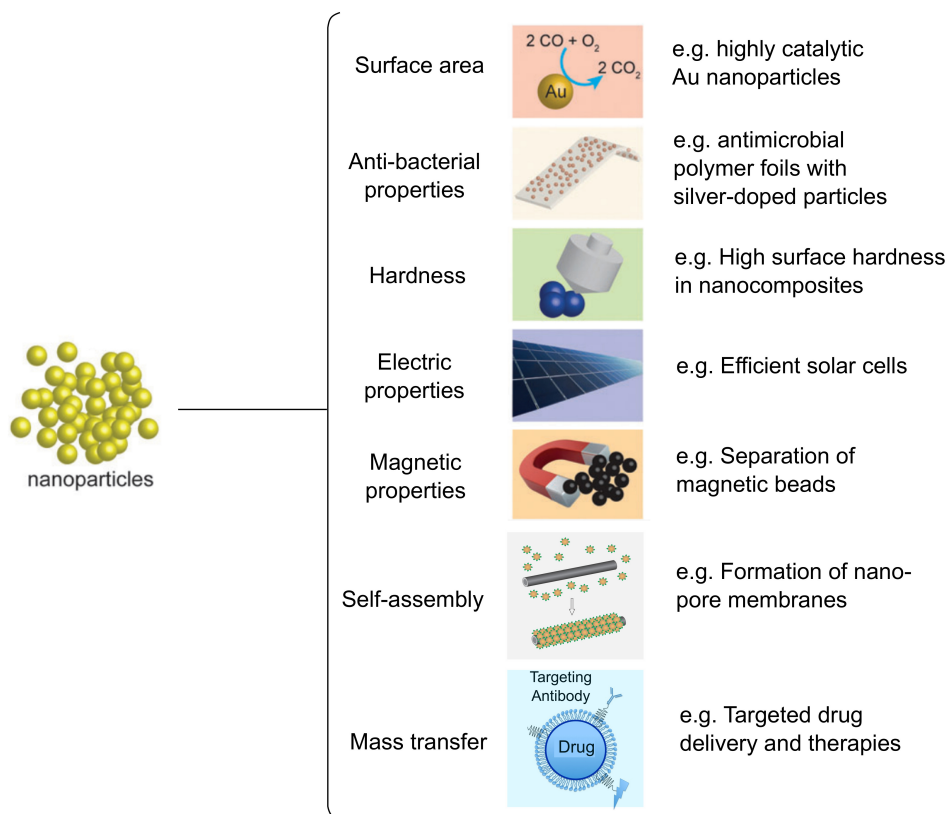
FIGURE 1.2: **Nanoparticle applications based on particle properties.** Examples of key applications of nanoparticles based on the fundamental properties conferred by the use or addition of the particles. From enhanced cathalysis and coating additives to drug delivery and assembly of complex patterns, there is a broad range of applications using unique features of nanometer-sized materials. Adapted from [8].

heterogeneous catalysts; VI) Area dependent industries that profit from advances in nanoparticle research using cost effective nanometer-thick active coatings with particles of 50 nm as a monolayer. VII) silver nanoparticles as antimicrobial agents in consumer surfaces.[15, 16, 8]

Catalysis:

As highlight before, addition of nanoparticles can initiate, promote, or accelerate chemical reactions due to increase reactivity, chemical composition, and high surface area/volume ratio. The surface activity of gold is undoubtedly the most prominent example with industrial relevance[55]. Nonetheless, catalyst using Ni, Pd and Pt nanoparticles where employer for over half a century. Since gold nanoparticles combine mobility, strong coloration, and the possibility for attachment of biomolecules,

these metal particles are used in diagnostic tools, and multiple biological assays[15]. Recently, liposomes and vesicles have been used as nanoreactors to control the rate of reaction and produce small quantities of special solutes as well as the production of smaller nanoparticles[3].

Photonics:

Nanoparticles have been recognized by their ability to absorb and diffract light, changing the optical properties of material and offering unique advantages in fields like coatings, dies and paints and color filters[16]. The electromagnetic radiation interacts with small particles resulting in scattering, angle dependent reflection and various non-linear optic effects. These size-dependent effects are typical for a given size range, with visible light is strongly scattered in the 20–500 nm range. the complex interaction between nanoparticles and light provides a large source for new and improved optical properties on materials[8]. Quantum dots, small semiconductor particles with size controlled electronic levels and therefore also color, have shown a remarkable versatility to absorb, emit or reflect photons while the organization of particle permits control of tunability and control of complex optical responses with reduced noise[56, 57].Thus, the organization of nanoparticles into self-assembled structures has reduced the size of optoelectronic devices and components such as plasmon waveguides, focusing lenses, light generators, and optical switches[35, 58]. The emerging applications of coupled self-assembled nanoparticles have been mostly demonstrated for sensing and imaging purposes. Self-assembled nanoparticle structures have been used in sensors exploiting changes in the plasmonic wavelengths of metal nanoparticles, changes in the photoluminescence of semiconductor nanoparticles, or variations in the magnetic relaxation of magnetic nanoparticles in different chemical or biological environments[35]. In contrast, nanoparticle-based components produced by nanofabrication techniques such as electron beam lithography have been included in optical devices[59, 60]. In addition, the co-self-assembly of several types of semiconductor nanoparticles with different bandgaps may create a stack of cascaded multiple p–n junctions with bandgaps matched to the solar spectrum, thereby reducing the heat loss due to carrier relaxation. Furthermore,

the efficiency of photovoltaic devices may benefit from the ordering, orientation, and close packing of anisotropic rod-shaped semiconductor nanoparticles[61].

Biology:

Synthetic nanomaterials can interact with biological processes on cell surfaces, inside living cells, and even within specific intracellular compartments[4]. The size, physico-chemical control, and resulting biological interactions of nanomaterials have facilitated abundant investigative directions, including chemical-, cell-, and mechanobiology, for studying a wide range of biomolecules and cellular processes[4]. Multiple broad classes of nanomaterials, from inorganic to biodegradable polymers, have been developed for molecular delivery, enzymatic catalysis, molecular imaging, and molecular sensing. In addition, several nanomaterial applications have reached the clinic[62]. Potent modulators, including agonists, antagonists, degraders of biomolecules may not exhibit ideal functionality in vivo due to limited solubility, stability, biocompatibility, poor pharmacokinetics, and off-target activity[63].

Drug delivery:

Controlling the size, shape, and surface chemistry of nanocarriers can target them to specific organs or tissues. Most nanoparticles carriers < 200 nm in size exhibit localization to the liver and spleen, resulting in hepatobiliary clearance[64]. Similarly, nanoparticles exhibit some tumor localization due to leakiness of the tumor vasculature in tumor-bearing animals, enhancing permeability and retention[65]. Ultra-small nanoparticles exhibit renal clearance from the body[66], whereas mesoscale nanoparticles and carbon nanotubes exhibit renal tubular localization and retention[67, 68]. In addition, Particles 10–80 nm in size can localize to the glomeruli of the kidneys[69]. These differences allow specific targeting using nanoparticles that can be supplemented by adding surface ligands or proteins. Nanoparticles have the potential to improve the stability and solubility of encapsulated cargos, promote transport across membranes and prolong circulation times to increase safety and efficacy[63]. For these reasons, nanoparticle research has been widespread, generating promising results in vitro and

in small animal models[70, 71]. A wide range of materials have been explored as nanocarriers of bioactive cargos, including lipids, polymers, metals, and other inorganic materials. In parallel, scientists have developed tools to improve delivery and pharmacokinetics of poorly behaved molecules using encapsulation of active cargos and specific targeting of tissues, cells, or organelles[4]. Nanoparticles often enter cells via endocytosis, sequestering particles in late endosomes and lysosomes. In addition, methods such as electroporation, mechanical cellular manipulation via microfluidics, and direct injection enable insertion of nanoparticles into the cytoplasm[16, 72, 4]. Thus, nanoparticles can be engineered to deliver encapsulated chemicals and control release within subcellular organelles or specific organs and tissues. Pharmacokinetic properties of delivered molecules, such as their half-life, can be enhanced by nanocarrier loading. This strategy allows substantial accumulation and functional modifications of encapsulated molecules at nanoparticle-targeted sites compared to free diffusion[73]. Compartmentalization of self-assembled nanoparticles in polymersomes, liposomes or polymer capsules paves the way for producing multifunctional carriers for the delivery of biologically active species or sensing applications in the biological, medical, and pharmacological fields [74, 75, 76]

1.2   Nematic liquid crystals

There are many fluids we interact with regularly in daily routines that exhibit different properties and behaviors to those from simple fluids like pure water, including cosmetics, personal care products, foods, and medical products. In contrast with simple fluids that exhibit Newtonian behavior, complex fluids can be considered broadly as systems with physical attributes intermediate between solids and liquids. In most cases, the solid properties manifest more prominently over the liquid ones at short time scales. However, at long times scales the overall flow properties become visible. The existence of different time scales defines the characteristic non-linear mechanical response of complex fluids to shear stresses and render them viscoelastic, with the non-Newtonian behavior of complex fluids been exploited in engineering applications[77]. Liquid crystals constitute a special class of complex fluid due to the inherent ordering of the molecules. These nematic fluids are liquid materials that show long-range orientational order of the building blocks, which tend to align along a common axis known as the director[78, 79]. In contrast with other states of matter, homogeneous isotropic liquid crystals maintain translational and rotational symmetry while lacking periodicity. However, the translational order is not complete, as the molecules are disordered in at least in one direction. While classical viscoelastic liquids are isotropic, liquid crystals possess anisotropic properties owing to the inherent ordering. In contrast with the isotropic phase, the anisotropic properties of the mesophases arise from the spontaneously breaking of internal symmetry in the liquid crystalline phase[78]. This anisotropy explains why most liquid crystals are made of mesophases of rod-like or disk-like molecules, intermediate between ordered (crystalline) solid phase and disordered (isotropic) liquid phase. The ordering in the mesophase is observed within a finite temperature range Beyond which the material reaches the disordered isotropic phase. Towards the lower end of the temperature range the mesophase approaches a state of perfect ordering similar to solid crystals[80]. Thus, the degree of ordering around the director field is dependent on variables such as temperature, pressure, or density. On the mesoscale, nematic fluids show an effective elastic response to the deformation of

the director. These soft materials are highly responsive to external fields and confinement effects, with a strong coupling between the orientational order and the material flow, which can lead to complex spatial and dynamic patterns within the structure of the director field, degree of order, and material flow[78]. As a consequence, liquid crystals possess hydrodynamic features of complex fluids while exhibiting anisotropy in physical properties. The coupling interaction between the liquid–crystal-ordering and the flow field increases the complexity of these systems, providing a rich system to investigate different competing effects[80]. The dynamics of non-equilibrium liquid crystals structures can be driven by external mechanisms, such as force fields, pressure differences and electromagnetic fields, and internal mechanisms driven by the activity and entropy of the material. Due to the unique functionality of nematic materials and its connection to the material structure, liquid crystals have been used extensively for applications in photonics[81, 82], optics[83, 84, 85], colloidal suspensions[86, 87] and as sensors[88, 89]. For instance, the relative orientation of the electric field and the molecules, combined with the anisotropy in elasticity, viscosity, and dielectric coefficient of the material, have been used for devising liquid crystal displays[85]. In addition, nematic order is an important part of microtubule and actin-based dynamics and morphology of cells[90], behavior of bacterial colonies[91] and tissues[92, 93], and can be also used to guide trajectories of swimming bacteria in materials[94, 95].

1.2.1   Nematic order

As mentioned above, liquid crystals are mesophases that exhibits long-range orientational order comprising molecules with high shape-anisotropy. Due to the high asymmetry in shape, liquid crystal molecules are generally modeled as rigid rods or ellipsoids. Liquid crystalline materials can be divided into two classes: I) thermotropic liquid crystals where the characteristic ordering depends on temperature; and II) lyotropic liquid crystals typically formed by aqueous solution of amphiphilic molecules, where the ordering depends also on the surfactant concentration[79]. These classifications are complemented by different phases that indicate special orientations and symmetries of the fluid under specific thermodynamic conditions (FIG?): The isotropic, nematic,

18

smectic, columnar, cholesteric and crystalline phases.
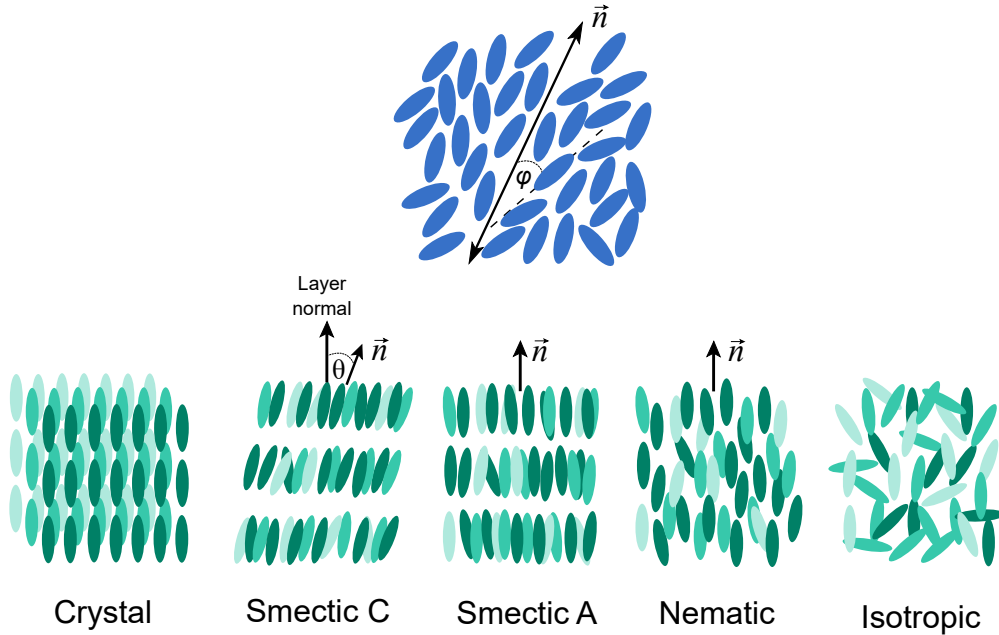
FIGURE 1.3: **Directional Order and liquid crystal mesophases.** Nematic molecules aling along a common axis defined by the director vector **n**. Here, the tilt angle of individual molecules ϕ varies from the director due to thermal fluctuations. Nematic liquid crystal shows long-range organization as function of the temperature ranging from the crystalline phase to the isotropic phase.

The isotropic phase is characterized by disorder in the molecular orientation with random orientation of the molecules in all the orthogonal, commonly observed at high temperatures. Upon cooling, molecules nucleate, organize, and create orientational order. The first phase to arise after cooling an isotropic nematic liquid crystal is the nematic phase. As the least ordered of the mesophases, the nematic phase is characterized by orientational order while having a random distribution of the molecules center of mass[96]. The molecules in the nematic phase align on average parallel to a particular direction defined by the unit vector n called the director[78]. After further cooling, a second mesophase arise known as the smectic phase[97]. Having positional ordering in one direction in addition to orientational order, smectic liquid crystals exhibit defined planes that have a random distribution of the molecules within. The segregation of the molecules into planes leads to the additional ordering in smectic Liquid crystals. Depending upon the extent and nature of ordering, smectic liquid crystals are further categorized as smectic A, smectic B, and smectic C phases. While

smectic A and C phases retain their fluidity as an essential feature, the smectic B phase manifests as a lamellar phase[79]. Eventually, the system temperature can be reduced enough to recover the crystalline state. It is important to highlight that the temperature dependence of the material mesophases is reversible[80]. A variant of the nematic phase is the cholesteric phase, in which the director changes its direction in a helical fashion[98]. Often, a cholesteric phase is obtained after doping the nematic with a chiral molecule and thus this phase is also known as the chiral nematic phase. The structure of the molecules in a liquid crystal can also be used to classify nematic liquid crystals. Calamitic nematic crystals are those formed by molecules with a rod-like structure. Alternatively, discotic nematic crystals contain disc-shaped molecules which usually stack up to form columns forming the columnar phase.

Order parameter in nematic liquid crystals

The nematic order parameter characterizes the orientational ordering of nematic molecules about the ordering axes and provides information on the degree of order along those axes. Given that the nematic mesophases are distinguished by changes in the orientational order and the translational symmetries, the order parameter serves as a quantifying parameter of the molecular order in a liquid crystal. As discussed above, the director $\mathbf{n}$ denotes the average long-range orientation of the molecules. Given the symmetric of the molecules, the apolar order implies that $\mathbf{n} = -\mathbf{n}$. For bi-axial molecules such as discotic nematics a secondary director $\mathbf{e}^{(1)}$ is defined as well. Despite the simplicity and usefulness of the director n, individual molecules will generally be skewed off the director due to thermal fluctuations. These fluctuations can be quantified by the scalar order parameter S. This parameter is evaluated as the ensemble average of the second Legendre polynomials of the scalar product between the molecular vector $\mathbf{u}$ and $\mathbf{n}$.

In a Cartesian coordinate system with the director $\mathbf{n}$ parallel to the z axis, the orientation of individual molecules characterized by the vector $\mathbf{u}$ can be parametrized

with:

$$u_x = sin\theta \, cos\phi, \quad u_y = sin\theta \, sin\phi, \quad u_z = cos\theta \tag{1.1}$$

Here θ and ϕ denote the angular deviations of the molecule along the polar and azimuthal directions, respectively. Defining $f(\theta, \phi)$ as the angular distribution describing the state of molecular orientation, The probability $d\Psi$ to find a molecule oriented within a solid angle $d\Omega$ is given by:

$$d\Psi = \frac{1}{4\pi} f(\theta, \phi) \, d\Omega \tag{1.2}$$

So that, in the isotropic phase where the molecules are evenly distributed with equal probability in all directions we obtain:

$$\int_\Omega f_{iso}(\mathbf{x}) \, d\Omega = 1 \tag{1.3}$$

$$f_{iso}(\mathbf{x}) = \frac{1}{4\pi} \tag{1.4}$$

For uniaxial nematics, $f(\theta, \phi) = f(\theta)$ due to the axial symmetry. Expanding $f(\theta)$ as a sum of the Legendre polynomials we get:

$$f(\theta) = \sum_{n=0}^{\infty} f_n P_n(cos\theta) \tag{1.5}$$

With $P_n(x)$ the nth Legendre polynomial and

$$f_n = \frac{2n+1}{2} \int_{-1}^{1} f(\theta) P_n(cos\theta) \, d(cos\theta) \tag{1.6}$$

The non-zero contributions are due to even terms only, as $f(\theta) = f(\pi - \theta)$ due to the apolarity of the nematic molecules. Given that $f_0 = 1$, the scalar order parameter

is defined by the next non-zero contribution originating from the quadrupolar term:

$$S = \frac{1}{5}f_2 = \frac{1}{2}\int_{-1}^{1} f(\theta) P_2(cos\theta) d(cos\theta) = \langle P_2(cos\theta)\rangle \tag{1.7}$$

$$S = \frac{3}{2}\left\langle cos^2\theta - \frac{1}{3}\right\rangle \tag{1.8}$$

The scalar order parameter S lies within the interval $-1/2 \leq S \leq 1$, where the value of $S = 1$ indicates perfect order, while $S = 0$ indicate no order, corresponding to isotropic case. The negative value of the lower bound $S = -1/2$ corresponds to a theoretical order where all the molecules are perpendicular to the director. In similar fashion, an average alignment along the secondary director $\mathbf{e}^{(1)}$ is given by the biaxiality parameter:

$$P = \frac{3}{2}\left\langle sin^2\theta \, cos(2\phi)\right\rangle \tag{1.9}$$

The scalar order parameter and the biaxial order parameter can be expressed using the tensorial order parameter $\mathbf{Q}$ defined as:

$$Q_{ij} = \frac{S}{2}\left(3n_i n_j - \delta_{ij}\right) + \frac{P}{2}\left(e_i^{(1)}e_j^{(1)} - e_i^{(2)}e_j^{(2)}\right) \tag{1.10}$$

with $\mathbf{e}^{(2)} = \mathbf{n} \times \mathbf{e}^{(1)}$. The tensor $\mathbf{Q}$ a robust platform for the theoretical and numerical study of nematic equilibrium and dynamics, as the tensor approach requires no special treatment of defects[78, 80].

1.2.2 Surface anchoring

The equilibrium nematic director field is dictated by the internal ordering of the mesophase in the absence of external fields or interacting surfaces. The presence of an interface can affect the inherent ordering of the nematic, leading to a modified equilibrium state. Based on the intermolecular interactions at the interface, the liquid crystal molecules in the vicinity of a surface adopt a preferential orientation commonly known as surface anchoring[98].

In general, the director n alignment at the interface is determined by the interaction
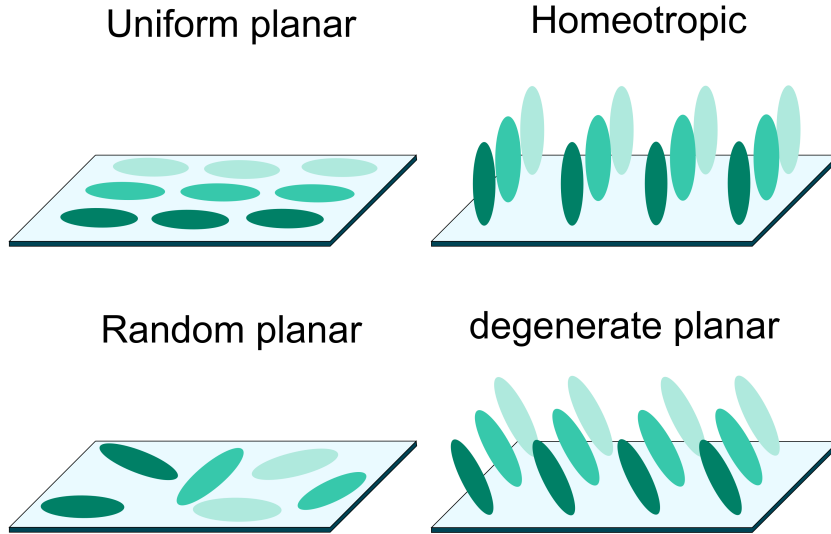
FIGURE 1.4: **Types of surface anchoring.** The most common type of anchoring for liquid crystals are uniform planar and hometropic anchoring. In some instances, the molecules will show a random planar orientation or a degenerate anchoring.

between the liquid crystal and the aligning surface in absence of an elastic torque. Most liquid crystals exhibit one of four surface anchoring configurations: I) Uniform planar anchoring, where the molecules are oriented uniformly parallel to the surface; II) Homeotropic anchoring, where the molecules align perpendicular to the surface; III) random planar anchoring, where the molecules are parallel to the surface but have random orientation in the surface plane; IV) degenerate planar anchoring, where the molecules align at an angle with respect to the surface plane. Orientation of the molecules on the surface is characterized using two angular components[99]: azimuthal anchoring ϕ and polar anchoring θ. The angle ϕ between the director projection and a reference direction on the substrate plane gives the measure of the orientation of $\mathbf{n}$. The pretilt angle θ formed between $\mathbf{n}$ and the vector normal to the substrate provides the tilt of $\mathbf{n}$. Thus, the orientation of the director in terms these angles can be denoted as: I) $\theta = \pi/2$, $\phi = constant$ for uniform planar; II) $\theta = 0$ for homeotropic anchoring; III)$\theta = \pi/2$, $\phi = arbitrary$; and IV) $0 < \theta < \pi/2$, $\phi = constant$ for tilted anchoring. The orientation of $\mathbf{n}$ at the surface extends into the bulk as a consequence of the long-range ordering, minimizing the elastic energy of the system. The anchoring strength is characterized by the amount of energy necessary to deviate the director $\mathbf{n}$. For a

nematic LC in confinement with multiple surface anchoring, the minimization of the energy leads to a continuous tilt of **n**, This is known as hybrid alignment.

1.2.3   Optical anisotropy

The anisotropy observed in multiple properties of liquid crystalline materials stems from the anisotropic shape of the constituting molecules and the resulting molecular order of the mesophase. Anisotropic behaviour is observed in the material optical, magnetic, electrical and thermal and flow properties, among others[80]. In general, the magnitude of the physical property along the director vector **n**, is different from that measured orthogonal to the director. For example, measurement of the Stokes drag on a particle in an NLC mixture conclusively shows the existence of anisotropic diffusion constants[100].

The optical anisotropy in nematic mesophases is made manifest by the distinct values of the refractive indices: $n_\parallel$ along the optical axis and parallel to the director, and $n_\perp$ perpendicular to the director. Most of the nematic and smectic phases have $n_\parallel > n_\perp$ and thus, are optically positive. In addition, uniaxial nematics are characterized by one principal optical axis, making them optically uniaxial[101], while biaxial species with two principal axes are optically biaxial. Due to the optical anysotropy of liquid crystals, a light beam transmitted toward the material at an angle ϕ relative to the optical axis splits into two components: One denominated ordinary ray, having index of refraction n_o; another denominated the extraordinary ray, having index of refraction n_e. The refractive indices corresponding to the ordinary and extraordinary components are related to $n_\parallel$ and $n_\perp$ through the relative angle ϕ as:

$$n_e = \frac{n_\parallel n_\perp}{\sqrt{n_\parallel^2 cos^2\phi + n_\perp^2 sin^2\phi}} \tag{1.11}$$

$$n_o = n_\perp \tag{1.12}$$

As a consequence of the different refractive indices, the ordinary and extraordinary rays propagate through the material at different speeds resulting in a phase difference

of:

$$\delta = \frac{2\pi}{\lambda} \left(n_e - n_o\right) d \tag{1.13}$$

Where λ is the wavelength of the beam propagating in vacuum and d the optical distance within the sample. The difference bewteen the refractive indices is called **optical birefringence**:

$$\Delta n = n_e - n_o \tag{1.14}$$

When the liquid crystals is exposed to a linearly polarized light, a component of the light can pass through a crossed polarizer due to changes in the light path induced by the molecular orientation. The intensity of light coming out the analyzer is given by:

$$I = I_0 \; sin^2\phi \; sin^2 \left(\frac{\delta}{2}\right) \tag{1.15}$$

where I_0 is the intensity of the light after the first polarizer, and ϕ is the angle between the and the optics axis projection. The first term quantifies the intensity of the light transmitted through the crossed polarizers while the second term is responsible for the birefrigent colors in thin nematic films.

1.2.4   Nematic free energy

Multiple models have been developed over the years with the purpose to describe the thermodynamics of phase transition in liquid crystals. In the case of thermotropic liquid crystals, the Landau-de Gennes model if commonly used [78]. This model express the free energy of the nematic as an expansion around the order parameter $\mathbf{Q}$. This formalism assumes that small values of the order parameter near the isotropic-nematic transition to avoid divergence in the series expansion. To maintain the scalar nature of the energy while using the tensorial order parameter, the expansion uses the tensor trace $Tr\left[\mathbf{Q}\right]$. Thus, for a liquid crystal without influence of external fields or

confinement the free energy density can be defined as[102, 103]:

$$f_{phase}\left(T\right) = f_0 + \alpha\left(T\right)Q_{ii} + \frac{1}{2}A\left(T\right)Q_{ij}Q_{ji} + \frac{1}{3}B\left(T\right)Q_{ij}Q_{jl}Q_{li} + \frac{1}{4}C\left(T\right)Q_{ij}Q_{jl}Q_{lm}Q_{mi}$$
(1.16)

Where f_0 corresponds to the free energy of an isotropic reference state with $\mathbf{Q} = 0$. As $Q_{ii} = 0$ by construction, we obtain:

$$f_{phase}\left(T\right) = f_0 + \frac{1}{2}a\left(T - T^*\right)Tr\left[\mathbf{Q}\right]^2 + \frac{1}{3}BTr\left[\mathbf{Q}\right]^3 + \frac{1}{4}C\left(Tr\left[\mathbf{Q}\right]^2\right)^2$$
(1.17)

With $A = a\left(T - T^*\right)$ being the only phenomenological coefficient observed to vary as a function of temperature experimentally [99]. The temperature T^* denotes the super-cooling temperature that marks the metastable limit of the isotropic phase.

While f_{phase} describes the free energy of the liquid crystal without external influence, this condition may not be satisfied even at equilibrium, due to external fields and boundary conditions that impose deformation in the nematic order. The surface-induced order differs from the equilibrium values in the bulk, leading to elastic deformations in the director field as combinations of the basic deformation modes: splay, twist and bend.

Gradients of the order parameter are penalized by the elastic free energy volume density, contributions formed out of the first order space derivatives $\partial Q_{ij}/\partial x_k$ of the order tensor and the elastic constants L1, L2, and L3[78]:

$$f_E = \frac{1}{2}L_1\frac{\partial Q_{ij}}{\partial x_k}\frac{\partial Q_{ij}}{\partial x_k} + \frac{1}{2}L_2\frac{\partial Q_{ij}}{\partial x_j}\frac{\partial Q_{ik}}{\partial x_k} + \frac{1}{2}L_3 Q_{ij}\frac{\partial Q_{kj}}{\partial x_i}\frac{\partial Q_{kl}}{\partial x_j}$$
(1.18)

This equation expressing the elastic energy density can be written using the model proposed by Frank-Oseen as:

$$f_{E,Frank-Oseen} = \frac{1}{2}K_1\left(\nabla \cdot \mathbf{n}\right)^2 + \frac{1}{2}K_2\left[\mathbf{n}\left(\nabla \cdot \mathbf{n}\right) + q_0\right]^2 + \frac{1}{2}K_3\left[\mathbf{n} \times \left(\nabla \times \mathbf{n}\right)\right]^2$$
(1.19)

Where K_1 is the elastic constant due to splay, K_2 is the elastic constant due to twist, and K_3 is the elastic constant due to bend. The Frank-Oseen elastic constants relate the L constants having $L_1 = (K_3 + 2K_2 - K_1)/9S^2$, $L_2 = 4(K_1 - K_2)/9S^2$, and $L_3 = 2(K_3 - K_1)/9S^3$. The constant q_0 is included only in systems lacking inversion symmetry like those in a chiral phase. Typically, $K_3 > K_2 > K_1$ but for simple nematic systems where all the elastic constant can be assumed to be equal $K \approx 1 \times 10^{-11} N$ [78].

The Landau-de Gennes (LdG) formalism incorporate different free energy contributions from multiple factors: the nematic order, the elasticity, contributions due to surface anchoring (f_{Sup}), and effects from external fields (f_F).

$$f_{LdG} = f_{phase} + f_E + f_F + f_{Sup} \tag{1.20}$$

For uniaxial nematics, the surface contribution to the free energy can be expressed as[80, 104]:

$$f_{Sup} = \frac{9}{8}W_e \left[\frac{2}{3}S_s^2 + \frac{2}{3}S_0^2 - 2S_sS_0 \left((\mathbf{n}_s \cdot \mathbf{n}_0)^2 - \frac{1}{3} \right) \right] \tag{1.21}$$

Where W_e represent the strength of the anchoring in energetic terms. Setting $S_0 = S_s$ we obtain the Rapini-Papoular form of the surface anchoring free energy [104]:

$$f_{Sup} = -\frac{1}{2}W_e (\mathbf{n}_s \cdot \mathbf{n}_0)^2 = -\frac{1}{2}W_e cos^2\alpha \tag{1.22}$$

Similarly, The coupling to external fields to the free energy can be introduced through the term f_F. The classical example in nematics involves the use of electric fields. For an anisotropic material, the electric displacement is defined as $\mathbf{D} = \epsilon_0\epsilon\mathbf{E}$, where ϵ_0 is the dielectric permitivity constant in a vacuum and $\mathbf{E}$ the electic field vector. For an uniaxial nematic system, the dielectric tensor ϵ is written as:

$$\epsilon = \begin{bmatrix} \epsilon_\perp & 0 & 0 \\ 0 & \epsilon_\perp & 0 \\ 0 & 0 & \epsilon_\parallel \end{bmatrix} \tag{1.23}$$

Where $\epsilon_\parallel$ and $\epsilon_\perp$ are the relative parallel and perpendicular dielectric constants of the liquid crystal. Thus, the electric displacement is

$$\mathbf{D} = \epsilon_0 \epsilon_\perp \mathbf{E} + \epsilon_0 \epsilon_\alpha \left(\mathbf{E} \cdot \mathbf{n} \right) \mathbf{n} \tag{1.24}$$

The total electic energy contribution from the electric field $\mathbf{E}$ can be calculated as:

$$f_{elec} = \frac{1}{2} \mathbf{D} \cdot \mathbf{E} = \frac{1}{2} \epsilon_0 \epsilon_\perp E^2 + \frac{1}{2} \epsilon_0 \epsilon_a \left(\mathbf{E} \cdot \mathbf{n} \right)^2 \tag{1.25}$$

which can be re-writen in terms of the order parameter tensor $\mathbf{Q}$ as:

$$f_{elec}^Q = -\frac{1}{2} \epsilon_0 \left(\Delta \epsilon E_i^2 + \frac{\epsilon_a}{S} \left(\mathbf{E} \cdot \mathbf{Q} \cdot \mathbf{E} \right) \right) \tag{1.26}$$

Where $\Delta \epsilon = 2\epsilon_\perp + \epsilon_\parallel$ is the average liquid crystal permitivity. In cases where the electic field is is invariant, the first term can be neglected. An external magnetic field couple with the nematic in a similar way, with the dimagnetic permitivity replaces the dielectric constant while the magnetic field $\mathbf{H}$ replaces the electric field $\mathbf{E}$ such that the external field energy contribution assumes the form $f_{Mag} \sim \left(\mathbf{H} \cdot \mathbf{Q} \cdot \mathbf{H} \right)$[105].

1.2.5   Nematodynamics

The term Nematodynamics refers to the hydrodynamic behavior of nematic liquid crystals based on the coupling between the molecular ordering and the material flow. The macroscopic theoretical description of the flow-director coupling has been formalized by Ericksen[106, 107], Leslie[108, 109], and de Gennes[78]. The flow field of a nematic is described by the generalized Navier-Stokes equation:

$$\rho \left[\frac{\partial v_i}{\partial t} + \left(v_j \partial_j \right) v_i \right] = \partial_j \sigma_{ij} \tag{1.27}$$

Where ρ is the density, $\mathbf{v}$ is the velocity, and the stress tensor can be defined as:

$$\sigma_{ij} = \sigma_{ij}^{Er} + \sigma_{ij}^{Maxwell} + \sigma_{ij}^{viscous} + p_0 \delta_{ij} \tag{1.28}$$

With individual contributions from pressure, stress, elasticity and external fields. The Elasticity of the nematic structure can transmit stresses through the bulk as the nematic acts to minimize the free energy by forcing the colloidal particlesto be at an optimal distance from each other. This force can be calculated through the Ericksen stress tensor defined as:

$$\sigma_{ij}^{Er} = -\frac{\delta F}{\delta \partial_j n_k} \partial_i n_k + F_E \delta_{ij} \tag{1.29}$$

Similarly, stress caused by electromagnetic fields can be included using the Maxwell stress tensor defined as:

$$\sigma_{ij}^{Maxwell} = E_i D_j + f_{F,electric} \delta_{ij} \tag{1.30}$$

Derivations of the viscous stress tensor are beyond the introductory nature of this chapter. Shortly, the Ericksen-Leslie-Parodi (ELP) approach has been used to estimate this tensor using the coupling of the nematic director and the velocity field and the relationship between the stress tensor, the molecular field $h_i = -\frac{\delta F}{\delta n_i}$, the rotation rate of the director $N_i = \dot{n}_i - ((\nabla \times \mathbf{v}) \times \mathbf{n})_i /2$,and the symmetric velocity tensor $A_{ij} = (\partial_i v_j + \partial_j v_i) /2$. Consequently, The viscous stress tensor written within the ELP theory takes the form:

$$\sigma_{ij}^{viscous} = \alpha_1 n_i n_j n_k n_l A_{kl} + \alpha_2 n_j N_i + \alpha_3 n_i N_j + \alpha_4 A_{ij} + \alpha_5 n_j n_k A_{ik} + \alpha_6 n_i n_k A_{jk} \tag{1.31}$$

Where α_i are known as the Leslie viscosity coefficients.

1.3   Introduction to acoustofluidics

The use of acoustic waves in microfluidic technologies has emerged as a promising platform for the precise actuation of fluids and the manipulation of particles across a broad size range. Thus, the field of acoustofluidics encompass multiple application where acoustic vibrations are used in conjunction with flow microchannels and electronic circuits. A key feature of acoustofluidic is their spatial and temporal manipulation of matter by using the interaction of sound waves with solids, liquids, and gases. Furthermore, fluid actuation by acoustic waves is complex in analysis but simple in practice, with little hardware required to operate, and offering large actuation forces and force gradients[110]. The use of vibration to manipulate particles within fluids has interested the scientific community for decades, and a substantial number of applications have been developed for science and engineering involving acoustic trapping of particles. These systems are also named 'acoustical tweezers', modeled after their predecessor optical tweezers[111]. Acoustic waves are easily generated within a piezoelectric material through the transduction of electric fields; such waves propagate within and onward to the boundaries of the material in diverse ways dependent on the field and material geometries[112]. While the initial acoustic microfluidic resonators used piezoelectric transducers generating bulk acoustic waves (BAWs), most recent developments use surface acoustic waves (SAWs). The phenomenon of surface acoustic wave (SAW) propagation on a substrate was first reported by Lord Rayleigh[113] but were only properly produced with the maturation of microfabrication technologies to form interdigital transducers (IDTs)[110, 112]. This enables a host of microfluidic operations to be carried out entirely on a chip-scale substrate powered by a palm-sized portable electronic driver circuit[114] Many of the most recent reports in micro/nano acoustofluidics have relied on SAW generation at tens to hundreds of MHz, which was not possible prior to IDTs and reduces the acoustic wavelength to a scale compatible with microfluidics[110]. One of the most attractive aspects of using SAWs for microfluidic actuation and manipulation is their very efficient fluid-structural coupling owing to the presence of most of the energy adjacent to the interface. In addition, the elastic en-

ergy present at high SAW frequencies is responsible for extreme accelerations that can be used for droplet manipulation and mixing[114, 112, 115]. The versatility to generate acoustic waves with frequencies in the kHz-to-MHz range using IDTs[116, 117, 111] , allows I) the manipulation of particles across a length scale spanning more than five orders of magnitude (10^{-7} to 10^{-2}) m); II) access to multiple resonance chambers by combining high frequencies with small features in microfluidics produced through advanced nanofabrication techniques[118]. In addition, the applied acoustic power and frequencies typically used are similar to those used in ultrasonic imaging, which has been safely used in diagnostic applications[111].

1.3.1 Waves in liquids

When the acoustic waves propagate in liquids, the associated fast-moving and rapidly oscillating pressure and velocity fields can impart a slow non-oscillating velocity component to the liquid or to small particles suspended in the liquid[119]. Due to the small length scales in microfluidic systems, these minute effects can be of significance. The acoustic effects on fluids confined by microchannels arise from the non-linearity of the Navier-Stokes equation and the small but non-zero compressibility of ordinary liquids. The wave equation for acoustics is only an approximate equation derived by combining the thermodynamic equation of state, the continuity equation and the dynamic Navier-Stokes equation. Without gravitational and electromagnetic effects, these equations are defined as:

$$p = p\left(\rho\right) \tag{1.32}$$

$$\partial_t \rho = -\nabla \cdot \left(\rho \mathbf{v}\right) \tag{1.33}$$

$$\rho \partial_t \mathbf{v} = -\nabla p - \rho\left(\mathbf{v} \cdot \nabla\right)\mathbf{v} + \eta \nabla^2 \mathbf{v} + \beta \eta \nabla\left(\nabla \cdot \mathbf{v}\right) \tag{1.34}$$

As the acoustic contributions to the pressure, density and velocity of the fluid

31

are small, a systematic method so solve this notoriously complex set of equations is to employ perturbation theory to solve for the main contribution term within the expansion.

Perturbation theory and the acoustic wave equation

For a stationary fluid at equilibrium with $\mathbf{v}_0 = 0$, and constant density ρ_0 and pressure p_0, a an acoustic wave induce a small perturbation on the density, pressure, and velocity fields such that

$$\rho = \rho_0 + \rho_1 + \rho_2 \qquad p = p_0 + p_1 + p_2 \qquad \mathbf{v} = \mathbf{v}_1 + \mathbf{v}_2 \tag{1.35}$$

Where $p_1 = \left(\frac{\partial p}{\partial \rho}\right)_s \rho_1 = c_a^2 \rho_1$. Neglecting product of first-order terms,we obtain the first-order continuity and Navier-Stokes equations:

$$\partial_t \rho_1 = -\rho_0 \nabla \cdot \mathbf{v}_1 \tag{1.36}$$

$$\rho_0 \partial_t \mathbf{v}_1 = -c_a^2 \nabla \rho_1 + \eta \nabla^2 \mathbf{v}_1 + \beta \eta \nabla (\nabla \cdot \mathbf{v}_1) \tag{1.37}$$

Taking the time derivative of equation 1.36 and insertion of equation 1.37 in the resulting expression yields:

$$\partial_t^2 \rho_1 = c_a^2 \left[1 + \frac{(1+\beta)\eta}{\rho_0 c_a^2} \partial_t\right] \nabla^2 \rho_1 \tag{1.38}$$

to facilitate further analytical treatment, we assume a harmonic time dependance of the main fields, with the harmonic expressed by the complex phase $e^{-i\omega t}$, where $\omega = 2\pi f$ is the angular frequency and f the frequency of the acoustic field. Thus, we can express the system scalar and vector fields as:

$$\rho_1 (\mathbf{r}, t) = \rho_1 (\mathbf{r}) e^{-i\omega t} \tag{1.39}$$

32

$$p_1(\mathbf{r}, t) = c_a^2 \rho_1(\mathbf{r}) e^{-i\omega t} \tag{1.40}$$

$$\mathbf{v}_1(\mathbf{r}, t) = \mathbf{v}_1(\mathbf{r}) e^{-i\omega t} \tag{1.41}$$

Consequently, equation 1.38 reduces into the Helmholtz equation for a damped wave with wave number k and angular frequency ω:

$$\nabla^2 p_1 = -k^2 p_1 \tag{1.42}$$

$$k = (1 + i\gamma) k_0 = (1 + i\gamma) \frac{\omega}{c_a} \tag{1.43}$$

$$\gamma = \frac{(1 + \beta) \eta \omega}{2 \rho_0 c_a^2} \tag{1.44}$$

Where γ is the viscous damping factor. As $\gamma \ll 1$ for aqueous systems, we can ignore the viscosity in the bulk part of the acoustic wave obtaining the wave equation

$$\nabla^2 p_1 = \frac{1}{c_a^2} \partial_t^2 p_1, \qquad for \quad \eta = 0 \tag{1.45}$$

The solution of this equation in one dimension have the form $p_1 = p_1(x \pm c_a t)$, showing that a pressure pertubation $p_1(x)$ at $t = 0$ propagates a distance $\mp c_a t$ in time t. Thus, the isentropic constant c_a can be interpreted as the speed of sound. Furthermore, it follows from the solution of the Helmholtz equation for $\eta = 0$ that

$$\mathbf{v}_1 = -i \frac{1}{\rho_0 \omega} \nabla p_1 = \nabla \phi_1 \tag{1.46}$$

$$\phi_1 = \frac{-i}{\rho_0 \omega} p_1 \tag{1.47}$$

Consequently, both the density ρ_1 and the velocity $\mathbf{v}_1$ can be calculated from the pressure p_1 having the velocity as a gradient of the potential ϕ_1. Assuming that the

33

zero-order and first-order terms of the expansion in equation 3.3 are known, we can collect the second-order terms for the fields p_2, ρ_2, $\mathbf{v}_2$ obtaining the second-order equation of state and Navier-Stokes equation

$$p_2 = c_a^2 \rho_2 + \frac{1}{2} \left(\partial_\rho c_a^2 \right)_0 \rho_1^2 \tag{1.48}$$

$$\partial_t \rho_2 = -\rho_0 \nabla \cdot \mathbf{v}_2 - \nabla \cdot (\rho_1 \mathbf{v}_1) \tag{1.49}$$

$$\rho_0 \partial_t \mathbf{v}_2 = -\nabla p_2 - \rho_1 \partial_t \mathbf{v}_1 - \rho_0 \left(\mathbf{v}_1 \cdot \nabla \right) \mathbf{v}_1 + \eta \nabla^2 \mathbf{v}_2 + \beta \eta \nabla \left(\nabla \cdot \mathbf{v}_2 \right) \tag{1.50}$$

From these equations we can determine the time average $\langle X \rangle$ of the second-order fields, integrating over a full oscillating period τ

$$\langle X \rangle = \frac{1}{\tau} \int_0^\tau X(t) dt \tag{1.51}$$

Obtaining

$$\nabla \langle p_2 \rangle = - \langle p_1 \partial_t \mathbf{v}_1 \rangle - \rho_0 \langle \left(\mathbf{v}_1 \cdot \nabla \right) \mathbf{v}_1 \rangle \tag{1.52}$$

$$\langle p_2 \rangle = \frac{1}{2} k_0 \langle p_1^2 \rangle - \frac{1}{2} \rho_0 \langle v_1^2 \rangle \tag{1.53}$$

where $k_0 = 1/ \left(\rho_0 c_a^2 \right)$ is the compressibility of the fluid.

So far, we have neglected the viscous damping by assuming $\eta = 0$. To analyze the effect of viscosity on a fluid under acoustic waves, we begin by taking the divergence of equation 1.37 and changing the order of differentiation for various terms to obtain

$$\rho_0 \partial_t \left(\nabla \cdot \mathbf{v}_1 \right) = -c_a^2 \nabla^2 \rho_1 + \left(1 + \beta \right) \eta \nabla^2 \left(\nabla \cdot \mathbf{v}_1 \right) \tag{1.54}$$

using the first order continuity equation we can obtain a wave equation for ρ_1

$$\partial_t^2 \rho_1 = -c_a^2 \nabla^2 \rho_1 - \frac{\left(1 + \beta \right) \eta}{\rho_0} \nabla^2 \left(\partial_t \rho_1 \right) \tag{1.55}$$

34

which reduces into

$$\omega^2 \rho_1 = -\left[1 - i2\gamma\right] c_a^2 \nabla^2 \rho_1 \tag{1.56}$$

when assuming harmonic time dependence of the fields. For ultrasound waves in water with $\omega \approx 10^7$ s^{-1}, the value of γ is small, with $\gamma \simeq 10^{-5} \ll 1$. This allows for the approximation $\left[1 - i2\gamma\right] \approx \left[1 + i\gamma\right]^{-2}$ to be quite accurate, allowing us to obtain equation 1.42 from equation 1.56. It is important to note that the wave vector $k = k_0 \left(1 + i\gamma\right)$ has an immaginary component that depends on the viscous damping factor. Such immaginary numbers appear in systems with dissipation or amplification, and have a significant physical interpretation[119]. The characteristic damping length x_c is defined by the condition $e^{-\gamma k_0 x_c} = e^{-1}$, from which we obtain

$$x_c \equiv \frac{1}{\gamma k_0} \tag{1.57}$$

1.3.2 Acoustic radiation Force

Consider a compressible, spherical, nanometer sized particle of radius a, density ρ_p and compressibility κ_p, suspended in an inviscid fluid in an ultrasound field of wavelength λ. The nanoparticle acts as a weak point-scatterer and can thus, its effect on the wave can be treated using first-order scattering theory[120]. An incoming wave described a velocity potential ϕ_{in} results in a scattered wave ϕ_{sc} propagating away from the particle. the total first order field is then $\phi_1 = \phi_{in} + \phi_{sc}$. Similarly, from equation 1.46 we have that $\mathbf{v}_1 = \nabla \phi_{in} + \nabla \phi_{sc}$.

Having the scattering first-order fields allows us to estimate the time averaged second-order radiation pressure on the particle by integrating the body forces and stresses over the surface. Thus,

$$\mathbf{F}_{rad} = -\int_{\partial \omega} da \left\{ \langle p_2 \rangle \mathbf{n} + \rho_0 \langle \left(\mathbf{n} \cdot \mathbf{v}_1\right) \mathbf{v}_1 \rangle \right\} \tag{1.58}$$

Where $\mathbf{n}$ is a vector normal to the surface. After replacing equation 1.53 into
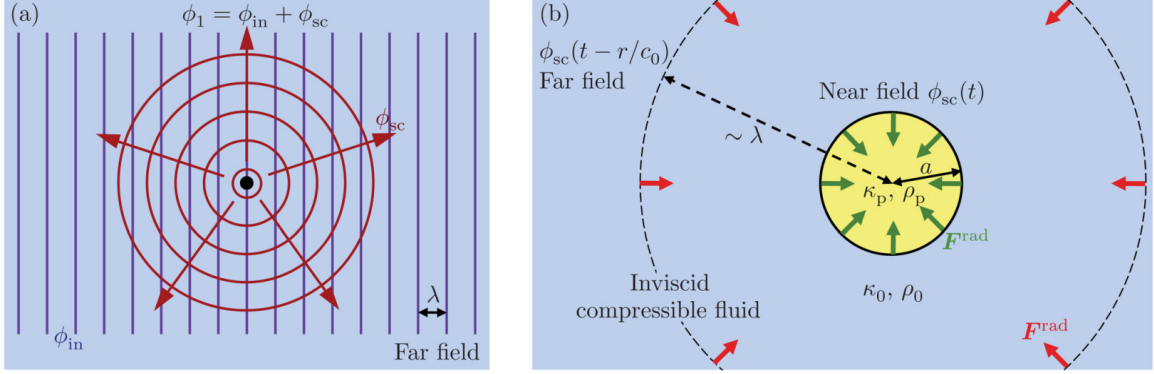
FIGURE 1.5: **Scattering theory and the acoustic radiation force.** (a) At $r \gg \lambda$, an incoming acoustic wave ϕ_{in} of wavelength λ generates a scattering field ϕ_{sc} after interacting with a small particle of radius $a \ll \lambda$. (b) An analyisis in the far field region for $r \gg \lambda$ with the instantaneous scattering ϕ_{sc} and the time-retarded field $\phi_{sc}(t - r/c - a)$ allows for the evaluation of the total radiation force on the surface of the particle. Figure adapted from [120].

equation 1.58 we obtain

$$\mathbf{F}_{rad} = -\int_{\partial\omega} da \left\{ \left[\frac{1}{2}k_0 \langle p_1^2 \rangle - \frac{1}{2}\rho_0 \langle v_1^2 \rangle \right] \mathbf{n} + \rho_0 \langle (\mathbf{n} \cdot \mathbf{v}_1) \mathbf{v}_1 \rangle \right\} \tag{1.59}$$

From first-order scattering theory, ϕ_{sc} in the far field region must have the form:

$$\phi_{sc}(\mathbf{r}, t) = -f_1 \frac{a^3}{3\rho_0} \frac{\partial_t \rho_{in}(t - r/c_a)}{r} - f_2 \frac{a^3}{2} \nabla \cdot \left(\frac{v_{in}(t - r/c_a)}{r} \right) \tag{1.60}$$

Where f_1 and f_2 are the dimensionless scattering coefficients. After inserting the velocity fields into equation 1.59, the mixed products $\phi_{in}\phi_{sc}$ that are proportional to a^3 are the most dominant. Therefore, keeping these interference terms we obtain in index notation

$$F_i^{rad} = -\int_{\partial\Omega} n_j \left\{ \left[\frac{c_a^2}{\rho_0} \langle \rho_{in}\rho_{sc} \rangle - \rho_0 \langle v_k^{in} v_k^{sc} \rangle \right] \delta_{ij} + \rho_0 \langle v_i^{in} v_j^{sc} \rangle + \rho_0 \langle v_i^{sc} v_j^{in} \rangle \right\} dA \tag{1.61}$$

$$F_i^{rad} = -\int_\Omega \rho_0 \left\langle v_i^{in} \left(\partial_j \partial_j \phi_{sc} - \frac{1}{c_a^2} \partial_t^2 \phi_{sc} \right) \right\rangle \tag{1.62}$$

Where equation 1.62 arise after using the Gauss' theorem and the first order Navier-Stokes equation 1.37. From equation 1.62, we can now extract delta function distribu-

36

tions based on the d'Alembert operator to obtain

$$\partial_j^2 \phi_{sc} - \frac{1}{c_a^2}\partial_t^2 \phi_{sc} = f_1 \frac{4\pi a^3}{3\rho_0}\partial_t \rho_{in}\delta\left(\mathbf{r}\right) + f_2\, 2\pi a^3 \nabla \cdot \left[\mathbf{v}_{in}\delta\left(\mathbf{r}\right)\right] \tag{1.63}$$

Where f_1 is the complex monopole coefficient and f_2 the complex dipole coefficient. The acoustic radiation force is then:

$$\mathbf{F}_{rad} = -\frac{4\pi}{3}a^3 \langle f_1 \mathbf{v}_{in}\partial_t \rho_{in}\rangle + 2\pi a^3 \rho_0 \langle f_2\left(\mathbf{v}_{in}\cdot\nabla\right)\mathbf{v}_{in}\rangle \tag{1.64}$$

$$\mathbf{F}_{rad} = -\frac{4\pi}{3}a^3 \nabla \left[\frac{1}{2}Re\left[f_1\right]\kappa_0 \langle p_{in}^2\rangle - \frac{3}{4}Re\left[f_2\right]\rho_0 \langle v_{in}^2\rangle\right] \tag{1.65}$$

with

$$f_1\left(\tilde{\kappa}\right) = 1 - \tilde{\kappa} \quad with \quad \tilde{\kappa} = \frac{\kappa_p}{\kappa_0} \tag{1.66}$$

$$f_2\left(\tilde{\rho}\right) = \frac{2\left(\tilde{\rho} - 1\right)}{2\tilde{\rho} + 1} \quad with \quad \tilde{\rho} = \frac{\rho_p}{\rho_0} \tag{1.67}$$

Assume now a one-dimensional planar standing wave of the form $p_1\left(z\right) = p_a cos\left(kz\right)$, with $k = 2\pi/\lambda$, and $\lambda/2 = w$ having w be the width of the channel confining the fluid. The acoustic radiation force on a spherical particle of radius a reduces to

$$F_{rad,z} = 4\pi\Phi\left(\tilde{\kappa},\tilde{\rho}\right)ka^3 E_{ac}sin\left(2kz\right) \tag{1.68}$$

where

$$E_{ac} = \frac{p_a^2}{4\rho_0 c_a^2} \tag{1.69}$$

$$\Phi\left(\tilde{\kappa},\tilde{\rho}\right) = \frac{1}{3}f_1\left(\tilde{\kappa}\right)\frac{1}{2}f_1\left(\tilde{\rho}\right) \tag{1.70}$$

Here, E_{ac} is the acoustic energy density and $\Phi\left(\tilde{\kappa},\tilde{\rho}\right)$ is the so-called acoustophoretic contrast factor. The sign of the contrast factor can be used to determine the preferential direction of displacement of nanoparticles driven by the acoustic radiation force.

1.3.3 Acoustic Streaming

Acoustic streaming is the phenomenon that takes place when a steady flow field is generated by the interaction with an oscillatory field. This can be generated by the attenuation in the case of quartz winds, or by interaction with a vibrating enclosure or boundary[121]. The latter mechanism of acoustic streaming arises from the friction between the fluid and a vibrating solid wall. This effect is largely confined to a thin viscous boundary layer with thickness $\delta = (\nu/\omega)^{-1/2}$ located near the boundary, often referred to as the Stokes layer or shear-wave layer (Fig 1.6). Here ν is the kinematic viscosity and ω is the radial frequency. This layer not only represent a significant dissipation mechanism, but also provides a strong force driving the acoustic streaming[119, 122].In contrast with the irrotational nature of the bulk, one of the key characteristics of the stokes layer is the required rotational vibration of the medium within the layer in order to satisfy the non-slip boundary condition on the oscillating wall.
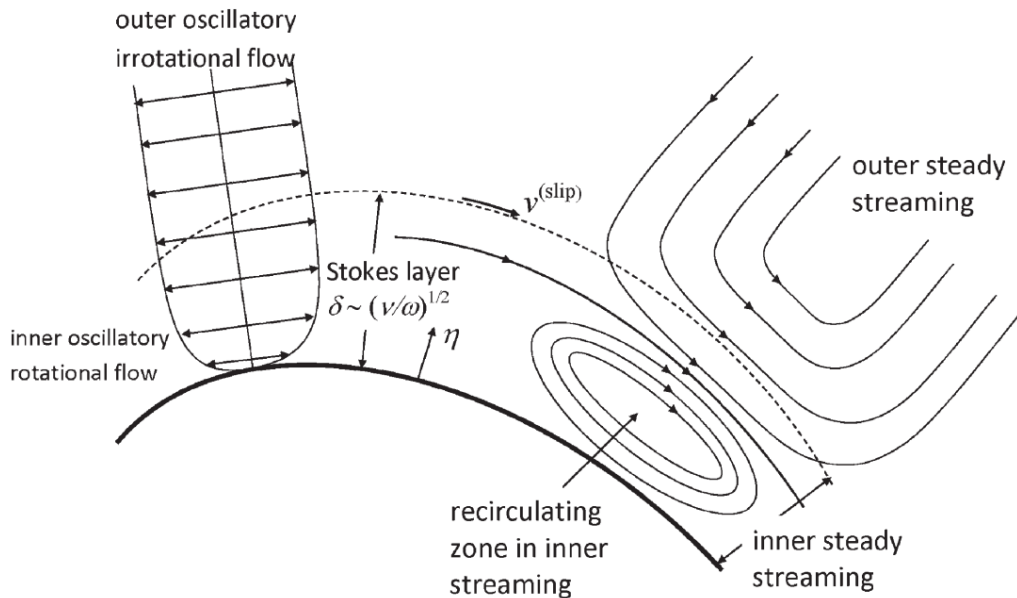
FIGURE 1.6: **Acoustic streaming and the Stokes layer.** An oscillatory, irrotational flow forms a small region of rotational flow defined by the Stokes layer. Within, the rotational flow that develops satisfy the non-slip boundary condition. The acoustic streaming originates as through momentum transfer from the Stokes layer to the bulk. Figure adapted from [122].

Due to the non-linear character of the fluid flow within the Stokes layer, there is a non-zero steady flow generated by the oscillations that carries through the stokes layer into the fluid bulk driving the steady streaming flow in the bulk of the fluid (Fig 1.7. The edge of the Stokes layer is considered as a transition point between the rotational viscous flow and the irrotational flow in the bulk.

FIGURE 1.7: **Secondary streaming induced by an oscillating cylinder.** A long circular cylinder oscillates normal to its axis in a mixture of water and glycerine.Suspended glass beads are illuminated in a cross plane.The steady second-order streaming motion is directed towards the body along the axis of oscillation. Figure reproduced from [123].

By taking the time average of the second-order continuity equation1.49 and Navier-Stokes equation 1.50, we obtain

$$\rho \nabla \cdot \langle \mathbf{v}_2 \rangle = -\nabla \cdot \langle \rho_1 \mathbf{v}_1 \rangle \tag{1.71}$$

$$\eta \nabla^2 \langle \mathbf{v}_2 \rangle + \beta \eta \nabla \left(\nabla \cdot \langle \mathbf{v}_2 \rangle \right) - \nabla \langle p_2 \rangle = \langle \rho_1 \partial_t \mathbf{v}_1 \rangle + \rho_0 \langle \left(\mathbf{v}_1 \cdot \nabla \right) \mathbf{v}_1 \rangle \tag{1.72}$$

From this equations we can see that, in general, the second order velocity field is non-zero due to the time-averaged products of first order terms acting as source points. Physically, the velocity $\langle \mathbf{v}_2 \rangle$ is the acoustic streaming, as it signifies the motion of fluid in the bulk as a consequence of energy and momentum absorption from the acoustic wave[119, 121]. One of the earliest examples of this type of streaming is Rayleigh's third problem[124]. Here, standing sound waves between two walls a distance $2h$ apart interact with an inviscid fluid generating an irrotational flow. Assuming only an x-component of the velocity field, the dimensionless solution is of the form:

$$\mathbf{v}(x,t) = sin\left(\frac{2\pi}{\lambda}hx\right) cos(t)\, \hat{e}_x \tag{1.73}$$

while the second-order streaming flow has the from (Fig 1.8):

$$\mathbf{v}_2^{(s)} = \frac{3}{16}\left(1-3y^2\right)sin\left(2hkx\right)\,\hat{e}_x - \frac{3}{8}h^2k^2\left(y-3y^3\right)cos\left(2hkx\right)\,\hat{e}_y \tag{1.74}$$
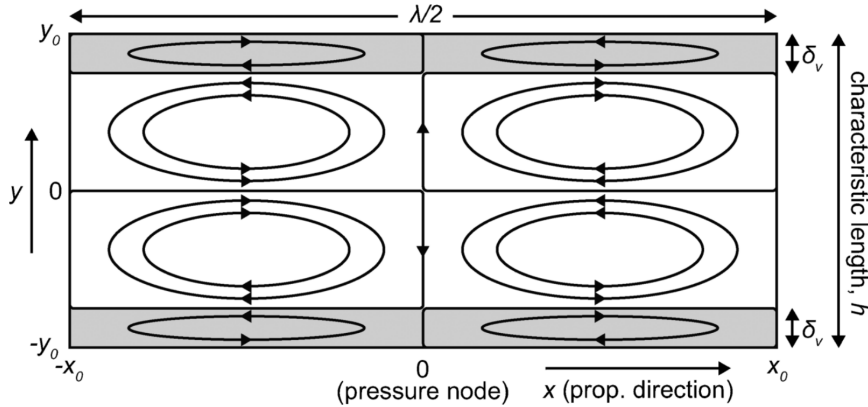
FIGURE 1.8: **Rayleigh streaming in a channel.** A standing wave between two walls generate vortices in a channel. The inner streaming within the viscous boundary layer of thinkness δ_v drive the streming flow vortices in the bulk. The pressure node is located at $x = 0$. Figure adapted from [125].

Following Riley's [121], Taking the curl of the Navier-Stokes equation 1.34 for an incompressible fluid we obtain the dimensionless equation for vorticity

$$\frac{\partial \omega}{\partial t} - \epsilon \nabla \times (v \times \omega) = \nabla \times \mathbf{F} + \frac{\epsilon}{R_e}\nabla^2\omega \tag{1.75}$$

40

Here, the notation has changed to reflect the convention most commonly used for the vorticity. Thus, p' denotes the pressure, v' denotes the velocity, $\omega = \nabla \times v'$ denotes the vorticity, $\nu = \mu/\rho$ the kinematic viscosity and F' a body force per unit mass. Taking a as the characteristic length, F_0 as the characteristic value of the force associated with $U_0 = F_0/\zeta$ the characteristic velocity of the acoustic-induced flow, and ζ as the frequency of the oscillations, we derive the dimensionless quantities to be

$$\mathbf{F} = \mathbf{F}'/F_0, \qquad \mathbf{x} = \mathbf{x}/a, \qquad \mathbf{t} = \zeta t', \qquad \mathbf{v} = \mathbf{v}'/U_0, \qquad \omega = a\omega'/U_0 \qquad (1.76)$$

From equation 1.75 we can observe that the oscillatory flow can be characterized by two dimensionless parameters: $\epsilon = U_0/\zeta a$ which is essentially an inverse of the Strouhal number, and $R_e = U_0 a/\nu$ a Reynolds number. No streaming induced by an oscillatory body force will occur if the body force is conservative and $R_e >> 1$. Equation 1.75 can also be expressed as

$$\frac{\partial \omega}{\partial t} - \epsilon \nabla \times (v \times \omega) = \nabla \times \mathbf{F} + \frac{\epsilon^2}{R_s} \nabla^2 \omega \qquad (1.77)$$

Where the dimensionless number $R_s = \epsilon R_e$ is essentially a Reynolds number based on the velocity ϵU_0. Thus, the magnitude of R_s determines the contribution of the vorticity Laplacian in these flows. R_s is commonly known as the streaming Reynolds number, which is used to study the development of streaming flows using acoustic waves in fluids. The streaming Reynolds relates the oscillation-driven forces and the viscous dissipation forces and is defined as

$$R_s = \frac{U_0^2}{\nu \zeta} \qquad (1.78)$$

1.3.4 Fluid flow and diffusion in microfluidics

Poiseuille flow

The motion of fluids in a microfluidic system is governed by the Navier-stokes equations, the continuity equation and the equations of state. These equations also describe fluid flows that originate by applying a pressure gradient or external fields. Due to the prevalence of pressure-driven flows in microfluid channels with simple geometries, it is useful to consider analytical solutions for analysis and design. The pressure-driven flows, also known as Poiseuille flows are defined as systems where the fluid is driven through a long, straight and rigid channel by imposing a pressure difference between two ends of the channel. When the aspect ratio of a microfluidic channel is large enough, it can be approximated as by an infinite parallel-plate configuration.

Here, the solution to the Navier-Stokes equation with no-slip boundary conditions is

$$v_x\left(z\right) = \frac{\Delta p}{2\eta L}\left(h - z\right)z \tag{1.79}$$

Where h is the channel height and L the length over which we have a pressure drop Δp. Similarly, the flow rate Q trough a section of width w is found as

$$Q = \frac{h^3 w}{12\eta L}\Delta p \tag{1.80}$$

For a circular cross section of radius a, often used in microfluidic applications that use capillaries, the velocity field $\mathbf{v} = v_x\left(r\right)\tilde{\mathbf{e}}_x$ due to the symmetry of the system. Thus, the solution of the Poiseuille is found to be

$$v_x\left(z\right) = \frac{\Delta p}{4\eta L}\left(a^2 - y^2 - z^2\right) \tag{1.81}$$

$$v_x\left(z\right) = \frac{\pi a^4}{8\eta L}\Delta p \tag{1.82}$$

Despite the usefulness and simplicity of these solutions, most of the microfluidic

channels developed using nanofabrication methods involving soft lithography and etching have a rectangular cross-section. In spite of the high symmetry of the boundaries, there is no analytical solution to the Navier-Stokes equation for Poiseulle flow in a rectangular channel. However, one can find an approximate solution using a Fourier expansion. Lets assume a rectangular channel of width w and height h, where $w > h$. The Navier-Stokes equation 1.34 for this system simplifies to:

$$\left[\partial_y^2 + \partial_z^2\right] v_x\left(y,z\right) = \frac{\Delta p}{\eta L}, \qquad -\frac{1}{2}w < y < \frac{1}{2}w, \;\; 0 < z < h \qquad (1.83)$$

Solving the partial differential equation 1.83 with no-slip boundary conditions using fourier series expansion yields the solution to the velocity field for the Poiseuille flow of a rectangular channel,

$$v_x\left(y,z\right) = \frac{4h^2\Delta p}{\pi\eta L}\sum_{n,odd}^{\infty}\frac{1}{3}\left[1 - \frac{cosh\left(n\pi\frac{y}{h}\right)}{cosh\left(n\pi\frac{w}{2h}\right)}\right]sin\left(n\pi\frac{z}{h}\right) \qquad (1.84)$$

After integration, the flow rate is expressed as,

$$Q = \frac{h^3 w\Delta p}{12\eta L}\left[1 - \sum_{n,odd}^{\infty}\frac{1}{5}\frac{192}{\pi^5}\frac{h}{w}tanh\left(n\pi\frac{w}{2h}\right)\right] \qquad (1.85)$$

For flat and very wide rectangular channels, the limit $\frac{h}{w} \to 0$ can be useful to approximate the channel flow rate. At the limit, Q becomes

$$Q \approx \frac{h^3 w\Delta p}{12\eta L}\left[1 - 0.630\frac{h}{w}\right] \qquad (1.86)$$

Diffusion

As discussed before, there is plethora of applications that involve the manipulation of solutions in microfluidic devices, where a solute or a mixture of solutes often comprised of nanoparticles are dissolved in a liquid solvent. The presence of multiple components in the system indicate the posibility of mass transport due to convection or to diffusion processes. The prevalent convection-driven mass transfer is directly linked with the motion of the fluid bulk and is therefore linked with the solution to the Navier-stokes

43

equations. Diffusion on the other hand, involves the motion of particles or molecules from regions of high concentration to regions of low concentration driven by thermal vibrations of the molecules such as Brownian motion. As Diffusion has been extensively studied, here we will limit the analysis to two cases relevant to acoustofluidic applications: I) Diffusion-driven purification in H-filters, and II) Taylor dispersion in field-flow approaches.

The H-filter was one of the first microfluidic devices to be commercialized, as a simple method to purify ions in solution. the name is derived for the geometrical shape of the channel configuration, having two inlets and two outlets connected by a straight channel (Fig 1.9). Here a pure buffer liquid is introduced at one inlet while another liquid containing a mixture of with large and small molecules is introduced on the other inlet. As the flow is laminar due to the small scales of the microchannel, the liquid do not mix by convection. The concentration of the particles on the other hand, changes as both particles flow through the straigh channel. This is due to differences in the diffusion constant of the molecules in the liquid. Here, the time required to be convected downstream τ_{conv} and the time it takes to diffuse across the channel τ_{diff} given by,

$$\tau_{conv} = \frac{L}{v_0} \qquad \tau_{diff} = \frac{w^2}{4D} \tag{1.87}$$

can be controlled to significantly reduce the concentration of one molecule while maintaining a high concentration of the other. For a solute with $\tau_{conv} \ll \tau_{diff}$ diffusion does not have time to act, while for the case $\tau_{conv} \gtrsim \tau_{diff}$ the solute has time enough to diffuse across. Thus, The Peclet number $Pe = a\nu/D_a$ is useful to determine the purification efficiency of microfluidic devices with a diffusion component. Taking the average flow speed in the channel to be v_0, the steady-state advection diffusion problem in an H-filter becomes

$$v_0 \partial_x c_\alpha = D_\alpha \partial_y c_\alpha \tag{1.88}$$

Where c_α is the concentration of the α component. The solution to this equation

44

becomes (Fig 1.9),

$$c_\alpha\left(y, t > 0\right) = \frac{1}{2}c_0 \; erfc\left(\frac{y}{\sqrt{4D_0 t}}\right) \tag{1.89}$$
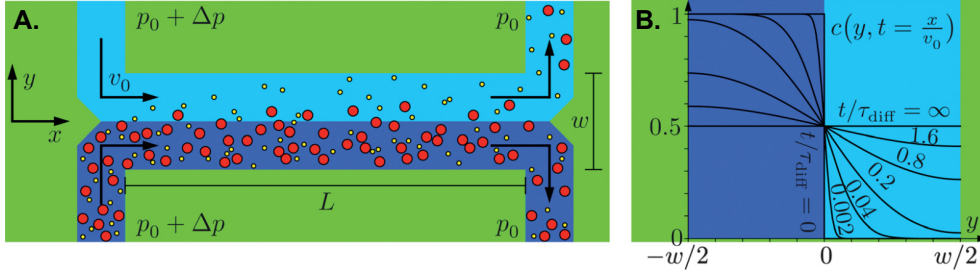
FIGURE 1.9: **Diffusion separation in microfluidic H-filters. A**. An xy-plane top view of a H-filter consiting of a central channel with two inlets (left) and two outlets (right). Here, a pure liquid and a solution of particles containing big and small solutes are introduced and froming a steady Poiseuille flow. The concentration of solutes changes along the channel. **B**. Concentration profile in the central channel as a function of the transverse direction y at different positions x along the channel based on τ_{diff} [119].

1.3.5 Generation of surface acoustic waves (SAWs)

Microscale acoustofluidic actuation relies on the generation of acoustic waves in piezo-electric materials. Rochelle salt and quartz were employed in the first large-scale application of piezoelectrics to detect submarines during World War using sonar[110]. The earliest medical applications were for ultrasonic imaging of tissues in medicine[126, 127] High-power ultrasound has been applied in industrial mixing and cleaning, applications familiar to most researchers.30,31 Other common uses include non-contact sensors and range-finders[128]. more recently, local harvesting of energy from motion to eliminate or reduce the need for batteries have driven innovative use of piezoelectric materials[129]. The waves generated by piezoelectric media were generally limited to bulk acoustic waves (BAW) until the advent and broad acceptance of IDTs[130], which enabled high frequency SAW. Rayleigh waves are confined within three to four wavelengths of the surface of the material. Other wave types associated with Raylegh waves include Leaky SAW (LSAW)[131], Love waves[132], Bleustein–Gulyaev waves[132], surface skimming bulk waves [133], and surface transverse waves [134].

Piezoelectricity

The well-known piezoelectric effect generates electric charge upon the application of mechanical stress in certain materials. The generation of mechanical strain from the application of an electric field is known as the inverse piezoelectric effect. There are different types of piezoelectric materials been used to generate and detect acoustic waves. Polycrystalline piezoelectrics have greater electromechanical coupling coefficients than single crystalline piezoelectrics, implying a greater ability to transform energy from one form to the other[110]. Despite this, single crystal materials have higher quality factors and lower damping[135]. Single-crystal piezoelectric materials are compatible with most microfabrication facilities in contrast with lead zirconate titanate (PZT)[136], the most common polycrystalline ceramic piezoelectric material PZT has high toxicity and a significant excess lead oxide present, leading to imposed regulations that aiming to eliminate it from use[137, 138]. for SAW devices, common piezoelectric materials include quartz, lithium tantalate (LiTaO$_3$) and lithium niobate (LiNbO$_3$). Others piezoelectric materials used include gallium arsenide (GaAs), cadmium sulfide (CdS), zinc oxide (ZnO), lithium tetraborate (Li$_2$B$_4$O$_7$), and langasite (La$_3$Ga$_5$SiO$_{12}$). All piezoelectric materials are anisotropic and thus, the type of wave generated from them is strongly dependent on the material orientation. for example, lithium tantalate and lithium niobate exhibit stronger electromechanical coupling coefficients than quartz when the proper cut angle is used. Due to its exceptionally high coupling coefficient and lower manufacturing cost, Lithium Niobate crystals have been used extensively in applications[139]. Finding that different rotated cuts of the polycrystalline material enhance the material properties led to further studies on the performance of piezoelectric crystals. The 131° Y-rotated cut of lithium Niobate was found to have exceptional electromechanical coupling and low beam steering[140, 141], but also exhibited spurious parasitic waves. It was later determined that the 127.86° Y-rotated cut reduced the generation of these parasitic waves, having the highest electromechanical coupling coefficient and lowest insertion loss[142]. Consequently, The 127.86° Y-rotated X-propagating cut of lithium Niobate became the most popular and

widely accepted orientation for applications requiring Rayleigh waves.

Interdigitated Transducers (IDTs)

To generate a SAW in a piezoelectric material we apply an oscillating electrical signal matching the resonant frequency of the piezoelectric transducer that translates into an acoustic wave via the inverse piezoelectric. The simplest piezoelectric transducer to generate SAWs consist of a straight rectangular metal bars deposited onto the surface of the piezoelectric substrate that are alternately connected on either end to the bus bars (see Fig. 1.10) [110, 143] Here, the bars are commonly referred as "fingers", which leads to the name of interdigitated transducer (IDT). This structure creates an array of electric fields of alternating direction between the transducer finger pairs. In turn, the inverse piezoelectric effect creates alternating regions of compressive and tensile strain in the substrate. Thus, each finger pair produces displacement in the substrate that oscillates with the electric field and radiates a SAW. The periodicity of the finger pairs defines the wavelength of the resulting SAW, such that the distance from one finger to the next is $\lambda_{SAW}/4$. Consequently, the center frequency ($f_r = \omega/2\pi = \nu R/\lambda_{SAW}$) of a given device is determined by the choice of substrate, propagation direction, and IDT design.[143] As the SAW propagates through subsequent finger pairs, the wave is diffracted, creating a near-field region of largely parallel wavefronts known as the Fresnel region. The far-field region, where the SAW is broadly diffracted along major and minor lobes, is known as the Fraunhofer region. To minimize diffraction losses, the aperture of the IDT must be contained within the Fresnel region. For design purposes, a Fresnel parameter (F) is defined as $F = 4\lambda_{SAW}d_f/a^2$ where a is the aperture width and d_f is the distance from the IDT edge. To remain within the Fresnel region, the aperture should be selected such that $F < 1$. The efficiency of a SAW device is commonly linked to its quality factor, $Q = f_r/\Delta f$, where Δf is the width of the resonant peak in frequency space measured at one-half the peak's highest amplitude. The quality factor is influenced by dielectric losses of the piezoelectric materials, loading effects, ohmic losses, and acoustic leakage to the substrate. Here, The number of finger pairs (N_p) of an IDT is an important parameter that affects the quality factor. [110, 143]

non-reflective transducers and the delta-function model

Based on the quasi-static method for non-reflective single-electrode transducers (See fig. 1.10) , the total wave amplitude that exits the transducer port is defined as:

$$\phi_s(\zeta) = \sum_{m=1}^{M} \phi_{sm}(0,\zeta) = V E(\zeta) \sum_{m=1}^{M} \hat{P}_m exp(-jkx_m) \tag{1.90}$$

Where it is assumed that all variables have harmonic dependance so that they are proportional to $e^{j\zeta t}$. Here V is the applied voltage, M is the total number of electrodes in the transducer, $k = \zeta/\gamma$ is the wavenumber with phase velocity γ and $\hat{P}_m = 0, 1, 0, 1, 0, 1, ...,$ is the electrode polarity for a single-electrode transducer. $E(\zeta)$ here is an element factor, wich varies slowly with ζ and is often consider to be constant. For a single electrode transducer the center frequency ζ_{s0} occurs when the electrode pith p_e equals $\lambda/2$, giving $\zeta_{s0} = \pi\gamma/p_e$. At this frequency it is found that $E(\zeta_{s0}) = 1.694j(\Delta\gamma/\gamma)$, getting $E(\zeta) \approx E(\zeta_{s0})$ for frequencies near to ζ_{s0}.

Definging an array factor as:

$$A(\zeta) = \sum_{m=1}^{M} \hat{P}_m exp(-jkx_m) \tag{1.91}$$

Gives $\phi_s/V = E(\zeta)A(\zeta)$. Of note, the transducer response $H_t(\zeta)$ is defined by the expression

$$H_t(\zeta) = -jE(\zeta)A(\zeta)\sqrt{\zeta W \epsilon_\infty / (\Delta\gamma/\gamma)} \tag{1.92}$$

So that the potential of the wave generated can be written as:

$$\Phi_s/V = -jH_t(\zeta)\sqrt{(\Delta\gamma/\gamma)/(\zeta W \epsilon_\infty)} \tag{1.93}$$

here, W is the width of the electrode fingers and ϵ_∞ is defined as the capacitance of a unit-aperture single electrode transducer per period. When a Voltage V is applied,

the power absorved by the transducer is:

$$P_a = G_a(\zeta)|V|^2/2 \tag{1.94}$$

where the conductance $G_a(\zeta)$ and the susceptance $B_a(\zeta)$ are part of the parallel elements added to the capacitance C_t to determine the electrical admittance $Y_t(\zeta)$:

$$Y_t(\zeta) = G_a(\zeta) + jB_a(\zeta) + j\zeta C_t \tag{1.95}$$

The power of a wave with surface potential ϕ_s can be shown to be:

$$P_s = \frac{1}{4}\zeta W \epsilon_\infty |\phi_s|^2/(\Delta\gamma/\gamma) \tag{1.96}$$

Which leads with equation 1.93 to the simple relation:

$$G_a(\zeta) = |H_t(\zeta)|^2 \tag{1.97}$$

The fundamental response of a uniform transducer has:

$$G_a(\zeta) \approx G_a(\zeta_0)\left[sin\left(X\right)/X\right]^2 \tag{1.98}$$

where $X \equiv N_p\theta = N_p(\zeta - \zeta_0)/\zeta_0$ and $N_p = M/2$ for single-electrode transducers (See Fig. 1.10).

Now, it can be shown that for single-electrode transducers:

$$G_a(\zeta_0) = \alpha\zeta_0\epsilon_\infty W N_p^2(\Delta\gamma/\gamma), \quad \alpha = 2.87 \tag{1.99}$$

Therefore, it follows from this development that as $\zeta \to \zeta_0$:

$$P_{s0} = \frac{1}{4}\alpha\zeta_0\epsilon_\infty W N_p^2(\Delta\gamma/\gamma)V^2 \tag{1.100}$$

Equation 1.100 relates the total voltage applied form the radiofrequency source to the Power of the acoustic wave leaving an interdigitated transducer that it operating

at it resonance frequency ζ_0. Asuming, for simplicity, that there are no losses in the system do to diffraction and dampening, we can relate the power of the traveling surface acoustic wave with the acoustic intensity of the leaking surface acoustic wave in the fluid. For the traveling wave within the fluid we have that the acoustic intensity is related with the amplitude of the velocity profile by:

$$I = \rho_o c u^2 \tag{1.101}$$

Where ρ_o is the fluid density, c is the speed of sound and u is the fluid velocity related with the oscillatory motion of the fluid. Hence, the we can relate the Power of the acoustic wave traveling within the fluid with the characteristic velocity through a cross section area A_o by:

$$P_f = A_o \rho_o c U_0^2 \tag{1.102}$$

Assuming that the power of the acoustic wave exiting the transducer is the power of the traveling wave within the fluid $P_s = P_f$ we can then estimate the characteristic velocity of the wave generated by the single-electrode interdigitated transducer to be:

$$U_0^2 \approx \frac{1}{4A_o\rho_o c}\alpha\zeta_0\epsilon_\infty W N_p^2(\Delta\gamma/\gamma)V^2 \tag{1.103}$$

Following this treatment we conclude that the streaming Reynolds number R_s can be estimated as a funtion of the voltage applied to the transducers:

$$R_s = \chi V^2 \tag{1.104}$$

where

$$\chi = \frac{1}{8}\frac{1}{\nu}\frac{\alpha\epsilon_\infty W N_p^2(\Delta\gamma/\gamma)}{A_o\rho_o c} \tag{1.105}$$

Is a constant defined by the properties of the fluid, the dimensions of the microfluidic channel, the piezoelectric properties of the material where the interdigitated transducers are located and the achitecture of the transducers.
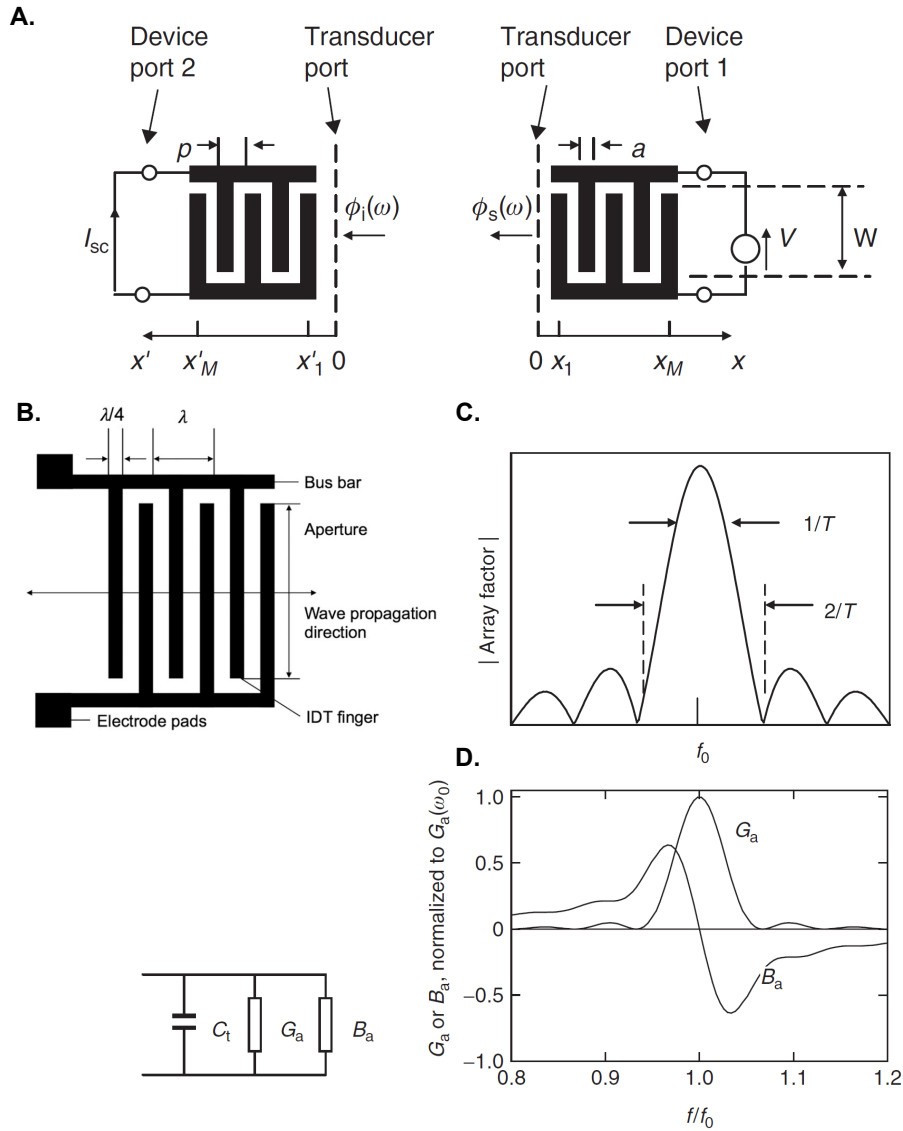
FIGURE 1.10: **Single-electrode Intedigitated Transducers (IDTs). A**. The non-reflective single-electrode IDTs generate a SAW with potential $\phi_s(\omega)$ that is absorved and reflected by a receiving IDT with a potential $\phi_i(\omega)$ Forming a standing wave. **B**. Each IDT is made of a set of metal finger connected to a bus bar in an alternating fashion. The spacing between fingers, or pitch, determines the IDTs primaty oscillation frequency f_0 and wavelength λ. **C**. Array factor plot showing the single-electrode bandwidth. **D** Following the equivalent circuit for an IDT transducer. we show the acoustic conductance and susceptance for uniform transducer. Figure adapted from [143].

CHAPTER 2

ACOUSTOFLUIDIC SEPARATION OF NANOPARTICLES

2.1 Introduction

Nanoparticle separation techniques have been employed for industrial and research applications for decades, with several gold-standard techniques widely implemented for synthetic nanoparticle and biomolecule separation[144]. Conventional techniques for nanoparticle separation involve filtration through physical barriers, selective precipitation based on colloidal stability, or application of external fields. Filtration methods employ membranes or columns made of different materials to purify particles based on physical properties. Commonly used filtration techniques for nanoparticle separation include chromatography and nanofiltration. In chromatography, samples are separated in a mobile phase through a stationary phase, and the rate of separation depends on the partitioning speed of the particle through the stationary phase[145]. There are several types of chromatography for nanoparticle separation, such as size-exclusion, affinity, ion-exchange, and high-performance liquid chromatography[146]. Chromatography has high separation efficiency, but requires a long time, multiple preparation steps, and specialized beads, antibodies, and buffers for separation. Different membrane materials have been implemented in these techniques to achieve separation of nanosized particles, including ceramic membranes[147], polymeric membranes, or supramolecular membranes with the capability to be recycled many times[148]. Although filtration techniques are fast, requires a small volume of solvent, and can be scaled to large sample separation for industrial application, the membranes are prone to clogging,

subsequent particle aggregation, and decreased throughput of separation. It also requires many steps to separate samples with multiple particle sizes[144]. Alternatively, external fields can be used to separate nanoparticles based on their physical properties. The most common external field used are centrifugal force field or an electric field. These two external forces have been commonly applied for nanoparticle sorting in ultracentrifugation and gel electrophoresis, respectively. Ultracentrifugation is the most common technique for separating and purifying nanoparticles, relaying on particle deposition through centrifugal force arising from the rotation of the ultracentrifuge[149]. Ultracentrifugation can separate nanoparticles by size and shape, and the resolution can be improved with an additional gradient agent. A density gradient is needed to achieve better separation at the nanoscale. sample loss during ultracentrifugation is inevitable, and particles have the tendency to form aggregates[150, 151]. Furthermore, the requirement for specialized equipment for ultracentrifugation and highly-trained personnel makes this technique relatively expensive to apply for nanoparticle separation. Gel electrophoresis separates samples based on their size/charge ratio when the particles are suspended in an electric field, with high resolution depending on the gel pore size[151]. Gel electrophoresis has also been shown to separate various metal nanoparticles by size, shape, and charge with high resolution[152, 153]. This technique is batch-limited and requires multiple steps to operate, takes a long time for sample separation, and is cumbersome for sample retrieval limiting its applicability for nanoparticle filtration[151].

As The traditional ways of nanoparticle sorting are time consuming, require batch operation and have inevitable sample loss during the separation process, there is a need for improved separation methods for nanoparticles. In this context, microfluidics offers multiple advantages for the development of new generation filtration systems[154, 144, 145]. First, microfluidics offers miniaturization of conventional techniques, which reduces the minimum sample volume. In addition, microfluidics techniques provide continuous separation for multiple sample sizes and with minimum aggregation and low sample losses during the separation process. by modulating the experimental parameters Microfluidics can provide real-time control and spatial control. Furthermore,

Comparison between microfluidic methods for nanoparticle separation		
Microfluidic Method	Advantages	Disadvantages
Filtration	Ease of use High purity Low cost	Complexity of fabrication clogging high sample losses Fixed size cutoff
Centrifugation	High purity wide separation range Can separate particles down to 50 nm	Complexity of fabrication complex operation Fixed size cutoff
Deterministic Lateral displacement (DLD)	Ease of use Low cost Can separate particles down to 20 nm	Clogging complex operation Fixed size cutoff
Inertial microfluidics	Ease of use Low cost	poor separation of nanoparticles Diffusion
Field flow fractionation (FFF)	High purity wide separation range Can separate particles down to 50 nm	Complex operation Extensive optimization clogging
Electrophoresis	Ease of use Low cost	restricted to charged or polarizable particles May require change in medium
Optofluidics	Can separate particles down to 50 nm wide separation range Great spatial control	Expensive equipment high optical stress local increase in temperature
Acoustofluidics	Ease of use Low cost Wide separation range Biocompatible	Complex fabrication local increase in temperature

TABLE 2.1: Comparison between the advantages and disadvantages of the main methods of microfluidic separation of nanoparticles.

microfluidics also provides a low-cost solution which could be easily integrated with other techniques, such as mixing, counting, detection and analysis.

There is a broad array of microfluidic filters for nanoparticles that use different separation principles (See table 2.1). In general, we can categorize these techniques based on their separation principles as passive or active methods. Passive separation methods use label-free strategies using hydrodynamics and surface forces as the primary separation mechanism. The most popular passive separation in microfluidics involves the use of filtration structures or filtering membranes[155]. Although filtration methods suffer from clogging and aggregation as traditional methods, these systems offer advantages having continuous operation, high throughput, and high potential for automation. An interesting method for passive separation of nanoparticles involve the use of an array of nanopillars that promote a deterministic lateral displacement (DLD)[156, 157, 158]. This method has been shown to separate nanoparticles down to 20 nm[158]. Alterna-

tively, the use of inertial microfluidics has been proposed as a simple method to focus nanoparticles using hydrodynamics [159, 160, 161].

In contrast with passive methods, active separation methods combine microfluidic flows with external fields. Here, multiple strategies have been explored including centrifugal forces[162], optical tweezers[163], magnetic fields[164, 165], electric fields[166, 167, 168], acoustic fields[169, 170, 171, 172] and affinity-based sorting[173, 174, 175, 176]. In particular, several attractive active separation methods combine of hydrodynamic forces, Brownian motion, and a perpendicular external force field in a strategy denominate field flow fractionation (FFF)[177, 178]. For this technique, The external force field is applied perpendicularly to the direction of the flow inducing the particles to laterally displace to the side walls. At the wall, nanosized particles are mostly affected by Brownian motion, which thereby displaces them away from the wall to an equilibrium position. As a result of the parabolic velocity profile, smaller nanoparticles travel faster and elute faster than larger particles providing a platform for effective separation of particles [178, 179]. Despite their performance, FFF microfluidic methods often require extensive optimization and complex operation, limiting the sensitivity of these methods. Electrophoresis and dielectrophoresis methods are easy to use and cheap to manufacture but are restricted to charged or polarizable particles, requiring changes in medium that might not be suitable to sensible nanoparticles. Acoustic tweezers can manipulate particles down to 50 nm but require expensive equipment and generate a significant local increase in temperature and high optical stress. Thus, all the microfluidic methods under development have multiple advantages and disadvantages relegating their use to niched applications.

Among the active microfluidic separation methods, the use of acoustic waves has gathered attention as recent development have consistently improved their performance. Acoustic microfluidics use the interaction of waves with fluids to create contactless filtering regions that separate particles base on size and other physical properties. As discussed in chapter 1, acoustofluidics methods are biocompatible and relatively cheap to manufacture with modern nanofabrication methods. Acoustofluidic methods allow a cheap purification based on size that offers high recovery. Despite their suc-

cess, most acoustic microfluidic methods rely on acoustophoresis (Separation based on displacement by the acoustic radiation force)[110, 180]. Consequently, their ability to separate nanoparticles has been put into question, as the magnitude of the acoustic radiation force and the drag forces exerted by the fluid are comparable for nanometer sized particles. Nobel acoustofluidic strategies for contactless, label-free and continuous filtration of nanoparticles could lead to exciting applications.

In this chapter we present experimental results describing a new acoustofluidic filtration method for the fractionation of nanoparticles in complex mixtures. We study the influence of acoustic wave intensity and flow rate on the concentration profiles of nanoparticles of different sizes. Furthermore, we study the effects of frequency variations, change in channel dimensions and temperature control. We analyze the particle recovery of fluorescent polystyrene nanoparticles and validate our results purifying extracellular vesicles extracted from cell culture. In addition, we study the fractionation of nanoparticles using tilted-angle surface acoustic waves.

2.2   Experimental setup

An acoustofluidic device was fabricated bonding a PDMS microfluidic channel between two interdigitated transducers (IDTs) deposited in the surface of a LiNbO3 piezoelectric substrate (Fig. 2.1A).The microfluidic channel was manufactured using well-stablished soft lithography techniques, having a square cross-section of height h = 40 μm, a width w = 200 μm, and a length $L \approx 12mm$, being coated with a thin layer of PEG (1% w/v) to reduce particle adsorption to the channel walls (Fig. 2.1B). The channels were fabricated out of polydimethylsiloxane (1:10 curing agent to PDMS base; RTV 615, Momentive) and bonded to the piezoelectric substrate after components were exposed to air plasma (Harrick Plasma, Plasma Cleaner Model PDC-001). The IDTs were patterned into a 128° Y-cut of LiNbO$_3$ piezoelectric substrate, Double sided polish, and 0.5 mm thickness. The IDTs metal layer was added using vapor deposition of a 10 nm Platinum adhesion layer followed by a 80 nm gold layer. The single electrode transducer pitch was set to 50 μm to achieve a wavelength of 200 μm. The number of

fingers was set to be $N = 20$, with an IDT length of 9.7 mm.
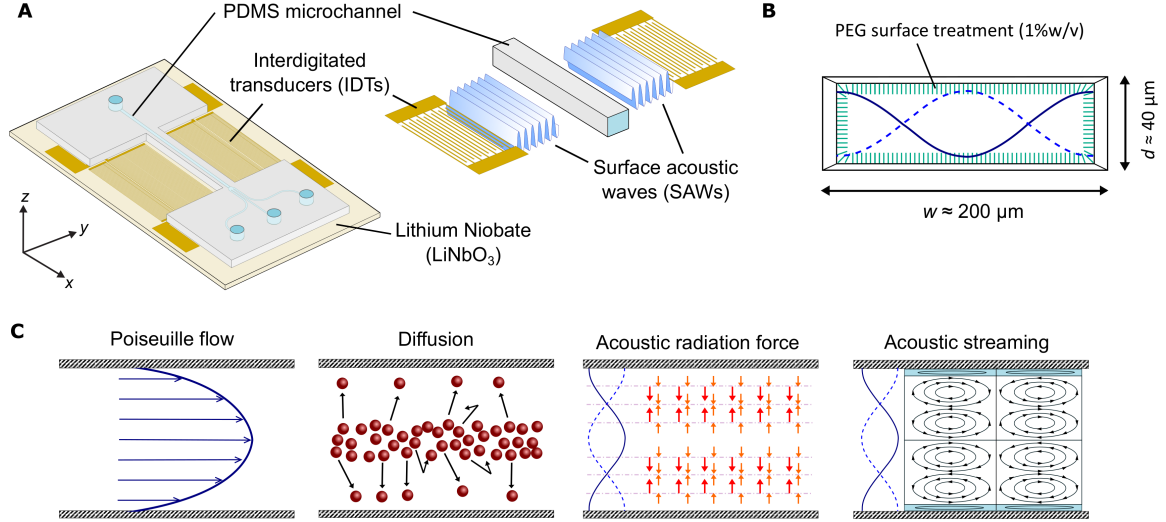
FIGURE 2.1: **Schematic of integrated acoustofluidic device for nanoparticle purification and working mechanisms.** A. Schematic of the acoustofluidic device. A microfluidic channel was bonded to the LiNbO3 substrate in between Interdigitated transducers. B. A standing surface acoustic wave (SSAW) was applied in a square channel of width = 200 μm and depth = 40 μm, coated with PEG (1% w/v). C. As the nanoparticles travel through the acoustofluidic device, they are subjected to four physical forces: drag forces induced by the applied Poiseuille flow, diffusion forces induced by gradients of chemical potential and Brownian motion, acoustic radiation forces induced by the SSAWs as well as secondary drag forces induced by the acoustic streaming.

The distance between transducers was set as 1.25 mm, while the PDMS wall thickness in the acoustic region was limited to 250 μm to minimize acoustic dissipation. Both IDTs were accompanied by an acoustic reflector on the opposite side to the channel that allows to contain the acoustic wave and focus more energy into the acoustic region. Once assembled, high voltage radio-frequency (RF) signals were generated using a GHz RF generator (Hewlett Packard, Model E4431B) coupled with a power amplifier (Minicircuits, Model ZHL-1-2W-N+). Using these equipment allows us to generate > 32 dbm of input power. As discussed in chapter 1, applying an RF signal to the IDT generates electric fields within the transducers that induce mechanical oscillations via the inverse piezoelectric effect. Thus, the IDTs transform the RF signal into a traveling acoustic wave that propagates through the surface of the substrate. the surface acoustic wave(SAW) interacts with the fluid within the microfluidic channel and its received by the opposite IDT, which reflect the SAW, generating an standing wave with frequency

equal to the oscillating frequency of the IDT (Fig. 2.1A). After assembled, A combination of solutions where introduced to the acoustofluidic device described to study the behavior of particles in solution when exposed to SAWs. Filling of microfluidic channels and fluid control was achieved using a microfluidic flow controller (OB1 MK3+, ELVESYS), while the flow rates were monitored using a microfluidic sensor (MFS-D-1, ELVESYS). The temperature was controlled using a temperature controller able to fit under the microscope (PE120, Linkam). Here, the flow control allows us to modulate the flow rate of the Poiseuille flow generated within the microfluidic channel. Depending on the test, the acoustofluidic devices used had configurations with one inlet and multiple outlets as well as multiple inlets and outlets. All solutions where transfered to the microfluidic device using PTFE tubing.

Monodisperse, fluorescent polystyrene nanoparticles (FSDG, FSFR, FSSY, Bang Laboratories) where used to generate both homogeneous and heterogeneous dilute, aqueous solutions of nanoparticles with concentrations between 0.1-5% (v/v). Some samples analyzed also contained 2% v/v fluorescent Albumin from bovine serum (555 BSA, A34786, Invitrogen). Samples containing extracellular vesicles were collected and isolated from cell culture. For this, human melanoma cells transduced to express CD9+ mcherry (Me260LN-CD9+) where maintained at 37° C in 5% $CO2$ in RPMI medium (Invitrogen) supplemented with 10% FBS. Once cell culture reached confluence, the culture medium was collected and centrifuged at 300 $\times g$ for 10 min to remove cell debris and apoptotic bodies. After centrifugation, The supernatant was collected and concentrated using 100 kDa Amicon centrifugal filter at $2000 \times g$ for 10 min. The remaining concentrated sample were detached from the filter and resuspended using phosphate-buffered saline (1×PBS; Thermo Fisher) and used for analysis. Solutions contained EVs where prepared diluting 5 μl of sample into 1 ml of 1×PBS. The size and concentration of EVs/exosomes purified from cell culture supernatants were determined using Nano-tracking analysis (NanoSight NS300, Malvern Instruments), which is equipped with fast video capture and particle-tracking software. Concentration of the samples collected at the outlet was verified using fluorescence signals detected by Microplate reader (BioTek Synergy Neo2, Agilent). The protein content of cell culture

samples validated using MicroBCA protein assay (Thermo Scientific). The interaction of samples with SSAWs within the microfluidic device was monitored using a motorized z-focus, motorized and coded 7x nosepiece, fully automated transmitted light axis, and fully automated 5x or 8x fluorescence axis research microscope (DM6000 B, Leica).

2.3 Acoustofluidic fractionation of nanoparticles

As detailed in Chapter 1, there are four primary mechanisms driving the dynamics of nanoparticles for such acoustofluidic device (Fig. 2.1 C): I) Drag forces originating from the Poiseuille flow along the microfluidic channel; II) Diffusive forces caused by Brownian motion and gradients of chemical potential; III) Acoustic radiation forces originated by scattering from the SSAWs; and IV) Secondary drag forces that arise from acoustic streaming flows. Here, both the acoustic radiation and the streaming arise when the acoustic waves or radiation propagating in liquids impart a slow, non-oscillating velocity component to the liquid or to small particles suspended in the liquid. The origin of these effects can be traced back to the non-linearity of the Navier-Stokes equation and the small but non-zero compressibility of ordinary liquids. The acoustic streaming is a phenomenon that emerges when the velocity field of the entire liquid acquires an additional, slowly varying component induced by the acoustic waves. On the other hand, the radiation force appears when small particles suspended in a liquid are moved by the momentum transfer from sound waves propagating in the liquid. We hypothesized that the dynamic behavior of the nanoparticles under Poiseulle flow and surface acoustic waves could lead to novel separation processes after finding proper operating parameters. In this section, we present the results of the experimental analysis performed using polystyrene particles of different sizes flowing in an acoustofluidic device where the fluid flow is orthogonal to the SSAW field.

2.3.1 Acoustofluidic focusing of polystyrene particles

For the first set of experiments, we built an acoustofluidic device with one inlet and multiple outlet. Controlling the flow rate, we introduced a mixture of albumin, 1 μm

and 200 nm particles into the channel and applied aSSAWs with an input power of 32 dBm (see Fig. 2.2). After applying the SSAW, A strong displacement of 1 μm particles towards the pressure nodes was observed,Fig 2.3D).
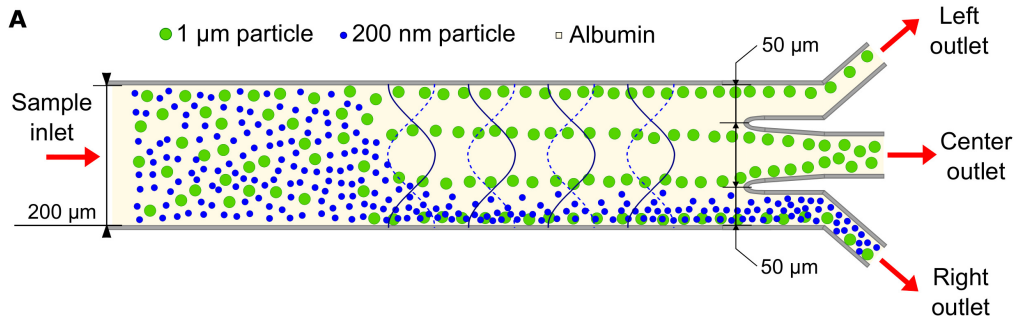
FIGURE 2.2: **Schematic representation of acoustofluidic separation of nanoparticles in heterogeneous solution.** A sample comprising a mixture of fluorescent 1 μm particles, 200 nm particles and albumin in DI water was subjected to high-intensity SSAW at different flow rates of a Poiseuille flow. The high-intensity acoustic field induce different concentration profiles in particles of different sizes.

The 1 μm particles are concentrate in the in the side walls of the channel as well. At a speed of 350 μm/s, no significant change was observed in the concentration of both 200 nm particles or fluorescent albumin (Fig 2.3E,F). This results are consistent with acoustophoretic microfluidic studies where particles with a diameter > 1 μm are displaced towards the acoustic wave pressure node due to the strong effect of the acoustic radiation force. Similarly, the radiation force in nanoparticles is small enough to compete with drag forces related to the Poiseuille velocity field as well as the acoustic streaming velocity field. Next, we decided to study the effect of the Poiseuille flow on the acoustofluidic displacement of particles in solution. Interestingly, we observed differences in the The behavior of the 200 nm particles after reducing the flow rate in the channel past a certain threshold (Fig 2.4). Applying the same 32 dBm input power to generate SSAW with a flow speed of 10 μm/s, we observed a focusing of the 200 nm particles towards one of the channel side walls(Fig 2.4E). No noticeable change was observed for the 1 μm particles under these conditions, having that they continue to migrate preferentially towards the pressure nodes and the walls in similar fashion as seen in Fig 2.3D.In addition, no changes in the concentration of albumin

was noticeable after applying the SSAWs (Fig.2.3F). To investigate the unusual stream of focused 200 nm particles observed in Fig 2.4, we performed experiments increasing the intensity of the SSAW while maintaining an average velocity of 10 μm/s in the microfluidic channel (Fig 2.5).Applied input power up to 27 dBm had no observable effect on the distribution of the 200 nm particles (Fig.2.5A).
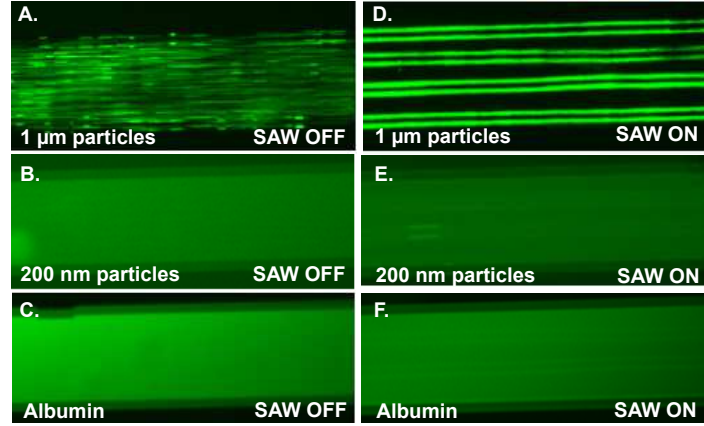
FIGURE 2.3: **Effect of SSAWs on a heterogeneous solution at 350 μm/s**. Fluorescent microscopy images showing the xy cross section (top view) of the microfluidic channel. Display of the effect of SSAWs on a heterogeneous solution containing a mixture of 1 μm fluorescent nanoparticles, 200 nm fluorescent particles and fluorescent albumin. **A-C**. No SSAWs applied. **C-E**. SSAWs generated using 32 dBm input power. Average flow velocity $v_{avg} = 350$ μm/s ($Re = 4.2 \times 10^{-4}$).
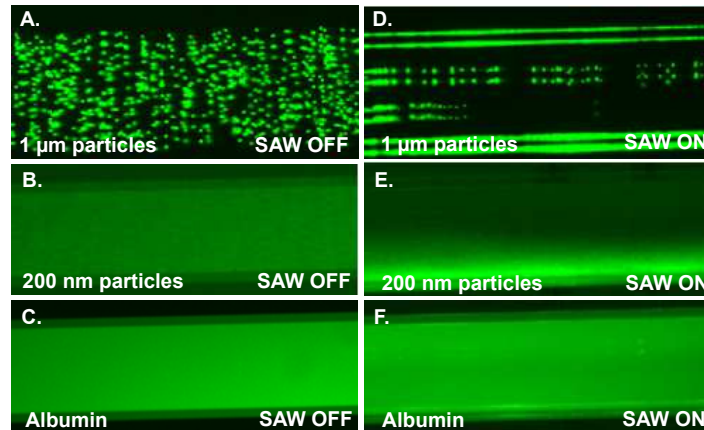
FIGURE 2.4: **Effect of SSAWs on a heterogeneous solution at 10 μm/s**. Fluorescent microscopy images showing the xy cross section (top view) of the microfluidic channel. Display of the effect of SSAWs on a heterogeneous solution containing a mixture of 1 μm fluorescent nanoparticles, 200 nm fluorescent particles and fluorescent albumin. **A-C**. No SSAWs applied. **C-E**. SSAWs generated using 32 dBm input power. Average flow velocity $v_{avg} = 10$ μm/s ($Re = 1.2 \times 10^{-5}$).

Increasing the applied input power up to 30 dBm displayed the formation of strong, streaming flow patterns originating from the walls. These streaming-induced rolls disrupt visibly the homogenous concentration profile of the sample (Fig. 2.5A). Increasing the input power to 31 dBm depleted the center of the channels of particles while reducing the width of the streaming-induced roll region. Here, we begin to observe an uneven distribution of nanoparticles where approximately 75% of particles are concentrated towards one wall while the remaining particles are concentrated on the other wall. Further Increasing the input power led to the formation of a highly concentrated stream of 200 nm particles towards one of the channel walls, followed by a significant depletion of particles the rest of the channel.A quantification of these results shows that increasing intensity of the SAW disrupt the homogeneous distribution of particles across the channel. Intially, the concentration increases near the walls with a reduction of concentration in the center with the exception of a small peak of concentration in between. As the power increases, the 200 nanoparticles are concentrated towards one of the channel walls. Here, the concentration profile resembles a Beta distribution with $\alpha = 10$ and $\beta = 2$ (Fig .2.6A). Based on these results, we studied the effect of SSAWs on particles of different sizes flowing at a speed of 10 μm/s.
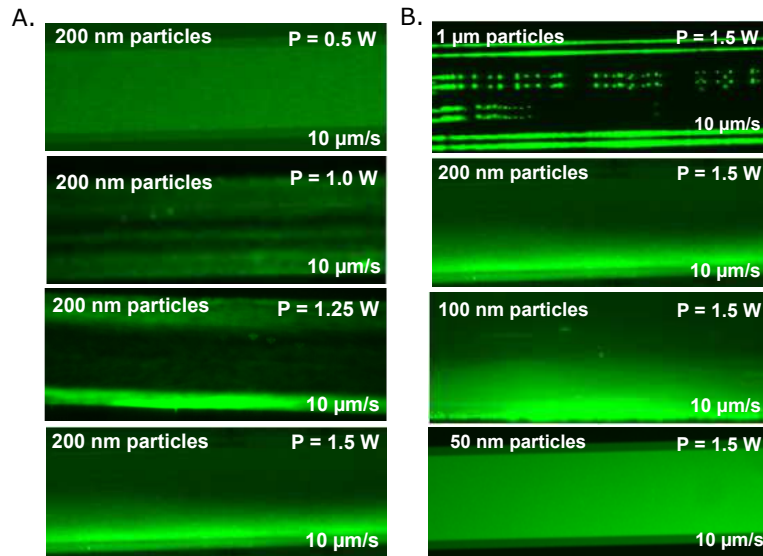
FIGURE 2.5: **Spatial distribution of nanoparticles under SSAWs at low flow**. **A**. Fluorescent microscopy image showing top view of the microfluidic channel. The 200 nm particles exhibit different spatial distribution in the channel as a function of the applied input power to the IDTs, which increases the acoustic wave intensity. Low Intensity (P = 0.5 W) present no visible changes, medium intensity (P = 1 W) shows disruption of the particle distribution and high intensity (P = 1.5 W) show particle focusing. **B**.Nanoparticles with different sizes show a different spatial distribution at low flow velocity ($v = 10$ μm/s) and high acoustic intensity (P=1.5W).
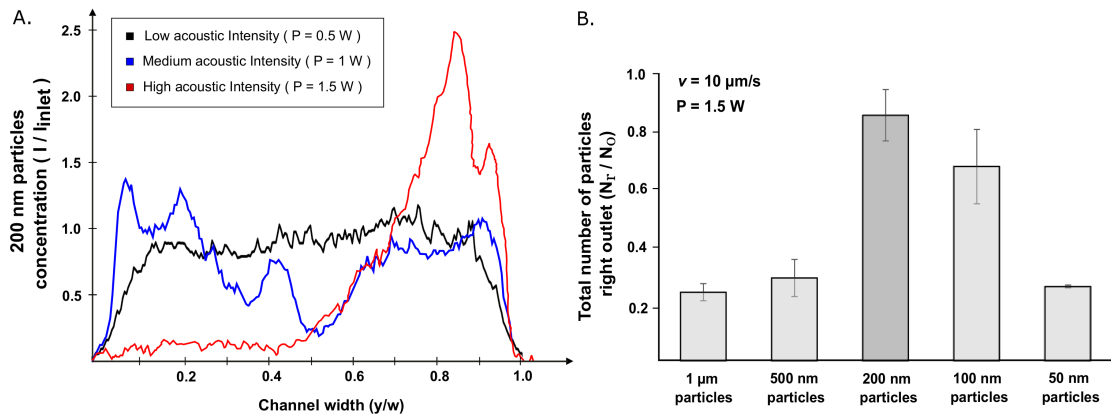
FIGURE 2.6: **Quantification of the differential separation of nanoparticles using SSAWs**. **A.** Concentration profile of 200 nm particles along the channel width for different values of applied input power. **B.** Am heterogeneous solution containing a mixture of 1 μm fluorescent nanoparticles, 200 nm fluorescent particles and fluorescent albumin was exposed to high-intensity SSAWs and collected from the outlets for quantification. Plot of Total particle numbercollected at the device right outlet after applying SSAWs at high acoustic intensity (P=1.5W) with low flow velocity (v=10 μm/s).

Both $1\mu m$ and 500 nm particles showed a preferential concentration around the pressure nodes, with the $1\mu m$ showing a strong focusing while the 500 nm particles showed a wider distribution around the pressure nodes. In contrast, particles of 200 nm and 100 nm in size where focused towards the channel wall. While the concentration of 200 nm particles was narrower, the concentration distribution of 100 nm particles showed a longer tail. Nanoparticles of 50 nm in size or albumin molecules (3.5 nm) showed no effect of the SSAWs, with a uniform concentration profile across the channel (Fig .2.5B). After collection of the samples at the channel outlet and quantification of the concentration by dynamic light scattering or NTA, we found that the total number of particles recovered at the right outlet varied significantly for different particle sizes (Fig .2.6B). Due to the focusing on the pressure nodes, both 1 μm and 500 nm particles showed a recovery of $\sim$ 25-30% of the initial number of particles. Consequently, $\sim$ 40-50% was recovered in the central outlet with the remainder in the left outlet. In contrast, we collected $\sim$ 85% of the 200 nm particles in the right outlet and 68% of the 100 nm particles.For particles smaller than 50 nm, the concentration profile was unchanged and thus, the total number of particles collected follows the outlet/inlet flow rate ratio (Fig 2.6).

These observations suggest that the operation of an acoustofluidic device using an average flow speed of 10 μm/s and input power of 32 dBm leads to a differential fractionation based on two different mechanisms: one dictating the behavior of 1 μm particles (dominated by the acoustic radiation force), and another controlling the motion of 100-200 nm particles (Influenced by the acoustic streaming). Furthermore, the Poiseuille flow appears to compete with these mechanisms at lower velocities while dominating at sufficiently high flow rates. In addition, This results indicate that this acoustofluidic technique can be used for differential separation of nanoparticles of 100-300 nm in diameter from larger particles and smaller molecular contaminants.

2.3.2 Acoustofluidics separation of nanoparticles using focused streams

We tested the efficacy of acoustofluidic nanoparticle separation when the particle mixture is forced into a narrow, straight beam by introducing two sheath flows through two adjacent inlets (Fig 2.7). Here the sheath flows do not contain particles and function as regions of low concentration that can be used to collect small molecules that diffuse across the channel. This additional filtration by diffusion is reminiscent of the H-filter microfluidic devices discussed in Chapter 1. Thus, the main advantage of implementing the sheath flows is to introduce a controlled stream of diluting medium able to significantly reduce the concentration of proteins and other small molecular contaminants.
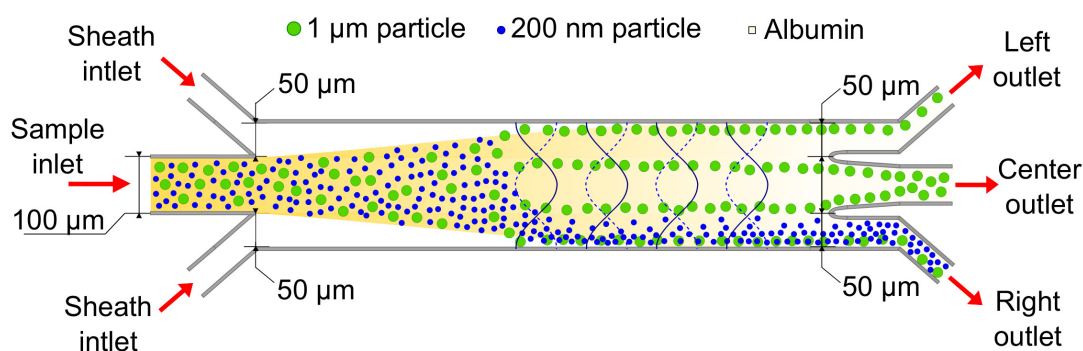
FIGURE 2.7: **Schematic representation of acoustofluidic separation of nanoparticles using a focused stream with sheath flows**. A focused stream of a sample comprising a mixture of fluorescent 1 μm particles, 200 nm particles and albumin was flowed into the Acoustofluidic device along with a sheath flow of DI water. The beam was subjected to high-intensity SSAW at different flow rates of the Poiseuille flow.

To test the potential of this technique for particle purification in combination with SAWs, we studied the fractionation of nanoparticles under the effect of i) diffusion gradients induced by the sheath flows; ii) and acoustic-induced forces resulting from the applied SSAWs (32 dBm input power); and iii) drag forces consequence of the Poiseuille flow. To this end, we performed a series of experiments reducing the flow rate in an acoustofluidic device with two sheath flows and a beam of the nanoparticle mixture used in the previous experiments. Consequently, taking a fixed input power we reduced systematically the Pe number of the particles in solution (Fig 2.8).
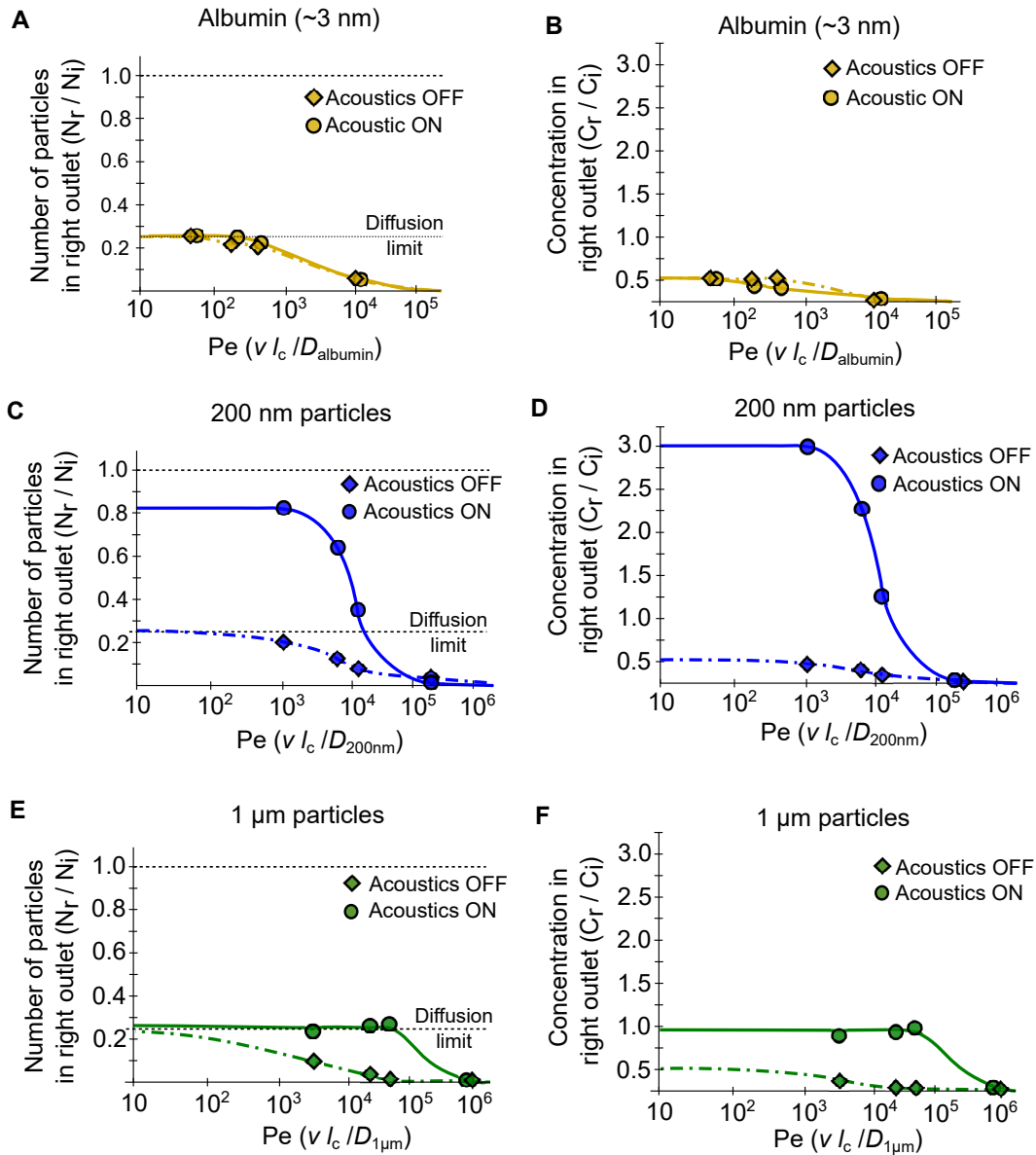
FIGURE 2.8: **Differential purification of nanoparticles using SSAWs in a microfluidic channel as a function of Pe**. Analysis of the effects of the Peclet number on the fractionation of nanoparticles using high intensity SSAWs. Plots show the change in total number of particles and particle concentration for albumin, 200 nm particles, and 1 μm particles collected on the device right outlet. Here, Diamonds represent experimental results without SSAWs, and circles represent values when SAWs are applied. Input power applied P = 1.5W.

As expected, the concentration of protein was dictated only by diffusion effects, exhibiting rapid mixing and a homogeneous concentration profile at sufficiently low values of Pe (Fig 2.8, top right). Thus, the introduction of sheet flows produced a 75% reduction in protein concentration in the channel right outlet. For 1μm particles (Fig 2.8, bottom right), the particle recovery using SSAWs differs from the diffusion-only

case. Similar to the results in Fig. 2.3D and Fig. 2.4D, The position of the focused beam of 1 μm particles is dictated strongly by the acoustic radiation force. Therefore, only high flow rates reduce the residence time enough to avoid significant focusing for particles larger or equal to 1 μm. For nanoparticles of 200 nm in size, we observed particle focusing after applying the SSAWs for low Pe number.

While the experimental results in the diffusion-only case agree with the theoretical expectation, the focusing of particles at low Pe numbers leads to a significant increase in the total number of particles recovered in the right outlet of the device. this results are in agreement with the observations made in Fig.2.3E and 2.4E. Quantification of particle recovery in the right outlet after applying SSAWs at low Pe yielded an 83% recovery, with a corresponding 16% of particles collected in the center outlet (Fig. 2.8, bottom left). Under the same operating conditions, the particle recovery in the right outlet for 1 μm particles was shown to be 15% of the initial concentration, with most particles (70% of the initial concentration) collected in the central outlet.

2.3.3 Effects of width and frequency variations

So far, we have studied the behavior or nanoparticle mixtures under SAWs when the microfluidic confinement has a 1:1 w/λ ratio. Our results show how the presence of pressure nodes in channels with this ratio generate strong focusing of large ($>$ 1μm) particles, while the confinement allows for the acoustic streaming to displace nanoparticles preferentially to one of the channel walls. Here we study the effect of SSAWs generated by identical IDTs in microfluidic channels with $w/\lambda > 1$. In particular, this scenario is of interest as the irrotational flows at the Stokes layer that generate the rolling streaming flows will have a lower impact the larger the width is compare to the wavelength that translate in significantly slower streaming flows. In order to understand the behavior of heterogeneous, dilute solutions of nanoparticles, we fabricated a microfluidic device having a width $w = 400$ μm.
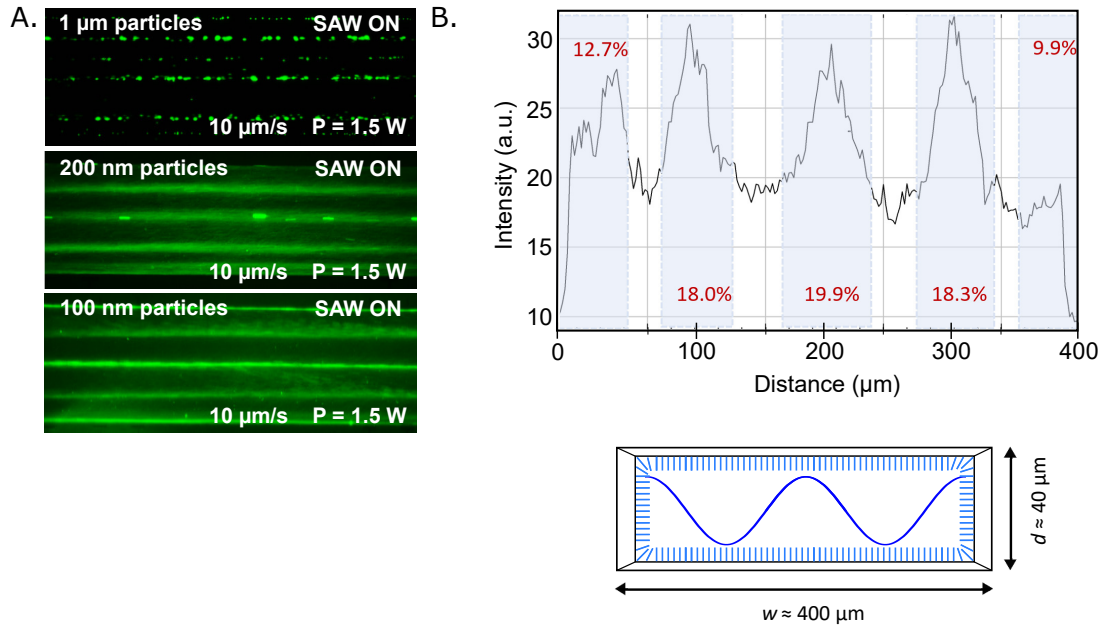
FIGURE 2.9: **Behavior of nanoparticles using SSAWs with multiple pressure nodes**. Applying a SSAW with multiple pressure nodes induce change in the concentration of nanoparticles, increasing the concentration in the vicinity of the pressure nodes. **A**. Fluorescent microscopy of channel top view showing the focusing of 1 μm, 200 nm, and 100 nm particles under a high-intensity acoustic field. **B**. Quantification of the concentration distribution of 200 nm particles across the channel under SSAWs. Channel width $w = 400$ μm, height $d = 40$ μm and wavelegth $\lambda = 200$ μm.

After filling the channel with a solution containing 100 nm, 200 nm, and 1 μm particles, we applied a SAW with a wavelegth of $\lambda = 200$ μm and input power of 32 dBm ($\sim$ 1.5 W) maintaining a flow with $v_{avg} = 10$ μm/s. For this experiment, we observed a dramatic change in the concentration profile of all the nanoparticles. In all cases we noted an increase in concentration of the nanoparticles in the vicinity of the pressure nodes (Fig. 2.9A). As expected, the 1 μm particles create focused beams. However, nanoparticles down to 100 nm also presented significant increase in the local concentration when exposed to SSAWs. Thus, the acoustic waves induce bands of concentration across the microfluidic channel with local maxima at the pressure nodes and channel walls. The peak-to-peak distance between this concentration bands was approximately 100 μm for node-node bands and 80 μm for wall-to-node bands. In the case of 200 nm particles, we quantified the fraction of the total number of articles accumulated in each peak (Fig. 2.9B). We found that the nodal bands have between 18-20% of particles while the wall bands have only between 10-13%. Here, the remainder

$\sim 20\%$ are found in bewteen the bands suggesting that 78-80% of nanoparticles are located at the bands. Consequently, efficient collection of the band streams could be used for nanoparticle concentration or purification.

So far, we have tested the changes in nanoparticle behavior following variations in input power, fluid flow, and particle size. As noted above, variations of the channel width can also have an significant effect on the particle behavior and distribution within the microfluidic channel. However, the effect of channel width is linked with the wavelength of the SAW generated by the IDT. As noted in chapter 1, the traveling SAW generated by the IDT has a center frequency defined by the pitch. Nevertheless, we can test the effect of small variations of the frequency using the same IDT as long as the frequency variations made fall within the Bandwidth of the device. The amplitude of surface acoustic waves with frequencies outside this bandwidth decay rapidly and thus, will not change the particle distribution in the channel. Despite this, we noted that small variations of the operating frequency of an acoustofluidic device can cause significant changes in the trajectory of nanoparticles flowing in the channel (Fig. 2.10A). Specifically, transition form a frequency of 17.95 MHz to 18.20 MHz in a microfluidic channel with $w/\lambda = 2$ induced a shift in the position of 1 μm particle beams ($v_{avg} = 350$ μm/s). Here, all the concentration bands where initially located at pressure nodes in the center of the channel and ± 100 μm from the center (Fig. 2.10B).In contrast, the change in frequency to 18.20 MHz induced a shift in the location of the peaks of concentration of approximately 50μm(Fig. 2.10B). Interestingly, a further increase on the oscillating frequency to 18.28 MHz revert the effect, returning the concentration peaks to their initial location(Fig. 2.10A,B). This effect is more noticeable in devices with a $w/\lambda \gg 1$, as the increased number of pressure nodes and the increased distance of the nodal bands to the wall facilitate the observation of these displacements do to frequency variations. In channels with $w/\lambda \leq 1$, The proximity of the nodes to the wall difficult the observation of this phenomena, as the band displacement is $\sim \lambda/4$. This suggest that frequency-induced band displacement may occur in devices with $w/\lambda \leq 1$, but the effect is mitigated by the proximity of the wall.
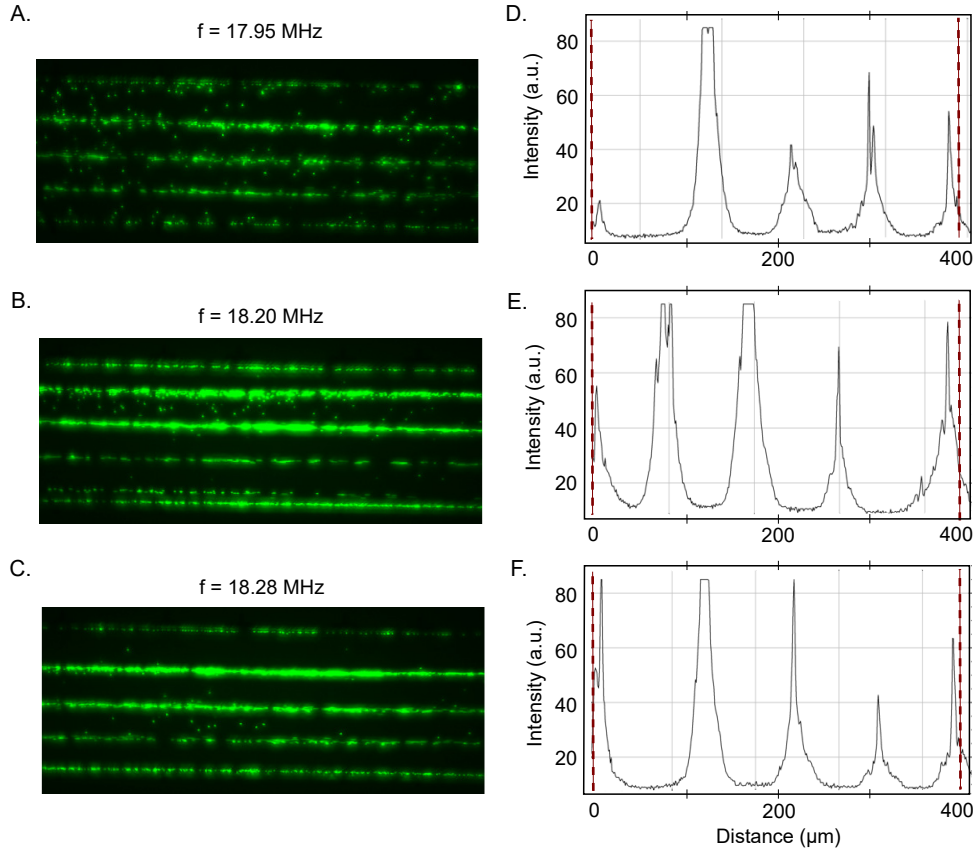
FIGURE 2.10: **Displacement of particle concentration peaks with frequency variations**. For a λ/w ratio < 1, nanoparticles focus towards the wave pressure nodes. Small changes in the frequency of the electric signal induce spatial displacement of the concentration beams. **A-C**. Fluorescent microscopy of 1 μm particles exposed to variations of the frequency near the basal oscillating frequency. **A.** $f = 17.95$ MHz; **B.** $f = 18.20$ MHz; **C.** $f = 18.28$ MHz. **D-E** Quantification of fluorescent intensity across the channel for**D.** $f = 17.95$ MHz; **E.** $f = 18.20$ MHz; **F.** $f = 18.28$ MHz. Channel width $w = 400$ μm, height $d = 40$ μm and wavelength $\lambda = 200$ μm.

2.3.4 Temperature control and energy dissipation

As discussed in chapter 1, acoustofluidic devices require careful temperature control along with energy efficiency considerations.In particular, the viscous dissipation of acoustic energy when in contact with fluids and the dissipation due to mechanical stresses in the solids can lead to an increase in the local temperature. This effect is problematic as temperature increases of small volumes of fluid subject to acoustic waves and gradients of pressure can facilitate cavitation leading to device failure. In addition, commonly used piezoelectric materials like Lithium Niobate have poor thermo-mechanical properties that can lead to fractures in the material.

70
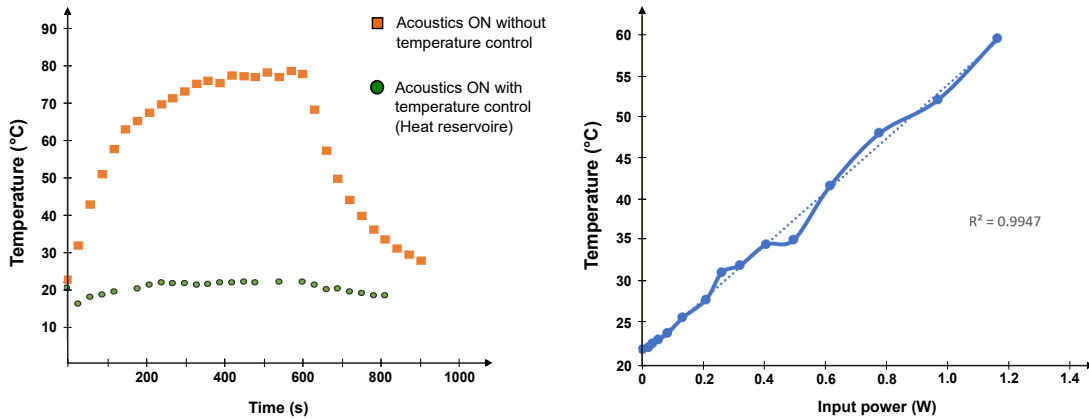
FIGURE 2.11: **Temperature changes in the acoustofluidic device**. After applying high-intensity SSAWs in a microfluidic channel, the temperature of the fluid raises. Once the SSAWs are turned off ($t = 400$ s), the temperature slowly decreases to room temperature. The fluid temperature increase linearly with the input power. To mitigate this effect it is necessary to use temperature control that allows they system to operate at a steady temperature.

Furthermore, in the case of temperature sensitive samples containing cells, proteins, vesicles, liposomes, or certain polymers, significant increases in the fluid temperature can lead to sample damage, protein denaturation, loss of viability and cell death. Consequently, its important to stablish an appropriate temperature control in acoustofluidic devices. Without temperature control, the acoustofluidic device described in the experimental setup was operated while monitoring the temperature of the fluid at the center of the channel (Fig. 2.11). For a fixed input power of 30 dBm, the temperature of the fluid increases over time in the absence of temperature control. A stream of deionized (DI) water flowing at a constant flow rate (350 μm/s) initially at room temperature (22° C) heats up to 80° C in 5 minutes. Once the input power is turned off and there is no SAWs, the temperature in the center of the channel returns to the initial value. The use of a temperature control systems in the form of a cooling plate provides a heat reservoir that absorbs the heat generated by viscous dissipation through conduction trough the piezoelectric substrate thickness. As seen in Fig. 2.11, the use of this temperature control is enough to maintain a stable temperature in the device for proper operation.We note here that the temperature increase in this acoustofluidic device scale linearly as a function of the applied input power. This suggest tha the use of high-intensity SAWs for nanoparticles purification strategies necessitate an effective

heat exchanging unit while temperature control might not be required for applications at low-intensity.

2.3.5 Acoustofluidic focusing of nanoparticles using tilted-angle SAWs

While most acoustofluidic devices are designed to have the acoustic waves orthogonal to the direction of flow, the maximal separation distance based on acoustophoretic effects is limited to a quarter of the acoustic wavelength. As a result, acoustofluidic separation techniques have struggled with separating a fraction of the target particles from the nontarget particles leading to low separation efficiency. In addition, two sets of particles with small size differences between them cannot be separated from each other leading to low sensitivity. Overcoming these limitations could pave the way for powerful label-free separation methods with many applications in biology research, disease diagnosis, and clinical practice. To achieve this, researchers have introduced a configuration called tilted-angle standing surface acoustic waves (taSSAW). Here, the acoustic waves are oriented at an optimally designed inclination to the flow direction in the microfluidic channel. Particles flowing in solution with different sizes and/or physical properties will experience different acoustic radiation forces and will require different times to migrate to the pressure nodes providing clear identifiers for separation.
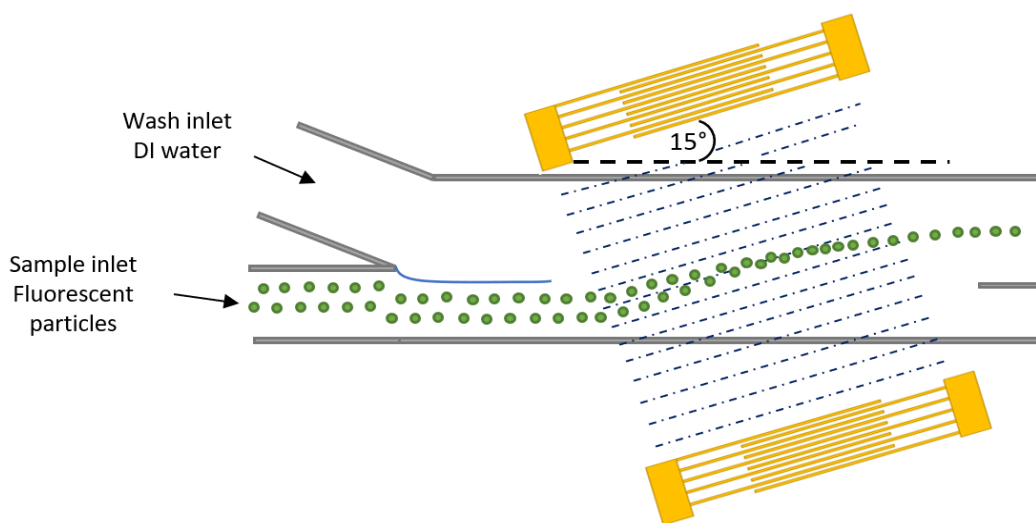
FIGURE 2.12: **Schematic of acoustofluidic focusing using tilted-angle SAWs.**
Schematic representation of tilted-angle acoustofluidic device. An IDT rotated by a 15° angle generates a SSAW that comes into contact with a solution flowing a straight channel. The waves promote a lateral displacement of the particles.

The pressure nodal lines induced by the SSAW inclined at a specific angle to the flow direction, rather than being parallel to each other. This configuration allows a particle in a fluid medium to experience both the acoustic radiation force and the laminar drag force, influencing the displacement across the channel. The competition between these two forces determines the position of the particle and defines its movement along the pressure nodal lines, which lie across the channel at a particular angle of inclination to the flow. As a result, the migration distance of the particle along the direction perpendicular to the flow could be a few times or tens of times the acoustic wavelength, depending on the geometry of the channel, achieving migration distances significantly higher than that of the traditional acoustic separation approaches. The ability of taSSAW to achieve much larger separation distances leads to better separation sensitivity. Because there are many parallel pressure nodal lines lying across the flow, target particles that escape from one pressure nodal line can be trapped again by the neighboring nodal line and be separated from the nontarget particles. This multiple-node design also produces higher separation efficiency [172, 181, 182].
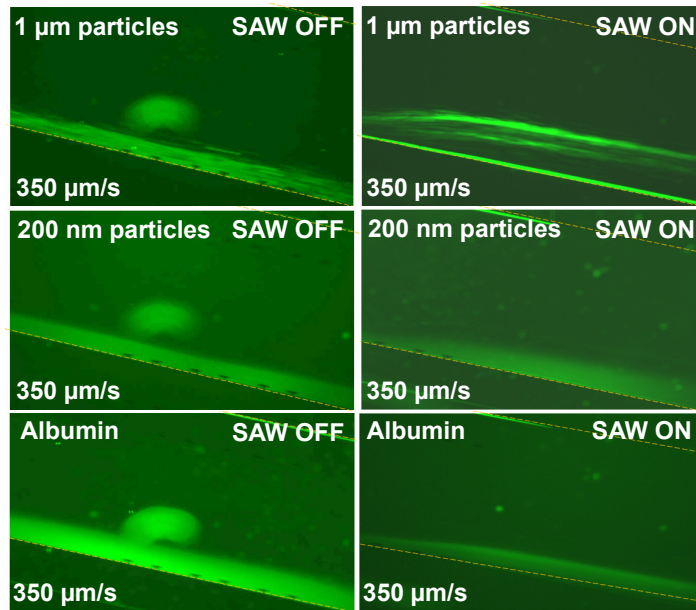
FIGURE 2.13: **Acoustofluidic focusing of nanoparticles using tilted-angle SAWs with intermediate flow**. Fluorescent microscopy showing the separation using tilted-angle SSAWs of a mixture containing albumin, 200 nm, and 1μm particles when the average fluid velocity is $v = 350$ μm. Channel width $w = 1$ mm.
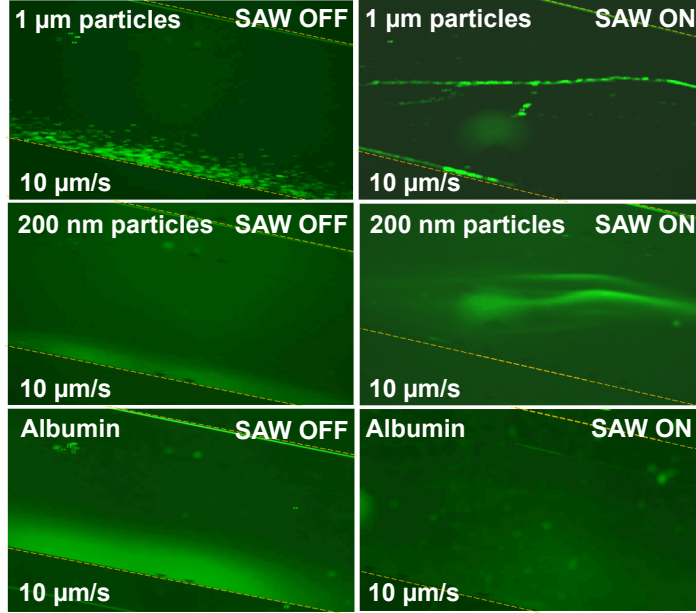
FIGURE 2.14: **Acoustofluidic focusing of nanoparticles using tilted-angle SAWs with intermediate flow**. Fluorescent microscopy showing the separation using tilted-angle SSAWs of a mixture containing albumin, 200 nm, and 1μm particles when the average fluid velocity is $v = 10$ μm. Channel width $w = 1$ mm.

Encouraged by this findings, we designed and fabricated a taSAWs device with the purpose of testing the ability of this strategy to separation nanoparticles. The microfluidic channel was aligned at a 15° angle with respect with the IDTs, having a wavelength $\lambda = 200$ μm and channel width set as $w = 1$ mm (Fig. 2.12. For this set of experiments we used the heterogeneus misxture of particles used before. The solution containing albumin, 200 nm, and 1 μm particles was introduced to the acoustic region through an inlet of 200 μm that was focused with a sheath flow of DI water. We followed the evolution of the fluorescent particles within the channel using fluorescence microscopy until the particles reached the channel outlet. Based on the observations made for the separation of nanoparticles in heterogeneus mixtures using SAWs orthogonal to the fluid flow, we performed experiments at a relative high flow speed ($v = 350$ μm/s) and compare the results with those obtained at a low flow rate ($v = 10$ μm/s) looking for differences in performance (Fig. 2.13, 2.14). As shown in figure 2.13, for 200 nm particles and soluble proteins the drag force imposed by the velocity field of the Poiseuille flow dominate at a flow speed of $v = 350$ μm/s. Having a large τ_{conv}, the concentration profile remains relatively constant through the channel,

with only small reductions in protein concentration due to diffusion into the sheath flow. Conversely, the 1 μm particles show a displacement induced by the acoustic field. At a flow speed of $v = 350$ μm/s under taSSAWs, these particles are displaced and form a concentration band. As the focused beam of particles moves further away from the channel wall and into the bulk of the fluid where the velocity is higher, the drag force overcomes the acoustic radiation force and pushes the beam of concentrated particles into the channel without further significant later displacement. Interestingly, we noted a band of particles slowly flowing at the channel wall. This observations are consistent with the behavior of these particles under similar parameters in orthogonal SSAW devices (See Fig 2.3 and 2.4).

At a slower flow speed of $v = 10$ μm/s, the behavior of the solutes in the mixture changes considerably. particles of 1 μ in size form a focused particle beam that displace the particles from the inlet across the channel until the beam reaches the opposite wall. This is consistent with the operating principle of taSSAWs, where the interplay between the drag forces and the acoustic radiation forces cause particles to displace parallel to the pressure node lines. Indeed, the angle formed between the particle beam and the channel wall is $\sim 15°$. Similarly, a band of increased concentration of 200 nm particles was observed at this flow rate. Here, the particle band is diffused instead of focused in a line, but exhibit significant concentration and displacement. furthermore, this concentration band was displaced up to 500 μm from the original position facilitating collection. The concentration of albumin is dramatically reduced at low flow rates, as the protein molecules diffuse into the diluting sheath stream. Moreover, the experimental results suggest that the taSSAWs may promote mixing for this particles as we observed faster dilution under the effect of the acoustic waves. Further studies are needed to validate this observations. Given that the 1 μm particle beam is displaced 800-900 μm, while the 200 nm band is displaced 500 μm, we can easily collect independent streams of highly concentrated particles. Furthermore, as the protein is highly diluted by the sheath flow, both streams of particles will have high purity ratios.

We quantified the fraction of particles in the particle beam focused using taSSAWs.
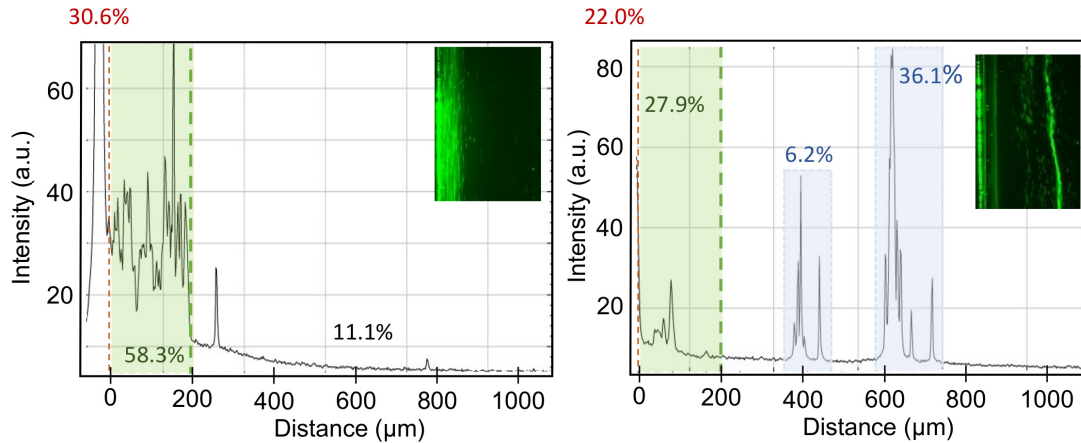
FIGURE 2.15: **Quantification of particle displacement using tilted-angle SSAWs**. When the SSAWs are off (left) most of the particles are concentrated in a band $d_1 \approx 200$ μm wide near the channel wall. Turning the SSAWs on (right) promotes a lateral displacement of the particles generating bands at a distance of $d_2 \approx 800$ μm. Channel $w = 1$ mm, height $d = 40$ μm and wavelength $\lambda = 200$ μm. Particles 1 μm in diameter.

Without the influence of taSSAWs, the 1 μm particles are mostly contained to the focused stream within the sample inlet width of 200 μm. A small fraction (11.1%) can be found in the bulk of the fluid as a consequence of diffusion at a low flow rate (Figure 2.15, left). In contrast, applying the taSSAWs generate a focused beam of particles that contain 36% of the initial particles (Figure 2.15, right). Interestingly, 22% of the particles acumulate at the channel wall with 50% of particles remaining in within the initial 200 μm. Furthermore, a smaller and highly variable band of particles was observed in between the 200 μm region and the focused beam containing approximately 6.2% of particles. Due to the proximity of this band to the center of the channel where the drag force due to the Poiseuille flow is maximum, we hypothesize that the drag on this area disrupts the path of the particles as the bound the pressure node lines. As the solution flows through the channel, particles in the intermediate band join the particle focused beam.

Our results are consistent with previous observations of particle displacement usign taSSAWs[180]. The formation of particle beams was initially employed to concentrate an separate particles in mixtures with microparticles [181]. In their work, Ding *et. al.* demonstrated that acoustofluidic devices with a tilted angle of 15° could be used to form distinct bands of 15 μm, 10 μm and 4 μm particles[181]. Further research from the

Huang lab showed that taSSAWs could be used to safely focus and separate circulating tumor cells from Leukocytes in solution or from plasma [181, 182] reporting a white cell removal of $\sim 99\%$ with a cancer cell recovery of $\sim 60-80\%$ [182]. Using a taSSAW device with an $15°$ angle, Wu *et. al.* First reported separation of nanoparticles [171]. Here, the acoustic waves succesfully displaced nanoparticles between 600-900 nm with a removal rate of 96.4% for 900 nm and 80.4% for 600 nm, achieving a recovery of 200 nm and 100 nm particles in solution of 85.6% and 90.7% respectively. Thus, this strategy did not displace and focus small nanoparticles, focusing on the removal of larger particles. No quantification of smaller molecular contaminants was provided in these studies. In addition, a separation of 300 nm particles from 100 nm particles was achieved by Sehgal and Kirby[170] using a Fabry-Perot acoustofluidic resonator. In this work the researchers used taSSAWs generated by IDTs coupled to Bragg reflectors having the microfluidic channel on top of the transducers. In this arrangement the researchers reported the formation of concentration bands with a separation efficiency of >80%.

The results presented here show a acoustofluidic method that promotes displacement of both large and small particles forming concentration bands. Control of the Pe number in the systems and the introduction of sheath flows greatly reduce the concentration of molecular contaminants and increase the efficiency of particle focusing. Thus, we obtain easy to collect streams of particles with high recovery and high purity. As this method has been proven to be safe for the separation of cells and vesicles, our approach improves uppon existing methods towards the development of high-efficiency and high sensitivity acoustofluidic methods for diagnostics and analytical applications.

2.3.6   Purification of extra-cellular vesicles

Exosomes represent an exciting set of cell-secreted vesicles that carry unique molecular cargoes containing proteins and RNA that can be seen as molecular fingerprints of the parent cell. These 50-150 nm vesicles act as signaling packages in a rich intercellular signaling network that has been recently described, with profound, yet not fully understood biological implications in the development, progression, and treatment of multiple pathologies of public health interest, including autoimmunity, transplant rejection, and cancer.

The field of exosomes biology burgeon after scientists reported that exosomes were enriched in major histocompatibility complex (MHC) proteins that bind tumor antigens and effectively activate T cells to promote antitumor responses, which indicated that exosomes act as intercellular signaling vehicles and paved the way to develop novel cell-free antitumor vaccines. In addition, the discovery of mRNA and miRNA in exosome samples led to the landmark discovery that exosomes can mediate epigenetic reprogramming of neighbor or distant cells to promote adaptation to danger signals or stress in the microenvironment. Combined, these properties of exosomes have established extracellular vesicles as key factors in the development of tolerogenic tumor microenvironment and the inhibition of antitumor responses induced by immunotherapies. Unfortunately, the mechanisms through which exosomes exert their biological functions in the context of disease are poorly understood. In addition, exosomes can be used to identify disease biomarkers from complex samples such as blood or lymph, to develop diagnostic tools. Consequently, improving our understanding of the underlying mechanisms of exosome signaling for cancer immunotherapies and other disease represent a matter of the utmost importance in the field. However, the progress to achieve this goal has been decelerated due to technical constraints, as the current technologies to isolate and purify exosomes require expensive equipment, are time consuming, produce high losses of valuable samples and exhibit low throughputs. Despite extensive efforts, there is no method to date that fulfill the needs of the field in terms of vesicles recovery, scalability, throughput and cost-effectiveness. Therefore, we propose to de-

velop a novel technology to purify exosomes by integrating a combination of ultrasound nanofilters and water-absorbent polymeric materials to remove molecular contaminants in a microfluidic chip. This strategy will be complemented with theoretically-informed chip design employing computer simulations of nanoparticles in confinement. The tools we propose to develop can be used to characterize exosomes from complex biological samples, like blood or cell culture, to obtain high quantity and quality data that helps to identify molecular signatures that shed light to the underlying mechanism involved in tumor development, and biomarkers for early diagnosis of disease. By tackling a key problem in experimental exosomes biology, we aim to promote a new wave of discoveries that improve the effectiveness of current cancer immunotherapies, inspire new approaches to treat cancer disease and translate into treatments for other pathologies of importance for public health.

The first reports of exosomes were made while researching the pathway of transferrin receptor externalization during reticulocytes maturation[183]. In these studies, the transferrin receptor was detected in the fraction obtained after centrifugation at $8000 \times g$ for 25 min followed by a ultracentrifugation at $100\ 000 \times g$ for 90 min[184]. This method is still widely used nowadays for exosome isolation. However, variants of this method can involve higher-speed ultracentrifugation at 140,000 x g [185] and can include different steps before final ultracentrifugation, such as filtration to eliminate debris and large vesicles [186] or size-exclusion chromatography to eliminate soluble proteins[187]. It is important to note that protocols used to purify larger EVs also involve centrifugation, although at lower speeds, from 10,000 x g [188] to 50,000 x g[189]. Isolation methods based on ultracentrifugation allows enrichment in exosomes, subtypes of EVs and other particles of the same size, including protein aggregates and small viruses, all of which co-sediment at 100,000 x g [190], highlighting the need for better protocols. The incorporation of differential centrifugation in sucrose gradient led to the isolation of different subtypes of exosomes within the heterogenous group that sediment at 100.000 x g. Using this technique, different groups described exosomes as equilibrating at densities ranging from 1.13 to 1.19 g/ml in sucrose [191]. Subsequent studies showed that EVs containing HSC70 and HSP70, flotillin-1, and MFGE8 equi-

librate at slightly different densities than does with ALIX or CD9[185, 192, 149, 193]. Furthermore, researchers observed that tetraspanin-rich vesicles recovered in the high-speed pellet take more time than others to reach their equilibrium density during centrifugation in a sucrose gradient [194, 192, 195] leading to the separation of EVs subtypes by differential buoyant velocity centrifugation[195]. Additionally, short-term sedimentation of EVs in iodixanol-based gradients may separate efficiently EVs from viruses, as showed by separating myeloid cell-derived vesicles from HIV virions [196]. Despite the significant success of combined approaches based on ultracentrifugation and ultrafiltration, there are important downsides associated with their use to isolate exosomes and other nanovesicles. Because the pellet from a high-speed spin will contain extravesicular proteins complexes/aggregates, lipoprotein particles, and other contaminants, ultracentrifugation methods achieve enrichment in nanovesicles rather than true isolation[191]. Additionally, vesicles losses during processing may occur, as small vesicles near the bottom of tubes can pellet at lower speeds. Aggregation of vesicle [197] and pellet of aggregates may further reduce the final yield [191]. Moreover, concerns have risen about the potential damage EVs during ultracentrifugation. Even though existing reports based on light-scattering techniques suggest that ultracentrifugation does not generate observable damage, This results have been put into question and well-controlled comparisons in terms of size, percentage of damaged vesicle, soluble protein contamination, and RNA are required[191]. When filtration steps are combined with centrifugation to improve purity, is important to note that forcing particles through filter pores may cause deformation and breakup of EVs, thereby potentially skewing results and increasing the losses due to processing. In certain studies, immuno-isolation was implemented to further purify EVs fractions and obtain highly pure vesicles using high-affinity antibodies specific to some surface proteins know to be enriched in some subpopulation of exosomes (e.g. CD63, CD9)[198, 199, 200]. Careful analysis of the results obtained must be assessed, as exosomes with similar origins and cargo may not be enriched in the same surface proteins [70].

Because the standard methods used to isolate exosomes produce low recovery yields, may damage the vesicles, require expensive equipment and are time consuming, re-

searching are investigating intensively novel strategies to purify exosomes and achieve low-cost solution with high throughput. New strategies to isolate exosomes and other nanoparticles include Polymeric precipitation kits [201], Protein organic solvent precipitation [202] and devices with nanoporous filter membranes [203, 204]. Notably, nanopore membrane methods have shown 4-1000 fold increase in exosome recovery from plasma, urine and cancer cells samples [204]. However, the purity of the samples in terms of protein contaminants was not reported. Microfluidics and nanofluidic devices have been used to separate vesicles [205, 206] and tumor derived exosomes using specific antibodies [207, 208], Nanoscale lateral displacement arrays [209] or induced nanoshearing[210]. Lastly, the development of exosome detection sensor in microfluidic devices using nano-plasmonic sensors have been reported [211].

Acoustic purification techniques have emerged as interesting approaches to recover EVs [212, 169, 213, 214]. Recent reports using this technology separate nanoscale vesicles < 200 nm in size from microvesicles, which can be integrated with microfluidic techniques as a cheaper automated alternative to ultracentrifugation/ultrafiltration [169]. Lee *et al* proposed an acoustofluidic device to separate EVs through acoustophoretic effects using orthogonal SSAWs[169]. They reported a separation efficiency of > 90% for polystyrene particles and a recovery rate of > 80% for exosomes. However, the separation strategy was based on the acoustic displacement and removal of larger particles without direct actuation on the vesicles. An alternative acoustofluidic strategy for the purification of exosomes was proposed by Wu *et. al.* using a taSSAWs[172]. Here, they isolated 110 nm particles from 5 μm particles and 970 nm beads achieving a recovery rate of $\sim$ 99%. Applying this strategy to separate exosomes from whole blood showed successful removal of cells, debree and larger vesicles with a reported recovery rate and purity of 82.3% and 98.4%[172]. Importantly, both strategies mentioned above used acoustic waves to remove larger particles from the EVs sample without mention on the concentration of smaller particles contaminants in solution.

Motivated by previous our results focusing and separating polystyrene particles, we tested the performance of our acoustofluidic separation strategy by applying orthogonal SSAWs on a sample containing extracellular vesicles collected from cell culture media.

For these experiments, we prepared a solution containing fluorescent vesicles derived from a genetically-modified human cell line expressing fluorescent CD9 — a surface protein enriched in EVs. This solution was focused with sheath flows, and exposed to SSAWs to promote streaming focusing of nanoparticles; radiation force focusing of larger particles; and diffusive dilution of small contaminants as previously described. The input power was 32 dbm ($\sim$1.5 W) and the flow speed was set to be 10 μm/s in a channel with $w/\lambda = 1$ ratio having $\lambda = 200$ μm, as before. After collection of the samples and analysis, we obtained an EV recovery of 81% with an approximate 2.5 fold increase in the sample purity ratio (Fig. 2.16).
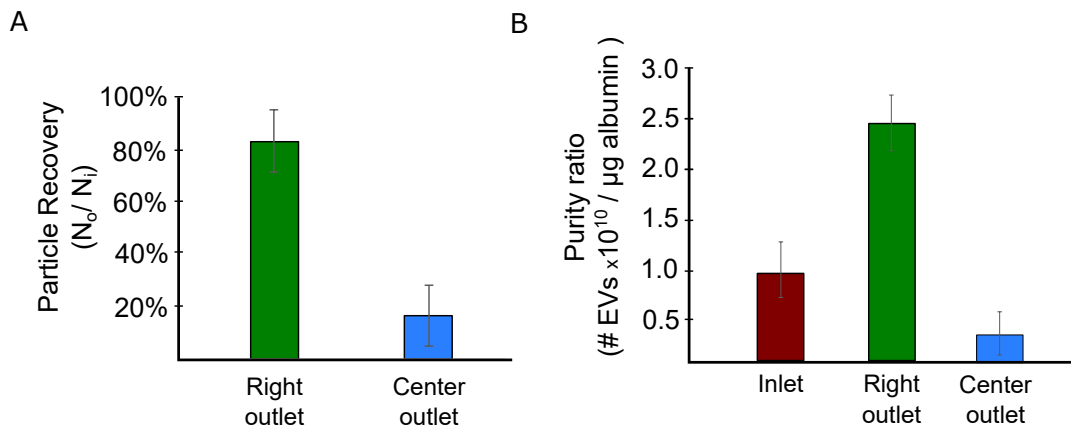
FIGURE 2.16: **Purity and particle recovery of extracellular vesicles**. **A**.Particle recovery of EVs. **B**. Purity ratio. Samples collected from the right outlet and center outlet and compared with the sample at the inlet.

The recovery rate of EVs reported in on par with previous acoustofluidic methods, while providing the additional advantage of small contaminant dilution. Nano-tracking Analysis (NTA) of the particle distribution showed that the size distribution of EVs in the right outlet was similar to the distribution at the inlet (Fig. 2.17B,C). These observations are consistent with the experimental results in Fig. 2.16 and Fig. 2.17, suggesting that the differential fractionation of nanoparticles is reproducible and can be used for both rigid and soft nanoparticles. The use of acoustofluidic filtration units in series or in parallel can be used to further increase the particle recovery and purity of three groups of particles: I) particles of > 1 μm diameter; II) nanoparticles between 100-300 nm in size; and III) small nanoparticles and soluble molecules.
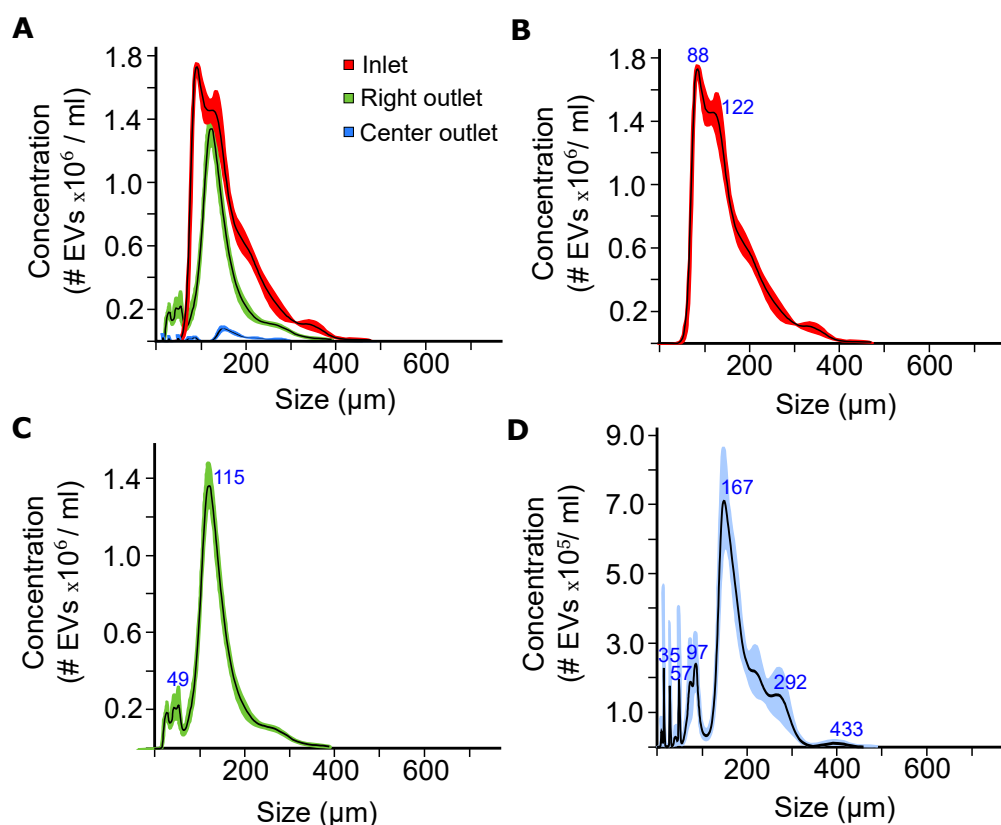
FIGURE 2.17: **Quantification of EVs Purification with SSAWs using Nano-tracking analysis**. A sample of fluorescently labeled extracellular vesicles (CD9+ mcherry) is analyzed after acoustofluidic purification. Nano-tracking analysis (NTA) was used to determine the size distribution and concentration of vesicles. **A** Size distribution before and after differential separation using SSAWs. **B-C**. Size distribution and peaks of concentration for the samples at **B**. the channel Inlet, **C**. Channel right outlet, and **D**. channel center outlet. The concentration of particles at the channel left outlet was negligible. Applied power $P = 1.5$W, average flow velocity $v = 10$ μm/s.

2.4 Conclusion

We have demonstrated an acoustofluidic platform capable of differential separation of nanoparticles. The device allows us to separate particles 150-300 nm in diameter from (i) cells and microparticles > 1 μm in diameter; and (ii) Molecular components in solution, including proteins, sugars, hormones, nucleic acids, and ions. Compared with other assays for nanoparticle isolation, our strategy provides continuous, label-free, contact-free, high-throughput separation with high reproducibility and potential for automation. The power intensity and frequencies used to manipulate soft particles like EVs are known to preserve morphology, content, and functions of the vesicles, highlighting the potential of these techniques for safe, on chip, point-of-care applications.

At first glance, the EVs recovery of approximately 85% obtained is only at par with other acoustofluidic systems that achieved $> 90\%$ separation yields. However, previous strategies do not offer an alternative to remove molecular contaminants from EV or other small nanoparticle samples. Our system exploits the fast diffusion of small molecules to our advantage, reducing concentration of contaminants in the outlets enriched with nanoparticles. In addition, this differential purification method can be combined with traditional orthogonal or tilted angle acoustofluidics techniques for precise and versatile filtration of complex samples. Our technology utilizes both acoustic radiation forces and acoustic streaming as mechanisms for the particle manipulation. In contrast, acoustofluidic focusing of nanoparticles traditionally consider streaming effects as a detrimental side effect setting a lower limit on particle size separation. Similarly, high-frequency nanoparticle actuation based on streaming circumvents radiation effect by limiting the size of the acoustic area. The combined use of diffusion, acoustic radiation, and acoustic streaming opens the door for novel acoustofluidic platforms that use a sophisticated yet controllable interplay of mechanisms for applications. As a tradeoff, stable focusing of nanoparticles using the acoustofluidic technique presented sets an upper limit on the flow rate. Operation at high Pe disrupt the balance of forces, allowing drag forces from the Poiseuille flow to overcome the Rayleigh flows. Further work in this area can bypass this limitation to improve device through-put and process times.

Some of the notable limitations of this technique include: i) Reliance on temperature control systems to avoid overheating, cavitation, and device failure; ii) The existence of an upper limit on flow rate for proper operation; iii) Dependance on operating principles that require dilute samples, iv) Isolation of non-exosomal particles and protein aggregates in the nanoparticle compartment, iv) adsorption and accumulation of lipids and proteins in channel walls promoting contamination of samples. In particular, the effect of high particle concentration on particle dynamics induced by streaming, the scattering disruption in high concentration, and other hydrodynamic effects are not well understood. Little is known about the combined effects of these forces in droplets, droplet shells, nanocrystals, and non-spherical particles. To overcome these challenges,

we need new and exciting engineering solutions, including different transducer designs, circuit optimization, cleaning protocols in continuum, integration of sensors, and additional external fields, among others.

CHAPTER 3

MECHANISMS OF ACOUSTOFLUIDIC FOCUSING

3.1 Introduction

With the development of modern devices capable of generating ultrasonic acoustic
fields, several industrial and clinical applications have emerged using contact-less ma-
nipulation of macroscale objects, microparticles, and biological particles like cells or
vesicles suspensions in MEMS and biologically oriented lab-on-a-chip systems[215]. In
parallel, the rise in applications using acoustic fields have stimulated the development
of analytical and computational models to understand the achievable fluid and particle
motions under diverse design and operating parameters. On the one hand, one can
develop algorithms to simulate the whole physical problem, including the excitation of
the SAW, the mechanical deformations in the piezoelectric and the consequent com-
pression of the fluid in the resonance chamber. This approach is more precise but
also time consuming and resource intensive. On the other hand, one can simplify the
simulation model calculating the fluid motion governed by the Navier-Stokes equation
induced by an oscillatory boundary. This approach is less precise and provides no in-
formation on the deformation of the substrate but can be performed much faster[216].
The canonical problem of transmission through a single channel, slit, or duct with rigid
walls has been studied widely over the years[217] . The resonances are set up within
the channel, associated with relations between the wavelength and the length of the
slit, with the exception of end-corrections. More recently these resonances have been
termed the Fabry-Perot resonances, owing to their similarities with the electromagnetic

resonances[218]. Particularly at small length scales, neglecting thermo-viscous effects is a significant assumption. Authors showed that including attenuation in-air results in the phase speed along a narrow duct or channel being substantially reduced, even when the channel width is an order of magnitude greater than the boundary layer parameter $\hat{\delta}_v = \sqrt{\nu/\omega}$ [219]. Here ν denotes kinematic viscosity, and ω is the angular frequency. It has been observed that thermo-viscous boundary layer effects can have a significant impact upon the propagation of sound along narrow, rigid-walled channels giving substantial acoustic absorption within the audio frequency range in air. This phenomenon is used routinely in the acoustics industry as a means to soften boundaries and attenuate unwanted sound[220]. It is important to note, that most of the literature is focused on the study of acoustic interactions with a perfect gas[220]. The study of thermo-viscous acoustic propagation in narrow water filled channels or slits appears to be lacking, although work has been done on viscous liquid-filled channels. This area of research was initiated by Del Grosso[221] and has been followed up recently with work including viscous effects[222, 223, 224, 225]. Cotterill et al provided a general framework with which to study thermo-viscous acoustic attenuation in narrow channels applicable to arbitrary Newtonian fluids, allowing the study of thermoviscous effects upon dense fluids of low compressibility for which the perfect gas assumption is inappropriate[220]. As the particle diameter $2a$ is reduced below 2 μm, viscous effects are expected to become significant, as this length corresponds to a few times the viscous penetration depth d. Analytical expressions for the viscous corrections to the radiation force have been given recently, valid in the range by $a \ll \lambda$ and $\delta \ll \lambda$. [215, 226, 119] As described in Chapter 1, when a standing ultrasound wave is established in a microchannel containing a microparticle suspension, the particles are subject to two acoustic forces: the acoustic radiation force from the scattering of sound waves on the particles, and the Stokes drag force from the induced acoustic streaming flow. The resulting motion of a given particle is termed acoustophoresis, migration by sound. Experimental work on acoustophoresis has mainly dealt with the radiation force, primarily because this force dominates over the streaming-induced drag force for the studied aqueous suspensions of polymer particles or cells [227, 228] In addition, the acoustic streaming flow induced

by viscous stresses in the boundary layers near rigid walls, significantly influencing the acoustophoretic particle motion as the size of the particle or the confining microchannel is reduced[229, 230] The cross-over from radiation-dominated to streaming-dominated motion has been observed in experiments, with a key depending on the channel geometry and boundary conditions[231, 232]. Although acoustic streaming is a well-known phenomenon in acoustics, streaming is often misunderstood due to the many forms in which it may arise in acoustofluidic microsystems. Not only is acoustic streaming difficult to predict quantitatively but there is also a lack of theoretical analysis in configurations that are the experimentally relevant.

In this chapter we present the results of numerical computations studying the effect of surface acoustic waves on nanoparticles flowing in a thermo-viscous fluid. We describe the interplay bewteen the acoustic radiation force and the acoustic streaming for different particle sizes, and study the effect of variation of wave amplitude due to viscous dissipation on particle dynamics. Our results recapitulate the experimental observations from Chapter 2, providing an insight on the mechanisms of differential fractionation of nanoparticles in acoustofluidic systems.

3.2   Theoretical analysis and computational model

The governing perturbation equations for the thermoacoustic fields are well-known. A brief introduction to this equations was presented in Chapter 1. Lets assume a quiescent fluid with equilibrium temperature T_0, density ρ_0 and pressure p_0. The fluid is described by the thermodynamic fields T, ρ, p, the entropy s, and the hydrodynamic velocity vector field $\mathbf{v}$. Changes in ρ and s are given by the thermodynamic relations

$$d\rho = \gamma \kappa \rho dp - \alpha \rho dT \tag{3.1}$$

$$ds = \frac{C_p}{T}dT - \frac{\alpha}{\rho}dp \tag{3.2}$$

Where C_p is the specific heat capacity at constant pressure, κ is the fluid isentropic

compressibility, α is the isobaric thermal expansion coefficient, and γ the heat capacity ratio. This equations relate the density and the entropy to changes of temperature and pressure, reducing the total number of variables to solve for. Consequently, we can express the variables describing the system with a perturbation series as:

$$T = T_0 + T_1 + T_2 \qquad p = p_0 + p_1 + p_2 \qquad \mathbf{v} = \mathbf{v}_1 + \mathbf{v}_2 \tag{3.3}$$

Introducing this expansion into the thermodynamic heat transfer equation, continuity equation and Navier-stokes equation we extract the first order equations:

$$\partial_t T_1 = \frac{\alpha}{\rho C_p} \nabla^2 T_1 + \frac{\alpha T_0}{\rho_0 C_p} \partial_t p_1 \tag{3.4}$$

$$\partial_t p_1 = \frac{1}{\gamma \kappa} \left[\alpha \partial_t T_1 - \nabla \cdot \mathbf{v}_1 \right] \tag{3.5}$$

$$\rho_0 \partial_t \mathbf{v}_1 = -\nabla p_1 + \eta \nabla^2 \mathbf{v}_1 + \beta \eta \nabla \left(\nabla \cdot \mathbf{v}_1 \right) \tag{3.6}$$

Assuming harmonic dependance of the variable fields, these equation simplify obtaining,

$$i\omega T_1 + \gamma \frac{\alpha}{\rho C_p} \nabla^2 T_1 = \frac{\gamma - 1}{\alpha} \nabla \cdot \mathbf{v}_1 \tag{3.7}$$

$$i\omega \mathbf{v}_1 + \nu \nabla^2 \mathbf{v}_1 + \nu \left[\beta + i\frac{1}{\gamma \rho_0 \kappa \nu \omega} \right] \nabla \left(\nabla \cdot \mathbf{v}_1 \right) = \frac{\alpha}{\gamma \rho_0 \kappa} \nabla T_1 \tag{3.8}$$

From this solution we can estimate the acoustic radiation force exerted on the particles. Following the derivation presented in Chapter 1, from equation 1.65 we have

$$\mathbf{F}_{rad} = -\frac{4\pi}{3} a^3 \nabla \left[\frac{1}{2} Re\left[f_1 \right] \kappa_0 \langle p_{in}^2 \rangle - \frac{3}{4} Re\left[f_2 \right] \rho_0 \langle v_{in}^2 \rangle \right] \tag{3.9}$$

with

$$f_1 \left(\tilde{\kappa} \right) = 1 - \tilde{\kappa} \qquad with \qquad \tilde{\kappa} = \frac{\kappa_p}{\kappa_0} \tag{3.10}$$

$$f_2\left(\tilde{\rho}\right) = \frac{2\left(\tilde{\rho} - 1\right)}{2\tilde{\rho} + 1} \quad with \quad \tilde{\rho} = \frac{\rho_p}{\rho_0} \tag{3.11}$$

Similarly, we showed in Chapter 1 how the time-averaged second-order pertubation terms in the Navier-Stokes equation and continuity equation lead to

$$\rho_0 \nabla \cdot \langle \mathbf{v}_2 \rangle = -\nabla \cdot \langle \rho_1 \mathbf{v}_1 \rangle \tag{3.12}$$

$$\eta \nabla^2 \langle \mathbf{v}_2 \rangle + \beta\eta\nabla\left(\nabla \cdot \langle \mathbf{v}_2 \rangle\right) - \nabla\langle p_2 \rangle = \langle \rho_1 \partial_t \mathbf{v}_1 \rangle + \rho_0 \langle \left(\mathbf{v}_1 \cdot \nabla\right)\mathbf{v}_1 \rangle \tag{3.13}$$

Where the first order pertubation fields act as source terms to calculate the time-averaged second order velocity $\langle \mathbf{v}_2 \rangle$. This velocity represent the acoustic streaming flow and, consequently, the time-averaged Stokes drag force $\mathbf{F}_{drag,s}$ on a spherical particle of radius a moving with velocity $\mathbf{u}$ in a fluid with streaming flow is given by

$$\mathbf{F}_{drag,s} = 6\pi\eta a\left(\langle \mathbf{v}_2 \rangle - \mathbf{u}\right) \tag{3.14}$$

To perform this computation, we implemented a finite-elements simulation using COMSOL Multiphysics, following the methodology proposed by Muller *et al.* [215]. We began by solving the first order acoustic field equations subject to the oscillating boundary conditions. This solution provides functional profiles for the first-order temperature T_1, density ρ_1, and pressure p_1, as well as the first-order velocity vector field. For this purpose, we adopted an idealization of the acoustofluidic channel using the cross-section as the system's domain. Assuming hard walls and anti-symmetric bottom wall actuation oscillatory boundary conditions, The results can then be used to compute the acoustic radiation force based on equation 3.9. In addition, we can use the Laminar flow physics interface to solve for the time-averaged second-order velocity $\langle \mathbf{v}_2 \rangle$ obtaining a solution for the secondary acoustically induced streaming flows. Lastly, we used the particle tracing module considering both streaming and acoustic radiation forces to track the position of nanoparticles within the domain. The parameters used for the simulation are summarized in Table 3.1.

Simulation parameters		
Variable	value	Description
w	200 μm	Channel cross section width
h	40 μm	Channel cross section height
λ_0	200 μm	Wavelength
f_0	7.5 MHz	frequency
ω_0	47.12 MHz	Angular frequency
k_0	31485 1/m	Wave number
T_0	298.15 K	Equilibrium temperature
p_0	1.0133×10^5 Pa	Equilibrium pressure
c_a	1496.7 m/s	Fluid speed of sound
ρ_f	997.05 kg/m^3	Fluid density
$\beta_{0,f}$	4.4773×10^{-10} 1/Pa	Fluid isentropic compressibility
$\alpha_{T,f}$	6.9099×10^{-4} 1/K	Fluid coefficient of thermal expansion
$C_{p,f}$	4181.3 J/(kg·K)	Fluid heat capacity at constant pressure
$C_{v,f}$	4137.6 J/(kg·K)	Fluid heat capacity at constant volume
γ_f	1.0106	Fluid ratio of specifc heats
κ_f	0.697 W/(m·K)	Fluid thermal conductivity
μ_f	$8.9E-4$ Pa·s	Fluid dynamic viscosity
$\mu_{B,f}$	0.0015 Pa·s	Fluid bulk viscosity
a	$50-400$ nm	Particle radius
ρ_p	1130 kg/m^3	Particle density
$\beta_{0,p}$	3.9331×10^{-10} 1/Pa	Particle isentropic compressibility
$\alpha_{0,p}$	2.9 1/K	Particle thermal expansion
$C_{p,p}$	1500 J/(kg·K)	Particle specific heat capacity at constant pressure
γ_p	1.04	Particle ratio of specific heats
κ_p	0.19 W/(m·K)	Particle thermal conductivity
$c_{a,p}$	1500 m/s	Particle longitudinal speed of sound
I_{scale}	10	Scaling constant for the intensity of oscillations
$d_{visc,0}$	3.651 m	Mesh viscous penetration depth at f_0
N_E	16562	Number of elements in mesh
N_{df}	289743	Number of degrees of freedom solved for

TABLE 3.1: Table of parameters for the finite element model of acoustofluidics.

Altogether, this algorithm allowed us to compute the dynamic evolution of nanoparticles in our model system.

3.3   Numerical predictions on acoustofluidic focusing

In order to understand the mechanisms driving the differential separation of nanoparticles observed in our experimental results, we perform a set of simulation using the computational model described above. This numerical calculations allows us to track the evolution of nanoparticles in a thermotropic fluid after applying SSAW by observing the change in position of particles under the influence of streaming-induced drag

3.3.1 Solution with undampened standing surface acoustic waves (uSSAWs)

First, we studied the dynamic evolution of nanoparticles after applying a standing acoustic wave with constant amplitude. Given that the amplitude of the SSAW is not affected by dampening effects, we labeled this first case as the undampened SSAWs (uSSAWs). For this case, the solution of the fist order expansion density, pressure and velocity field where obtained (Fig. 3.1A−C). The numerical solution on this case yield a pressure field and velocity field consistent with the solution of the fist order wave equation 1.45. Consequently, the pressure p_1 and density ρ_1 are maximum at the wall and minimum at the center of the channel − where the pressure anti-nodes are located (Fig. 3.1A−B). Furthermore, the fist order perturbation velocity $\mathbf{v}_1$ follows $\mathbf{v}_1 \sim \nabla p_1$ (Fig. 3.1C).
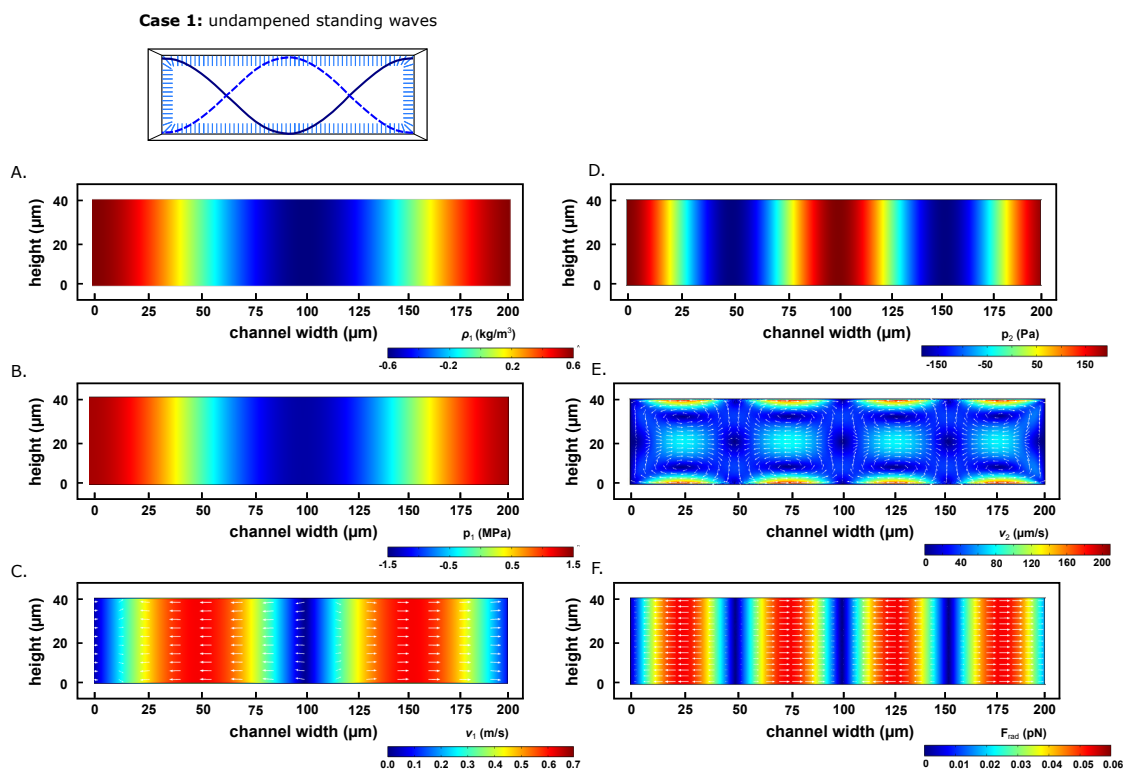
FIGURE 3.1: **Numerical prediction of acoustofluidics in microchannel with uSSAWs**. Finine element simulations predict the primary and secondary perturbation terms for the expansion of the Navier-Stokes equation under the influence of an undampened acoustic oscillation. **A**. Solution for ρ_1; **B**. Solution for p_1; **C**. Solution for v_1; **D**. Solution for p_2; **E**. Solution the acoustic streaming v_2; **F**; Solution for the acoustic radiation force F_{rad}.

The solution of the second order perturbation terms provided the pressure p_2 (Fig. 3.1D). From this solutions we computed the streaming flow computing the averaged value of the secondary perturbation velocity $\langle \mathbf{v_2} \rangle$ (Fig. 3.1E). The Rayleigh streaming profile exhibits eight streaming rolls with maximum at the top and bottom walls of the channel; local maxima were observed at $z = h/2$. The pertubation fields where used to calculate acoustic radiation force field (Fig. 3.1F), showing maxima of force at a location corresponding to the inflection points of the sinusoidal acoustic wave $\mathbf{x}_n(y) = \mathbf{r}\left(\frac{2n+1}{8}w, y\right)$, with $n = 0, 1, 2, 3$. In similar fashion, the acoustic radiation force was lowest at the pressure wave nodes and anti-nodes.

3.3.2 Acoustic streaming and radiation force interplay using uSSAWs

Now that we have an approximate solution for the equation of state and the equations of motion providing the main fields that describe our acoustofluidic system, we can perform analysis that relate to the experimental observations made in Chapter 2. As described in that chapter, the use of SSAWs promote the differential separation of nanoparticles in microfluidic channels. While the separation of 1 μm particles is driven by the acoustic radiation force, the focusing of 200 nm particles appear to be driven by acoustic streaming effects at low Pe. These experimental observations suggest an interplay between the acoustic radiation force and the drag forces on the particles due to the acoustic streaming velocity field. Thus, using our computational model we quantified and compared the magnitude of the radiation force F_{rad} and the streaming$-$induced drag $F_{drag,s}$. Due to the symmetry of the solution under uSSAWs, it is sufficient to analyze these forces at one of the inflection points of the acoustic wave, where both the streaming and the radiation force have maximum values. Thus, we calculated the value of F_{rad} and $F_{drag,s}$ at $\mathbf{x}_2 = \mathbf{x}_a(y) = \mathbf{r}\left(\frac{5}{8}w, y\right)$ for particles of different sizes (Fig. 3.2). For particles with a radius of $a \leq 50$nm, $F_{drag,s}$ is always larger than F_{rad}(Fig. 3.2A). Thus, the acoustic streaming dominates the dynamic of these particles leading to constant rotation in the fluid rolls created by the streaming. In contrast, particles between $100 \leq a \leq 200$ show regions where $F_{drag,s}$ and F_{rad} are of similar magnitude (Fig. 3.2B$-$C).

93
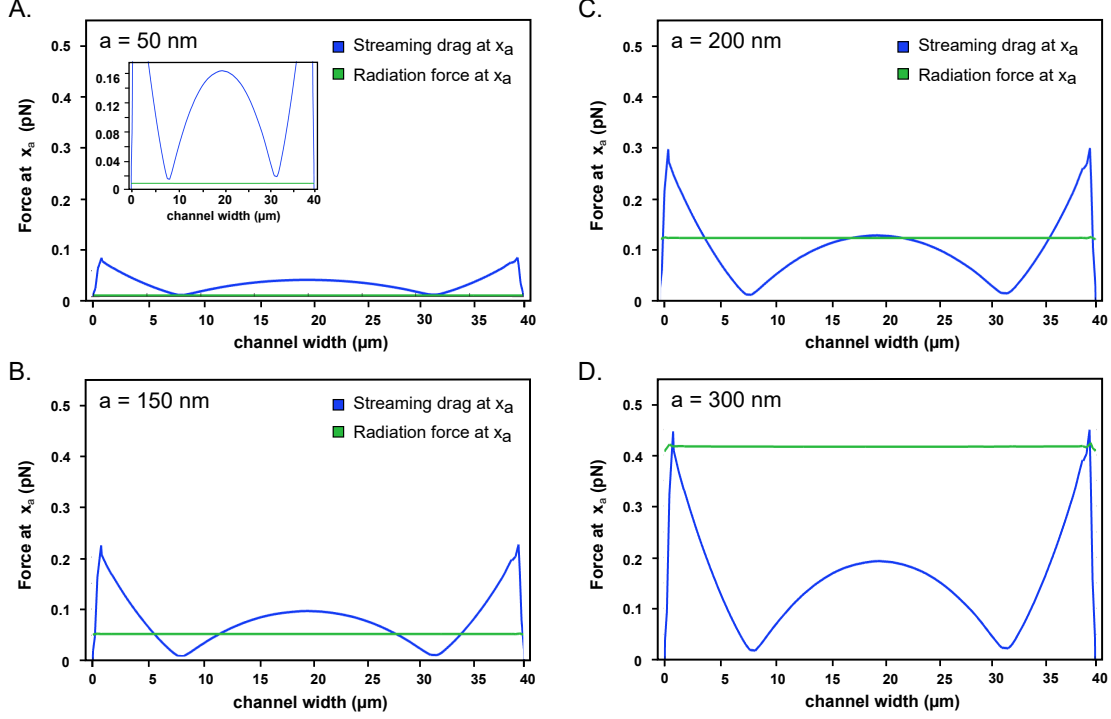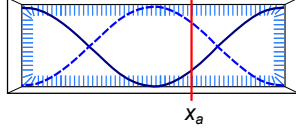
FIGURE 3.2: **Acoustic radiation force and acoustic streaming at an inflection point of under uSSAWs**. Prediction of the intensity of the acoustic radiation force F_{rad} and the streaming-induced drag force on particles of different sizes exposed to an uSSAW. All the measurements where made at along the line defined by $\mathbf{x}_a\left(y\right) = \mathbf{r}\left(\frac{5}{8}w, y\right)$ (red line in schematic). **A**. Particle radius $a = 50$ nm; **B**. Particle radius $a = 150$ nm; **C**. Particle radius $a = 200$ nm; **D**. Particle radius $a = 300$ nm. Legend: Streaming drag (Blue line). F_{rad} (Green line).

From Fig. 3.1E and Fig. 3.1F we see that the radiation force field and the streaming drag force field point in opposite directions, implying that $F_{drag,s}$ and F_{rad} compete in the center of the channel when $100 \leq a \leq 200$. In the case of particles with a radius $a \geq 300$ nm, F_{rad} is larger than $F_{drag,s}$. Consequently, our simulation indicate that the behavior of particles larger than 300 nm is dominated by the acoustic radiation force $F_{drag,s}$(Fig. 3.2D).

To complement this analysis, we calculated the value of F_{rad} and $F_{drag,s}$ for particles of different sizes across the channel. Here quantified the force fields along the central line $\mathbf{y}_c\left(x\right) = \mathbf{r}\left(x, h/2\right)$ (Fig. 3.3). As before, the streaming−induced drag force dominates over the radiation force for small nanoparticles with radius $a \leq 50$

nm (Fig. 3.3A). Furthermore, F_{rad} also dominate for particles with radius $a \leq 300$ nm (Fig. 3.3D). Interestingly, due to the symmetry of both $\langle \mathbf{v}_2 \rangle$ and F_{rad} across the channel, we have peaks of intensity in the same locations with opposite directions of the underlying vector fields. Thus, for $a \approx 150$ nm particles $F_{rad} < F_{drag,s}$ and the radiation force slows down but cannot reverse the direction of the particles (Fig. 3.3B). Moreover, we notice that in the case of $a = 200$ nm, $F_{rad} \approx F_{drag,s}$ indicating points of stagnation across the channel (Fig. 3.3C). Altogether, these results are important because they indicate that the behavior of large particles is dominated by the acoustic radiation force, while the dyanamics of nanoparticles of sizes between 100 nm to 300 nm is dominated by an interplay between the radiation and streaming vector fields.
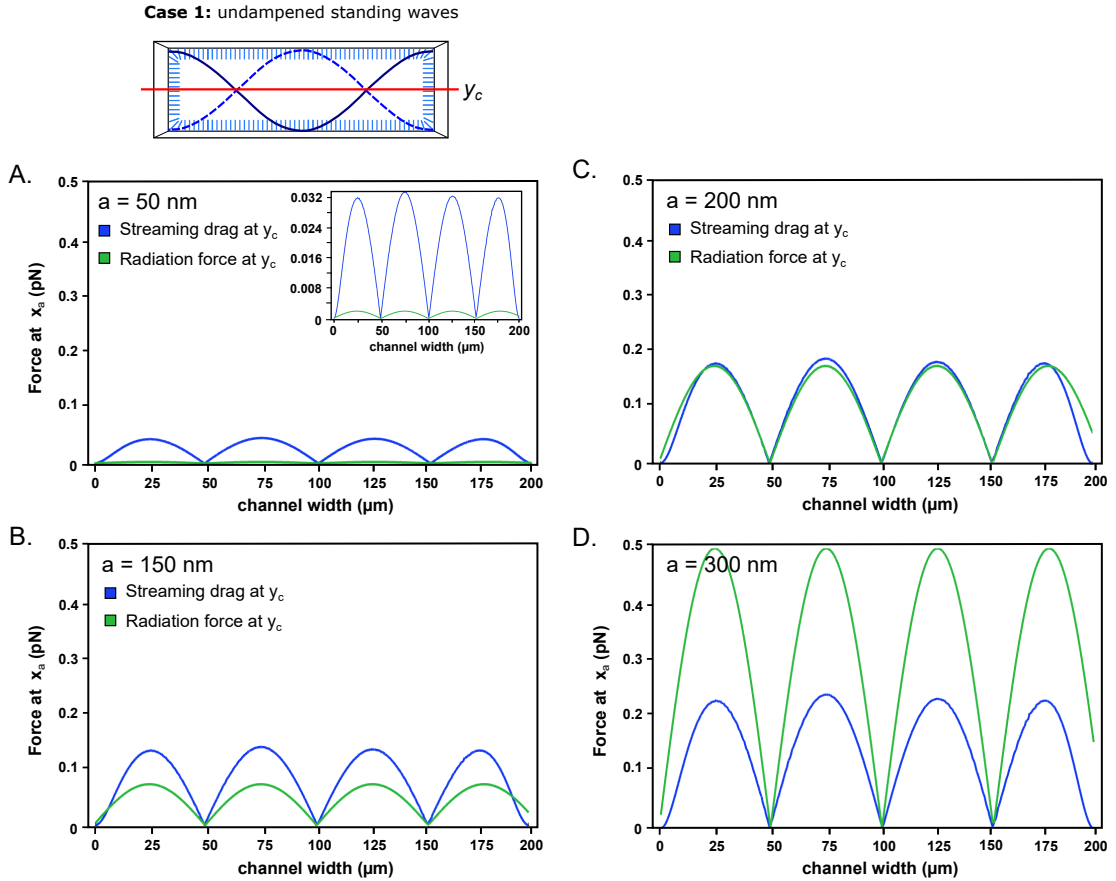
FIGURE 3.3: **Acoustic radiation force and acoustic streaming at the center of the channel under uSSAWs**. Prediction of the intensity of the acoustic radiation force F_{rad} and the streaming-induced drag force on particles of different sizes exposed to an uSSAW. All the measurements where made at the center of the channel line along a line defined by $\mathbf{y}_c (x) = \mathbf{r} (x, h/2)$ (red line in schematic). **A**. Particle radius $a = 50$ nm; **B**. Particle radius $a = 150$ nm; **C**. Particle radius $a = 200$ nm; **D**. Particle radius $a = 300$ nm. Legend: Streaming drag (Blue line). F_{rad} (Green line).

3.3.3 Particle tracing using uSSAWs

Having the solution to the velocity profile within the channel and the force fields affecting the particle dynamics we performed computations using particle tracing to follow the evolution of nanoparticles from homogeneous initial conditions (Fig. 3.4, Fig. 3.5, Fig. 3.6). Here, particles of 400 nm in size driven by the acoustic radiation force focus rapidly towards the acoustic wave anti-nodes located in the center of the channel and at the walls (Fig. 3.4).

FIGURE 3.4: **Particle tracing of 400 nm particles under uSSAWs**. Finite element simulation and particle tracing predict the temporal evolution of 400 nm particles affected by the acoustic radiation force and the acoustic streaming in a microchannel under uSSAWs. Channel height $h = 40$ μm, width $w = 200$ μm. Wavelength $\lambda = 200$ μm.

It is important to note here, that the simulated particles focus on a point at the center because our model consider non-interacting particles. On a similar note, particles at the wall remain fixed due to the imposed boundary condition $\mathbf{v} = 0$. The addition of reflective boundary condition or momentum conservation could provide a more realistic simulation. However, the results obtained here are sufficient for our subsequent analysis.In contrast with the behavior of the 400 nm particles, particles of 150 nm in size follow more complex dynamics (Fig. 3.5). In this case, the nanoparticles are quickly displaced by the force fields towards the center ($y \approx h/2$) and then laterally following the streaming rolls. However, the acoustic radiation force slows particles in the center of the channel where its magnitude is larger or equal than the streaming

drag. This promotes the accumulation of particles in slower stream lines that manifest as an local increase in particle concentration in the vicinity of the inflection points of the acoustic wave. Lastly, the dynamic behavior of 50 nm particles is much more chaotic, as the particle position is dictated primarily by the streaming flow (Fig. 3.6). Here, the nanoparticles recirculate constantly through the channel without collapsing into concentrated pockets.
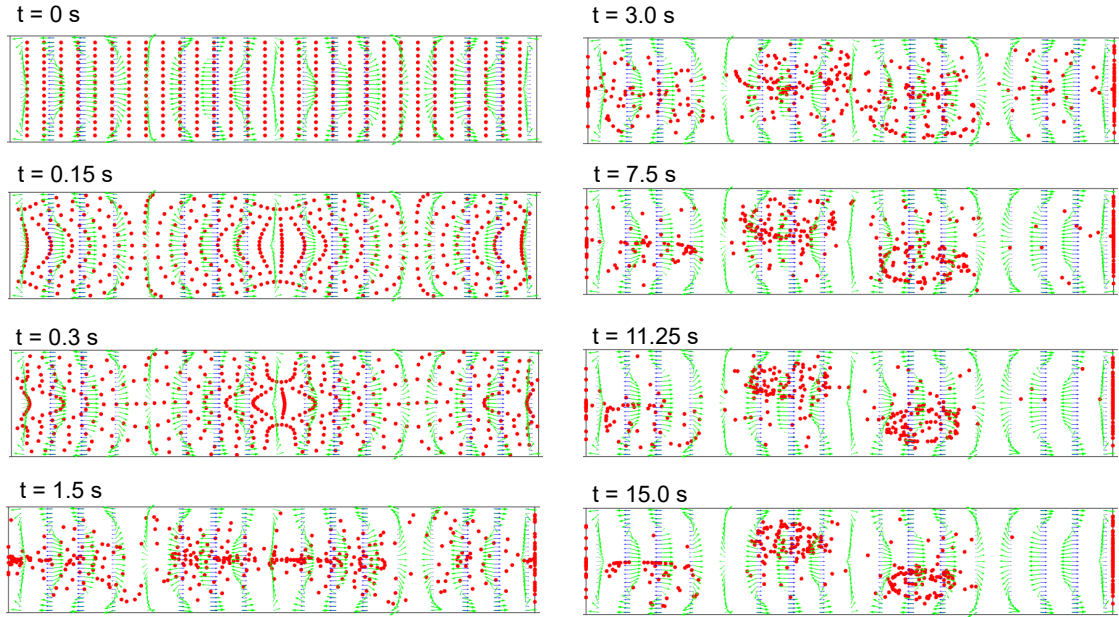
FIGURE 3.5: **Particle tracing of 150 nm particles under uSSAWs**. Finite element simulation and particle tracing predict the temporal evolution of 150 nm particles affected by the acoustic radiation force and the acoustic streaming in a microchannel under uSSAWs. Channel height $h = 40$ μm, width $w = 200$ μm. Wavelength $\lambda = 200$ μm.

While we note a slight increase of particle concentration around the inflection points, the concentration is close to homogeneous. In addition, as we reduce the particle size we increase the particle diffusivity. Consequently, the local increase in temperature and particle diffusion will homogenize small variations of the streaming flow when performing experiments.
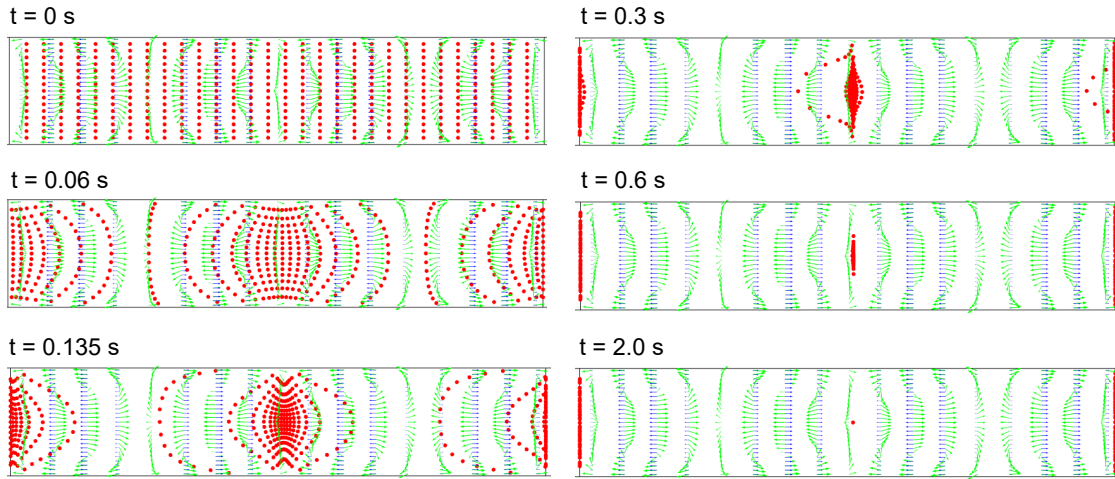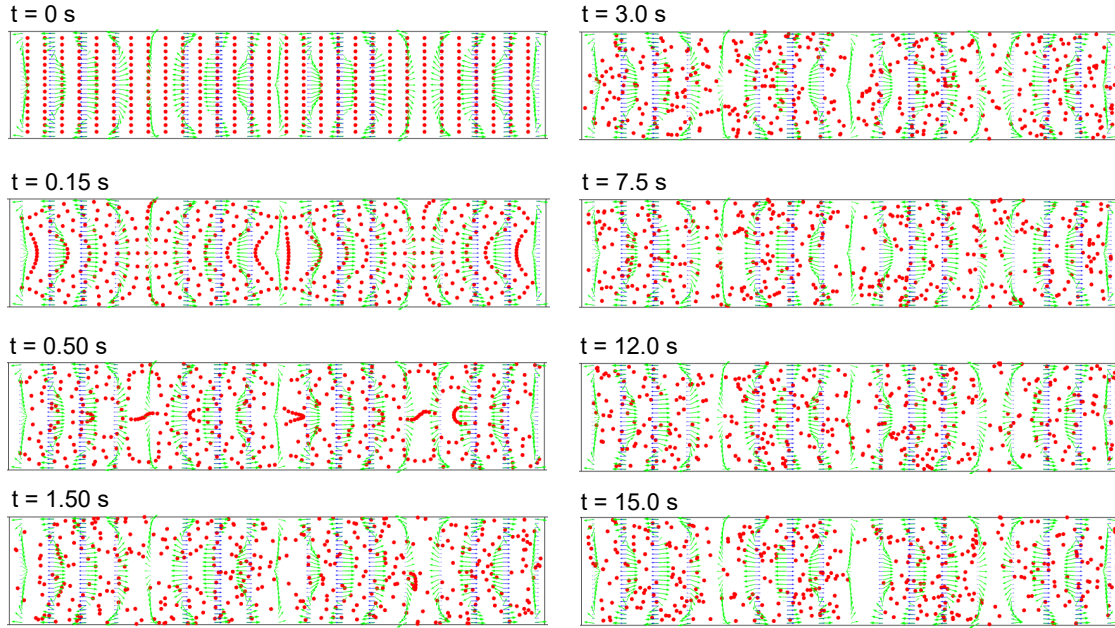
FIGURE 3.6: **Particle tracing of 50 nm particles under uSSAWs**. Finite element simulation and particle tracing predict the temporal evolution of 50 nm particles affected by the acoustic radiation force and the acoustic streaming in a microchannel under undapened standing waves. Channel height $h = 40$ μm, width $w = 200$ μm. Wavelength $\lambda = 200$ μm.

3.3.4 Solution with dampened standing surface acoustic waves (dSSAWs)

Although the results obtained from the numerical simulations of the acoustofluidic system under uSSAWs explain the mechanisms driving the behavior of large (≥ 300 nm) nanoparticles and small (≤ 50 nm) nanoparticles, the numerical results contradict the experimental observations of Fig. 2.4 and Fig. 2.5. While the experiment show a reproducible focusing of the 200 nm particles towards the channel walls, simulations of a rectangular channel with the same dimension under uSSAWs with the same wavelength predict a increase on the concentration of particles at the inflection points of the acoustic wave. In an effort to re-conciliate the results from the numerical computations with these experimental observations, we explored variations within our fundamental framework that lead to similar nanoparticle behavior as observed experimentally. This tasks is challenging because the numerical model must satisfy the continuity equation, the Navier-Stokes equation and mass conservation. In addition, we need to introduce changes that affect nanoparticles in the $100 \leq a \leq 200$nm size range while I) maintaining the focusing driven by radiation force of particles $> 300nm$; and II) mantaining

streaming-induced drag as the main mechanism for the dynamics of particles $\leq$ 50 nm.
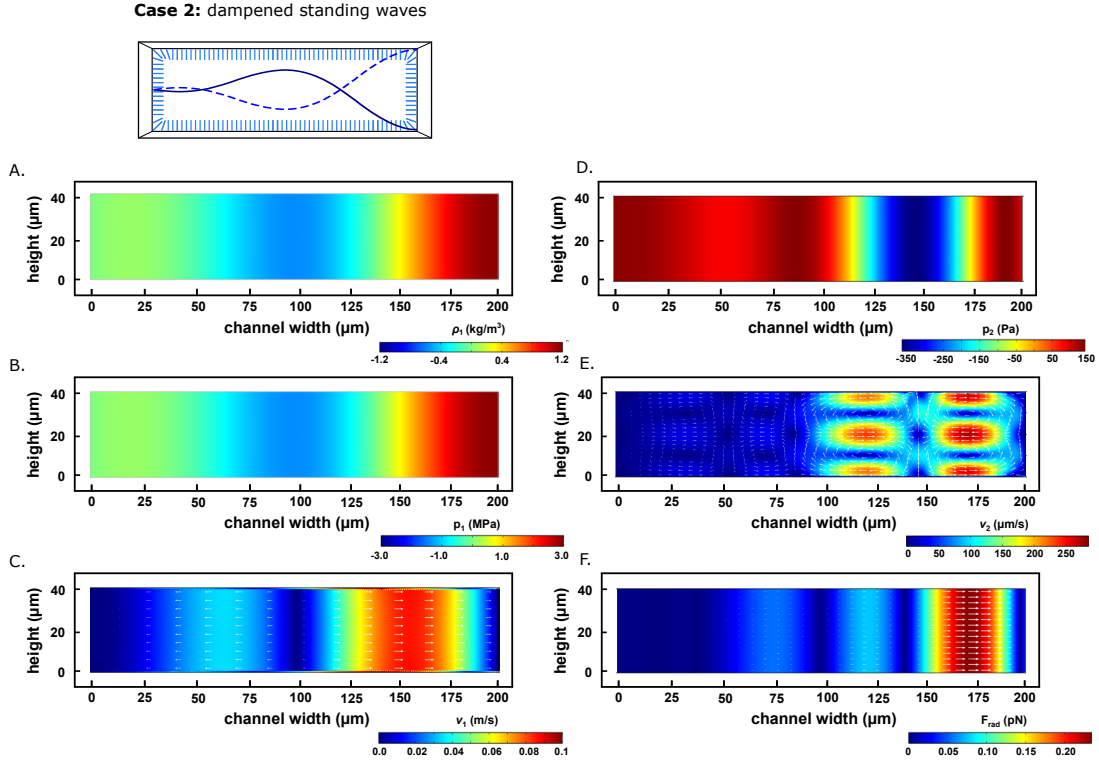
FIGURE 3.7: **Numerical prediction of acoustofluidics in microchannel with dS-SAWs**. Finine element simulations predict the primary and secondary perturbation terms for the expansion of the Navier-Stokes equation under the influence of a dSSAW. The Intensity of the acoustic waves decreases linearly along the channel width. **A**. Solution for ρ_1; **B**. Solution for p_1; **C**. Solution for v_1; **D**. Solution for p_2; **E**. Solution the acoustic streaming v_2; **F**; Solution for the acoustic radiation force F_{rad}.

Due to the strict limitations of these constraints, we studied the effect of variations of the waves amplitude on the dynamics of nanoparticles in an acoustofluidic channel. This approach has seldom been considered in application of SAWs in microfluidics, leading to a key assumption made in most numerical studies: The amplitude of the wave is constant along the channel. The main implication of this assumption is the consideration of a no dissipation system where the acoustic intensity remains equal regardless of the interaction with the liquid. In stark contrast, our experimental observations indicate important viscous dissipation of the acoustic energy that translate into increase in temperature within the device (Fig. 2.11). Thus, we repeated our simulations assuming a system where the amplitude of the pressure wave decreases across the channel (Case 2, Fig. 3.7). For simplicity, we assumed a linear decrease in amplitude across the channel. Due to the shape of the resulting pressure wave within the fluid

and the association with viscous dissipation, the acoustic waves are reminiscent of a dampened wave profile. Thus, we labeled this scenario as dampened standing surface acoustic waves (dSSAWs). The solution of the first order perturbation terms show that ρ_1 and p_1 have the same distribution as expected. Furthermore, the recapitulate the decrease in amplitude expected due to the imposed decrease in acoustic intensity (Fig. 3.7A−B). As before, the solution $\mathbf{v}_1$ follows $\mathbf{v}_1 \sim \nabla p_1$, indicating that the numerical method successfully capture the first order dynamics of the system under the constraints imposed for dSSAWs (Fig. 3.7C).

The solution to the second order pressure p_2 shows an asymmetric profile with strong maxima and minima near $x = w$, with oscillations of reduced magnitude as one move across the channel (Fig. 3.7D). Consequently the solution to the second order averaged perturbation velocity $\langle \mathbf{v}_2 \rangle$ shows an asymmetric streaming profile with eight streaming rolls where the magnitude of the velocity field is larger in the second half of the channel ($x \geq 100\ \mu$m) (Fig. 3.7E). Similarly, the solution of the acoustic radiation field yields four local maxima with increasing magnitude as you approach $x = 200\ \mu$m. In contrast with the results obtained using uSSAWs (Fig. 3.1), the dSSAWs disrupts the symmetry of both the acoustic streaming and the radiation force fields with the highest magnitude found close to the wall at $x = 200\ \mu$m where the pressure wave has the largest intensity.

3.3.5   Acoustic streaming and radiation force interplay using dSSAWs

Having an approximate solution for the equation of state and the equations of motion providing the main fields that describe the acoustofluidic system under dSSAWs, we performed an analysis of the relationship between F_{rad} and $F_{drag,s}$ similar as before. Thus, we calculated the value of F_{rad} and $F_{drag,s}$ at $\mathbf{x}_a\left(y\right) = \mathbf{r}\left(\frac{5}{8}w, y\right)$ and $\mathbf{x}_b\left(y\right) = \mathbf{r}\left(\frac{5}{8}w, y\right)$ for particles of different sizes (Fig. 3.8). Here, we include information from two different lines along the channel to account for differences that arise from the asymmetry of the solution under dSSAWs. For particles with a radius of $a \leq 50$nm, $F_{drag,s}$ is always larger than F_{rad}(Fig. 3.8A). Similarly, the acoustic radiation force is always larger than the streaming−induced drag for $a \geq 300$ nm (Fig. 3.8D).
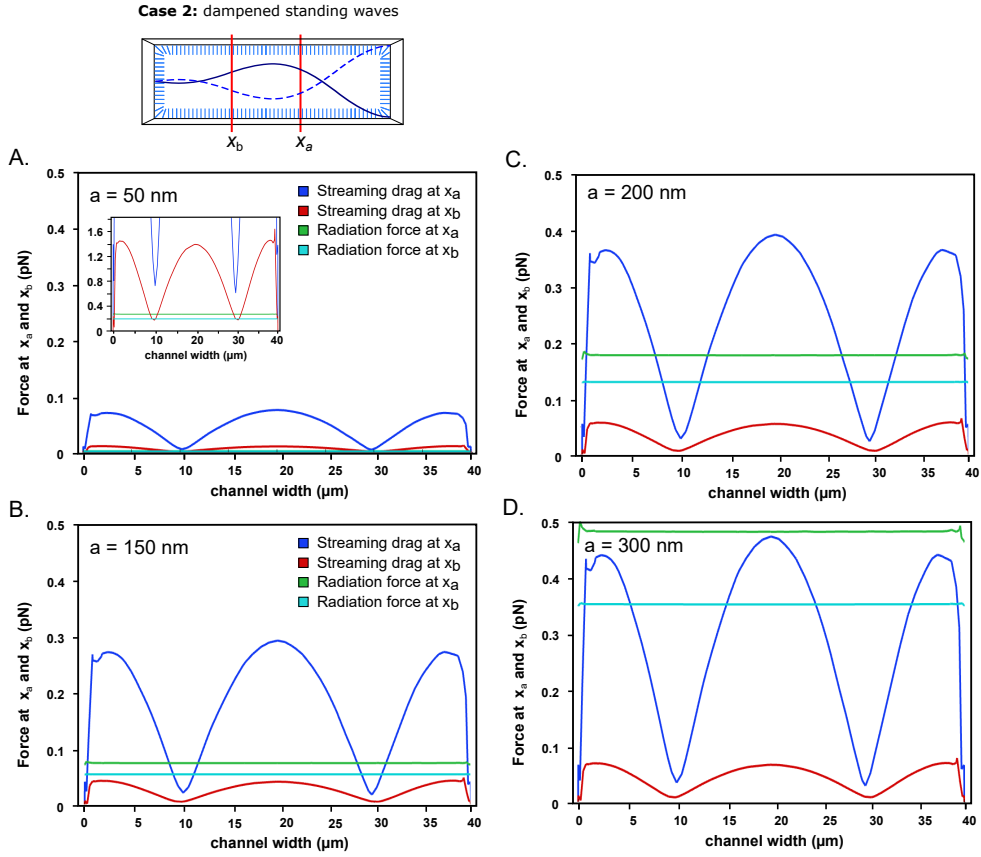
FIGURE 3.8: **Acoustic radiation force and acoustic streaming at an inflection point of under dSSAWs**. Prediction of the intensity of the acoustic radiation force F_{rad} and the streaming-induced drag force on particles of different sizes exposed to a dSSAW. The measurements where made at along the lines defined by $\mathbf{x}_a(y) = \mathbf{r}\left(\frac{5}{8}w, y\right)$, and $\mathbf{x}_b(y) = \mathbf{r}\left(\frac{3}{8}w, y\right)$ (red lines in schematic). **A.** Particle radius $a = 50$ nm; **B.** Particle radius $a = 150$ nm; **C.** Particle radius $a = 200$ nm; **D.** Particle radius $a = 300$ nm. Legend: Streaming drag at x_a (Blue line). Streaming drag at x_b (Red line). F_{rad} at x_b (Cyan line).

These results indicate that the streaming flow dominates the dynamics of small nanoparticles while the radiation force dominates the dynamics of larger particles, despite the asymmetry of the force field induced by the dampened waves. Interestingly, the interplay between the acoustic radiation force and the acoustic streaming drag for particles between $100 \leq a \leq 200$ nm appears to be affected by the established asymmetry (Fig. 3.2B−C). For particles in this size range, $F_{drag,s}$ and F_{rad} are of similar magnitude and compete when $x \geq 100$ μm (Blue and green lines in Fig. 3.2B−C). However, when $x < 100$ μm The acoustic radiation force dominate (red and cyan lines in Fig. 3.2B−C).
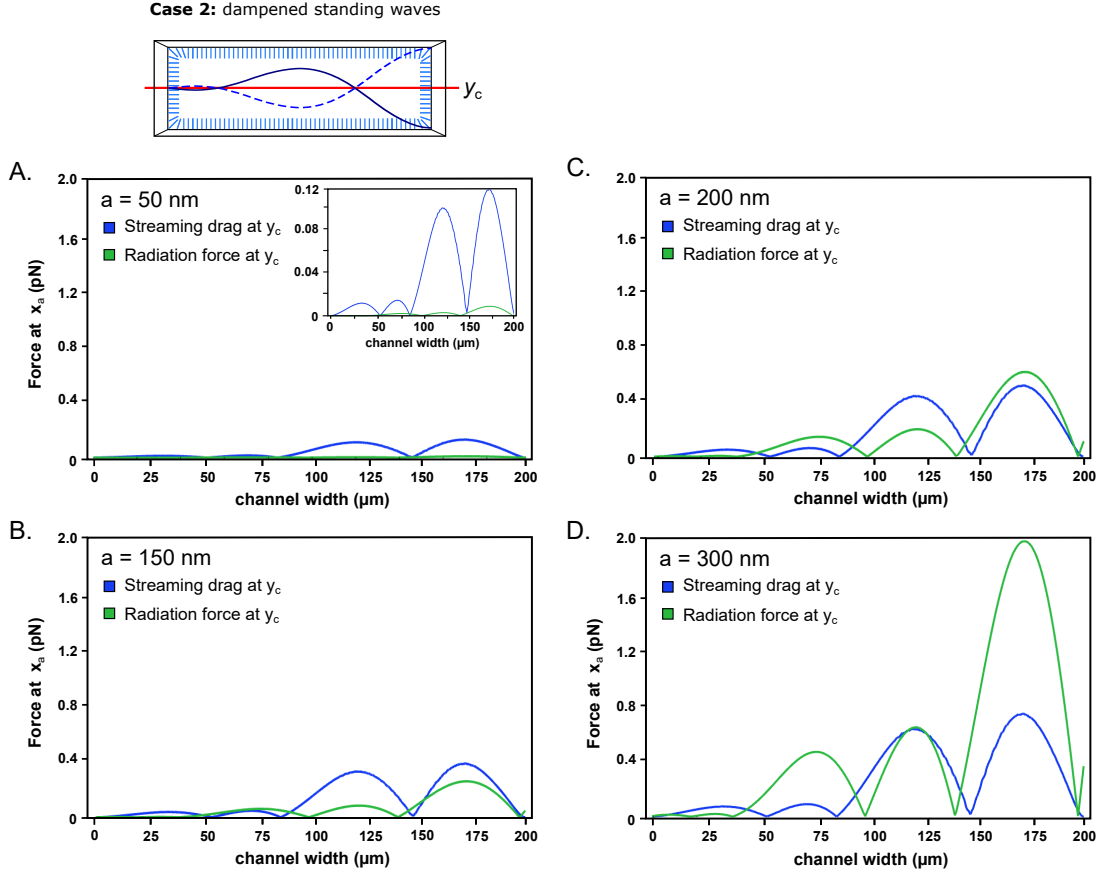
FIGURE 3.9: **Acoustic radiation force and acoustic streaming at the center of the channel under dSSAWs**. Prediction of the intensity of the acoustic radiation force F_{rad} and the streaming-induced drag force on particles of different sizes exposed to a dSSAW. All the measurements where made at the center of the channel line along a line defined by $\mathbf{y}_c(x) = \mathbf{r}(x, h/2)$ (red line in schematic). **A**. Particle radius $a = 50$ nm; **B**. Particle radius $a = 150$ nm; **C**. Particle radius $a = 200$ nm; **D**. Particle radius $a = 300$ nm. Legend: Streaming drag (Blue line). F_{rad} (Green line).

These results highlight a delicate balance between these forces acting on particles in the $100 \leq a \leq 200$ nm size range affected by the decrease in acoustic intensity across the channel.

To complement this analysis we studied the interplay between F_{rad} and $F_{drag,s}$ across the channel computing the forces along the line $\mathbf{y}_c(x) = \mathbf{r}(x, h/2)$, as before (Fig. 3.9). Here, we observe again that the streaming drag dominates for particles $a \leq 50$ nm (Fig. 3.9A), while the acoustic radiation force dominates for $a > 300$ nm (Fig. 3.9D). Furthermore, $F_{drag,s}$ larger than F_{rad} for $x \leq (3/4)w$. Past this point $F_{drag,s}$ is comparable to F_{rad} for particles between 100 to 200 nm, generating a stagnation point a the center of the channel.

3.3.6 Particle tracing using dSSAWs

Given the differences observed in between the acoustic radiation force and the acoustic streaming when using dSSAWs, we performed additional computations using particle tracing to track the dynamic evolution of nanoparticles from homogeneous initial conditions (Fig. 3.10, Fig. 3.11, Fig. 3.12). For particles of 400 nm in size, we found that the the acoustic radiation force focus these particles towards the acoustic wave anti-nodes located in the center of the channel and at the walls despite the asymmetric shape of the force field(Fig. 3.10). In contrast with the uSSAW case, the nanoparticles take longer to form regions of increased concentration having the majority of particles in the center of the channel.

FIGURE 3.10: **Particle tracing of 400 nm particles under dSSAWs**. Finite element simulation and particle tracing predict the temporal evolution of 50 nm particles affected by the acoustic radiation force and the acoustic streaming in a microchannel under dSSAWs. Channel height $h = 40$ μm, width $w = 200$ μm. Wavelength $\lambda = 200$ μm.

For particles with radius $a = 150$ nm, the evolution of the particles is complex (Fig. 3.11. Given the high velocities of the streaming flow, most particles with an initial position at $x \geq w/2$ are trapped by the streaming rolls and focus into a region around the inflection point closer to the wall. Most particles circulating around $\mathbf{x}_2$ are pushed towards $\mathbf{x}_3$ while a small fraction is trapped circulation around $\mathbf{x}_2$ as the forces balance.

FIGURE 3.11: **Particle tracing of 150 nm particles under dSSAWs**. Finite element simulation and particle tracing predict the temporal evolution of 150 nm particles affected by the acoustic radiation force and the acoustic streaming in a microchannel under dSSAWs. Channel height $h = 40$ μm, width $w = 200$ μm. Wavelength $\lambda = 200$ μm.
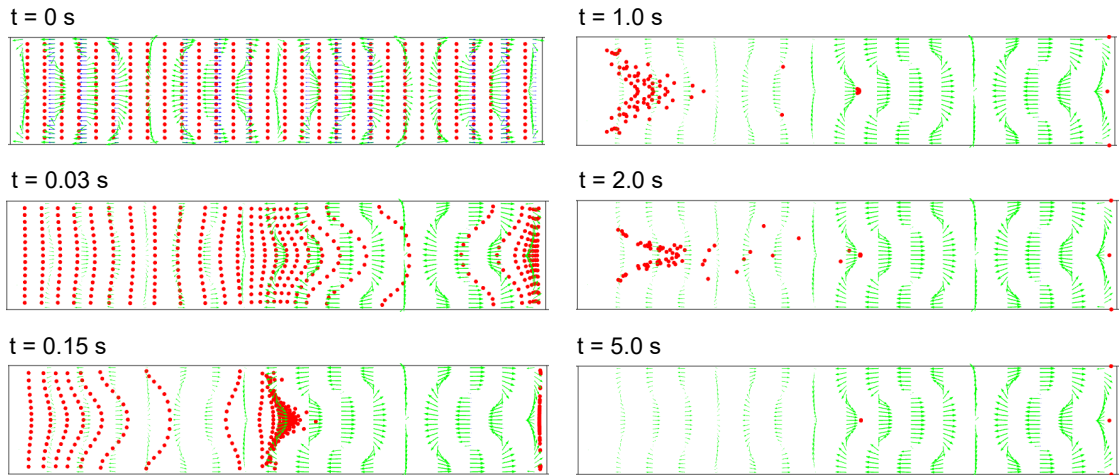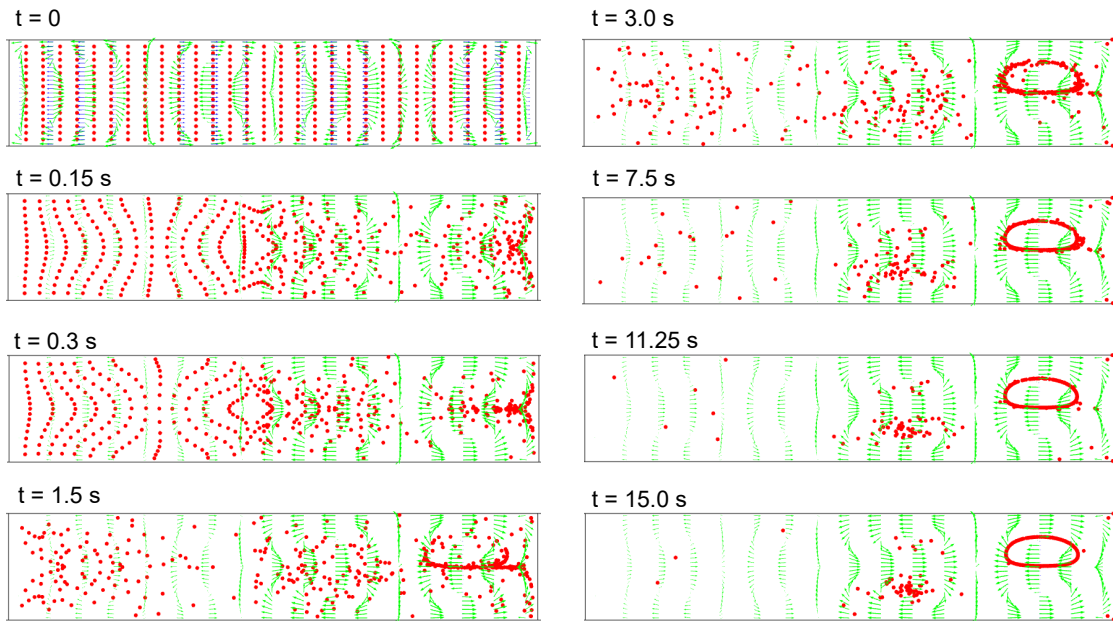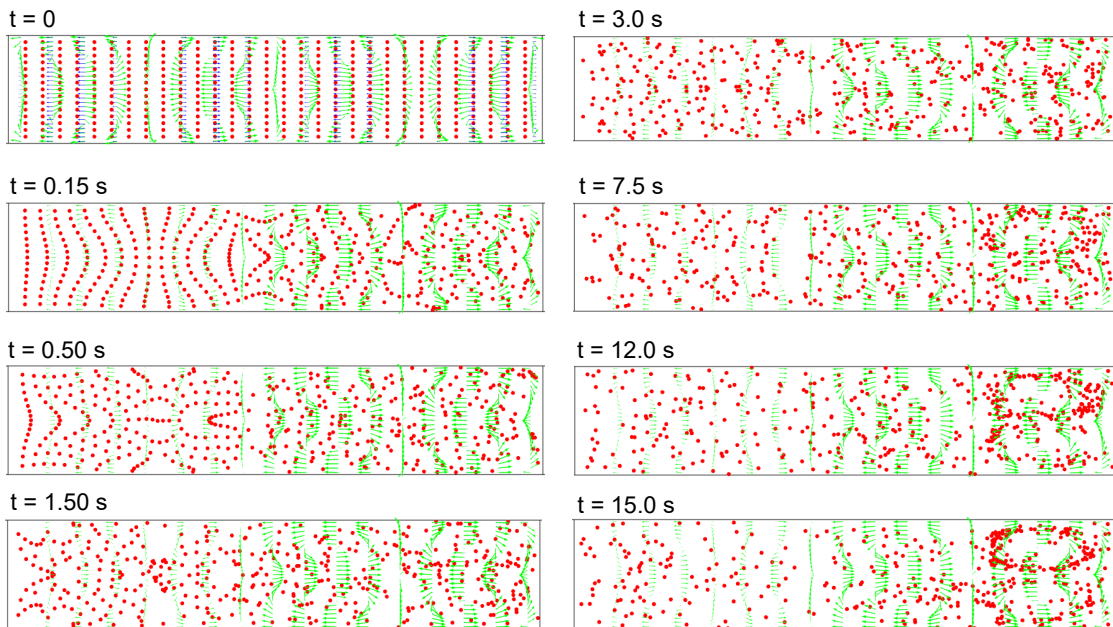

FIGURE 3.12: **Particle tracing of 50 nm particles under dSSAWs**. Finite element simulation and particle tracing predict the temporal evolution of 50 nm particles affected by the acoustic radiation force and the acoustic streaming in a microchannel under dSSAWs. Channel height $h = 40$ μm, width $w = 200$ μm. Wavelength $\lambda = 200$ μm.

While particles starting at $x \geq w/2$ tend to be trapped in streaming rolls, particles at $x \leq w/2$ tend to escape this region as the radiation force constantly pushes particles towards the central anti-node until the streaming pushes the particles to cross the central threshold $x = w/2$. As a consequence of this mechanisms, most nanoparticles of 150 nm localize near the wall when under the influence of dSSAWs (Fig. 3.11). As the particle size is reduced, this behavior becomes more difficult to observe, as the radiation force fails to create stable stagnation points. Consequently, smaller particles show a disorganized distribution with small increases in concentration locally (Fig. 3.12. this changes in the concentration of small nanoparticles will to homogenize due to thermal fluctuations in experiments.

3.3.7 Distribution of particles using uSSAWs and dSSAWs

Our numerical results indicate that for smaller particles (150 nm), uSSAW yield pockets of increased concentration of nanoparticles around the inflection points of the wave. here, Particles circulate the space without further focusing but are unable to escape neighboring concentration pockets. On the other hand, introducing asymmetries using dSSAWs where the amplitude is allowed to decrease yielded an asymmetric streaming velocity profile and acoustic radiation force field. Despite exhibiting eight streaming rolls as before, the magnitude of the velocity obtained was significantly higher for the circulatory flows at $x > w/2$. Similarly, the acoustic radiation force was strongest near the wall at y=w, while maintaining its periodicity. Thus, once particles reach the faster streaming rolls and stronger radiation force areas within the channel, it becomes exceedingly difficult for particles to migrate towards other areas in the channel. Consequently, the particles focus with significant increase in concentration of nanoparticles towards the channel wall. the difference in particle distribution obtained using uSSAWs or dSSAWs can be seen by comparing the histogram of particle distribution extracted from the simulations (Fig. 3.13). Of the two, the histogram obtained using dSSAWs is consistent with the experimental observations of the distribution of 200 nm particles under high-intensity acoustic waves shown in Fig. 2.6A. Altogether, this numerical study suggests that the displacement of small nanoparticles observed exper-

imentally can be explained because of anisotropies in both the acoustic radiation force field and acoustic streaming flow originating from changes in the wave amplitude along the channel.
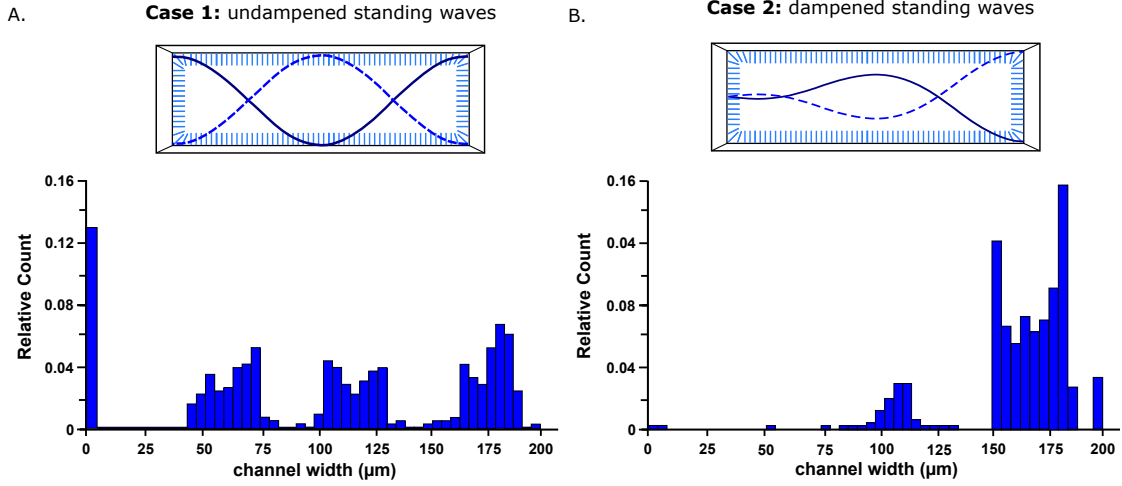
FIGURE 3.13: **Distribution of 150 nm particles under uSSAWs and dSSAWs**. Histograms of the distribution of 150 nm particles. Analysis made after particle tracing of 150 nm particles for $t = 15s$ under **A** uSSAWs (case 1); and **B**. dSSAWs (case 2). Channel height $h = 40$ μm, width $w = 200$ μm. Wavelength $\lambda = 200$ μm.

3.4 Conclusion

We have demonstrated that numerical solution of the continuity equation and the Navier-Stokes equation of motion with oscillating boundary conditions using a Finite Elements approach can be used to study the dynamics of nanoparticles in microchannels under an external acoustic field. This simulations provide insights into the role different mechanisms play on the distribution of particles, allowing us propose mechanisms to explain the experimental observations presented in Chapter 2. The numerical calculations presented here confirm that the mechanisms of differential fractionation of nanoparticles using acoustic waves combines an interplay between the acoustic radiation force and the acoustic streaming where: I) nanoparticles smaller than 50 nm are scattered by the streaming flow; II) nanoparticles larger than 300 nm are focused by acoustophoresis towards pressure wave anti-nodes; and III) nanoparticles between 100 to 200 nm are concentrated by a delicate balance between acoustic streaming and radiation forces.

We identify that in order to reproduce the lateral focusing of 200 nm particles observed experimentally, our model require the use of dampened standing surface acoustic waves. This waves are characterized by a decrease in acoustic intensity across the channel that promotes asymmetries in the streaming and radiation fields. The used of dSSAWs derives from the assumption that increase in temperature within the channel is caused by a loss of acoustic energy from viscous dissipation. As the numerical results support the experimental observations from chapter 2, we conclude that the acoustofluidic focusing of 200 nm particles is mediated by dampened acoustic waves in the fluid where the amplitude of the wave decreases across the channel.

CHAPTER 4

NEMATIC LIQUID CRYSTALS EXPOSED TO SAWS IN CONFINEMENT

4.1   Introduction

The optical properties of liquid crystals serve as the basis for display, diagnostic, and sensing technologies. Such properties are generally controlled by relying on electric fields. Here, we investigate the effects of acoustic fields on the molecular orientation and the corresponding optical response of nematic liquid crystals (NLCs). We employ an optofluidic system in which NLCs are confined into a PDMS microfluidic channel that is coupled to a SSAW generator. We show that different birefringent patterns arise in the NLCs as a function of the acoustic field intensity.

Harnessing optical properties of liquid crystals (LCs) due to their anisotropic shape and collective structural organization has transformed many different areas of research and daily life of human beings. Since the first compendium of molecular properties of liquid crystals by G. W. Gray[233], efforts to develop optically responsive technologies have evolved. Pioneer experimental studies on nematic LC displays[234] showed the appearance of straight patterns and clear domains when a thin layer of LC was subjected to an electric field, within the temperature range before the melting process. Phenomenological approaches were used to investigate this phenomenon[235]. Further experiments and phenomenological analysis within nematics whose molecular dipole moment lie perpendicular to their main axis and intense electric fields, conducted to the design of the first LC displays as alphanumeric tunable indicators. The

transparent LC becomes highly bright in localized centers (Williams domains) with index of refraction gradients where the light is dynamically scattered, due to collective electro-hydrodynamic effects of ions in transit in the direction on the applied electric field and perpendicular to the orientation of the mesogens[236]. However, the study of liquids under the actuation of other sorts of external fields attracted attention in earlier years. Velocity propagation and attenuation of ultrasound waves (bulk acoustic waves (BAWs)) were originally of interest for an extended list of liquids[237]. Afterwards, anisotropic liquids showed unlike responses due to their structural organization, particularly cholesteric liquid crystals[238]. Later on, investigations showed optical responses spanning the entire visible electromagnetic spectrum on cholesterics when BAWs were applied, observed by the naked eye and under the microscope [239, 240, 241]. BAWs experiments demonstrated similar responses and formation of swarm-like domains on nematics, within the dynamic scattering regime, as Heilmeier formerly did [242, 243]. The anisotropy of the mesogenic structures and the collective responses previously observed with electric fields, brought the idea to analyze the mesogen orientation dependence on the actuation of acoustic fields. Different works were carried out in this regard, especially when a magnetic field firstly align the LC nematic phase[244, 245, 246, 247]. K. Miyano and R. Shen were the first in inducing Surface Acoustic Waves (SAWs) on a nematic LC glass cell with the actuation on an interdigital transducer (IDT) built up on a quartz surface, mounted on the actual cell, introduced by R. M. White and F. W. Voltmer a decade before[248, 249, 250]. The use of SAWs brings some advantages, while BAWs have larger power consumption and, as will me commented later, SAWs permitted the use of acoustic waves in modern miniaturized devices compatible with soft lithography techniques. Further understanding on the acoustic waves' actuation leaded to the publication of significant statements. A sound wave in the LC absorbing medium exerts a net force to conserve momentum. Such a force causes a stationary flow or vortices, which is known as acoustic streaming. Due to the stationary fluid, the streaming flow reorients the mesogens. When nematics are anchored homeotropically to the glass substrate, stripe patterns show up and become increasingly clear when the acoustic field intensity increases. With increasing

intensity, colored striations appear within each stripe, consequently disclinations grow with more intense acoustics, and at yet higher intensity, the director orientation is completely randomized and the disclination lines tumble around in a way resembling the dynamic scattering mode. Since then, several experiments have been done on nematic LC confined between glass slides, with piezoelectric materials to produce BAWs, or with the design of IDT to induce SAWs[251, 252, 253, 254, 247] Recent applications are focused on the tunability of transparency and light scattering of cholesteric LCs[255, 256], polymer-dispersed liquid crystal screens[257] , acoustic images visualized on LCs[258, 259], medical imaging[260] and LC tunable lenses[261].

4.2   Experimental setup

An acoustofluidic device was fabricated bonding a PDMS microfluidic channel between two interdigitated transducers (IDTs) deposited in the surface of a LiNbO$_3$ piezoelectric substrate (Fig. 4.1A). The channels were fabricated out of polydimethylsiloxane (1:10 curing agent to PDMS base; SYLGARD 184, Dow Corning) and bonded to the piezoelectric substrate after components were exposed to air plasma (Harrick Plasma, Plasma Cleaner Model PDC-001). The microfluidic channel was manufactured using well-stablished soft lithography techniques, having a square cross-section of height h = 40 μm, a width w = 200 μm, and a length L = 10 mm. We used the NLC 5CB (Sigma-Aldrich), which exhibits the nematic phase between 22°C and 35°C. The channel walls were chemically treated with a 0.4 wt% aqueous solution of N-dimethyl-n-octadecyl-3-aminopropyl-trimethoxysilyl chloride (DMOAP, Sigma-Aldrich) to induce strong homeotropic surface anchoring for 5CB molecules (Fig. 4.1B). Without treatment, the piezoelectric substrate has random planar anchoring while PDMS shows weak homeotropic anchoring. Interdigitated transducers (IDTs) were patterned into a 128° Y-cut of LiNbO$_3$ piezoelectric substrate (Roditi, double polished, 0.5 mm thickness) by using standard lithography techniques and vapor deposition of 10 nm Platinum adhesion layer followed by 80 nm gold layer. The single electrode transducer pitch was set to 50 μm to achieve a wavelength of 200 μm. The high voltage of RF signal

was generated using a GHz generator (Hewlett Packard, Model E4431B) subsequently amplified using a power amplifier (Minicircuits, Model ZHL-1-2W-N+). Before experimenting, channels were filled up with the 5CB in the isotropic phase and then slowly cooled down to room temperature. The temperature was controlled using a Linkam PE120 temperature allowing to set the hot stage under the microscope.
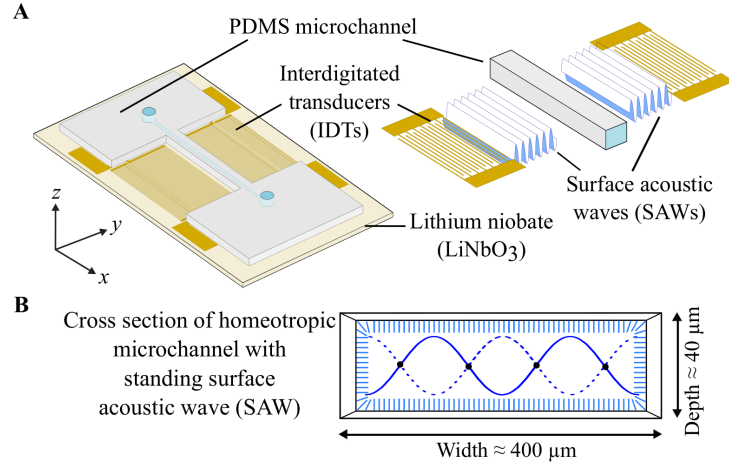
FIGURE 4.1: **Experimental setup and device schematic A**. Schematic representation of a PDMS channel on a Lithium Niobate substrate (LiNbO$_3$) with two pairs of parallel IDTs to generate SSAWs. **B**. Cross section of the square channel of size 400×40 μm displaying the nodes and anti-nodes of the standing pressure wave. Wavelength of 200 μm. Homeotropic anchoring is obtained by surface treatment with 0.4 wt% DMOAP

The optical characterization was performed by polarizing optical microscope in reflection mode(POM) (Olympus BX60, with 4x/10x air objectives). A fluorescence confocal polarizing microscope (FCPM) (Leica SP5 STED under 5x/10x air objectives) was used to study molecular reorientation. For FCPM imaging, 5CB was doped with 0.01 wt% of the fluorescent dye Nile Red (Sigma Aldrich) and excited by a laser at wavelength of 561 nm. We precisely controlled and manipulated the flow by using a pressure controller-driven system (OB1 MK3+, ELVESYS). The flow rate was varied in the range from 0.01 to 10.80 μl/h corresponding to a flow velocity ranging from 0.05 to 85 μm/s. The characteristic Reynolds number $Re = \rho v l / \nu$ ranged between 10^{-7} and 10^{-4} with an effective dynamic viscosity $\nu = 50 mPas$, and material density $\rho = 1.024 kg/m_3$. The hydraulic diameter is defined as $l = 4wd/2(w+h) = 72.7\mu m$ of the rectangular channels. The corresponding Ericksen number is $Er = hvl/K$, with single elastic constant approximation K = 5.5 pN, varied between 0.03 and 55.

4.3 Identification of acoustically induced patterns of confined nematic liquid crystals

The bulk of literature describing the effect of acoustic oscillations on nematic liquid crystals has focused on the study of these materials in liquid crystal cells: Small rectangular chambers with height defined by Mylar spacers of fixed thickness. Despite the interesting results found, the effects of channel confinement on the behavior of NLCs is poorly understood. To study the behavior of nematics on small channels where both the upper-lower walls and side walls are separated by a distance $sim\lambda$, we introduced 5CB in an acostofluidic device and applied an standing surface acoustic wave (Fig. 4.1A). The the channel is centrally positioned between two parallel interdigitated transducers (IDTs) patterned on the piezoelectric substrate, allowing us to control the position of the wave pressure nodes and antinodes within the microfluidic channel after applying a RF signal to the IDTs (Fig. 4.1B).

Acoustically induced patterns of NLC in the homeotropic microfluidic channel are observed (Fig. 4.2 A-J). Due to the homeotropic anchoring, the channel appears dark in the absence of an acoustic field. This corresponds to a uniformly aligned director field along the z-axis (Fig. 4.2A). Applying SSAWs at very low intensities ($P \leq 10$ mW) did not cause any observable changes in the POM images of the microfluidic channel. After surpassing an input power threshold of about $P \approx 14$ mW, faint bright patterns start to appear in the form of lines at the acoustic wave pressure nodes; two lines appear in the center of the channels and two lines near each of the lateral walls. With an applied input power equal to $P = 15$ mW, the SSAW induces the formation of clear, well developed and stable birefringent stripe patterns or bands perpendicular to the sound propagation. These bands look bright white and are located at the SSAW pressure nodes (white lines, Fig. 4.2B).

Increasing the input power to 20 mW induces birefringence within the bands, creating visible colors on the stripes at the pressure nodes (color lines, Fig. 4.2C). By further increasing the power, the stripes undergo a discontinuous transition (Brown lines, Fig. 4.2D). The bands in the center form disclination loops, with a transition reminiscent
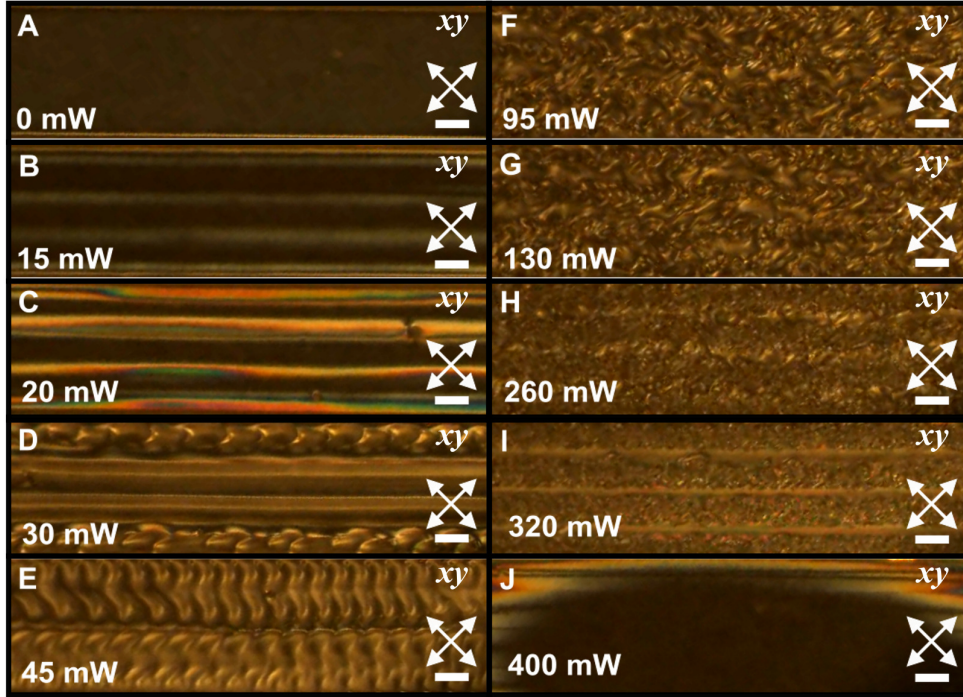
FIGURE 4.2: **NLC under SSAWs in microfluidic channel with homeotropic anchoring.A - J** Experimental POM images show the top view of the NLC in a channel under SSAWs. Different values of the input power applied to the IDTs lead to the observation of **A**. no optical patterns, **B**. white stripe patterns, **C**. color stripe patterns, **D**. brown stripe patterns, **E**. dynamical behavior of spatially periodic flows, **G-H**. dynamic scattering characterized by a turbulent-like flow, **H-I**. dynamic scattering with stripes, **J** and isotropic phase transition. White crossed double arrows show the orientation of the polarizers. Scale bars, 100 μm.

of the homeotropic-dowser transition typically observed in homeotropic nematic samples — the so-called quasi-planar texture in which director rotates by Pi between the top and bottom confinement [99, 262]. In contrast, one can observe a disruption on the texture at the channel walls characterized by periodic fluid swirling that is likely driven by acoustic streaming rolls from propagating from the stokes layer into the bulk. In contrast with unstructured fluids like water, the elastic penalties of NLC allow for interesting flow patterns. Around an input power of $P = 45$ mW, the stripes transition into a fascinating set of spatially periodic flow patterns whose dynamical behavior is dictated by the interplay between the acoustic streaming, acoustic reorientation and the Landau-de Gennes free energy out of equilibrium (Fig. 4.2E). Beyond this point, higher acoustic intensity sets the transition into a chaotic turbulent-like flow behavior. The POM of the NLC under the turbulent-like flow is characterized by dynamic

scattering analogous to the dynamic scattering observed with an electric field (Fig. 4.2F−G). Further increasing the acoustic intensity promotes the formation of stripes within the dynamic scattering. This stripes appear as regions of birefrigence located at the acoustic pressure anti-nodes (Fig. 4.2H−I). Lastly, applying an input power $P \leq 400$ mW induces transition into an isotropic phase (Fig. 4.2J).

The presence of bands of optical intensity on NLC with hometropic anchoring was described in studies using liquid crystal cells. They also reported the onset of the dynamic scattering regime at suficiently high acoustic intensities, as well as the acoustically-induced transtion to the isotropic phase. Thus, our observations of the behavior of NLCs in a microchannel are in agreement with previous reports. In addition, we observe the formation of periodic patterns forming soon after the formation of disclination lines at the stripe patterns but before reaching the dynamic scattering. Furthermore, we observed the onset of lines of high birefringence emerging on top of turbulent-like flows at in the dynamic scattering regime before reaching the critical input power that triggers the transition into the isotropic phase. Consequently, these states induced by the acoustic field are a consequence of the confinement. Here, the proximity of the side walls accentuates the effect of streaming effects as the distance of the Stokes layer from the center channel is highly reduced. As seen in Fig 4.2, the optical intensity of light observed through POM changes greatly as a function of the applied input power that directly affects the intensity of the acoustic waves. In particular, the change in optical intensity is more noticeable at the SSAW pressure nodes, where the stripe patterns initially appear. Thus, we quantified the total optical intensity observed after shining a NLC under acoustic waves using POM (Fig. 4.3A). Here, the optical intensity increases after surpasing the $P \approx 14$ mW threshold, reaching a peak of optical intensity in the color stripes stage. Then, the optical intensity decreases as the birefringence of the color stripes stage is replaced by low-optical-intensity disclination lines at the brown line stage. After this drop the optical intensity plateaus, as the NLC reach a steady value given by the disclination lines formed in the Brown line stage and the periodic flows. Increasing the power into the dynamic scattering stage reduces the optical intensity as the NLC reaches a homogeneous flow behavior

across the channel. During the transition to a dark, low optical intensity isotropic phase we observed a small peak of optical intensity. This peak is generated while the dynamic scattering is replace by a bright, thin-film birefrigent layer that signal the nematic-isotropic transition induced by the acoustic waves.
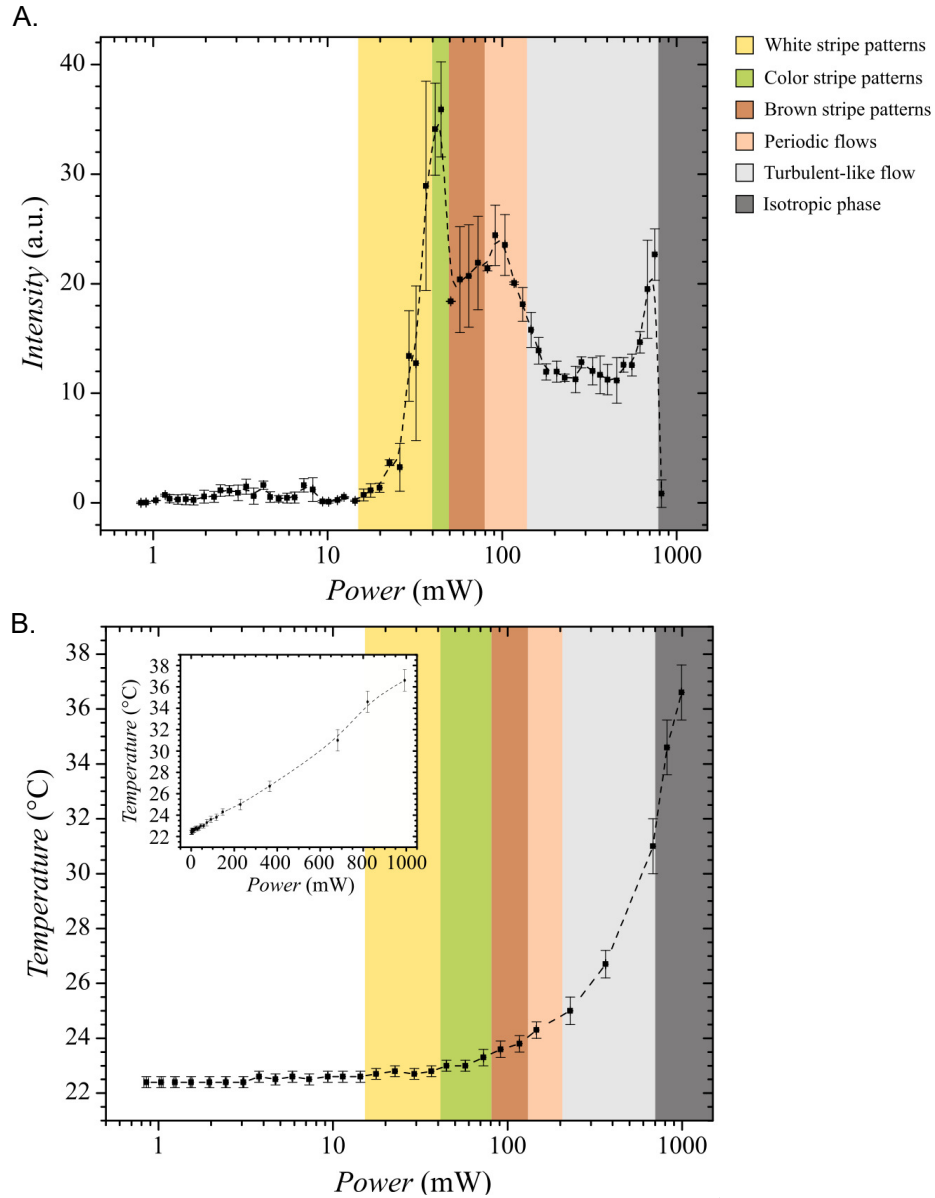
FIGURE 4.3: **Temperature and optical intensity of NLC under SSAWs.A**. Optical intensity of acoustic-induced patterns with the peak in the region of color stripe patterns. **B**. Change in temperature of a nematic in a microfluidic device as a function of input power of RF signal (inset: linear plot). In the region of white and color stripe patterns, the temperature is not significantly elevated whereas the turbulent-like flow regime significantly increases the temperature of the system. Color legend represents a specific pattern region.

Besides the acoustically-induced molecular reorientation and acoustic streaming driving, the system temperature plays and important role in understanding the behavior of NLC in our experimental setup. Despite the use of a temperature control system in the form of a cooling plate, The viscous dissipation of acoustic energy in the microfluidic channel generates a heat flow large enough to ofset the equilibrium temperature of the fluid in the center of the channel. This means that even with a fixed setpoint temperature given by the temperature control, the NLC reaches a different steady-state temperature as a function of the acoustic wave input power. To account for changes of temperature in the nematic, we quantified the temperature of the fluid as a function of the applied input power (Fig. 4.3B). Our measurements indicate that the temperature within the channel increases linearly with the input power. The temperature increase at the input power values where we observed the nematic-isotropic transition suggest that the phase transition is driven by heating of the system. For low acoustic intensities, the temperature increase is very small and therefore negligible, which supports a constant temperature assumption when analyzing low intensity acoustically-induced patterns. Fig 4.3B also indicates that the temperature increases linearly with the input power, with most of the heating occurring during the dynamic scattering stage.

We studied the time scales for the emergence and disappearance of acoustically induced patterns of NLCs. For this, we measure the time to reach a stable optical response after applying the acoustic field, which we labeled response time. We also measure the time it takes the system to relax back to the initial homeotropic dark state after the acoustic field is switched off, which we labeled relaxation time. The response and relaxation times of all patterns are of the order of seconds (Fig. 4.4). The response time gradually increases with increasing the input power until it reaches the maximum in the color stripes regime; this peak corresponds to the highest optical intensity (Fig. 4.4A). After that, the response time decreases, reaching a plateau during the brown stripes. In contrast, the relaxation time increases with increasing input power throughout the stripe patterns regimes, reaching a plateau during the dynamic scattering regime (Fig. 4.4B). Once the system reaches dynamic scattering

with lines, the relaxation time increases again until the isotropic phase.
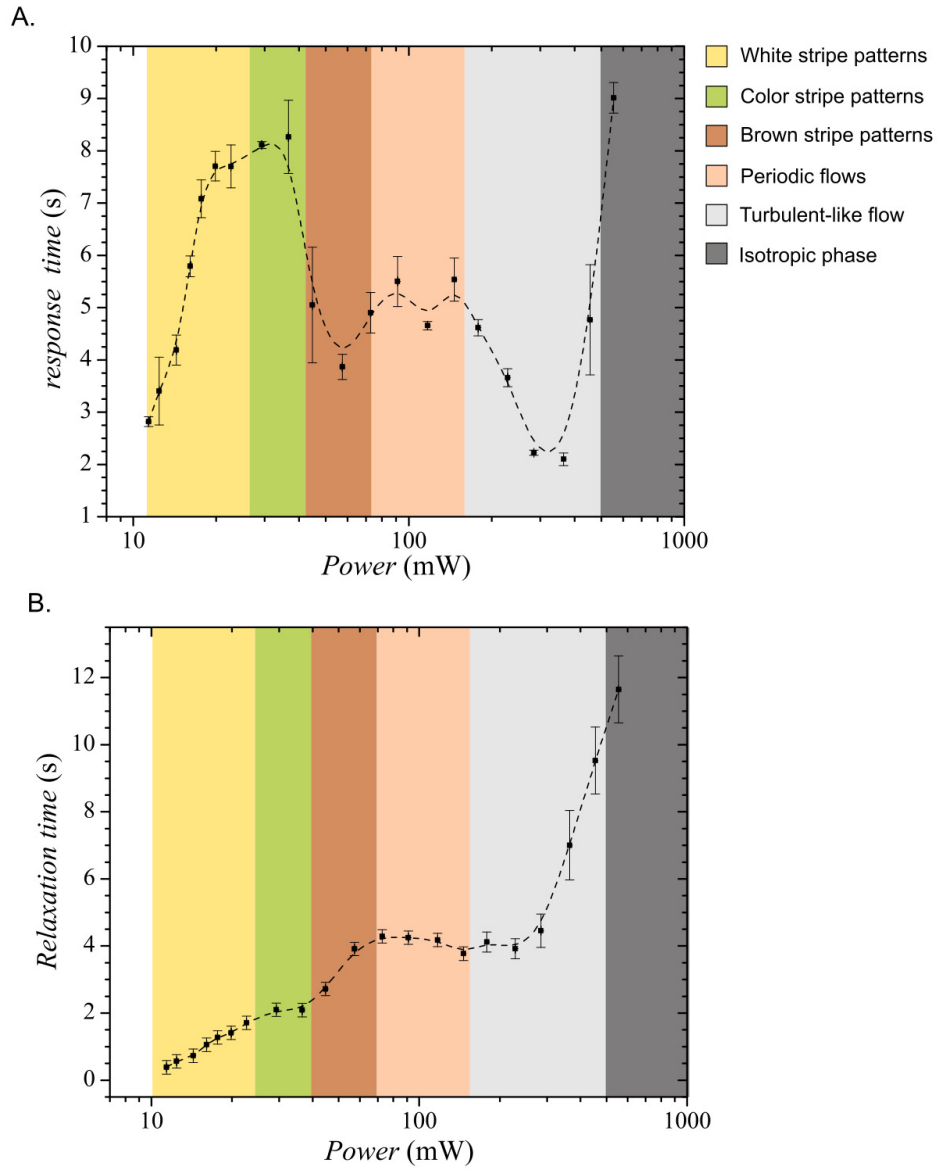
FIGURE 4.4: **Response time and relaxation time of NLC under SSAWs**.
A. Response time for the nematic system to reach steady state after applying SSAWs.
B. Relaxation time for the nematic system to go back to steady state after turning the
SAWs OFF. Color legend represents a specific pattern region.

4.4 Molecular reorientation of nematics driven by standing surface acoustic waves

It is well known that liquid crystal molecules align with applied electric fields. Given that the energetic contribution of an external acoustic field are similar to those from electric fields, it has been proposed that the director of a nematic liquid crystals aligns with the wave vector once exposed to an acoustic field[263]. Based on the results from Fig. 4.2 however, the dynamics of nematic liquid crystals in confinement show a diverse array of stages and patterns. As mentioned before, for high-intensity acoustic waves the dynamic behavior of the nematic is strongly influenced by streaming effects and temperature increases. Conversely, in the case of low intensity waves the temperature remains approximately constant without disruptions from periodic or streaming flows. Thus, the onset of stripe patterns induced by low-intensity SSAWs might be driven by molecular realignment of the director field towards the direction of the acoustic field wave vector.

To test this hypothesis, we studied the The spatial orientation of the NLC molecules of acoustically induced patterns is resolved by performing fluorescence confocal polarizing microscopy (FCPM) imaging along the top view (xy plane) and cross section (yz plane) of the channel (Fig 4.5). The fluorescent dye added aligns with the NLC director, allowing us to quantify changes of orientation as increases in the fluorescence intensity. Thus, in these experiments high fluorescence intensity indicates that the director field is oriented parallel to the polarization of the laser beam, while low fluorescence signal indicates an orthogonal orientation. As seen from Fig. 4.5)A, without an acoustic field the NLC is aligned ortogonal to the polarization beam consistent with a molecular orientation induced by the homeotropic anchoring as depicted in Fig. 4.5)E. Applying an input power of $P = 15$ mW form the white stripes pattern, we observe an increase of fluorescence in the vicinity of the acoustic pressure nodes (Fig. 4.5)B). Given that this effect is observed both in the xy and yz plane, we can conclude that the orientation of the director field is changed locally with a slight tilting of the molecules at the pressure nodes (Fig. 4.5)F).
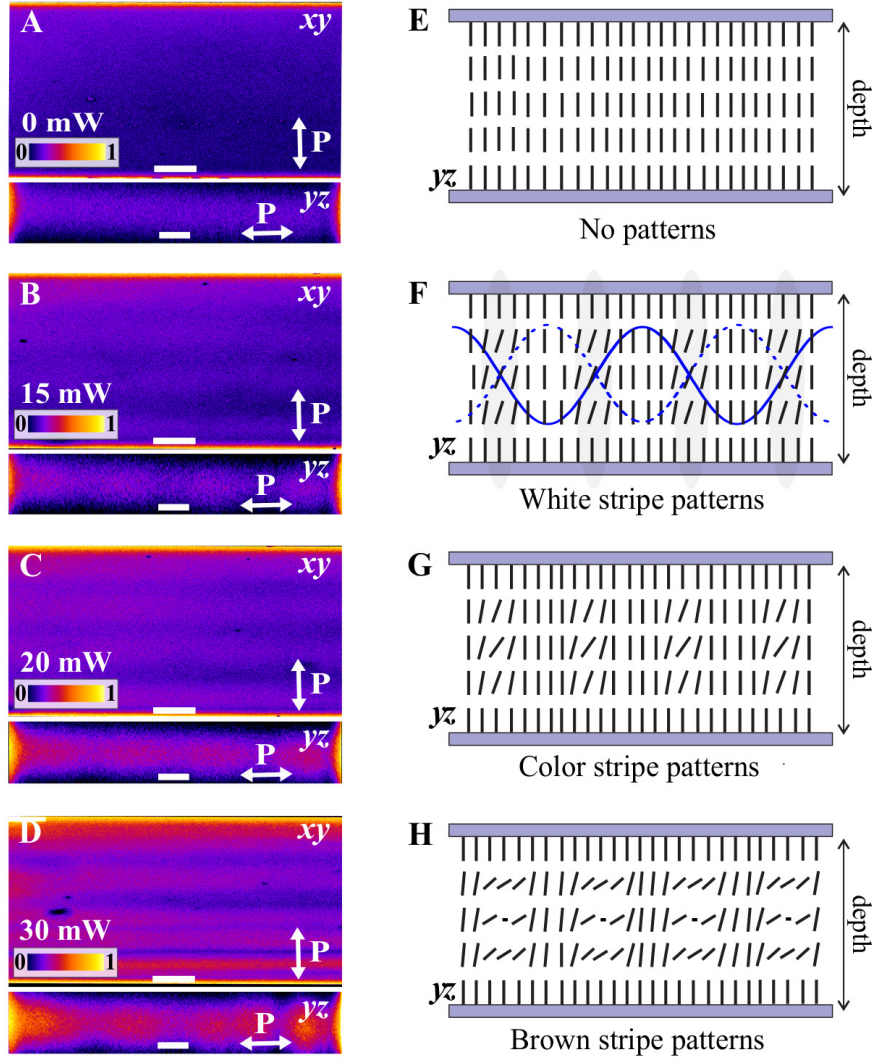
FIGURE 4.5: **Analysis of molecular reorientation of NLCs driven by SSAWs**. **A-D**. FCPM imaging of the top view (xy plane) and cross section (yz plane) of a channel corresponding to NLC with **A**. no stripes, **B.** white stripes, **C** color stripes, and **D**. brown stripe patterns (D) as described in Fig. 4.1. **E-H**. Corresponding schematic representation of director orientation for stripe patterns for **E**. no stripes, **F** white stripes, **G** color stripes, and **H** brown stripe patterns. The grey area in **F** indicates the pressure nodes region tilting the NLC molecules. Side walls are not included. Scale bars, 100 μm (xy plane) and 20 μm (yz plane).

Further increase of the acoustic intensity into the color stripes pattern is followed by an increase in fluorescent intensity at the pressure nodes (Fig. 4.5)C). Consequently, as we increase the acoustic intensity the angle by which we tilt the director field at the pressure node also increases (Fig. 4.5)G). Once we reach the brown stripe patterns (Fig. 4.5)D) the onset of disclination lines generate disturbances in the reading of fluorescent images. Despit this, this stage also show an increase of fluorescence, allowing us to

hypothesize that the orientation of the nematic follow Fig. 4.5)H. Altogether, This results paint a consistent picture, where director of the nematic is tilted in the vicinity of the pressure nodes as a function of the acoustic intensity.

We quantify the fluorescent intensity in the xy plane under FCPM (Fig. 4.6). Consistent with the observations made before, Applying SSAWs to the NLCs induce an intense fluorescent signal on the vicinity of acoustic pressure nodes indicating tilting of the director field. The reorientation gradually evolves from relatively small tilting, which corresponds to the formation of the white stripes, to more pronounced tilted director, corresponding to the colored stripes, and a larger inclination of the molecules due to the formation of disclination loops on stripes.
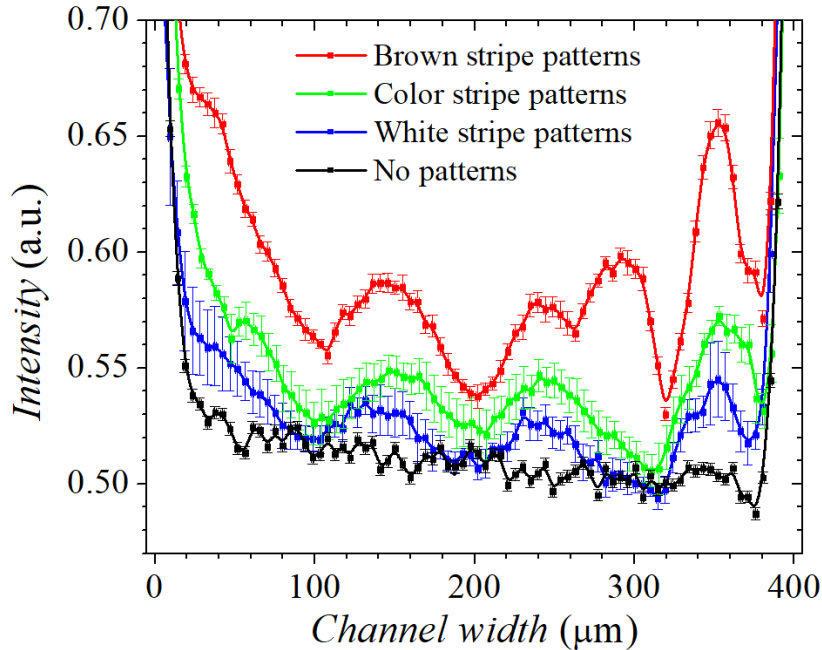
FIGURE 4.6: **Optical intensity of NLC patterns induced by SSAWs**. Optical intensity as a function of the channel width for stripe patterns induced by applying a SSAWs in a NLC. (Black line) No stripe pattern, P = 0 mW. (Blue line) white stripe pattern, P = 15 mW. (Green line) Color stripe pattern, P = 20 mW. (Red line) Brown stripe pattern, P = 30 mW. Channel width 400 μm. Wavelength λ = 200 μm.

4.5 Nematic liquid crystals under acoustic waves in channels with hybrid anchoring

The results and discussion on the behavior of NLCs under acoustic waves has been focused on microfluidic channels with homeotropic anchoring. In addition, we studied the behavior of NLCs in microfluidic channels with hybrid anchoring. If untreated, the PDMS walls on the channel will have a weak homeotropic anchoring while the LiNbO$_3$ piezoelectric substrate has random planar anchoring. This difference in anchoring leads to differences in the observed patterns using POM when exposing the NLC to SSAWs. The first important difference is the absence of the stripe patterns at low intensities. While the director field will still tilt locally in the vicinity of the pressure nodes, the anchoring condition at the substrate precludes this system to show any lines as a consquency of light difraction induced by the new molecular orientation. Thus, in the case of hybrid anchoring the NLC shows no acoustically-induced patterns at low or intermediate intensities (Fig. 4.7A). For input powers of $P = 200mW$ or greater however, the system undergo interesting transitions until reaching the nematic-isotropic transition.

Without temperature control, an input power of $P = 200mW$ is sufficient to trigger an perplexing dynamic evolution of the nematic under POM. Here, removing the temperature control implied that the system gradually heats up due to viscous dissipation. Consequently, the evolution of this system in time allows us to follow the evolution of the system as the temperature of the system increases. Starting with a NLC at equilibrium (Fig. 4.7A), the interaction of the acoustic field creates a turbulent-like flow reminiscent to the dynamic scattering stage in homeotropic channels. As time progresses however, the oscillations form flows in the bulk of the nematic that differ greatly from those observed during the dynamic scattering (Fig. 4.7B). Here, the nematic shows transient domains with high birefrigence that merge and divide dynamically with clear disclinations. Eventually, these domains merge and sync, forming periodic flow structures(Fig. 4.7C). In contrast with the periodic flows in homeotropic channel which exhibit two set of perodic flows in oposite directions ((Fig. 4.2E), here the periodic

flow occupy the entire channel with repeating structures separate approximately 40-50 μ from each other. Eventually, the periodic flow devolve into oscillating patterns characterized by columns that run across the microfluidic channel(Fig. 4.7D). From here, the system relaxes in to a thin-film birefringence that expands homogeneusly across the channel (Fig. 4.7E). Similar to the response of NLC in homeotropic channels, this stage signals the transition into the isotropic phase. Interestingly, the transition to isotropic in a channel with hybrid anchoring is very different from the homeotropic case. Here, instead of a homogeneous phase transition starting from the center of the channel outwards ((Fig. 4.2J), The NLC forms thin columns from the walls into the center of the channel, leaving a trail of droplets that resemble droplets in a hydrophobic surface (Fig. 4.7F). Even though the evolution of these system in time is driven by local heating of the nematic, one can slow down or reverse the progression between these stages by reducing the intensity of the acoustic field. This can be explained as above room temperature the system will exchange temperature locally with the room serving as a temperature reservoir.
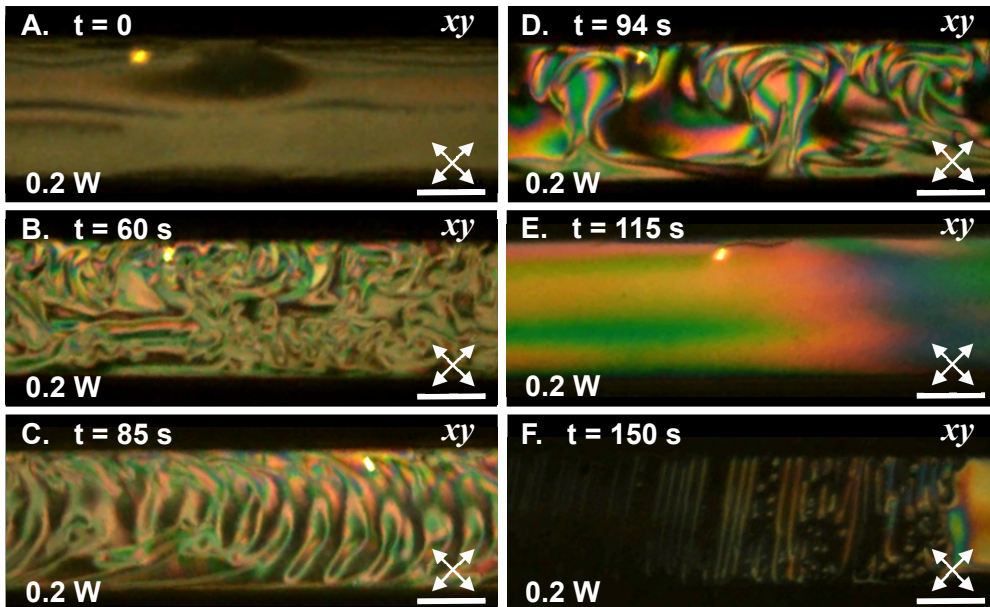
FIGURE 4.7: **Response of NLC under SSAWs in channels with planar anchoring without temperature control**. 5CB was introduced in a microfluidic channel with planar anchoring and exposed to SSAWs without temperature control. **A**. At $t = 0$ the LC is in a nematic phase at room temperature.**B**. Applying SSAW induced dynamic scattering promoting chaotic bulk flow. **C-D**. Onset of periodic patterns. **E**. Formation of birefringent layers. **F**. Transition into isotropic phase through a dripping phase. Channel width $w = 200$ μm and $\lambda = 200$ μm. Scale bar is 100 μm.

When the temperature control unit is used, the behavior of the NLC in channels with hybrid anchoring is straight forward: Low intensities do not generate disruptions in the nematic while high intensities induce dynamic scattering until the system transitions to the isotropic phase for suficiently high input power (Fig. 4.8). Even though one cannot observe the stripe patterns with hybrid anchoring, the dynamic scattering also shows variations in the optical intensity across the channel that is consistent with the density variations the SSAW creates in the resonating cavity (Fig. 4.8A). In this case the darker areas in the POM images correspond to regions with pressure antinodes in the center while the brighter areas indicate the location of pressure nodes. This effect can be useful as a cheap way to determine optically the density profile in an acoustic microfluidic chamber which can provide information about the acoustic waves generated by the IDTs.
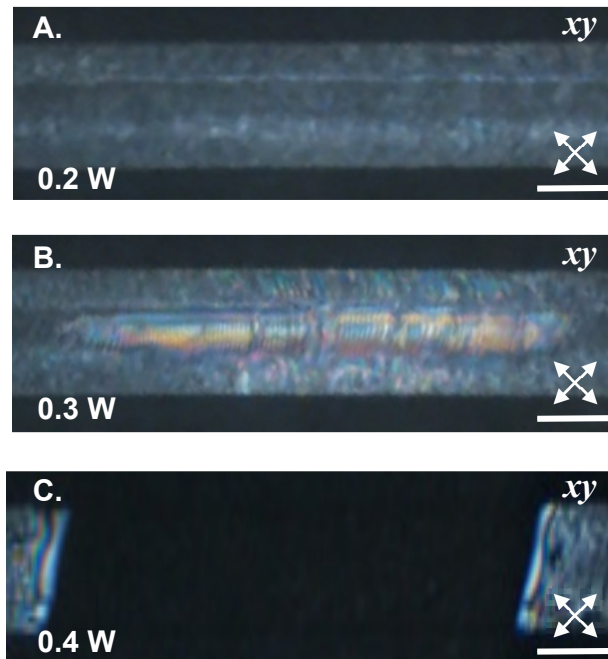
FIGURE 4.8: **Response of NLC under SSAWs in 200 μm channels with planar anchoring**. Under temperature control, exposure of NLCs to SSAWs in a 200 μm microfluidic channel with planar anchoring. **A**. Acoustic-induced density variations and streaming flows. Input power P = 200 mW. **B**. Periodic patterns in channel center. Input power P = 300 mW. **C**. transition to isotropic phase. Input power P = 400 mW.

In addition, we observed that at specific acoustic intensity close to the nematic-isotropic transition (Fig. 4.8C), the nematic forms a periodic structure around the pressure anti-node characterized by small, perpendicular bands with short pitch generating high birefringence in this region with lower density (Fig. 4.8B). It is not possible to determine from POM alone the characteristics of this novel topological structure. However, we can observe similar structures in microfluidic channels with hybrid anchoring that have a higher w/λ ratio (Fig. 4.9). In the case of channels having a width of 400 μm, the nematic shows a homogeneous brightness across the channel induced by the anchoring in the absence of acoustic waves (Fig. 4.9A). Turning the SSAWs ON is followed by the formation of stripe patterns. In contrast with the homeotropic channels however, the bright stripes correspond to areas of high density at the pressure anti-nodes while the dark bands are areas of lower density at the pressure nodes (Fig. 4.9B). Similar to the results for the 200 μm channel, the nematic forms a periodic structures of small, perpendicular bands with high birefringence around the pressure anti-nodes (Fig. 4.9C). Increasing the input power to $P = 400mw$ induce the nematic-isotropic transition.
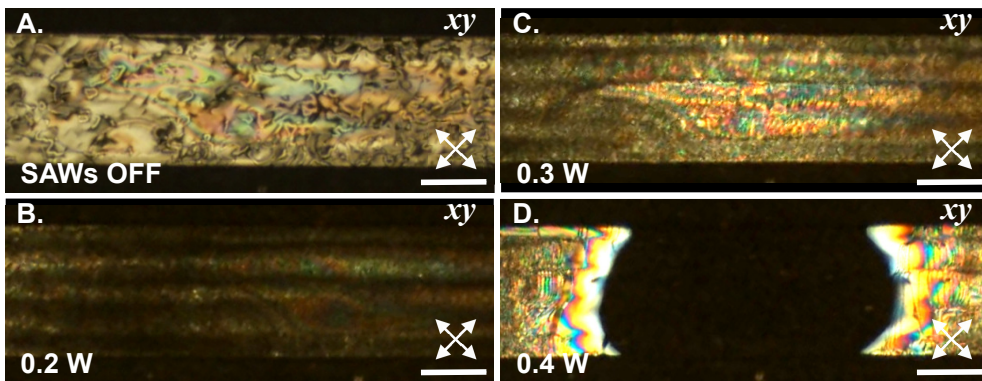
FIGURE 4.9: **Response of NLC under SSAWs in 400 μm channels with planar anchoring**. Under temperature control, exposure of NLCs to SSAWs in a 400 μm microfluidic channel with planar anchoring. **A**. Steady state without SAWs. **B**. Acoustic-induced density variations and streaming flows. Input power P = 200 mW. **C**. Periodic patterns in channel center. Input power P = 300 mW. **D**. transition to isotropic phase. Input power P = 400 mW.

4.6 Conclusion

The experimental results obtained from SAWs on NLCs in confined microfluidic channels expand upon the known phenomenological behavior of liquid crystals under acoustic waves. While early work reported the presence of stripe patterns, birefringent color lines at pressure nodes, and dynamic scattering behavior, our experiments show for the first time the onset of periodic patterns with structures reminiscent of cholesteric fingers along with eddies near the walls during the formation of the brown line stripes using acoustic waves in NLCs (Fig. 4.2). Following theoretical models of acoustic waves in fluids, it is likely to attribute the formation of eddies near the walls to acoustic streaming effects that propagate from the Stokes layer into the bulk. The combined effects of acoustic streaming and the material elastic response appear to be the main contributors in the formation of the spatial periodic structures at high acoustic intensity, while the nematic reorientation toward the wave vector dictates the behavior at low acoustic intensities. At high input power, the experiments report for the first time the formation of birefringent lines at the pressure nodes embedded in the surrounding turbulent-like flow characteristic of the dynamic scattering regime. These results expand the scope of the dynamic behavior of NLCs under SAWs that can find further exploration in chiral nematic and lyotropic LC systems.

Consistent with the results presented by Moritake et al. in a LC cell with isotropic anchoring[264], an increase in the applied voltage of a traveling SAW generates a change in the orientation of the LC director field up to $\approx 25°$. This is close to our measurement of the maximum Rayleigh angle of $\theta_{Rayleigh} = \approx 23°$ for 5 CB. Interestingly, the applied voltage necessary to reach this maximum change in orientation of the director is significantly smaller in the acoustic optofluidic setup ($28V$ compared to $150V$). Inoue and Moritake showed how shear horizontal (SH) surface acoustic waves can be used to determine the director orientation change based on estimation of the fractional velocity change based on phase delay changes of the wave[265]. These measurements were viable under planar or hybrid anchoring with homeotropic on the top glass. However, they showed that homeotropic anchoring on the bottom layer as the mechanical dis-

placement in the LC layer decays rapidly. In contrast, as shown in Fig. 4.5, the use of SSAWs generates displacements of the LC director field in homeotropic anchoring conditions that propagate vertically from the surface throughout the channel height. This distance is larger than the decay from the LC layer of 5 μm predicted by developing Farnell's [266] and Campbell and Jone's methods [267].

Following the theoretical analysis by Helfrich[268] and Nagai-Izuka[269], we got that the ultrasonic intensity threshold for 5CB exposed to a 200 μm wavelength is around 23 W/cm^2 which corresponds to $Re_s = 5 \times 10^{-13}$. In contrast, the observed threshold applying acoustic waves in microfluidics is closer to 15 W/cm^2 or $Re_s = 1 \times 10^{-13}$. This observation indicates that the confinement of the LC enhances the streaming-induced reorientation of the LC, reducing the threshold.

Nagai et al. quantified the optical response of LC cells under acoustic fields [270]. This seminal study explored the behavior of the LC in the range of acoustic intensity from 10 to 80 mW/cm^2 showing that the optical intensity peaks at low values of intensity and decays as intensity increases. Following their observations, the rise time decreases rapidly as you increase intensity while the decay time increases. Nagai et al [270] attributed this behavior to the onset of dynamic scattering. In agreement with these observations, the measurements presented in Fig. 4.3A show a peak of optical intensity at around 35 mW/cm^2 which corresponds with the rise of periodic flows and early onset of the dynamic scattering regime where the intensity increases as the light transmission decrease. Similarly, the response time in the dynamic scattering regime $(30-150$ mW/cm$^2)$ is reduced while increasing the relaxation time, consistent with Nagai et al [270] (Fig. 4.4). Nagai and Izuka [269] showed that the decay time of the acousto-optical response of the LC can be reduced by applying an erasing pulse (100 Hz, 40 V$_{pp}$) to restore the initial orientation. This indicates that a combined electroacoustic approach can be used as a strategy to reduce the response times of these systems thus supporting acoustic optofluidic devices coupled with orthogonal electric fields where the reorientation effect of the electric field can be used to interplay with the acoustic and fluid flow fields to achieve higher control on the molecular reorientation with improved response times.

CHAPTER 5

NEMATODYNAMICS OF CONFINED LIQUID CRYSTALS UNDER ACOUSTIC FIELDS

5.1 Introduction

The optical properties of liquid crystals are generally controlled by relying on electric fields. The effect of other external fields including acoustic waves and fluid flow is not well understood. In this chapter we investigate the effects of combining microfluidic flows and acoustic fields on the molecular orientation and the corresponding optical response of nematic liquid crystals. Previously unknown ordered phases are identified, which are rationalized in terms of an out-of-equilibrium phase diagram as a function of the strengths of the flow and the acoustic field. The new phases are interpreted by relying on calculations with a free energy functional expressed in terms of the director tensor. Taken together, the findings presented here offer promise for development of new acoustofluidic systems based on judicious combinations of sound, flow and confinement.

Although optical properties of LCs have been analyzed in earlier years, microfluidics represent a pathway to control and understand the development of light integrated liquid systems to harness their use for applications, better known as optofluidic devices[271]. From the point of view of structure and mechanism, optofluidic systems has been divided in solid-liquid hybrids in which the optical properties of both media are relevant, colloid-based solutions systems in which the optical interactions with colloids are the central role, and fully liquid systems in which the optical properties

of liquids, as changes of refractive index, are the most important data[272]. In this category lie the LCs optofluidic devices, like the used for modulating peristaltic microflows with fast optical responses[273], or to improve the design of optical lenses for 2- and 3-dimensional imaging[274]. Nevertheless, to the best of our knowledge, we have designed the first optofluidic device that confine nematic LCs within a PDMS channel, under the actuation of standing surface acoustic waves and pressure driven flows. Here we present the implementation of these two external fields that allowed the manipulation of the orientation of the nematic ordered mesogens. We characterized different responsive regimes with variable acoustic intensities and tunable pressure flows, with quite fast optical responses. The experimental results were compared with continuum simulation predictions, in perfect agreement. The obtained results kick off the engineering of applications of these compound devices for different medical, imaging, and sensing applications.

Optofluidic devices combine the optical and transport features of liquids to develop novel technologies and analytical methods. These devices can be used for precise control of light, chemical reactions control, colloidal trapping, biomolecules manipulation, novel imaging and sensing applications, among others[275, 276, 272, 277]. In particular, the integration of liquid crystals (LCs) into solid-liquid hybrids or fully liquid optofluidic systems has shown promise for applications in photonics and displays [273, 278, 274, 279] . LCs are attractive materials for optofluidic applications, as they exhibit unique optical responses due to their anisotropic nature and collective structural organization with remarkable sensitivity to external stimuli[280, 245, 281]. Although most of the literature has focused on the effect of light illumination, thermal gradients, electric fields, and magnetic fields on LC reorientation, other fields can have an important effect on the structural organization of these materials. Among the potential candidates, advances in nanofabrication techniques have shifted interest towards two attractive external fields: fluid flow fields and acoustic fields.

The effect that fluid flow has on LCs confined in microchannels has been recently studied, making use of well-stablished nanofabrication techniques of microfluidic channels[282]. This stud shows a strong effect of flow field on the orientation and the

order of nematic fluids. In addition, recent studies have revealed the existence of different topological states in channel-confined nematic flows — referred to as bowser, chiral, and dowser states[262]. The bowser state is stable only in a weak flow regime, where the orientational order and flow are only weakly coupled and the structure is largely dictated by the surface anchoring. In the chiral state, the coupling of orientational order and flow leads to backflow effects. A flow-aligned dowser state is observed in the strong flow regime, in which the LC molecules are primarily oriented along the main axis of the microfluidic channel. Experiments with laser tweezers have shown that these topological states can in fact be created and controlled[283]. The creation of microfluidic devices made of polydimethylsiloxane (PDMS) promoted an exponential growth with new confinement geometries and Poiseuille flows allowed new studies of LCs under the actuation of an extra external field. These flows affect the orientation and the order of nematic fluids. It has been found out that the Poiseuille profile transforms into three general complex non-Poiseuille profiles: I) a weak-flow regime (called bowser state), where the nematic flow and orientational order are only weakly coupled and are mostly determined by the surface anchoring; II) A medium-flow regime (called chiral state), where the largest variability occurs in both flow and nematic profile, caused by the intricate backflow coupling; and III) The strong-flow regime (called dowser state), determined by alignment of the LC molecules in the direction of the flow [282]. In recent studies within microfluidic PDMS channels, a fine tuning of the flow pressure permitted the control of the bowser, chiral and dowser states. Moreover, the creation of topological states was controlled using a laser tweezer[262].

The development of Interdigitated transducers (IDTs) permitted the use of acoustic waves in modern miniaturized devices. The surface acoustic waves (SAWs) generated by IDTs facilitated the manufacture of devices generating waves with frequencies of more than 100 GHz, inspiring a new wave of technologies using acoustic fields that include radio-electronic components and sensors[284, 285]. Recently, techniques using standing SAWs (SSAWs) formed by two opposite and coaxial waves have been used for manipulation of biological cells and microparticles, displaying their versatility manipulating solutions of complex fluids[286, 287, 288, 289, 290, 291]. Studies

of the effects of SAWs on nematic LCs (NLCs) confined between glass slides examined the effects of periodic pressure fields, acoustic streaming flows and other external fields[265, 245, 292, 253, 254, 247]. They show that for perpendicular (homeotropically) anchored nematics, SAWs lead to the formation of stripe patterns that gradually transition into a dynamic scattering regime characterized by a turbulent-like flow where the nematic director orientation is randomized. Based on this results, Recent demonstrations have focused on the tuning of transparency and light scattering in cholesteric LCs, polymer-dispersed LC screens, acoustic images visualized on LCs, medical imaging, and LC tunable lenses[293, 258, 257, 294, 256, 260, 261].

5.2   Acoustically induced patterns in nematic flow

In order to explore the combined the effect of acoustic fields and pressure-driven nematic flows on the optical response of NLCs, we introduced 5CB in the acoustofluidic devices described in Chapter 4. While the expermients so far have focused on the effect of the acoustic waves on the nematic, here we introduce an additional field by generating a Poiseuille flow in the microfluidic channel using a pressure controller. For this experiments the channel was treated with 0.4 wt% aqueous solution of DMOAP to induce homeotropic anchoring in a channel of $width = 400$ μm, height h $= 40$ μm, , length $L = 10$ mm, and wavelength $\lambda = 200$ μm.

To characterize the behavior of the NLC under the combined effect of these fields, we used the Ericksen number, a relative measure of the viscous and elastic forces, as a dimensionless quantity that changes as a function of the flow velocity of the NLC. The Ericksen number is defined as $E_r = ((\nu \mu L))/K$, with ν being the rotational viscosity, μ being average measured flow velocity, L being the channel hydraulic diameter, and K being the single elastic constant of nematic 5CB. Similarly, we used the Streaming Reynolds Number as a dimensionless quantity that changes as a function of the acoustic wave intensity. In contrast with the well know Reynolds number, the Streaming Reynolds number relates the oscillatory forces and the viscous dissipation forces, being defined as $R_s = (U_o^2)/\nu\zeta$. Here, U_o is the characteristic velocity of the wave, ν is the

kinematic viscosity, and ζ is the frequency associated with the oscillatory flow. As shown in the Materials and Methods, $R_s \sim V^2$, where V is the input voltage from the RF signal generator.

Having defined these dimensionless parameters to characterize the response of the optofluidic system as a function of the flow velocity and the acoustic wave intensity (Fig. 5.1). we start by validating the previous observations of nematic flows in microfluidics. Without an acoustic field ($R_s = 0$), the director field is influenced by the velocity field in the Poiseuille flow. As expected, the channel appears dark under POM without flow in the absence of and acoustic field due to the homeotropic alignment of the NLC. Once a Poiseuille flow is established, birefringent colors appear (Fig. 5.1, $R_s = 0$). In the weak flow regime ($0 < Er < 21$) the birefringent colors arise as a the fluid flow bend the uniform director field, slightly bowed towards the flow direction. This correspond to the Bouser state. An increase in velocity to a medium flow regime ($21 \leq Er < 50$) induces continuous transformation of the bowser state into a characteristic chiral state, with left and right-handed domains separated by a flexible soliton-like structure in the center of the channel. With higher flow rates ($Er \geq 50$), the nematic undergoes a discontinuous transition into a flow-aligned state known as a dowser state. These nematic flow states are in good agreement with observations reported in previous publications [283, 295].

By applying low intensity SSAWs to nematic flows in microfluidic channels ($0 < R_s \leq 1.8 \times 10^{-12}$), we observe the emergence of different patterns with stripes reminiscent of those observed in with SSAWs without fluid flow (Fig. 4.2). Due to the resemblance of the observed pattern with the ones obtain with SSAWs only and flow only, we conclude that for low intensity acoustic waves the is a superposition of effect from the fluid flow alignment and SSAWs reorientation of the director field (Fig. 5.1, $0 < R_s \leq 1.8 \times 10^{-12}$). It is important to know that for intermediate to high flow rates, the orientation of the director is dominated by the velocity field even for low intensity acoustic waves. As the input power is increased ($R_s \sim 4.4 \times 10^{-12}$), the stripe patterns transition into a phase characterized by brown stripes with discontinuous transitions into disclination loops. At even higher input powers ($R_s > 5.5 \times 10^{-12}$), the system transition into an acoustically induced dynamic scattering. At higher acoustic inten-

sities, acoustically induced reorientation competes with the flow realignment until the system reaches dynamic scattering phase. Regardless of the flow velocity, the system evolves into the isotropic phase when sufficient input power of SAW is applied (Fig. 5.1). When $1.8 \times 10^{-12} \leq R_s \leq 4.4 \times 10^{-12}$ and the flow is close to the transition between the bouser and chiral flow ($12 \leq Er \leq 36$), the acoustic waves and fluid flow compete to dominate the orientation of the director field, showing a combination of chiral flows with stripes forming disinclination loops lines.
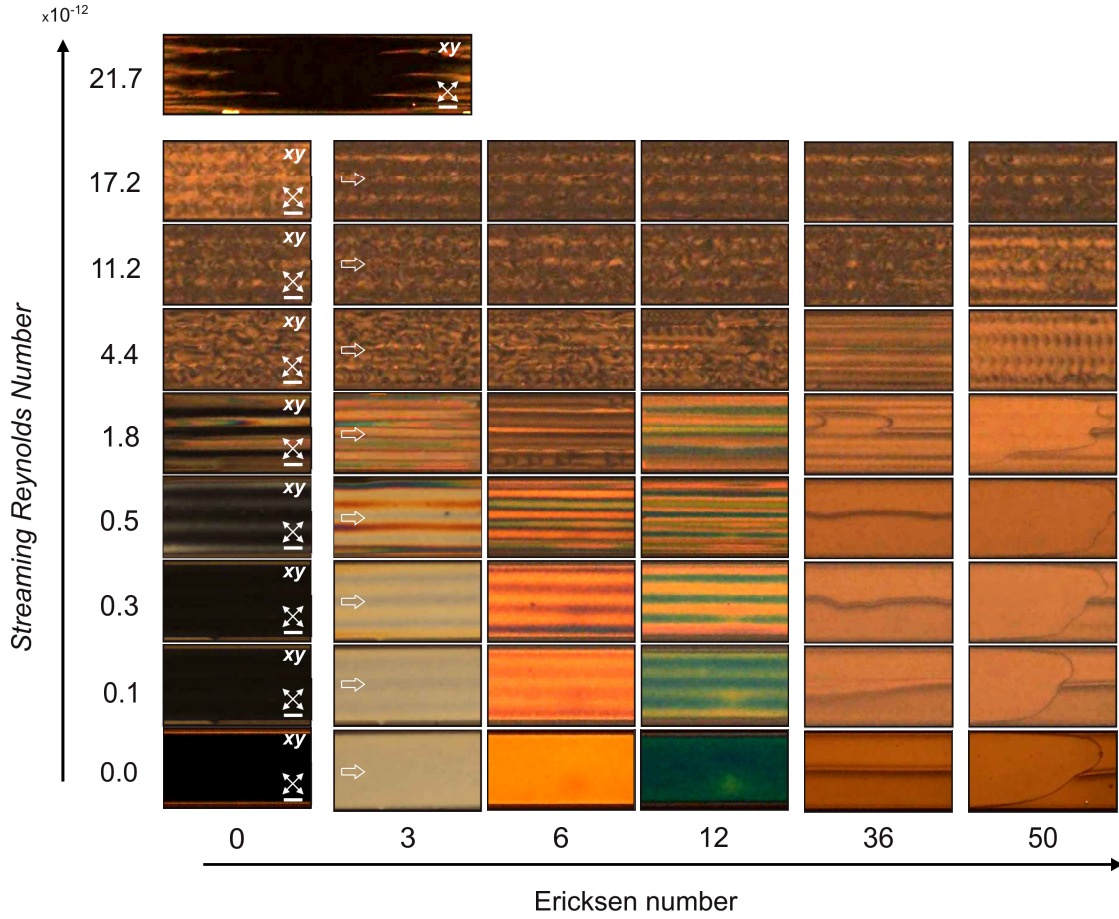
FIGURE 5.1: **Acoustically induced patterns in nematic flow.** Behavior of 5CB after applying SSAWs and a Poiseuille flow. Without acoustics, characteristic bowser, chiral and dowser states arise for $Er < 12$, $12 < Er < 50$, and $Er \geq 50$, respectively. In the bowser state, low acoustic intensities ($Rs < 1.8 \times 10^{-12}$) lead to characteristic colored stripe patterns. As the acoustic intensity is increased, the nematic transitions into a dynamic scattering regime. The orientation of the molecules induced by the flow dominates in chiral and dowser states, until the acoustic intensity is high enough ($Rs > 5.5 \times 10^{-12}$) to transition into the dynamic scattering regime. At $Rs > 1.7 \times 10^{-11}$ the nematic transitions into an isotropic phase regardless of nematic flow. White empty arrows indicate direction of pressure-driven nematic flow. White crossed double arrows show the orientation of the polarizers. Scale bars, 100 μm.

A phased diagram was constructed based on these observations, containing all the NLC patterns induced by combining an acoustic field and nematic flow (Fig. 5.2). The phase diagram shows three main areas of interest: The first area (B, C, and D on Fig. 5.2) corresponds to the section where the molecular orientation of the NLC is dominated by nematic flow. Here we have the characteristic bowser (B), chiral (C), and dowser states (D). The second area (T and TT on Fig. 5.2) exhibits a molecular orientation dominated by dynamic scattering and a turbulent-like flow driven by acoustic streaming flows. The third area (BAS, DAS, and CFS on Fig. 5.2) include the different phases with bands, where the molecular orientation is driven by a superposition between the tilting induced by the acoustic field in the vicinity of the pressure nodes and the bending of the director by the velocity field of the Poiseuille flow. Thus, we observe a combination of patterns between the acoustically-induced stripe patterns and the nematic flow-mediated bowser or chiral state. The area of birefringent acoustic stripes (BAS, on Fig. 5.2) shows an interesting optical response with high optical intensity.
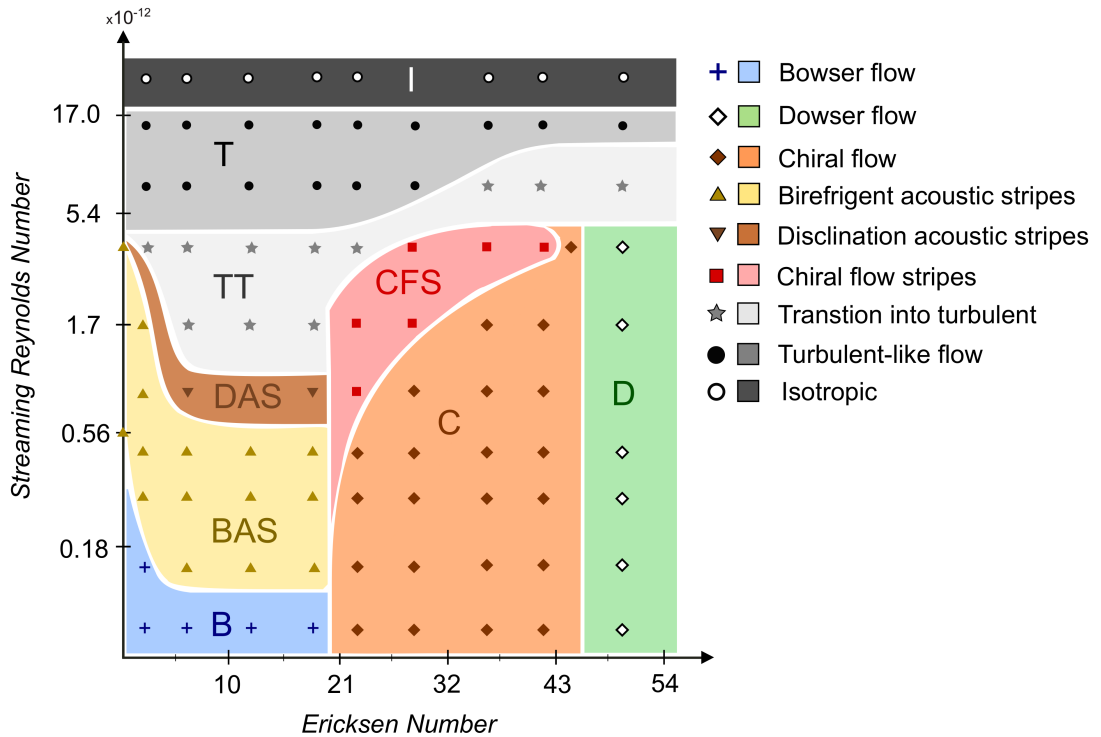
FIGURE 5.2: **Phase diagram of 5CB under SSAWs and fluid flow.**

We noted that in the BAS region the stripe patterns are visible at a lower intensity threshold. While for the stationary case (no Poiseuille flow) the thereshold was $P_{th} \approx 14$ mW or $R_s \approx 7.5 \times 10^{-13}$, the use of fluid flow into a B state lowered the treshold to observe acoustic stripes to $P_{th} \approx 2$ mW or $R_s \approx 1.2 \times 10^{-13}$.

In contrast to the BAS phase, the area of disclination acoustic stripes (DAS on Fig. 5.2) shows a similar stripe pattern where the disclination characteristic of the Brown lines appears (Fig. 4.2D), reducing the optical intensity observed in the channel. At Ericksen numbers close to the Bouser-chiral transition under medium-low intensity acoustic waves, we observed a small region where the stripes pattern appear with a flow orientation reminiscent to the chiral state in forming the chiral flow stripes region of the phase diagram (CFS on Fig. 5.2). Lastly, the differentiating factor between the transition into turbulent and the turbulent-like flow areas of the phase diagram (TT and T on Fig. 5.2) was the onset of stable birefringent lines at the pressure antinode, similar to those observed in the stationary case (see Fig 4.2H$-$I).

The superposed orientation effect observed in the BAS of phase diagram can be useful to modulate the orientation of the nematic, as one can tune independently the director field by controlling the intensity of the acoustic wave and the velocity of the Poiseuille flow. Consequently, we hypothesized that a precise spatio-temporal control of the nematic orientation can be achieved in this phase, where we can increase the tilting across the channel in the bands formed at the pressure nodes by increasing the SSAW input power while controlling the bending along the channel by changing the applied pressure for the Poiseuille flow. To inquire into these modulation capabilities, we studied the changes in optical intensity in the presence of absence of SSAWs for a constant flow rate. Here, we used the results obtain with flow only as a control to asses the advantages of the SSAW coupling in an acoustofluidic system. As shown in Fig.5.3, applying a nematic flow with Er = 2.5 generates a uniform increase in optical intensity within the channel in the absence of an acoustic field. For the same flow, application of an acoustic intensity corresponding to $Rs = 2.5 \times 10^{-13}$ induces optical intensity peaks on the pressure nodes (Fig.5.3A).
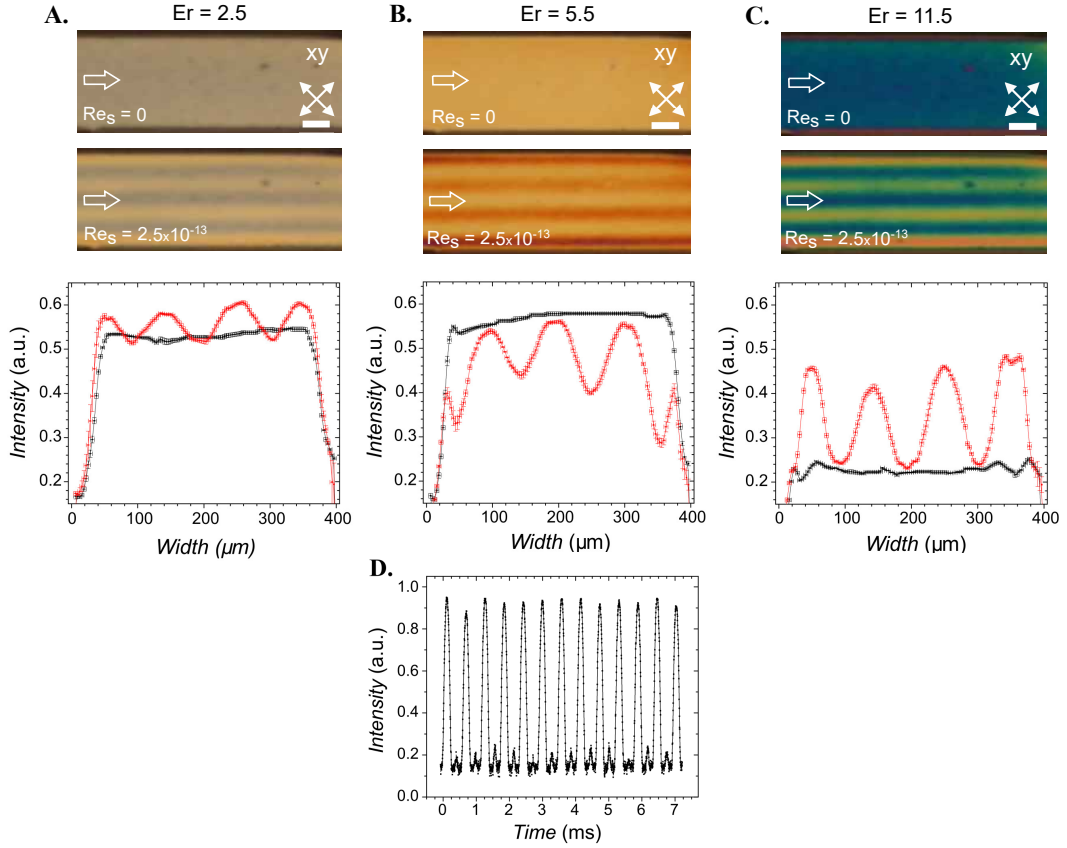
FIGURE 5.3: **Optical intensity of stripe patterns in a weak nematic flow**. **A**. Applying acoustic field with $Re_s = 2.5 \times 10^{-13}$ in a flowing bowser with $Er = 2.5$ leads to peaks of optical intensity in the vicinity of pressure nodes of SSAWs. **B**. The same acoustic field in higher nematic flow with $Er = 5.5$ shows peaks of optical intensity at SSAWs anti-nodes. **C**. Further increasing of flow velocity to Er = 11.5 switch peaks of optical intensity back to acoustic pressure nodes. Black lines in graphs represent optical response without acoustic ($Re_s = 0$) whereas red lines with acoustic ($Re_s = 2.5 \times 10^{-13}$). (D) Experiments show that sub-millisecond response time of acoustically induced stripe patterns can be obtained by the help of applying alternative flow between $-5.5 < Er < 5.5$. Scale bars, 100 μm

In contrast, increasing the flow to Er = 5.5 while maintaining the same acoustic intensity induced a shift in the spatial location of the peaks of optical intensity Fig.5.3B). Here, the peaks appear by the pressure anti-nodes along with a reduction in the maximum value of optical intensity compared with the base value obtained with flow only. An increase in flow to Er = 11.5 with the same acoustic intensity, shifts the location of the optical intensity peaks back to the pressure nodes Fig.5.3C. In this case, the optical intensity was significantly higher compared with the base value observed only with flow only. These results show the system's ability to generate and control patterns of light intensity by controlling the intensity of SSAWs and the flow rate in the channel.

135

In addition, POM experiments to quantify the response time of the LC to changes in flow rate showed submillisecond responses (Fig. 5.3D), indicating that the NLC can respond much faster changes induced by flow than changes induced by switching the SSAWs on and off (Fig. 4.4). These results indicate that the optofluidic response of NLC in the BAS phase allows for a precise spatial control of the location and intensity of the optical response. Given that changes in the flow allow for sub-millisecond transitions with peaks of intensity in different areas, we can also control the temporal response of the system. The remarkable response of our acoustofluidic system can thus be used to novel optofluidic applications of liquid crystals.

5.3 Numerical simulations of liquid crystal nematodynamics under acoustic fields

The increased tilting of the NLC molecules at the pressure nodes with increasing SAW intensity observed in Fig 4.5, 4.6, and 5.1 suggest that for the formation of the stripe patterns observed experimentally are arise as a consequency of tilting of the nematic director by the acoustic field. To support the validity of this mechanism, we performed numerical simulations that combine an acoustic field with the hydrodynamic evolution of confined NLC. To perform numerical calculations on the spatio-temporal evolution of the nematodynamics, we used a finite difference method solving simultaneously the Beris-Edwards equation and the momentum equation 1.27 employing a hybrid lattice Boltzmann method.

5.3.1 Nematodynamics and the Beris-Edwards equation

As discussed in Chapter 1, the degree of order and the local orientation of the liquid crystal can be characterized by a scalar order parameter S, a position dependent director $\mathbf{n}$, and a tensor order parameter $\mathbf{Q}$. The scalar order parameter assumes a small value for isotropic fluids, and adopts a value above 0.5 in a nematic system. From the molecular orientation one can define an orientation vector u and a system

director vector n by performing a local average over a specified number of molecules. Near a surface, the LCs can adopt a perpendicular(homeotropic) or parallel (planar) configuration, depending on the type of chemistry or topology of the confining walls. In the case of nematodynamics, the coupling of the orientational order parameter and the material flow can be described by models such as the Eriksen-Leslie-Parodi (ELP) model. however, A key drawback of this formulation arise when dealing with topological defects on the nematic, leading to complications for theoretical and numerical calculations. To circumvent such problem one can adopt a tensor order parameter representation. Here the tensor Q is defined by:

$$\mathbf{Q} = \int f\left(\mathbf{u}\right) \left(\mathbf{uu} - \frac{1}{3}\delta\right) d\mathbf{u} \tag{5.1}$$

where δ represents a 3x3 identity matrix, $\mathbf{u}$ a unit vector describing molecular orientations, and $f(\mathbf{u})$ describe the orientation distribution function. Thus, Q represents a coarse-grained average over the distribution of orientations. By definition, Q is traceless and can be diagonalized in terms of eigenvalues related to the scalar S and biaxiality order parameters. For a uniaxial system $\mathbf{Q}$ becomes

$$\mathbf{Q} = S_{bulk}\left(\mathbf{nn} - \frac{1}{3}\delta\right) \tag{5.2}$$

In addition, we have stablished that the free energy of the nematic is defined by the Landau - d Gennes free energy,

$$f_{LdG} = f_{phase} + f_E + f_F + f_{Sup} \tag{5.3}$$

Where the short-range internal energy f_{phase} is defined by equation 1.17, the elastic energy f_E derived from the Frank-Oseen model is defined by equation 1.18, and the surface anchoring contribution f_{sup} is defined by the Rapini-Papoular equation 1.22. For the case of acoustofluidics, the external field contribution f_F is included adding

the contribution of the acoustic field derived from the Selinger model [263],

$$f_F = f_{Ac} = \left(\frac{u_2 \rho_0 k^2}{\nu^3} \right) I cos^2 \left(2\pi x / L_x \right) \mathbf{k} \cdot \mathbf{Q} \cdot \mathbf{k} \tag{5.4}$$

Where I represent the acoustic intensity of the wave, $\mathbf{k}$ is the wave vector of the leaking Surface acoustic wave and u_2 is coefficients representing the strength of one of the couplings between the director and density gradients. If we adopt the one-elastic-constant approximation, the elastic free energy takes the form:

$$f_E = \frac{L_1}{2} \left(\nabla \mathbf{Q} \right)^2 \tag{5.5}$$

Thus, the total free energy of a uniaxial nematic in confinement exposed to acoustic waves is defined as

$$F = \int_\Omega \left(f_{phase} + f_E + f_{Ac} \right) d\Omega + \int_{\delta\Omega} f_{sup} dS \tag{5.6}$$

Following the Beris-Edwards model [296], the relaxation of the tensor order parameter $\mathbf{Q}$ with velocity $\mathbf{v}$ of a nematic with free energy F is defined as

$$\left(\partial_t + \mathbf{v} \cdot \nabla \right) \mathbf{Q} - \mathbf{S} \left(\nabla \mathbf{v}, \mathbf{Q} \right) = \Gamma \mathbf{H} \tag{5.7}$$

Where Γ is the collective rotational-diffusion constant, $\mathbf{W} = (1/2) \left(\nabla \mathbf{v} - \nabla \mathbf{v}^T \right)$ is the anti-symmetric part of the velocity gradient (the vorticity tensor), and $\mathbf{D} = (1/2) \left(\nabla \mathbf{v} + \nabla \mathbf{v}^T \right)$ is the symmetric part of the velocity gradient (deformation tensor). $S \left(\Omega, \mathbf{Q} \right)$ is defined as

$$S \left(\nabla \mathbf{v}, \mathbf{Q} \right) = \left(\xi \mathbf{W} + \mathbf{D} \right) \left(\mathbf{Q} + \frac{1}{3} \mathbf{I} \right) + \left(\mathbf{Q} + \frac{1}{3} \mathbf{I} \right) \left(\xi \mathbf{W} - \mathbf{D} \right) - 2\xi \left(\mathbf{Q} + \frac{1}{3} \mathbf{I} \right) Tr \left(\mathbf{Q} \nabla \mathbf{v} \right) \tag{5.8}$$

The term $\mathbf{H}$ in the Beris-Edwards equation 5.7 is the free energy gradient in $\mathbf{Q}$,

which is defined according to the free energy functional,

$$\mathbf{H} = \left[\frac{\delta F}{\delta \mathbf{Q}}\right]^{ST} = -\frac{\delta F}{\delta Q} + \left(\frac{1}{3}\mathbf{I}\right) Tr \frac{\delta F}{\delta Q} \tag{5.9}$$

The velocity field must also satisfy the continuity equation and the generalized Navier-Stokes equation for the nematic :

$$\rho \left(\frac{\partial}{\partial t} + \mathbf{v} \cdot \nabla\right) \mathbf{v} = \nabla \cdot \Pi - \nu \mathbf{v} \tag{5.10}$$

Where the asymmetric stress tensor Π takes the form

$$\begin{aligned}
\Pi = \;& 2\eta \mathbf{W} - P_0 \mathbf{I} + 2\xi \left(\mathbf{Q} + \frac{1}{3}\mathbf{I}\right) (\mathbf{Q} : \mathbf{H}) - \xi \mathbf{H} \cdot \left(\mathbf{Q} + \frac{1}{3}\mathbf{I}\right) \\
& - \xi \left(\mathbf{Q} + \frac{1}{3}\mathbf{I}\right) \cdot \mathbf{H} - \nabla \mathbf{Q} : \frac{\delta F}{\delta \nabla \mathbf{Q}} + \mathbf{Q} \cdot \mathbf{H} - \mathbf{H} \cdot \mathbf{Q}
\end{aligned} \tag{5.11}$$

Where the hydrostatic pressure P_0 is taken to be

$$P_0 = \rho T - \frac{1}{2}\kappa \left(\nabla \mathbf{Q}\right)^2 \tag{5.12}$$

5.3.2   Lattice Boltzmann algorithm for liquid crystal hydrodynamics

lattice Boltzmann algorithms describing the Navier–Stokes equations of a simple fluid are defined in terms of a single set of partial distribution functions, the scalars $f_i(\mathbf{x})$, which sum on each lattice site $\mathbf{x}$ to give the density[297]. For liquid-crystal hydrodynamics this must be supplemented by a second set, the symmetric traceless tensors $\mathbf{G}_i(\mathbf{x})$, which are related to the tensor order parameter $\mathbf{Q}$.

Each f_i, $\mathbf{G}_i$, is associated with a lattice vector $\mathbf{e}_i$. We choose a 15-velocity model on the cubic lattice (D3Q15) with lattice vectors:

$$\mathbf{e}_i^{(0)} = (0, 0, 0) \tag{5.13}$$
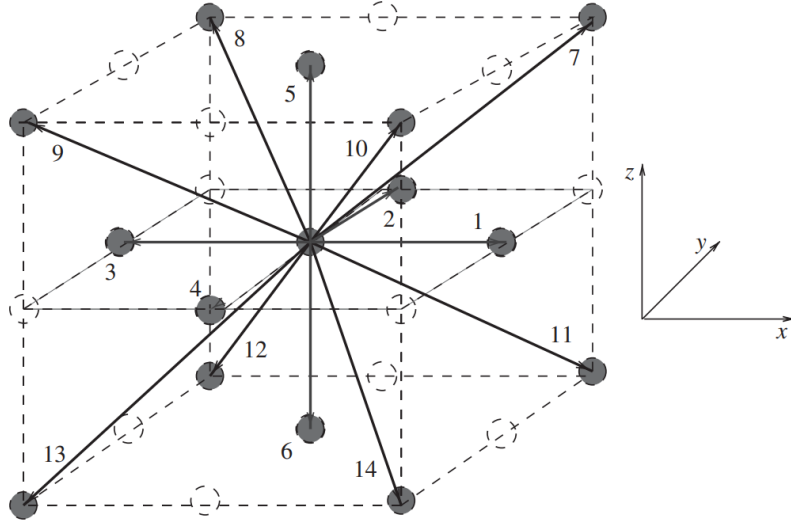
FIGURE 5.4: **Lattice geometry for three-dimensional lattice Boltzmann model**.
Schematic showing the location of the lattice nodes defining the vectors $\mathbf{e}_i^{(0)}$, $\mathbf{e}_i^{(1)}$ and
$\mathbf{e}_i^{(2)}$.

$$\mathbf{e}_i^{(1)} = (\pm 1, 0, 0), (0, \pm 1, 0), (0, 0, \pm 1), \tag{5.14}$$

$$\mathbf{e}_i^{(2)} = (\pm 1, \pm 1, \pm 1) \tag{5.15}$$

Here, the indices i are ordered so that $i = 0$ corresponds to $\mathbf{e}_i^{(0)}$, $i = 1, ..., 6$ corresponds to the $\mathbf{e}_i^{(1)}$ set and $i = 7, .., 14$ to the $\mathbf{e}_i^{(2)}$ set, as illustrated in Fig. 5.4. The physical variables are discretized as moments of the distribution function:

$$\rho = \sum_i f_i \qquad \rho v_\alpha = \sum_i f_i e_{i\alpha} \qquad \mathbf{Q} = \sum_i \mathbf{G}_i \tag{5.16}$$

Using finite differences, the distribution function evolve in a time-step Δt as,

$$f_i(\mathbf{x} + \mathbf{e}_i \Delta t, t + \Delta t) - f_i(\mathbf{x}, t) = \tag{5.17}$$
$$\frac{1}{2} \Delta t \left[C_{fi}(\mathbf{x}, t, \{f_i\}) + C_{fi}(\mathbf{x} + \mathbf{e}_i \Delta t, t + \Delta t, \{f_i^*\}) \right]$$

140

$$\mathbf{G}_i \left(\mathbf{x} + \mathbf{e}_i \Delta t, t + \Delta t \right) - \mathbf{G}_i \left(\mathbf{x}, t \right) =$$
$$\frac{1}{2} \Delta t \left[C_{\mathbf{G}i} \left(\mathbf{x}, t, \{ \mathbf{G}_i \} \right) + C_{\mathbf{G}i} \left(\mathbf{x} + \mathbf{e}_i \Delta t, t + \Delta t, \{ \mathbf{G}_i^* \} \right) \right] \tag{5.18}$$

Which represents free motion with velocity $\mathbf{e}_i$ followed by a collision step, which allows the distribution to relax towards equilibrium. f_i^* and $\mathbf{G}_i^*$ are first order approximations to $f_i \left(\mathbf{x} + \mathbf{e}_i \Delta t, t + \Delta t \right)$ and $\mathbf{G}_i \left(\mathbf{x} + \mathbf{e}_i \Delta t, t + \Delta t \right)$, respectively. Discretizing in this way has the advantage that the lattice viscosity terms are eliminated to second order and that the stability of the algorithm is improved. The collision operators have the form of a single relaxation time Boltzmann equation with a forcing term

$$C_{fi} \left(\mathbf{x}, t, \{ f_i \} \right) = -\frac{1}{\tau_f} \left(f_i \left(\mathbf{x}, t \right) - f_i^{eq} \left(\mathbf{x}, t, \{ f_i \} \right) + p_i \left(\mathbf{x}, t, \{ f_i \} \right) \right) \tag{5.19}$$

$$C_{\mathbf{G}i} \left(\mathbf{x}, t, \{ \mathbf{G}_i \} \right) = -\frac{1}{\tau_{\mathbf{G}}} \left(\mathbf{G}_i \left(\mathbf{x}, t \right) - \mathbf{G}_i^{eq} \left(\mathbf{x}, t, \{ \mathbf{G}_i \} \right) + \mathbf{M}_i \left(\mathbf{x}, t, \{ \mathbf{G}_i \} \right) \right) \tag{5.20}$$

Where f_i^{eq} and $\mathbf{G}_i^{eq}$ are the equilibrium distributions and the driving terms p_i and M_i are selected based on the form of the equations of motion and thermodynamic equilibrium:

$$\sum_i p_i = 0 \qquad \sum_i p_i e_{i\alpha} = \partial_\beta \tau_{\alpha\beta}, \qquad \sum_i p_i e_{i\alpha} e_{i\beta} = 0 \tag{5.21}$$

$$\sum_i \mathbf{M}_i = \Gamma \mathbf{H} \left(\mathbf{Q} \right) + \mathbf{S} \left(\nabla \mathbf{v}, \mathbf{Q} \right) \equiv \mathbf{H} \tag{5.22}$$

$$\sum_i \mathbf{M}_i e_{i\alpha} = \left(\sum_i \mathbf{M}_i \right) v_\alpha \tag{5.23}$$

In this model, the moments of p_i impose the antisymmetric part of the stress tensor, while the evolution of the order parameter ensures that the fluid minimizes its free energy at equilibrium.

The numerical implementation of the Lattice Boltzmann method uses the parameters chosen for an approximation of 5CB with the coherence length ξ_N as the unit length.As we are considering the one-elastic-constant approximation, we selected $L = 0.1$ with the LdG parameters $A = 0.1$ and $U = 3.0$. The rotational viscosity constant used was $\Gamma = 0.133775$. We selected the strength of homeotropic anchoring to be $W_H = 0.1$. In our algorithm, the intensity of the acoustic field was selected in the range between $0.000 < I < 0.020$. We implemented periodic boundaries condition the on x-axis, and the number of simulated nodes in the grid was $N_x = 120$, $N_y = 200$, and $N_z = 40$.

5.3.3   Numerical prediction of acoustically-induced nematic reorientation

Using the Latice Boltzmann method to solve the nematodynamics problem under affected by an acoustic field, as described above, we performed a set of simulations to validate our experimental observations. From the numerical solution obtained we extracted the director field and velocity profile at equilibrium, which we used to predict the POM image resulting from exposing the NLC with the resolved director field to a light source passing through the sample and cross-polarizers. For a system without Poiseuille flow, the simulations show a stripe pattern in the predicted POM (Fig. 5.5A) that arise as a consequence of the periodic distribution of the order parameter across the channel imposed by the periodicity of the acoustic wave, and balance between the elastic forces of NLC and acoustic forces. The predicted POM is in good agreement with the white stripe pattern observed in Fig 4.2B. We obtain an increase in the values of the scalar order parameter S in the vicinity of the wave pressure nodes, indicating a tilting in the director in this area (Fig. 5.5B). The simulations are also able to capture the onset of acoustic streaming flows although with small magnitudes for the streaming velocity (Fig. 5.5C).Importantly, these flows have been theorized as driving phenomenon for the alignment of molecules under SSAWs [263]. We hypothesize Based on these results that the stripe patterns become unstable and collapse into a turbulent-like flow behavior once the acoustic forces and the acoustic streaming dominate over the elastic forces. While numerical predictions support experimental

observation in the case of low acoustic intensity, high acoustic intensity dynamics are beyond the limitations and assumptions of our model.
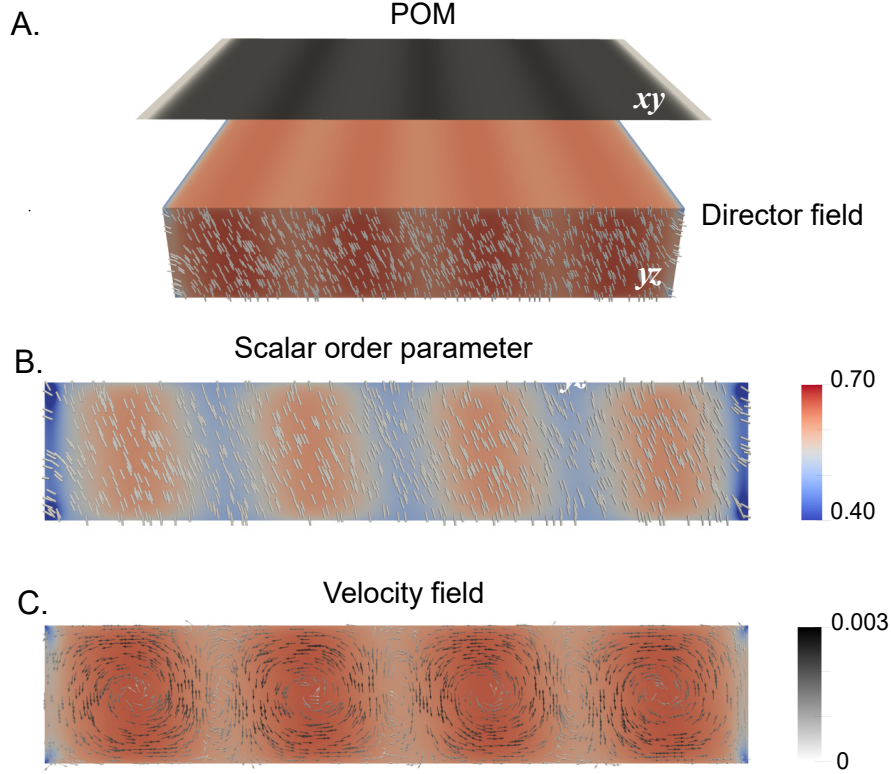
FIGURE 5.5: **Numerical simulations of molecular reorientation of NLCs induced by SSAWs**. **A**. POM image of stripe patterns with the corresponding director field orientation predicted by numerical simulations. **B**. Spatial distribution of the scalar order parameter predicted by numerical simulations. Pressure nodes tilt the molecules which results in a periodic distribution of the order parameter across the channel. **C**. Numerically predicted acoustic streaming flow around the pressure nodes.

5.3.4 Nematodynamics under acoustic fields and Bouser flow

Numerical simulations were performed to complement the experimental observations presented in Fig 5.1. As before, the spatio−temporal evolution of the nematodynamics was solved employing a hybrid lattice Boltzmann method, solving simultaneously the Beris-Edwards equation 5.7 and the momentum equation 5.10, with the inclusion of a Poiseuille pressure flow in the x direction. Here we begin by imposing the pressure-driven velocity flow until we reach a system in equilibrium. Then, we apply the acoustic wave contribution to the free-energy functional and minimize the free energy solving our system of equations. These calculations revealed how the initial orientation of

the director field imposed by the bowser state change once exposed to the external acoustic field (Fig. 5.6). In a bowser state with $Er = 0.05$ without an acoustic field (Fig. 5.6A), the uniform homeotropic director becomes only slightly bowed toward the flow direction. Applying a low intensity acoustic field in the presence of fluid flow promotes the tilting of the molecules across the channel in the vicinity of the acoustic pressure nodes (Fig. 5.6B), consistent with the experimental observations in (Fig. 5.1).
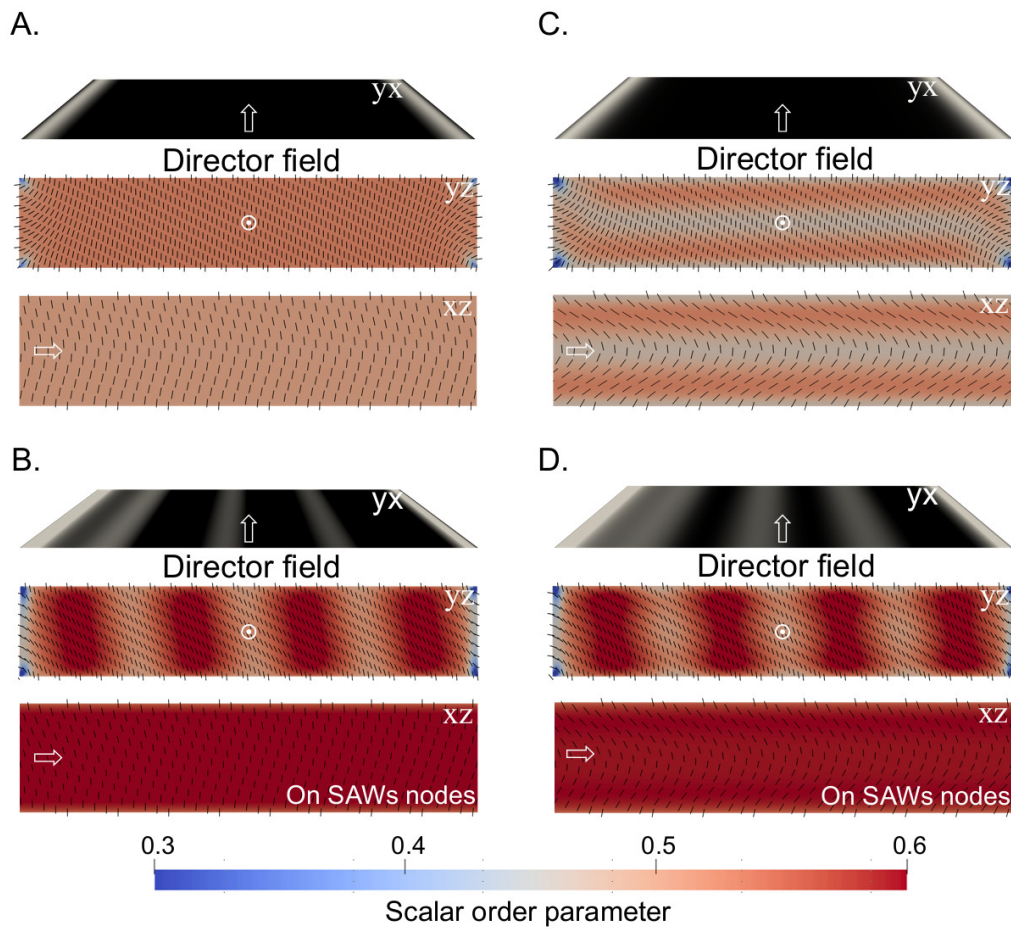
FIGURE 5.6: **Numerical prediction of acoustically induced patterns in weak nematic flow**. Numerical prediction of POM and director field reorientation. **A.** Bowser state with $Er = 0.05$ slightly bowed the director field toward the flow direction (x-axis). **B.** In the vicinity of acoustic pressure nodes, applying an acoustic field in a bowser state with $Er = 0.05$ promotes tilting the director across the channel and decreasing its bowed shape along the flow direction. **C.** Bowser state with $Er = 0.65$ bowed the director toward the flow direction. **D.** Applying an acoustic field in a nematic flow with $Er = 0.65$ promotes tilting of the director across the channel and decreases its bowed shape along the flow direction in the vicinity of acoustic pressure nodes. White empty arrows and circles indicate direction of pressure-driven nematic flow.

An increment of the flow rate to Er = 0.65 increases the bowing of the director toward the direction of flow in the absence of an acoustic field (Fig. 5.6C). The application of acoustic waves for this flow also results in tilting of the molecules across the channel in the vicinity of the acoustic pressure nodes which can be seen as stripe patterns in the predicted cross-polarized image (Fig. 5.6D).

From this simulations we performed a quantification of the orientation changes across (angle θ) and along (angle ϕ) the channel induced by the acoustic field under a weak flow (Fig. 5.7). This analysis was performed on the pressure nodes area at $z/h = 1/6$, where the bowing induced by the fluid flow is most pronounced (xz plane, Fig 5.6). I increments in the acoustic intensity increase the tilting of molecules across the channel as the acoustic forces overcome the elastic forces, reaching a plateau around the Rayleigh angle $\theta_r = sin^{(-1)}(v_{LC}/v_s) \approx 23°$ (Fig 5.7A). Here, $v_{LC} \approx 1500 m/s$ and $v_s \approx 3900 m/s$ is the speed of sound in 5CB and Lithium Niobate, respectively. The tilting of the nematic across the channel was not significantly affected by increasing the fluid flow, with small variations at $Er = 0.65$ that suggest a small decrease in the tilting of the molecules across the channel in the vicinity of the pressure nodes when increasing the intensity of the flow field. As seen in Fig 5.7B, an increase in flow velocity bowed the director along the channel increasing the angle ϕ. In addition, increments in the acoustic intensity reduce the values of ϕ, competing with the reorientation of the director field in the direction of the flow. Similar behaviors regarding angles θ and ϕ are observed on the pressure nodes area at $z/h = 1/2$ (Fig. 5.7C−D).

Althogether, the results from this simulations show that the reorientation effect of across the channel due to the applied SSAW do not disrupt the reorientation effect along the channel induced by the Poiseuille flow. For low-intensity surface acoustic waves both mechanism are present and superposed which is in good agreement with the experimental observations from Fig. 5.1 and Fig. 5.2. Moreover this indicate that the use of the Lattice Boltzmann model to solve the Beris-Edwards and Navier stokes equations couple with Selinger's model for the acoustic field free energy can be used as a powerful tool to describe the nematodynamics in acoustofluidic systems.
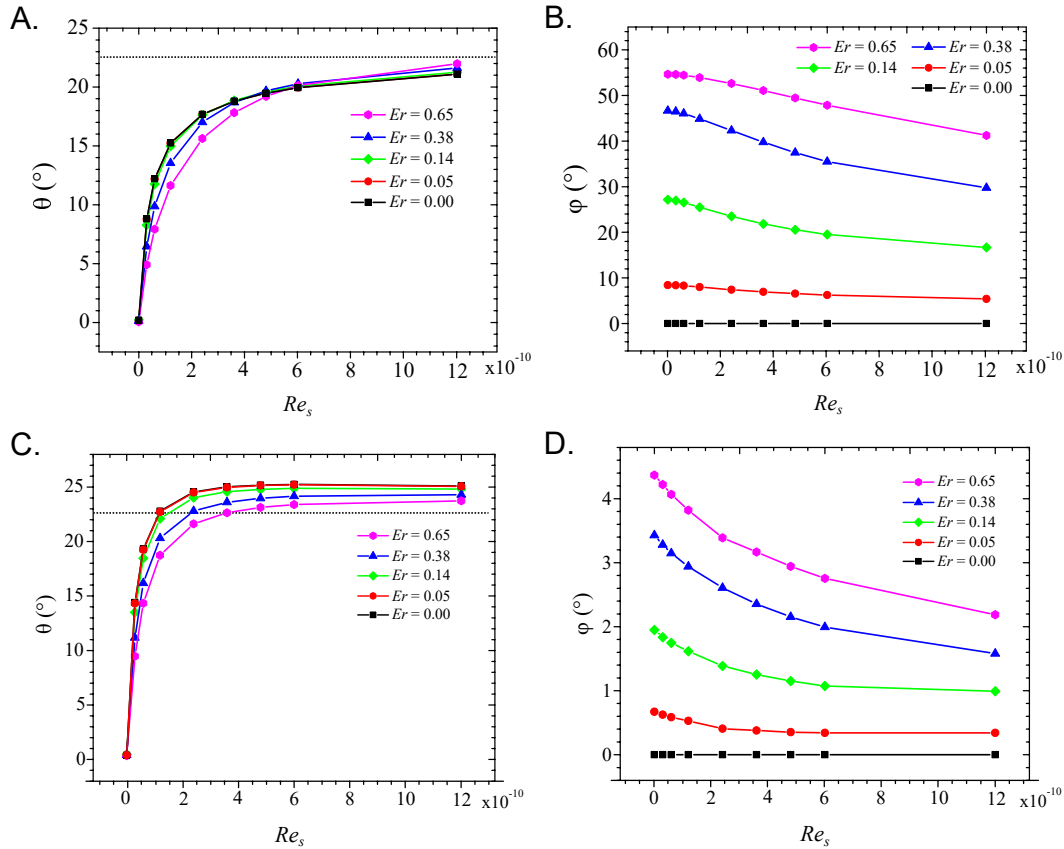
FIGURE 5.7: **Quantification of changes in molecules angle at acoustic pressure nodes across (angle θ) and along (angle ϕ) the channel.** Under an acoustic field and weak pressure-driven flow, simulations predict changes in orientation of NLC molecules. **A**. Angle θ of tilted nematic molecules across the channel on the acoustic pressure nodes at $z/h = 1/6$. Molecules tilt more at a higher acoustic intensity and less at the same acoustic intensity with a higher nematic flow. The dotted line indicates the Rayleigh angle of incidence. **B**. Angle ϕ of tilted nematic molecules along the channel measured on acoustic pressure nodes at $z/h = 1/6$. Stronger flow bowed the molecules more along the channel whereas higher acoustic intensity decreases the bowed shape. Numerical analysis is done in the weak flow regime with Er between 0 and 0.65. **C**. Molecules across the channel tilt more at a higher acoustic intensity and less at the same acoustic intensity with a higher nematic flow. $z/h = 1/2$. **D**. Stronger flow bowed the molecules more along the channel whereas higher acoustic intensity decreases the bowed shape at $z/h = 1/2$. Numerical analysis is done in the weak flow regime with Er between 0 and 0.65. Note that the scale in simulations is orders of magnitude smaller than that in experiments. Note that the acoustic intensity is proportional to Rs.

5.4   conclusion

The implementation of NLCs materials for new optofluidic technologies shows promise for accurate spatio-temporal control of the material optical properties on small spatial scales, integrating microfluidics, electronics, and materials science [273]. The field of LC optofluidics is in its infancy, but initial findings have shown remarkable progress in increasing the response speed by orders of magnitude compared with traditional LC display technologies [279]. The incorporation of strategies for reliable control of small flow using well-stablished microfluidic techniques and the reliance on nanofabrication techniques is advantageous for 3D integration, automation, and rapid prototyping of optofluidics, thus increasing the attractiveness of NLCs optofluidic devices for commercial applications.

Modulation of the SAWs and fluid flow allows for sub-millisecond on/off states of brightness that can cover the entire channel or can be localized electronically in narrow bands located in the corresponding pressure nodes of the acoustic waves. In addition, increased complexity of the IDTs (i.e. including chirping, grating, focusing or slanting structures) has the potential to affect dramatically the control over the shape, location, and frequency of the SAW. Furthermore, acoustic optofluidic devices could be coupled with orthogonal electric fields to further increase the control over the molecular re-orientation within the LC. Altogether, our observations point towards an unexplored research field where different combinations between orthogonal fields in confined microchannels can exhibit novel optical, rheological and hydrodynamic behaviors when interacting with pure or complex mixtures of liquid crystals. Caution must be taken to avoid overheating the system when implementing SAWs, but the experimental results point towards operating conditions in the birefringent acoustic-induced stripes area where the temperature effect is low. The molecular re-orientation achieved under the influence of acoustic and fluid flow fields could also be used to perform chemical reactions in specific domains within the microfluidic channels, sequestering components based on orientational or dielectric affinity.

BIBLIOGRAPHY

[1] S. A. M. Ealia and M. Saravanakumar, "A review on the classification, characterisation, synthesis of nanoparticles and their application," in *IOP conference series: materials science and engineering*, vol. 263, p. 032019, IOP Publishing.

[2] S. Machado, J. Pacheco, H. Nouws, J. T. Albergaria, and C. Delerue-Matos, "Characterization of green zero-valent iron nanoparticles produced with tree leaf extracts," *Science of the total environment*, vol. 533, pp. 76–81, 2015.

[3] J. H. Swisher, L. Jibril, S. H. Petrosko, and C. A. Mirkin, "Nanoreactors for particle synthesis," *Nature Reviews Materials*, vol. 7, no. 6, pp. 428–448, 2022.

[4] R. M. Williams, S. Chen, R. E. Langenbacher, T. V. Galassi, J. D. Harvey, P. V. Jena, J. Budhathoki-Uprety, M. Luo, and D. A. Heller, "Harnessing nanotechnology to expand the toolbox of chemical biology," *Nature chemical biology*, vol. 17, no. 2, pp. 129–137, 2021.

[5] L. Liu and A. Corma, "Metal catalysts for heterogeneous catalysis: from single atoms to nanoclusters and nanoparticles," *Chemical reviews*, vol. 118, no. 10, pp. 4981–5079, 2018.

[6] M. E. Davis, Z. Chen, and D. M. Shin, "Nanoparticle therapeutics: an emerging treatment modality for cancer," *Nanoscience and technology: A collection of reviews from nature journals*, pp. 239–250, 2010.

[7] J. Liu, H. He, D. Xiao, S. Yin, W. Ji, S. Jiang, D. Luo, B. Wang, and Y. Liu,

"Recent advances of plasmonic nanoparticles and their applications," *Materials*, vol. 11, no. 10, p. 1833, 2018.

[8] W. J. Stark, P. R. Stoessel, W. Wohlleben, and A. Hafner, "Industrial applications of nanoparticles," *Chemical Society Reviews*, vol. 44, no. 16, pp. 5793–5805, 2015.

[9] Z. Nie, A. Petukhova, and E. Kumacheva, "Properties and emerging applications of self-assembled structures made from inorganic nanoparticles," *Nature nanotechnology*, vol. 5, no. 1, pp. 15–25, 2010.

[10] R. J. White, R. Luque, V. L. Budarin, J. H. Clark, and D. J. Macquarrie, "Supported metal nanoparticles on porous materials. methods and applications," *Chemical Society Reviews*, vol. 38, no. 2, pp. 481–494, 2009.

[11] S. E. Pratsinis, "Flame aerosol synthesis of ceramic powders," *Progress in Energy and Combustion Science*, vol. 24, no. 3, pp. 197–219, 1998.

[12] J. P. Rao and K. E. Geckeler, "Polymer nanoparticles: Preparation techniques and size-control parameters," *Progress in polymer science*, vol. 36, no. 7, pp. 887–913, 2011.

[13] M. J. Mitchell, M. M. Billingsley, R. M. Haley, M. E. Wechsler, N. A. Peppas, and R. Langer, "Engineering precision nanoparticles for drug delivery," *Nature Reviews Drug Discovery*, vol. 20, no. 2, pp. 101–124, 2021.

[14] M. Salavati-Niasari, F. Davar, and N. Mir, "Synthesis and characterization of metallic copper nanoparticles via thermal decomposition," *Polyhedron*, vol. 27, no. 17, pp. 3514–3518, 2008.

[15] M. Aliofkhazraei, *Handbook of nanoparticles*. Springer, 2016.

[16] M. F. Bertino, "Introduction to nanotechnology," 2022.

[17] C. Y. Tai, C.-T. Tai, M.-H. Chang, and H.-S. Liu, "Synthesis of magnesium hydroxide and oxide nanoparticles using a spinning disk reactor," *Industrial and engineering chemistry research*, vol. 46, no. 17, pp. 5536–5541, 2007.

[18] A. Courty, A. Mermet, P. Albouy, E. Duval, and M. Pileni, "Vibrational coherence of self-organized silver nanocrystals in fcc supra-crystals," *Nature materials*, vol. 4, no. 5, pp. 395–398, 2005.

[19] A. Tao, P. Sinsermsuksakul, and P. Yang, "Tunable plasmonic lattices of silver nanocrystals," *Nature nanotechnology*, vol. 2, no. 7, pp. 435–440, 2007.

[20] A. P. Alivisatos, "Semiconductor clusters, nanocrystals, and quantum dots," *science*, vol. 271, no. 5251, pp. 933–937, 1996.

[21] S. Mann, S. L. Burkett, S. A. Davis, C. E. Fowler, N. H. Mendelson, S. D. Sims, D. Walsh, and N. T. Whilton, "Sol-gel synthesis of organized matter," *Chemistry of materials*, vol. 9, no. 11, pp. 2300–2310, 1997.

[22] S. Ramesh, "Sol-gel synthesis and characterization of ag," 2013.

[23] S. Bhaviripudi, E. Mile, S. A. Steiner, A. T. Zare, M. S. Dresselhaus, A. M. Belcher, and J. Kong, "Cvd synthesis of single-walled carbon nanotubes from gold nanoparticle catalysts," *Journal of the American Chemical Society*, vol. 129, no. 6, pp. 1516–1517, 2007.

[24] M. Adachi, S. Tsukui, and K. Okuyama, "Nanoparticle synthesis by ionizing source gas in chemical vapor deposition," *Japanese journal of applied physics*, vol. 42, no. 1A, p. L77, 2003.

[25] S. Mohammadi, A. Harvey, and K. V. Boodhoo, "Synthesis of tio2 nanoparticles in a spinning disc reactor," *Chemical Engineering Journal*, vol. 258, pp. 171–184, 2014.

[26] H. K. Kammler, L. Mädler, and S. E. Pratsinis, "Flame synthesis of nanoparticles," *Chemical Engineering and Technology: Industrial Chemistry-Plant Equipment-Process Engineering-Biotechnology*, vol. 24, no. 6, pp. 583–596, 2001.

[27] S. Hasan, "A review on nanoparticles: their synthesis and types," *Res. J. Recent Sci*, vol. 2277, p. 2502, 2015.

[28] P. Kuppusamy, M. M. Yusoff, G. P. Maniam, and N. Govindan, "Biosynthesis of metallic nanoparticles using plant derivatives and their new avenues in pharmacological applications–an updated report," *Saudi Pharmaceutical Journal*, vol. 24, no. 4, pp. 473–484, 2016.

[29] Q. Jiang and M. D. Ward, "Crystallization under nanoscale confinement," *Chemical Society Reviews*, vol. 43, no. 7, pp. 2066–2079, 2014.

[30] S. H. Petrosko, R. Johnson, H. White, and C. A. Mirkin, "Nanoreactors: small spaces, big implications in chemistry," 2016.

[31] N. T. Thanh, N. Maclean, and S. Mahiddine, "Mechanisms of nucleation and growth of nanoparticles in solution," *Chemical reviews*, vol. 114, no. 15, pp. 7610–7630, 2014.

[32] M. R. Jones, K. D. Osberg, R. J. Macfarlane, M. R. Langille, and C. A. Mirkin, "Templated techniques for the synthesis and assembly of plasmonic nanostructures," *Chemical reviews*, vol. 111, no. 6, pp. 3736–3827, 2011.

[33] K. A. Brown, J. L. Hedrick, D. J. Eichelsdoerfer, and C. A. Mirkin, "Nanocombinatorics with cantilever-free scanning probe arrays," *ACS nano*, vol. 13, no. 1, pp. 8–17, 2018.

[34] Y. Kang, K. J. Erickson, and T. A. Taton, "Plasmonic nanoparticle chains via a morphological, sphere-to-string transition," *Journal of the American Chemical Society*, vol. 127, no. 40, pp. 13800–13801, 2005.

[35] Z. Nie, D. Fava, E. Kumacheva, S. Zou, G. C. Walker, and M. Rubinstein, "Self-assembly of metal–polymer analogues of amphiphilic triblock copolymers," *Nature materials*, vol. 6, no. 8, pp. 609–614, 2007.

[36] Z. Tang, Z. Zhang, Y. Wang, S. C. Glotzer, and N. A. Kotov, "Self-assembly of cdte nanocrystals into free-floating sheets," *Science*, vol. 314, no. 5797, pp. 274–278, 2006.

[37] M. S. Nikolic, C. Olsson, A. Salcher, A. Kornowski, A. Rank, R. Schubert, A. Frömsdorf, H. Weller, and S. Förster, "Micelle and vesicle formation of amphiphilic nanoparticles," *Angewandte Chemie*, vol. 121, no. 15, pp. 2790–2792, 2009.

[38] S. Y. Park, A. K. Lytton-Jean, B. Lee, S. Weigand, G. C. Schatz, and C. A. Mirkin, *DNA-programmable nanoparticle crystallization*, pp. 515–525. Jenny Stanford Publishing, 2020.

[39] J. Sharma, R. Chhabra, A. Cheng, J. Brownell, Y. Liu, and H. Yan, "Control of self-assembly of dna tubules through integration of gold nanoparticles," *Science*, vol. 323, no. 5910, pp. 112–116, 2009.

[40] C.-C. Liu, A. Ramírez-Hernández, E. Han, G. S. Craig, Y. Tada, H. Yoshida, H. Kang, S. Ji, P. Gopalan, and J. J. De Pablo, "Chemical patterns for directed self-assembly of lamellae-forming block copolymers with density multiplication of features," *Macromolecules*, vol. 46, no. 4, pp. 1415–1424, 2013.

[41] M. P. Stoykovich, H. Kang, K. C. Daoulas, G. Liu, C.-C. Liu, J. J. de Pablo, M. Müller, and P. F. Nealey, "Directed self-assembly of block copolymers for nanolithography: fabrication of isolated features and essential integrated circuit geometries," *Acs Nano*, vol. 1, no. 3, pp. 168–175, 2007.

[42] M. A. Correa-Duarte, J. Pérez-Juste, A. Sánchez-Iglesias, M. Giersig, and L. M. Liz-Marzán, "Aligning au nanorods by using carbon nanotubes as templates," *Angewandte Chemie International Edition*, vol. 44, no. 28, pp. 4375–4378, 2005.

[43] H. Wang, W. Lin, K. P. Fritz, G. D. Scholes, M. A. Winnik, and I. Manners, "Cylindrical block co-micelles with spatially selective functionalization by nanoparticles," *Journal of the American Chemical Society*, vol. 129, no. 43, pp. 12924–12925, 2007.

[44] E. Dujardin, C. Peet, G. Stubbs, J. N. Culver, and S. Mann, "Organization of metallic nanoparticles using tobacco mosaic virus templates," *Nano Letters*, vol. 3, no. 3, pp. 413–417, 2003.

[45] F. A. Aldaye, A. L. Palmer, and H. F. Sleiman, "Assembling materials with dna as the guide," *science*, vol. 321, no. 5897, pp. 1795–1799, 2008.

[46] Z. Tang and N. A. Kotov, "One-dimensional assemblies of nanoparticles: preparation, properties, and promise," *Advanced Materials*, vol. 17, no. 8, pp. 951–962, 2005.

[47] J. S. Benjamin, "Mechanical alloying—a perspective," *Metal powder report*, vol. 45, no. 2, pp. 122–127, 1990.

[48] T. P. Yadav, R. M. Yadav, and D. P. Singh, "Mechanical milling: a top down approach for the synthesis of nanomaterials and nanocomposites," *Nanoscience and Nanotechnology*, vol. 2, no. 3, pp. 22–48, 2012.

[49] A. Pimpin and W. Srituravanich, "Review on micro-and nanolithography techniques and their applications," *Engineering Journal*, vol. 16, no. 1, pp. 37–56, 2012.

[50] J. C. Hulteen, D. A. Treichel, M. T. Smith, M. L. Duval, T. R. Jensen, and R. P. Van Duyne, "Nanosphere lithography: size-tunable silver nanoparticle and surface cluster arrays," *The Journal of Physical Chemistry B*, vol. 103, no. 19, pp. 3854–3863, 1999.

[51] V. Amendola and M. Meneghetti, "Laser ablation synthesis in solution and size manipulation of noble metal nanoparticles," *Physical chemistry chemical physics*, vol. 11, no. 20, pp. 3805–3821, 2009.

[52] P. Shah and A. Gavrin, "Synthesis of nanoparticles using high-pressure sputtering for magnetic domain imaging," *Journal of magnetism and magnetic materials*, vol. 301, no. 1, pp. 118–123, 2006.

[53] E. Lugscheider, S. Bärwulf, C. Barimani, M. Riester, and H. Hilgers, "Magnetron-sputtered hard material coatings on thermoplastic polymers for clean room applications," *Surface and Coatings Technology*, vol. 108, pp. 398–402, 1998.

[54] E. Cussler, S. E. Hughes, W. J. Ward III, and R. Aris, "Barrier membranes," *Journal of membrane science*, vol. 38, no. 2, pp. 161–174, 1988.

[55] A. Corma and H. Garcia, "Supported gold nanoparticles as catalysts for organic reactions," *Chemical Society Reviews*, vol. 37, no. 9, pp. 2096–2126, 2008.

[56] P. Lodahl, "Quantum-dot based photonic quantum networks," *Quantum Science and Technology*, vol. 3, no. 1, p. 013001, 2017.

[57] E. Roduner, "Size matters: why nanomaterials are different," *Chemical Society Reviews*, vol. 35, no. 7, pp. 583–592, 2006.

[58] E. Ozbay, "Plasmonics: merging photonics and electronics at nanoscale dimensions," *science*, vol. 311, no. 5758, pp. 189–193, 2006.

[59] S. A. Maier, P. G. Kik, H. A. Atwater, S. Meltzer, E. Harel, B. E. Koel, and A. A. Requicha, "Local detection of electromagnetic energy transport below the diffraction limit in metal nanoparticle plasmon waveguides," *Nature materials*, vol. 2, no. 4, pp. 229–232, 2003.

[60] L. Yin, V. K. Vlasko-Vlasov, J. Pearson, J. M. Hiller, J. Hua, U. Welp, D. E. Brown, and C. W. Kimball, "Subwavelength focusing and guiding of surface plasmons," *Nano letters*, vol. 5, no. 7, pp. 1399–1402, 2005.

[61] S. Gupta, Q. Zhang, T. Emrick, and T. P. Russell, ""self-corralling" nanorods under an applied electric field," *Nano letters*, vol. 6, no. 9, pp. 2066–2069, 2006.

[62] A. C. Anselmo and S. Mitragotri, "Nanoparticles in the clinic," *Bioengineering and translational medicine*, vol. 1, no. 1, pp. 10–29, 2016.

[63] E. Deu, M. Verdoes, and M. Bogyo, "New approaches for dissecting protease functions to improve probe development and drug discovery," *Nature structural and molecular biology*, vol. 19, no. 1, pp. 9–16, 2012.

[64] J. P. M. Almeida, A. L. Chen, A. Foster, and R. Drezek, "In vivo biodistribution of nanoparticles," *Nanomedicine*, vol. 6, no. 5, pp. 815–835, 2011.

[65] Y. Matsumura and H. Maeda, "A new concept for macromolecular therapeutics in cancer chemotherapy: mechanism of tumoritropic accumulation of proteins and the antitumor agent smancs," *Cancer research*, vol. 46, no. 12 Part 1, pp. 6387–6392, 1986.

[66] A. A. Burns, J. Vider, H. Ow, E. Herz, O. Penate-Medina, M. Baumgart, S. M. Larson, U. Wiesner, and M. Bradbury, "Fluorescent silica nanoparticles with efficient urinary excretion for nanomedicine," *Nano letters*, vol. 9, no. 1, pp. 442–448, 2009.

[67] S. Alidori, N. Akhavein, D. L. Thorek, K. Behling, Y. Romin, D. Queen, B. J. Beattie, K. Manova-Todorova, M. Bergkvist, and D. A. Scheinberg, "Targeted fibrillar nanocarbon rnai treatment of acute kidney injury," *Science translational medicine*, vol. 8, no. 331, pp. 331ra39–331ra39, 2016.

[68] R. M. Williams, J. Shah, B. D. Ng, D. R. Minton, L. J. Gudas, C. Y. Park, and D. A. Heller, "Mesoscale nanoparticles selectively target the renal proximal tubule epithelium," *Nano letters*, vol. 15, no. 4, pp. 2358–2364, 2015.

[69] C. H. J. Choi, J. E. Zuckerman, P. Webster, and M. E. Davis, "Targeting kidney mesangium by nanoparticles of defined size," *Proceedings of the National Academy of Sciences*, vol. 108, no. 16, pp. 6656–6661, 2011.

[70] M. J. Mitchell, M. M. Billingsley, R. M. Haley, M. E. Wechsler, N. A. Peppas, and R. Langer, "Engineering precision nanoparticles for drug delivery," *Nature Reviews Drug Discovery*, vol. 20, no. 2, pp. 101–124, 2021.

[71] S. Mitragotri, T. Lammers, Y. H. Bae, S. Schwendeman, S. C. De Smedt, J. C. Leroux, D. Peer, I. C. Kwon, H. Harashima, and A. Kikuchi, "Drug delivery research for the future: expanding the nano horizons and beyond," 2017.

[72] J. Lee, A. Sharei, W. Y. Sim, A. Adamo, R. Langer, K. F. Jensen, and M. G. Bawendi, "Nonendocytic delivery of functional engineered nanoparticles into the cytoplasm of live cells using a novel, high-throughput microfluidic device," *Nano letters*, vol. 12, no. 12, pp. 6322–6327, 2012.

[73] Y. Shamay, J. Shah, M. Işık, A. Mizrachi, J. Leibold, D. F. Tschaharganeh, D. Roxbury, J. Budhathoki-Uprety, K. Nawaly, and J. L. Sugarman, "Quantitative self-assembly prediction yields targeted nanomedicines," *Nature materials*, vol. 17, no. 4, pp. 361–368, 2018.

[74] G. Gopalakrishnan, C. Danelon, P. Izewska, M. Prummer, P.-Y. Bolinger, I. Geissbuhler, D. Demurtas, J. Dubochet, and H. Vogel, "Multifunctional lipid/quantum dot hybrid nanocontainers for controlled targeting of live cells," *Angewandte Chemie International Edition*, vol. 45, no. 33, pp. 5478–5483, 2006.

[75] A. G. Skirtach, A. Munoz Javier, O. Kreft, K. Köhler, A. Piera Alberola, H. Möhwald, W. J. Parak, and G. B. Sukhorukov, "Laser-induced release of encapsulated materials inside living cells," *Angewandte Chemie International Edition*, vol. 45, no. 28, pp. 4612–4617, 2006.

[76] B. Zebli, A. S. Susha, G. B. Sukhorukov, A. L. Rogach, and W. J. Parak, "Magnetic targeting and cellular uptake of polymer microcapsules simultaneously functionalized with magnetic and luminescent nanocrystals," *Langmuir*, vol. 21, no. 10, pp. 4262–4265, 2005.

[77] R. G. Larson, *The structure and rheology of complex fluids*, vol. 150. Oxford university press New York, 1999.

[78] P.-G. De Gennes and J. Prost, *The physics of liquid crystals.* Oxford university press, 1993.

[79] M. Kleman and O. D. Lavrentovich, *Soft matter physics: an introduction.* Springer, 2003.

[80] A. Sengupta, *Topological microfluidics: nematic liquid crystals and nematic colloids in microfluidic environment.* Springer Science and Business Media, 2013.

[81] K. Busch and S. John, "Liquid-crystal photonic-band-gap materials: the tunable electromagnetic vacuum," *Physical Review Letters*, vol. 83, no. 5, p. 967, 1999.

[82] H. Coles and S. Morris, "Liquid-crystal lasers," *Nature Photonics*, vol. 4, no. 10, pp. 676–685, 2010.

[83] A. Bregar, T. White, and M. Ravnik, "Refraction of light on flat boundary of liquid crystals or anisotropic metamaterials," *Liquid Crystals Reviews*, vol. 5, no. 1, pp. 53–68, 2017.

[84] Y.-H. Lin, Y.-J. Wang, and V. Reshetnyak, "Liquid crystal lenses with tunable focal length," *Liquid Crystals Reviews*, vol. 5, no. 2, pp. 111–143, 2017.

[85] P. Yeh and C. Gu, *Optics of liquid crystal displays*, vol. 67. John Wiley and Sons, 2009.

[86] P. Poulin, H. Stark, T. Lubensky, and D. Weitz, "Novel colloidal interactions in anisotropic fluids," *Science*, vol. 275, no. 5307, pp. 1770–1773, 1997.

[87] H. Stark, "Physics of colloidal dispersions in nematic liquid crystals," *Physics Reports*, vol. 351, no. 6, pp. 387–474, 2001.

[88] L. E. Aguirre, A. de Oliveira, D. Seč, S. Čopar, P. L. Almeida, M. Ravnik, M. H. Godinho, and S. Žumer, "Sensing surface morphology of biofibers by decorating spider silk and cellulosic filaments with nematic microdroplets," *Proceedings of the National Academy of Sciences*, vol. 113, no. 5, pp. 1174–1179, 2016.

[89] I.-H. Lin, D. S. Miller, P. J. Bertics, C. J. Murphy, J. J. De Pablo, and N. L. Abbott, "Endotoxin-induced structural transformations in liquid crystalline droplets," *Science*, vol. 332, no. 6035, pp. 1297–1300, 2011.

[90] J. Prost, F. Jülicher, and J.-F. Joanny, "Active gel physics," *Nature physics*, vol. 11, no. 2, pp. 111–117, 2015.

[91] C. Dombrowski, L. Cisneros, S. Chatkaew, R. E. Goldstein, and J. O. Kessler, "Self-concentration and large-scale coherence in bacterial dynamics," *Physical review letters*, vol. 93, no. 9, p. 098103, 2004.

[92] K. Kawaguchi, R. Kageyama, and M. Sano, "Topological defects control collective dynamics in neural progenitor cell cultures," *Nature*, vol. 545, no. 7654, pp. 327–331, 2017.

[93] T. B. Saw, A. Doostmohammadi, V. Nier, L. Kocgozlu, S. Thampi, Y. Toyama, P. Marcq, C. T. Lim, J. M. Yeomans, and B. Ladoux, "Topological defects in epithelia govern cell death and extrusion," *Nature*, vol. 544, no. 7649, pp. 212–216, 2017.

[94] P. C. Mushenheim, R. R. Trivedi, H. H. Tuson, D. B. Weibel, and N. L. Abbott, "Dynamic self-assembly of motile bacteria in liquid crystals," *Soft Matter*, vol. 10, no. 1, pp. 88–95, 2014.

[95] C. Peng, T. Turiv, Y. Guo, Q.-H. Wei, and O. D. Lavrentovich, "Command of active matter by topological defects and patterns," *Science*, vol. 354, no. 6314, pp. 882–885, 2016.

[96] L. Onsager, "The effects of shape on the interaction of colloidal particles," *Annals of the New York Academy of Sciences*, vol. 51, no. 4, pp. 627–659, 1949.

[97] W. L. McMillan, "Simple molecular model for the smectic a phase of liquid crystals," *Physical Review A*, vol. 4, no. 3, p. 1238, 1971.

[98] S. Chandrasekhar, *Liquid crystals*. Cambridge Univ Pr, 1992.

[99] P. Oswald and P. Pieranski, *Nematic and cholesteric liquid crystals: concepts and physical properties illustrated by experiments*. CRC press, 2005.

[100] J. Loudet, P. Hanusse, and P. Poulin, "Stokes drag on a sphere in a nematic liquid crystal," *Science*, vol. 306, no. 5701, pp. 1525–1525, 2004.

[101] M. Born and E. Wolf, "Principles of optics, 6th edn oxford," *UK: Pergamon Press.[Google Scholar]*, 1980.

[102] L. Onsager, "The effects of shape on the interaction of colloidal particles," *Annals of the New York Academy of Sciences*, vol. 51, no. 4, pp. 627–659, 1949.

[103] T. Rasing and I. Musevic, *Surfaces and interfaces of liquid crystals*. Springer Science and Business Media, 2004.

[104] A. A. Sonin, "The surface physics of liquid crystals," 1995.

[105] Y. Zhou, *Modeling of Nematic Liquid Crystals under the Effect of Chirality, External Fields and Surface Conditions*. Thesis, 2018. Copyright - Database copyright ProQuest LLC; ProQuest does not claim copyright in the individual underlying works. Last updated - 2021-08-03.

[106] J. Ericksen and C. Truesdell, "Archs ration. mech," *Analysis*, vol. 4, p. 231, 1960.

[107] J. Ericksen, "Inequalities in liquid crystal theory," *The Physics of Fluids*, vol. 9, no. 6, pp. 1205–1207, 1966.

[108] F. M. Leslie, "Some constitutive equations for liquid crystals," *Archive for Rational Mechanics and Analysis*, vol. 28, no. 4, pp. 265–283, 1968.

[109] F. Leslie, "Arch. ration. mech," *Analysis*, vol. 28, p. 265, 1968.

[110] W. Connacher, N. Zhang, A. Huang, J. Mei, S. Zhang, T. Gopesh, and J. Friend, "Micro/nano acoustofluidics: materials, phenomena, design, devices, and applications," *Lab on a Chip*, vol. 18, no. 14, pp. 1952–1996, 2018.

[111] A. Ozcelik, J. Rufo, F. Guo, Y. Gu, P. Li, J. Lata, and T. J. Huang, "Acoustic tweezers for the life sciences," *Nature Methods*, vol. 15, no. 12, pp. 1021–1028, 2018.

[112] L. Y. Yeo and J. R. Friend, "Surface acoustic wave microfluidics," *Annu. Rev. Fluid Mech*, vol. 46, no. 1, pp. 379–406, 2014.

[113] L. Rayleigh, "On waves propagated along the plane surface of an elastic solid," *Proceedings of the London mathematical Society*, vol. 1, no. 1, pp. 4–11, 1885.

[114] L. Y. Yeo and J. R. Friend, "Ultrafast microfluidics using surface acoustic waves," *Biomicrofluidics*, vol. 3, no. 1, p. 012002, 2009.

[115] S. P. Zhang, J. Lata, C. Chen, J. Mai, F. Guo, Z. Tian, L. Ren, Z. Mao, P.-H. Huang, and P. Li, "Digital acoustofluidics enables contactless and programmable liquid handling," *Nature communications*, vol. 9, no. 1, pp. 1–11, 2018.

[116] D. Baresch, J.-L. Thomas, and R. Marchiano, "Observation of a single-beam gradient force acoustical trap for elastic particles: acoustical tweezers," *Physical review letters*, vol. 116, no. 2, p. 024301, 2016.

[117] G. Destgeer and H. J. Sung, "Recent advances in microfluidic actuation and micro-object manipulation via surface acoustic waves," *Lab on a Chip*, vol. 15, no. 13, pp. 2722–2738, 2015.

[118] J. Friend and L. Y. Yeo, "Microscale acoustofluidics: Microfluidics driven via acoustics and ultrasonics," *Reviews of Modern Physics*, vol. 83, no. 2, p. 647, 2011.

[119] H. Bruus, *Theoretical microfluidics*, vol. 18. Oxford university press, 2007.

[120] H. Bruus, "Acoustofluidics 7: The acoustic radiation force on small particles," *Lab on a Chip*, vol. 12, no. 6, pp. 1014–1021, 2012.

[121] N. Riley, "Steady streaming," *Annual review of fluid mechanics*, vol. 33, p. 43, 2001.

[122] S. Sadhal, "Acoustofluidics 13: Analysis of acoustic streaming by perturbation methods," *Lab on a Chip*, vol. 12.

[123] M. Van Dyke and M. Van Dyke, *An album of fluid motion*, vol. 176. Parabolic Press Stanford, 1982.

[124] L. Rayleigh, "On the circulation of air observed in kundt's tubes, and on some allied acoustical problems," *Philosophical Transactions of the Royal Society of London*, vol. 175, pp. 1–21, 1884.

[125] M. F. Hamilton, Y. A. Ilinskii, and E. A. Zabolotskaya, "Acoustic streaming generated by standing waves in two-dimensional channels of arbitrary width,"

The Journal of the Acoustical Society of America, vol. 113, no. 1, pp. 153–160, 2003.

[126] A. Manbachi and R. S. Cobbold, "Development and application of piezoelectric materials for ultrasound generation and detection," *Ultrasound*, vol. 19, no. 4, pp. 187–196, 2011.

[127] P. G. Newman and G. S. Rozycki, "The history of ultrasound," *Surgical clinics of north America*, vol. 78, no. 2, pp. 179–195, 1998.

[128] N. Dam, "Non-contact ultrasonic micromeasurement system," 1999.

[129] S. Saadon and O. Sidek, "A review of vibration-based mems piezoelectric energy harvesters," *Energy conversion and management*, vol. 52, no. 1, pp. 500–504, 2011.

[130] R. M. White and F. W. Voltmer, "Direct piezoelectric coupling to surface elastic waves," *Applied physics letters*, vol. 7, no. 12, pp. 314–316, 1965.

[131] S. T. S. Tonami, A. N. A. Nishikata, and Y. S. Y. Shimizu, "Characteristics of leaky surface acoustic waves propagating on linbo 3 and litao 3 substrates," *Japanese journal of applied physics*, vol. 34, no. 5S, p. 2664, 1995.

[132] Y. V. Gulyaev, "Review of shear surface acoustic waves in solids," *IEEE transactions on ultrasonics, ferroelectrics, and frequency control*, vol. 45, no. 4, pp. 935–938, 1998.

[133] F. Martin, "Propagation characteristics of harmonic surface skimming bulk waves on st quartz," *Electronics Letters*, vol. 38, no. 16, p. 1, 2002.

[134] V. L. Strashilov and V. M. Yantchev, "Surface transverse waves: properties, devices, and analysis," *IEEE transactions on ultrasonics, ferroelectrics, and frequency control*, vol. 52, no. 5, pp. 812–821, 2005.

[135] S. Collignon, O. Manor, and J. Friend, "Improving and predicting fluid atomization via hysteresis-free thickness vibration of lithium niobate," *Advanced Functional Materials*, vol. 28, no. 8, p. 1704359, 2018.

[136] B. Jaffe, R. Roth, and S. Marzullo, "Piezoelectric properties of lead zirconate-lead titanate solid-solution ceramics," *Journal of Applied Physics*, vol. 25, no. 6, pp. 809–810, 1954.

[137] I. Bretos, R. Jiménez, J. García-López, L. Pardo, and M. L. Calzada, "Photochemical solution deposition of lead-based ferroelectric films: Avoiding the pbo-excess addition at last," *Chemistry of Materials*, vol. 20, no. 18, pp. 5731–5733, 2008.

[138] E. Directive and I. RoHS, "Restriction of the use of certain hazardous substances in electrical and electronic equipment," *European Union, Brussels, Belgium, Report*, no. A7-0196, 2010.

[139] R. Thurston, A. D. Pierce, and E. P. Papadakis, *Reference for Modern Instrumentation, Techniques, and Technology: Ultrasonic Instruments and Devices I: Ultrasonic Instruments and Devices I.* Academic Press, 1998.

[140] A. Slobodnik and E. Conway, "New high-frequency high-coupling low-beam-steering cut for acoustic surface waves on linbo3," *Electronics Letters*, vol. 6, no. 6, pp. 171–173, 1970.

[141] A. Takayanagi, K. Yamanouchi, and K. Shibayama, "Piezoelectric leaky surface wave in linbo3," *Applied Physics Letters*, vol. 17, no. 5, pp. 225–227, 1970.

[142] K. Shibayama, K. Yamanouchi, H. Sato, and T. Meguro, "Optimum cut for rotated y-cut linbo 3 crystal used as the substrate of acoustic-surface-wave filters," *Proceedings of the IEEE*, vol. 64, no. 5, pp. 595–597, 1976.

[143] D. Morgan, *Surface acoustic wave filters: With applications to electronic communications and signal processing.* Academic Press, 2010.

[144] T. Salafi, K. K. Zeming, and Y. Zhang, "Advancements in microfluidics for nanoparticle separation," *Lab on a Chip*, vol. 17, no. 1, pp. 11–33, 2017.

[145] A. Van den Berg and L. Segerink, "Microfluidics for medical applications," 2014.

[146] E. Heftmann, *Chromatography: Fundamentals and applications of chromatography and related differential migration methods-Part B: Applications*. Elsevier, 2004.

[147] S. Benfer, P. Árki, and G. Tomandl, "Ceramic membranes for filtration applications—preparation and characterization," *Advanced Engineering Materials*, vol. 6, no. 7, pp. 495–500, 2004.

[148] E. Krieg, H. Weissman, E. Shirman, E. Shimoni, and B. Rybtchinski, "A recyclable supramolecular membrane for size-selective separation of nanoparticles," *Nature nanotechnology*, vol. 6, no. 3, pp. 141–146, 2011.

[149] B. J. Tauro, D. W. Greening, R. A. Mathias, H. Ji, S. Mathivanan, A. M. Scott, and R. J. Simpson, "Comparison of ultracentrifugation, density gradient separation, and immunoaffinity capture methods for isolating human colon cancer cell line lim1863-derived exosomes," *Methods*, vol. 56, no. 2, pp. 293–304, 2012.

[150] O. Akbulut, C. R. Mace, R. V. Martinez, A. A. Kumar, Z. Nie, M. R. Patton, and G. M. Whitesides, "Separation of nanoparticles in aqueous multiphase systems through centrifugation," *Nano letters*, vol. 12, no. 8, pp. 4060–4064, 2012.

[151] H. Zorbas, "Bioanalytics: Methods on molecular biotechnology and modern biotechnology," 2010.

[152] M. Hanauer, S. Pierrat, I. Zins, A. Lotz, and C. Sönnichsen, "Separation of nanoparticles by gel electrophoresis according to size and shape," *Nano letters*, vol. 7, no. 9, pp. 2881–2885, 2007.

[153] X. Xu, K. K. Caswell, E. Tucker, S. Kabisatpathy, K. L. Brodhacker, and W. A. Scrivens, "Size and shape separation of gold nanoparticles with preparative gel electrophoresis," *Journal of Chromatography A*, vol. 1167, no. 1, pp. 35–41, 2007.

[154] N.-T. Nguyen, S. T. Wereley, and S. A. M. Shaegh, *Fundamentals and applications of microfluidics*. Artech house, 2019.

[155] R. T. Davies, J. Kim, S. C. Jang, E.-J. Choi, Y. S. Gho, and J. Park, "Microfluidic filtration system to isolate extracellular vesicles from blood," *Lab on a Chip*, vol. 12, no. 24, pp. 5202–5210, 2012.

[156] L. R. Huang, E. C. Cox, R. H. Austin, and J. C. Sturm, "Continuous particle separation through deterministic lateral displacement," *Science*, vol. 304, no. 5673, pp. 987–990, 2004.

[157] S. M. Santana, M. A. Antonyak, R. A. Cerione, and B. J. Kirby, "Microfluidic isolation of cancer-cell-derived microvesicles from hetergeneous extracellular shed vesicle populations," *Biomedical microdevices*, vol. 16, no. 6, pp. 869–877, 2014.

[158] B. H. Wunsch, J. T. Smith, S. M. Gifford, C. Wang, M. Brink, R. L. Bruce, R. H. Austin, G. Stolovitzky, and Y. Astier, "Nanoscale lateral displacement arrays for the separation of exosomes and colloids down to 20 nm," *Nature Nanotechnology*, vol. 11, no. 11, pp. 936–940, 2016.

[159] A. A. S. Bhagat, S. S. Kuntaegowdanahalli, and I. Papautsky, "Inertial microfluidics for continuous particle filtration and extraction," *Microfluidics and nanofluidics*, vol. 7, no. 2, pp. 217–226, 2009.

[160] D. Di Carlo, "Inertial microfluidics," *Lab on a Chip*, vol. 9, no. 21, pp. 3038–3046, 2009.

[161] J. Zhang, S. Yan, D. Yuan, G. Alici, N.-T. Nguyen, M. E. Warkiani, and W. Li, "Fundamentals and applications of inertial microfluidics: A review," *Lab on a Chip*, vol. 16, no. 1, pp. 10–34, 2016.

[162] P. Arosio, T. Muller, L. Mahadevan, and T. P. Knowles, "Density-gradient-free microfluidic centrifugation for analytical and preparative separation of nanoparticles," *Nano letters*, vol. 14, no. 5, pp. 2365–2371, 2014.

[163] Y. Yang, Y. Shi, L. Chin, J. Zhang, D. Tsai, and A. Liu, "Optofluidic nanoparticles sorting by hydrodynamic optical force," in *2013 Transducers and Eurosensors XXVII: The 17th International Conference on Solid-State Sensors, Actuators and*

Microsystems (TRANSDUCERS and EUROSENSORS XXVII), pp. 2122–2125, IEEE.

[164] S. H. S. Lee, T. A. Hatton, and S. A. Khan, "Microfluidic continuous magnetophoretic protein separation using nanoparticle aggregates," *Microfluidics and nanofluidics*, vol. 11, no. 4, pp. 429–438, 2011.

[165] A. Munir, Z. Zhu, J. Wang, and H. S. Zhou, "Experimental investigation of magnetically actuated separation using tangential microfluidic channels and magnetic nanoparticles," *IET nanobiotechnology*, vol. 8, no. 2, pp. 102–110, 2014.

[166] E. Ban, Y. S. Yoo, and E. J. Song, "Analysis and applications of nanoparticles in capillary electrophoresis," *Talanta*, vol. 141, pp. 15–20, 2015.

[167] S. Dash, S. Mohanty, S. Pradhan, and B. Mishra, "Cfd design of a microfluidic device for continuous dielectrophoretic separation of charged gold nanoparticles," *Journal of the Taiwan Institute of Chemical Engineers*, vol. 58, pp. 39–48, 2016.

[168] H. Jeon, Y. Kim, and G. Lim, "Continuous particle separation using pressure-driven flow-induced miniaturizing free-flow electrophoresis (pdf-induced u-ffe)," *Scientific reports*, vol. 6, no. 1, pp. 1–9, 2016.

[169] K. Lee, H. Shao, R. Weissleder, and H. Lee, "Acoustic purification of extracellular microvesicles," *ACS nano*, vol. 9, no. 3, pp. 2321–2327, 2015.

[170] P. Sehgal and B. J. Kirby, "Separation of 300 and 100 nm particles in fabry–perot acoustofluidic resonators," *Analytical chemistry*, vol. 89, no. 22, pp. 12192–12200, 2017.

[171] M. Wu, Z. Mao, K. Chen, H. Bachman, Y. Chen, J. Rufo, L. Ren, P. Li, L. Wang, and T. J. Huang, "Acoustic separation of nanoparticles in continuous flow," *Advanced functional materials*, vol. 27, no. 14, p. 1606039, 2017.

[172] M. Wu, Y. Ouyang, Z. Wang, R. Zhang, P.-H. Huang, C. Chen, H. Li, P. Li, D. Quinn, and M. Dao, "Isolation of exosomes from whole blood by integrating

acoustics and microfluidics," *Proceedings of the National Academy of Sciences*, vol. 114, no. 40, pp. 10584–10589, 2017.

[173] A. A. S. Bhagat, H. Bow, H. W. Hou, S. J. Tan, J. Han, and C. T. Lim, "Microfluidics for cell separation," *Medical and biological engineering and computing*, vol. 48, no. 10, pp. 999–1014, 2010.

[174] M. Ebara, J. M. Hoffman, A. S. Hoffman, P. S. Stayton, and J. J. Lai, "A photoinduced nanoparticle separation in microchannels via ph-sensitive surface traps," *Langmuir*, vol. 29, no. 18, pp. 5388–5393, 2013.

[175] C. L. Hisey, K. D. P. Dorayappan, D. E. Cohn, K. Selvendiran, and D. J. Hansford, "Microfluidic affinity separation chip for selective capture and release of label-free ovarian cancer exosomes," *Lab on a Chip*, vol. 18, no. 20, pp. 3144–3153, 2018.

[176] A. Sarkar, H. W. Hou, A. Mahan, J. Han, and G. Alter, "Multiplexed affinity-based separation of proteins and cells using inertial microfluidics," *Scientific reports*, vol. 6, no. 1, pp. 1–9, 2016.

[177] A. De Momi and J. R. Lead, "Size fractionation and characterisation of fresh water colloids and particles: split-flow thin-cell and electron microscopy analyses," *Environmental science and technology*, vol. 40, no. 21, pp. 6738–6743, 2006.

[178] J. C. Giddings, "Field-flow fractionation: analysis of macromolecular, colloidal, and particulate materials," *Science*, vol. 260, no. 5113, pp. 1456–1465, 1993.

[179] A. Lenshof and T. Laurell, "Continuous separation of cells and particles in microfluidic systems," *Chemical Society Reviews*, vol. 39, no. 3, pp. 1203–1217, 2010.

[180] P. Zhang, H. Bachman, A. Ozcelik, and T. J. Huang, "Acoustic microfluidics," *Annual review of analytical chemistry (Palo Alto, Calif.)*, vol. 13, no. 1, p. 17, 2020.

[181] X. Ding, Z. Peng, S.-C. S. Lin, M. Geri, S. Li, P. Li, Y. Chen, M. Dao, S. Suresh, and T. J. Huang, "Cell separation using tilted-angle standing surface acoustic waves," *Proceedings of the National Academy of Sciences*, vol. 111, no. 36, pp. 12992–12997, 2014.

[182] P. Li, Z. Mao, Z. Peng, L. Zhou, Y. Chen, P.-H. Huang, C. I. Truica, J. J. Drabick, W. S. El-Deiry, and M. Dao, "Acoustic separation of circulating tumor cells," *Proceedings of the National Academy of Sciences*, vol. 112, no. 16, pp. 4970–4975, 2015.

[183] B.-T. Pan, K. Teng, C. Wu, M. Adam, and R. M. Johnstone, "Electron microscopic evidence for externalization of the transferrin receptor in vesicular form in sheep reticulocytes," *The Journal of cell biology*, vol. 101, no. 3, pp. 942–948, 1985.

[184] R. M. Johnstone, M. Adam, J. Hammond, L. Orr, and C. Turbide, "Vesicle formation during reticulocyte maturation. association of plasma membrane activities with released vesicles (exosomes)," *Journal of Biological Chemistry*, vol. 262, no. 19, pp. 9412–9420, 1987.

[185] M. F. Baietti, Z. Zhang, E. Mortier, A. Melchior, G. Degeest, A. Geeraerts, Y. Ivarsson, F. Depoortere, C. Coomans, and E. Vermeiren, "Syndecan–syntenin–alix regulates the biogenesis of exosomes," *Nature cell biology*, vol. 14, no. 7, pp. 677–685, 2012.

[186] C. Théry, S. Amigorena, G. Raposo, and A. Clayton, "Isolation and characterization of exosomes from cell culture supernatants and biological fluids," *Current protocols in cell biology*, vol. 30, no. 1, pp. 3.22. 1–3.22. 29, 2006.

[187] D. D. TAYLOR, H. D. HOMESLEY, and G. J. DOELLGAST, ""membrane-associated" immunoglobulins in cyst and ascites fluids of ovarian cancer patients," *American Journal of Reproductive Immunology*, vol. 3, no. 1, pp. 7–11, 1983.

[188] V. Muralidharan-Chari, J. Clancy, C. Plou, M. Romao, P. Chavrier, G. Raposo,

and C. D'Souza-Schorey, "Arf6-regulated shedding of tumor cell-derived plasma membrane microvesicles," *Current Biology*, vol. 19, no. 22, pp. 1875–1885, 2009.

[189] M. Baj-Krzyworzeka, R. Szatanek, K. Węglarczyk, J. Baran, B. Urbanowicz, P. Brański, M. Z. Ratajczak, and M. Zembala, "Tumour-derived microvesicles carry several surface determinants and mrna of tumour cells and transfer some of these determinants to monocytes," *Cancer Immunology, Immunotherapy*, vol. 55, no. 7, pp. 808–818, 2006.

[190] G. Raposo and W. Stoorvogel, "Extracellular vesicles: exosomes, microvesicles, and friends," *Journal of Cell Biology*, vol. 200, no. 4, pp. 373–383, 2013.

[191] K. W. Witwer, E. I. Buzás, L. T. Bemis, A. Bora, C. Lässer, J. Lötvall, E. N. Nolte-'t Hoen, M. G. Piper, S. Sivaraman, and J. Skog, "Standardization of sample collection, isolation and analysis methods in extracellular vesicle research," *Journal of extracellular vesicles*, vol. 2, no. 1, p. 20360, 2013.

[192] A. Bobrie, M. Colombo, S. Krumeich, G. Raposo, and C. Théry, "Diverse subpopulations of vesicles secreted by different intracellular mechanisms are present in exosome preparations obtained by differential ultracentrifugation," *Journal of extracellular vesicles*, vol. 1, no. 1, p. 18397, 2012.

[193] B. J. Tauro, D. W. Greening, R. A. Mathias, S. Mathivanan, H. Ji, and R. J. Simpson, "Two distinct populations of exosomes are released from lim1863 colon carcinoma cell-derived organoids," *Molecular and Cellular Proteomics*, vol. 12, no. 3, pp. 587–598, 2013.

[194] M. Aalberts, F. M. van Dissel-Emiliani, N. P. van Adrichem, M. van Wijnen, M. H. Wauben, T. A. Stout, and W. Stoorvogel, "Identification of distinct populations of prostasomes that differentially express prostate stem cell antigen, annexin a1, and glipr2 in humans," *Biology of reproduction*, vol. 86, no. 3, pp. 82, 1–8, 2012.

[195] J. Palma, S. C. Yaddanapudi, L. Pigati, M. A. Havens, S. Jeong, G. A. Weiner, K. M. E. Weimer, B. Stern, M. L. Hastings, and D. M. Duelli, "Micrornas are

exported from malignant cells in customized particles," *Nucleic acids research*, vol. 40, no. 18, pp. 9125–9138, 2012.

[196] R. Cantin, J. Diou, D. Bélanger, A. M. Tremblay, and C. Gilbert, "Discrimination between exosomes and hiv-1: purification of both vesicles from cell-free supernatants," *Journal of immunological methods*, vol. 338, no. 1-2, pp. 21–30, 2008.

[197] N. Ismail, Y. Wang, D. Dakhlallah, L. Moldovan, K. Agarwal, K. Batte, P. Shah, J. Wisler, T. D. Eubank, and S. Tridandapani, "Macrophage microvesicles induce macrophage differentiation and mir-223 transfer," *Blood, The Journal of the American Society of Hematology*, vol. 121, no. 6, pp. 984–995, 2013.

[198] A. Clayton, J. Court, H. Navabi, M. Adams, M. D. Mason, J. A. Hobot, G. R. Newman, and B. Jasani, "Analysis of antigen presenting cell derived exosomes, based on immuno-magnetic isolation and flow cytometry," *Journal of immunological methods*, vol. 247, no. 1-2, pp. 163–174, 2001.

[199] G. Kim, C. E. Yoo, M. Kim, H. J. Kang, D. Park, M. Lee, and N. Huh, "Noble polymeric surface conjugated with zwitterionic moieties and antibodies for the isolation of exosomes from human serum," *Bioconjugate chemistry*, vol. 23, no. 10, pp. 2114–2120, 2012.

[200] C. E. Yoo, G. Kim, M. Kim, D. Park, H. J. Kang, M. Lee, and N. Huh, "A direct extraction method for micrornas from exosomes captured by immunoaffinity beads," *Analytical biochemistry*, vol. 431, no. 2, pp. 96–98, 2012.

[201] M. L. Alvarez, M. Khosroheidari, R. K. Ravi, and J. K. DiStefano, "Comparison of protein, microrna, and mrna yields using different methods of urinary exosome isolation for the discovery of kidney disease biomarkers," *Kidney international*, vol. 82, no. 9, pp. 1024–1032, 2012.

[202] X. Gallart-Palau, A. Serra, A. S. W. Wong, S. Sandin, M. K. Lai, C. P. Chen, O. L. Kon, and S. K. Sze, "Extracellular vesicles are rapidly purified from hu-

man plasma by protein organic solvent precipitation (prospr)," *Scientific reports*, vol. 5, no. 1, pp. 1–12, 2015.

[203] W. J. Goh, S. Zou, W. Y. Ong, F. Torta, A. F. Alexandra, R. M. Schiffelers, G. Storm, J.-W. Wang, B. Czarny, and G. Pastorin, "Bioinspired cell-derived nanovesicles versus exosomes as drug delivery systems: a cost-effective alternative," *Scientific reports*, vol. 7, no. 1, pp. 1–10, 2017.

[204] F. Liu, O. Vermesh, V. Mani, T. J. Ge, S. J. Madsen, A. Sabour, E.-C. Hsu, G. Gowrishankar, M. Kanada, and J. V. Jokerst, "The exosome total isolation chip," *ACS nano*, vol. 11, no. 11, pp. 10712–10723, 2017.

[205] A. A. S. Bhagat, S. S. Kuntaegowdanahalli, and I. Papautsky, "Continuous particle separation in spiral microchannels using dean flows and differential migration," *Lab on a Chip*, vol. 8, no. 11, pp. 1906–1914, 2008.

[206] C. Chen, J. Skog, C.-H. Hsu, R. T. Lessard, L. Balaj, T. Wurdinger, B. S. Carter, X. O. Breakefield, M. Toner, and D. Irimia, "Microfluidic isolation and transcriptome analysis of serum microvesicles," *Lab on a Chip*, vol. 10, no. 4, pp. 505–511, 2010.

[207] E. Reátegui, N. Aceto, E. J. Lim, J. P. Sullivan, A. E. Jensen, M. Zeinali, J. M. Martel, A. J. Aranyosi, W. Li, and S. Castleberry, "Tunable nanostructured coating for the capture and selective release of viable circulating tumor cells," *Advanced materials*, vol. 27, no. 9, pp. 1593–1599, 2015.

[208] E. Reátegui, K. E. van der Vos, C. P. Lai, M. Zeinali, N. A. Atai, B. Aldikacti, F. P. Floyd, A. H Khankhel, V. Thapar, and F. H. Hochberg, "Engineered nanointerfaces for microfluidic isolation and molecular profiling of tumor-specific extracellular vesicles," *Nature communications*, vol. 9, no. 1, pp. 1–11, 2018.

[209] B. H. Wunsch, J. T. Smith, S. M. Gifford, C. Wang, M. Brink, R. L. Bruce, R. H. Austin, G. Stolovitzky, and Y. Astier, "Nanoscale lateral displacement arrays for the separation of exosomes and colloids down to 20 nm," *Nature nanotechnology*, vol. 11, no. 11, pp. 936–940, 2016.

[210] R. Vaidyanathan, M. Naghibosadat, S. Rauf, D. Korbie, L. G. Carrascosa, M. J. Shiddiky, and M. Trau, "Detecting exosomes specifically: a multiplexed device based on alternating current electrohydrodynamic induced nanoshearing," *Analytical chemistry*, vol. 86, no. 22, pp. 11125–11132, 2014.

[211] H. Im, H. Shao, Y. I. Park, V. M. Peterson, C. M. Castro, R. Weissleder, and H. Lee, "Label-free detection and molecular profiling of exosomes with a nano-plasmonic sensor," *Nature biotechnology*, vol. 32, no. 5, pp. 490–495, 2014.

[212] B. W. Drinkwater, "Dynamic-field devices for the ultrasonic manipulation of microparticles," *Lab on a Chip*, vol. 16, no. 13, pp. 2360–2375, 2016.

[213] T. Leong, L. Johansson, P. Juliano, S. L. McArthur, and R. Manasseh, "Ultrasonic separation of particulate fluids in small and large scale systems: a review," *Industrial and Engineering Chemistry Research*, vol. 52, no. 47, pp. 16555–16576, 2013.

[214] F. J. Trujillo, P. Juliano, G. Barbosa-Cánovas, and K. Knoerzer, "Separation of suspensions and emulsions via ultrasonic standing waves–a review," *Ultrasonics sonochemistry*, vol. 21, no. 6, pp. 2151–2164, 2014.

[215] P. B. Muller, R. Barnkob, M. J. H. Jensen, and H. Bruus, "A numerical study of microparticle acoustophoresis driven by acoustic radiation forces and streaming-induced drag forces," *Lab on a Chip*, vol. 12, no. 22, pp. 4617–4627, 2012.

[216] F. Kiebert, S. Wege, J. Massing, J. König, C. Cierpka, R. Weser, and H. Schmidt, "3d measurement and simulation of surface acoustic wave driven fluid motion: A comparison," *Lab on a Chip*, vol. 17, no. 12, pp. 2104–2114, 2017.

[217] J. Allard and N. Atalla, *Propagation of sound in porous media: modelling sound absorbing materials 2e.* John Wiley and Sons, 2009.

[218] J. Christensen, L. Martin-Moreno, and F. J. Garcia-Vidal, "Theory of resonant acoustic transmission through subwavelength apertures," *Physical review letters*, vol. 101, no. 1, p. 014301, 2008.

[219] G. Ward, R. Lovelock, A. Murray, A. P. Hibbins, J. R. Sambles, and J. Smith, "Boundary-layer effects on acoustic transmission through narrow slit cavities," *Physical review letters*, vol. 115, no. 4, p. 044302, 2015.

[220] P. A. Cotterill, D. Nigro, I. D. Abrahams, E. Garcia-Neefjes, and W. J. Parnell, "Thermo-viscous damping of acoustic waves in narrow channels: A comparison of effects in air and water," *The Journal of the Acoustical Society of America*, vol. 144, no. 6, pp. 3421–3436, 2018.

[221] V. Del Grosso, "Analysis of multimode acoustic propagation in liquid cylinders with realistic boundary conditions–application to sound speed and absorption measurements," *Acta Acustica united with Acustica*, vol. 24, no. 6, pp. 299–311, 1971.

[222] K. Baik, J. Jiang, and T. G. Leighton, "Acoustic attenuation, phase and group velocities in liquid-filled pipes: Theory, experiment, and examples of water and mercury," *The Journal of the Acoustical Society of America*, vol. 128, no. 5, pp. 2610–2624, 2010.

[223] E. Dokumaci, "On the effect of viscosity and thermal conductivity on sound propagation in ducts: A re-visit to the classical theory with extensions for higher order modes and presence of mean flow," *Journal of Sound and Vibration*, vol. 333, no. 21, pp. 5583–5599, 2014.

[224] L. Elvira-Segura, "Acoustic wave dispersion in a cylindrical elastic tube filled with a viscous liquid," *Ultrasonics*, vol. 37, no. 8, pp. 537–547, 2000.

[225] P. Liangh and H. Scarton, "Coincidence of thermoelastic and thermoviscous acoustic waves in fluid-filled elastic tubes," *Journal of sound and vibration*, vol. 250, no. 3, pp. 541–565, 2002.

[226] M. Settnes and H. Bruus, "Forces acting on a small particle in an acoustical field in a viscous fluid," *Physical Review E*, vol. 85, no. 1, p. 016327, 2012.

[227] P. Augustsson, R. Barnkob, S. T. Wereley, H. Bruus, and T. Laurell, "Automated and temperature-controlled micro-piv measurements enabling long-term-stable microchannel acoustophoresis characterization," *Lab on a Chip*, vol. 11, no. 24, pp. 4152–4164, 2011.

[228] R. Barnkob, P. Augustsson, T. Laurell, and H. Bruus, "Measuring the local pressure amplitude in microchannel acoustophoresis," *Lab on a Chip*, vol. 10, no. 5, pp. 563–570, 2010.

[229] K. D. Frampton, S. E. Martin, and K. Minor, "The scaling of acoustic streaming for application in micro-fluidic devices," *Applied Acoustics*, vol. 64, no. 7, pp. 681–692, 2003.

[230] M. F. Hamilton, Y. A. Ilinskii, and E. A. Zabolotskaya, "Acoustic streaming generated by standing waves in two-dimensional channels of arbitrary width," *The Journal of the Acoustical Society of America*, vol. 113, no. 1, pp. 153–160, 2003.

[231] S. M. Hagsäter, T. G. Jensen, H. Bruus, and J. P. Kutter, "Acoustic resonances in microfluidic chips: full-image micro-piv experiments and numerical simulations," *Lab on a Chip*, vol. 7, no. 10, pp. 1336–1344, 2007.

[232] J. Spengler, W. Coakley, and K. Christensen, "Microstreaming effects on particle concentration in an ultrasonic standing wave," *AIChE journal*, vol. 49, no. 11, pp. 2773–2782, 2003.

[233] M. Hey, "Gw gray. molecular structure and the properties of liquid crystals. london and new york (academic press) 1962. vii+ 314 pp. price 63s," *Mineralogical magazine and journal of the Mineralogical Society*, vol. 33, no. 260, pp. 440–440, 1963.

[234] R. Williams, "Domains in liquid crystals," *The Journal of Chemical Physics*, vol. 39, no. 2, pp. 384–388, 1963.

[235] G. H. Heilmeier, "Transient behavior of domains in liquid crystals," *The Journal of Chemical Physics*, vol. 44, no. 2, pp. 644–647, 1966.

[236] G. H. Heilmeier, L. A. Zanoni, and L. A. Barton, "Dynamic scattering: A new electrooptic effect in certain classes of nematic liquid crystals," *Proceedings of the IEEE*, vol. 56, no. 7, pp. 1162–1171, 1968.

[237] J. R. Pellam and J. Galt, "Ultrasonic propagation in liquids: I. application of pulse technique to velocity and absorption measurements at 15 megacycles," *The journal of chemical physics*, vol. 14, no. 10, pp. 608–614, 1946.

[238] W. Hoyer and A. Nolle, "Behavior of liquid-crystal compounds near the isotropic-anisotropic transition," *The Journal of Chemical Physics*, vol. 24, no. 4, pp. 803–811, 1956.

[239] B. Cook and R. Werchan, "Mapping ultrasonic fields with cholesteric liquid crystals," *Ultrasonics*, vol. 9, no. 2, pp. 88–94, 1971.

[240] J. Havlice, "Visualisation of acoustic beames using liquid crystals," *Electronics Letters*, vol. 20, no. 5, pp. 477–478, 1969.

[241] Y. Kagawa, T. Hatakeyama, and Y. Tanaka, "Detection and visualization of ultrasonic fields and vibrations by means of liquid crystals," *Journal of Sound and Vibration*, vol. 36, no. 3, pp. 407–IN6, 1974.

[242] L. Kessler and S. Sawyer, "Ultrasonic stimulation of optical scattering in nematic liquid crystals," *Applied Physics Letters*, vol. 17, no. 10, pp. 440–441, 1970.

[243] H. Mailer, K. Likins, T. Taylor, and J. Fergason, "Effect of ultrasound on a nematic liquid crystal," *Applied Physics Letters*, vol. 18, no. 4, pp. 105–107, 1971.

[244] K. Kemp and S. Letcher, "Ultrasonic determination of anisotropic shear and bulk viscosities in nematic liquid crystals," *Physical Review Letters*, vol. 27, no. 24, p. 1634, 1971.

[245] E. D. Lieberman, J. D. Lee, and F. C. Moon, "Anisotropic ultrasonic wave propagation in a nematic liquid crystal placed in a magnetic field," *Applied Physics Letters*, vol. 18, no. 7, pp. 280–281, 1971.

[246] A. Lord Jr and M. Labes, "Anisotropic ultrasonic properties of a nematic liquid crystal," *Physical Review Letters*, vol. 25, no. 9, p. 570, 1970.

[247] M. Witkowska-Borysewicz and A. Sliwiński, "Optically detected variations of nematic liquid crystal orientation induced by ultrasound," *Journal de Physique*, vol. 44, no. 3, pp. 411–420, 1983.

[248] K. Miyano and Y. Shen, "Domain pattern excited by surface acoustic waves in a nematic film," *Applied Physics Letters*, vol. 28, no. 9, pp. 473–475, 1976.

[249] K. Miyano and Y. Shen, "Excitation of stripe domain patterns by propagating acoustic waves in an oriented nematic film," *Physical Review A*, vol. 15, no. 6, p. 2471, 1977.

[250] R. M. White and F. W. Voltmer, "Direct piezoelectric coupling to surface elastic waves," *Applied physics letters*, vol. 7, no. 12, pp. 314–316, 1965.

[251] W. Lee and S.-H. Chen, "Acousto-optical effect induced by ultrasound pulses in a nematic liquid-crystal film," *Applied Optics*, vol. 40, no. 10, pp. 1682–1685, 2001.

[252] H. Moritake, S. Morita, R. Ozaki, T. Kamei, and Y. Utsumi, "Fast-switching microwave phase shifter of coplanar waveguide using ferroelectric liquid crystal," *Japanese journal of applied physics*, vol. 46, no. 6L, p. L519, 2007.

[253] S. Sato and H. Ueda, "Effects of surface acoustic waves on molecular orientation in nematic liquid crystals," *Japanese Journal of Applied Physics*, vol. 20, no. 7, p. L511, 1981.

[254] C. Sripaipan, C. F. Hayes, and G. T. Fang, "Ultrasonically-induced optical effect in a nematic liquid crystal," *Physical Review A*, vol. 15, no. 3, p. 1297, 1977.

[255] R. Ozaki, T. Shinpo, M. Ozaki, and H. Moritake, "Reorientation of cholesteric liquid crystal molecules using acoustic streaming," *Japanese journal of applied physics*, vol. 46, no. 6L, p. L489, 2007.

[256] R. Ozaki, T. Shinpo, M. Ozaki, and H. Moritake, "Lasing in cholesteric liquid crystal oriented by acoustic streaming," *Japanese journal of applied physics*, vol. 47, no. 2S, p. 1363, 2008.

[257] Y. J. Liu, X. Ding, S. S. Lin, J. Shi, I. Chiang, and T. J. Huang, "Surface acoustic wave driven light shutters using polymer-dispersed liquid crystals," *Advanced materials*, vol. 23, no. 14, pp. 1656–1659, 2011.

[258] D. W. Gerdt, M. C. Baruch, and C. M. Adkins, "Ultrasonic liquid crystal-based underwater acoustic imaging," in *Liquid Crystal Materials, Devices, and Applications VII*, vol. 3635, pp. 58–65, SPIE.

[259] J. S. Sandhu, H. Wang, and W. J. Popek, "Liquid crystal-based acoustic imaging," in *Liquid Crystal Materials, Devices, and Flat Panel Displays*, vol. 3955, pp. 94–108, SPIE.

[260] J. Sandhu, R. Schmidt, and P. La Riviere, "Full-field acoustomammography using an acousto-optic sensor," *Medical physics*, vol. 36, no. 6Part1, pp. 2324–2327, 2009.

[261] Y. Shimizu, D. Koyama, M. Fukui, A. Emoto, K. Nakamura, and M. Matsukawa, "Ultrasound liquid crystal lens," *Applied Physics Letters*, vol. 112, no. 16, p. 161104, 2018.

[262] S. Copar, Z. Kos, T. Emersic, and U. Tkalec, "Microfluidic control over topological states in channel-confined nematic flows," *Nature communications*, vol. 11, no. 1, pp. 1–10, 2020.

[263] J. Selinger, M. Spector, V. Greanya, B. Weslowski, D. Shenoy, and R. Shashidhar, "Acoustic realignment of nematic liquid crystals," *Physical Review E*, vol. 66, no. 5, p. 051708, 2002.

[264] H. Moritake, J. Kim, K. Yoshino, and K. Toda, "Director orientation measurement of nematic liquid crystal using velocity change of shear horizontal wave," *Japanese journal of applied physics*, vol. 43, no. 9S, p. 6780, 2004.

[265] M. Inoue, K. Yoshino, H. Moritake, and K. Toda, "Evaluation of nematic liquid-crystal director-orientation using shear horizontal wave propagation," *Journal of applied physics*, vol. 91, no. 5, pp. 2798–2802, 2002.

[266] C. Tu and G. W. Farnell, "Thickness effects in overlay guides for elastic surface waves," report, MCGILL UNIV MONTREAL (QUEBEC) DEPT OF ELECTRICAL ENGINEERING, 1972.

[267] J. J. Campbell and W. R. Jones, "A method for estimating optimal crystal cuts and propagation directions for excitation of piezoelectric surface waves," *IEEE Transactions on Sonics and Ultrasonics*, vol. 15, no. 4, pp. 209–217, 1968.

[268] W. Helfrich, "Orienting action of sound on nematic liquid crystals," *Physical Review Letters*, vol. 29, no. 24, p. 1583, 1972.

[269] S. Nagai and K. Iizuka, "Ultrasonic imaging utilizing a nematic liquid crystal," *Molecular Crystals and Liquid Crystals*, vol. 45, no. 1-2, pp. 83–101, 1978.

[270] S. Nagai, A. Peters, and S. Candau, "Acousto-optical effects in a nematic liquid crystal," *Revue de Physique Appliquée*, vol. 12, no. 1, pp. 21–30, 1977.

[271] T. Wu, W. Qiao, Y. Chiu, and Y. Lo, *Optofluidic lab-on-a-chip devices for photomedicine applications*, pp. 169–184. Elsevier, 2015.

[272] D. Psaltis, S. R. Quake, and C. Yang, "Developing optofluidic technology through the fusion of microfluidics and optics," *nature*, vol. 442, no. 7101, pp. 381–386, 2006.

[273] J. Cuennet, A. Vasdekis, L. De Sio, and D. Psaltis, "Optofluidic modulator based on peristaltic nematogen microflows," *Nature Photonics*, vol. 5, no. 4, pp. 234–238, 2011.

[274] H. Huang and Y. Zhao, "Optofluidic lenses for 2d and 3d imaging," *Journal of Micromechanics and Microengineering*, vol. 29, no. 7, p. 073001, 2019.

[275] D. Erickson, D. Sinton, and D. Psaltis, "Optofluidics for energy applications," *Nature Photonics*, vol. 5, no. 10, pp. 583–590, 2011.

[276] C. Monat, P. Domachuk, and B. Eggleton, "Integrated optofluidics: A new river of light," *Nature photonics*, vol. 1, no. 2, pp. 106–114, 2007.

[277] A. H. Yang, S. D. Moore, B. S. Schmidt, M. Klug, M. Lipson, and D. Erickson, "Optical manipulation of nanoparticles and biomolecules in sub-wavelength slot waveguides," *Nature*, vol. 457, no. 7225, pp. 71–75, 2009.

[278] W. M. Gibbons, P. J. Shannon, S.-T. Sun, and B. J. Swetlin, "Surface-mediated alignment of nematic liquid crystals with polarized laser light," *Nature*, vol. 351, no. 6321, pp. 49–50, 1991.

[279] M. Schadt, H. Seiberle, and A. Schuster, "Optical patterning of multi-domain liquid-crystal displays with wide viewing angles," *Nature*, vol. 381, no. 6579, pp. 212–215, 1996.

[280] I.-C. Khoo, *Liquid crystals*. John Wiley and Sons, 2022.

[281] M. Schiekel and K. Fahrenschon, "Deformation of nematic liquid crystals with vertical orientation in electrical fields," *Applied Physics Letters*, vol. 19, no. 10, pp. 391–393, 1971.

[282] A. Sengupta, U. Tkalec, M. Ravnik, J. M. Yeomans, C. Bahr, and S. Herminghaus, "Liquid crystal microfluidics for tunable flow shaping," *Physical review letters*, vol. 110, no. 4, p. 048303, 2013.

[283] T. Emersic, R. Zhang, Z. Kos, S. Copar, N. Osterman, J. J. De Pablo, and U. Tkalec, "Sculpting stable structures in pure liquids," *Science advances*, vol. 5, no. 2, p. eaav4283, 2019.

[284] K.-y. Hashimoto and K.-Y. Hashimoto, *Surface acoustic wave devices in telecommunications*, vol. 116. Springer, 2000.

[285] B. Liu, X. Chen, H. Cai, M. M. Ali, X. Tian, L. Tao, Y. Yang, and T. Ren, "Surface acoustic wave devices for sensor applications," *Journal of semiconductors*, vol. 37, no. 2, p. 021001, 2016.

[286] Y. Chen, A. A. Nawaz, Y. Zhao, P.-H. Huang, J. P. McCoy, S. J. Levine, L. Wang, and T. J. Huang, "Standing surface acoustic wave (ssaw)-based microfluidic cytometer," *Lab on a Chip*, vol. 14, no. 5, pp. 916–923, 2014.

[287] X. Ding, S.-C. S. Lin, B. Kiraly, H. Yue, S. Li, I.-K. Chiang, J. Shi, S. J. Benkovic, and T. J. Huang, "On-chip manipulation of single microparticles, cells, and organisms using surface acoustic waves," *Proceedings of the National Academy of Sciences*, vol. 109, no. 28, pp. 11105–11109, 2012.

[288] X. Ding, Z. Peng, S.-C. S. Lin, M. Geri, S. Li, P. Li, Y. Chen, M. Dao, S. Suresh, and T. J. Huang, "Cell separation using tilted-angle standing surface acoustic waves," *Proceedings of the National Academy of Sciences*, vol. 111, no. 36, pp. 12992–12997, 2014.

[289] F. Guo, Z. Mao, Y. Chen, Z. Xie, J. P. Lata, P. Li, L. Ren, J. Liu, J. Yang, and M. Dao, "Three-dimensional manipulation of single cells using surface acoustic waves," *Proceedings of the National Academy of Sciences*, vol. 113, no. 6, pp. 1522–1527, 2016.

[290] K. Länge, F. J. Gruhl, and M. Rapp, *Surface Acoustic Wave (SAW) biosensors: coupling of sensing layers and measurement*, pp. 491–505. Springer, 2013.

[291] A. Zhang, Y. Zha, and J. Zhang, "A surface acoustic wave micropump to pump fluids from a droplet into a closed microchannel using evaporation and capillary effects," *AIP Advances*, vol. 4, no. 12, p. 127144, 2014.

[292] L. Migara and J.-K. Song, "Standing wave-mediated molecular reorientation and spontaneous formation of tunable, concentric defect arrays in liquid crystal cells," *NPG Asia Materials*, vol. 10, no. 1, pp. e459–e459, 2018.

[293] I. M. Daniel, S. Wooh, J. Sandhu, and W. Hamidzada, *Acoustographic nondestructive evaluation of composite materials*, pp. 325–332. 1988.

[294] H. Moritake, J. Kim, K. Yoshino, and K. Toda, "Director orientation measurement of nematic liquid crystal using velocity change of shear horizontal wave," *Japanese journal of applied physics*, vol. 43, no. 9S, p. 6780, 2004.

[295] P. Pieranski, S. Čopar, M. H. Godinho, and M. Dazza, "Hedgehogs in the dowser state," *The European Physical Journal E*, vol. 39, no. 12, pp. 1–10, 2016.

[296] A. N. Beris and B. J. Edwards, *Thermodynamics of flowing systems: with internal microstructure.* Oxford University Press on Demand, 1994.

[297] S. Chen and G. D. Doolen, "Lattice boltzmann method for fluid flows," *Annual review of fluid mechanics*, vol. 30, no. 1, pp. 329–364, 1998.